Title
Fantastic Lanthanides and Methods to Model their Photodetachment

Permalink
https://escholarship.org/uc/item/1nt782zz

Author
Harb, Hassan

Publication Date
2021

Peer reviewed|Thesis/dissertation

UNIVERSITY OF CALIFORNIA, MERCED

Fantastic Lanthanides and Methods to Model their Photodetachments

by

Hassan Harb

A dissertation submitted in partial satisfaction of the
requirements for the degree of
Doctor of Philosophy

in

Chemistry

Committee in charge:
Professor Christine Isborn, Chair
Professor Hrant P. Hratchian, Advisor
Professor Aurora Pribram-Jones
Professor Roummel Marcia

Spring 2021

The dissertation of Hassan Harb is approved:

_____   5/13/2021
Christine Isborn, Chair   Date

_____   5/12/2021
Hrant P. Hratchian, Advisor   Date

_____   5/14/2021
Aurora Pribram-Jones   Date

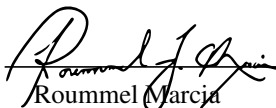   5/13/2021
_____
Roummel Marcia   Date

University of California, Merced

To my father, my mother, my sisters, my brother, my partner, and my comrades.
To the Lebanese October 2019 revolution and the hope it brought along with it.
To those who dare to dream of and struggle for a better world shared by all.
To Internationalism.

Acknowledgments

First and foremost, I would like to thank my advisor Professor Hrant P. Hratchian for his mentoring and guidance throughout this long journey. Hrant hasnnot only been a great research mentor to work for, but also provided the means for a safe and healthy work space where we all get to freely express ourselves and experiment with our own scientific ideas. hrant's way of motivating my scientific curiousity was like no other. He always encouraged me to think outside the box and seek answers that would fulfill both the small and the big questions in science.

I would also like to thank my committee members Professor Christine Isborn, Professor Aurora Pribram-Jones, and Professor Roummel Marcia for all the help and guidance in this rather long path through graduate school. The insightful comments and helpful discussions during our annual meetings and throughout the years have been fruitful in guiding me into the right path of critically thinking about scientific questions and properly addressing them to the scientific community.

Additionally, I would like to express my appreciation to all members of the Hratchian group. Namely, I would like to thank Dr Lee Thompson who was a postdoc in the lab at the time I joined (2015). Over the course of my first two years, Lee made sure to guide me into the proper ways of thinking about electron detachment processes. His help, comments, and discussions got me to be more interested in the underlying chemistry and physics of the problems we were tackling.

Most of the work done in this dissertation was driven by the very fruitful collaboration with Professor Caroline Chick Jarrold at Indiana University. I would like to express my thankfulness to Prof. Caroline and to the leading graduate student in her lab, Jarrett Mason. The intriguing and challenging problems that our two labs worked on together resulted in a new and profound understanding of the underlying chemistry of classes of lanthnaide-based molecules.

My sincerest thanks goes to my partner Zeena who has been by my side throughout this roller coaster. We have both gone through a lot together and she has expressed her support at every step of this. Even though Zeena's field lies under social sciences, she admired the beauty of simulating chemical reactions using supercomputers. She insisted to add her own touch to the dissertation, so she decided to design her own version of a rather more colorful form of Jacob's Ladder (figure 1.1). Without her special way of continuous support, this journey would have not been a manageable one.

I would also like to express my thanks to a group of supportive friends: Samantha Bidwell, whom we first met during our first days of graduate school, has always been by my side since day one. I can still remember the first weeks of graduate school when I was still homeless and she kindly offered her couch for me to stay at while the two of us were looking for a place for me to live. Zaher Slim, whom I shared an apartment with for years, and whom we have been friends for almost our lives. Zaher made sure to check on me and discuss my science. He was there to consolidate me when papers got rejected and share my joyful moments when I figure out a challenging problem in my research. Mohammed (Nour) Hodeib, who made sure to check up on me every single day and who always asks me about updates and progress on research projects, and who always knew when to provide me with a fun and sometimes an intellectual distraction whenever I felt like work was overwhelming. Elsa Saade, Rami Dinnawi, Ali Fahs, Sarah Bahr, Loulwa Sweid, Madison Martin,

Ahmed El Baradei, Vivienne Badaan, Assem Bazzi, Walid Slika and Sheyda Partovi for the fact that each one of them made this challenging journey much easier with every drink we had and every discussion we dragged ourselves into.

Lastly, I would like to express my my gratitude to my family. The sacrifices that they all made throughout the years have made me get to the point where I completed my doctoral degree. They all have shown me what it really means to give up on everything in order to provide the best opportunity for their ambitious kid who once used to dream about having their own small laboratory at home. All that I have achieved today could not have happened without their unconditional support.

<div align="center">**Curriculum Vitae**</div>

Hassan Harb

University of California, Merced	Email:	hharb@ucmerced.edu
Chemistry and Chemical Biology	Homepage:	mercedtobeirut.wordpress.com
5200 N. Lake Rd.	Twitter:	@hharb_92
Merced, CA 95343	GitHub:	@HassanHarb92

Personal

Date of Birth:	September 20, 1992
Country of Citizenship:	Lebanon

Education

2015 - Present	PhD candidate in Computational Quantum Chemistry Advisor: Prof. Hrant Hratchian Dept. of Chemistry and Chemical Biology University of California, Merced Dissertation Title: *Fantastic Lanthanides* *and Methods to Model their Photodetachment*
2013 - 2015	MS in Inorganic Chemistry https://aub.edu.lbAmerican University of Beirut Advisor: Prof. Faraj Hasanayn Thesis title: *Metathesis Model of Ester Hydrogenation by Ruthenium* *Octahedral Pincer Complex Using DFT Calculations*
2010-2013	BS in Chemistry Lebanese American University Beirut, Lebanon
2014 (December)	Theoretical f-element chemistry course University of Helsinki
2014 (July)	Molecular Electronic Structure Theory course Sostrup Summer School

Employment

2019 - Present	Graduate Research Assistant	
	University of California, Merced	
2018 - 2019	Graduate Tutor - The Chemistry Center	
	University of California, Merced	
2015 - 2019	Teaching Assistant	
	University of California, Merced	
2013 - 2015	Teaching Assistant	
	American University of Beirut	
2013 (June - August)	Research Assistant	
	American University of Beirut	

Awards

2019	Graduate Dean's Dissertation Fellowship ($11,000 + tuition)
2019	UC Merced CCB Travel Award ($800)
2018	UC Merced CCB Travel Award ($800)
2017	UC Merced CCB Travel Award ($800)
2010	Merit Scholarship ($40,000)
	Lebanese American University

Coding Experience

Python, LaTeX, perl, Fortran, Kotlin, C++.
Representative Code: *https://github.com/HassanHarb92/BEATLES*

Publications

Presentations

11. "Improving Photoionization Spectral Assignments From Calculations Using the Natural Ionization Orbitals Model", *American Chemical Society Spring 2021 National Meeting*, April 13, 2021.

10. "Modeling the photodetachment processes of lanthanide oxide and boride clusters ", 258th *American Chemical Society National Meeting*, August 25, 2019.

9. "Near-peer tutoring: Chemistry center designed to increase success of a diverse student body in STEM", 258th *American Chemical Society National Meeting*, August 25, 2019.

8. "Modeling the Photelectron Spectra of $CeO_2B_x^-$ (x=2,3) and CeB_6^- Clusters", *International Symposium on Molecular Spectroscopy*", June 18, 2019.

7. "Structure and Bonding of Lanthanide Hydroxides", *West Coast Theoretical Chemistry Symposium*, March 28, 2018.

6. "On the Structure and Bonding of Lanthanide Hydroxides", 255th *American Chemical Society National Meeting*, March 22, 2018.

5. "Integrating Writing and Computing in the General Chemistry Curriculum", 255th *American Chemical Society National Meeting*, March 18, 2018.

4. "A computational study of the photoelectron spectra of europium-oxide, -hydride, and -hydroxide", 253rd *American Chemical Society National Meeting*, April 4, 2017.

3. "Chemistry Abroad — Great Summer", *Lebanese American University*, November 14, 2014.

2. "On student activism", *TEDxLAU*, August 23, 2014.

1. "Panel discussion on perspectives of Lebanese secterianism", *American University of Beirut*, April 30, 2014.

subsection*Journal Articles

15. <u>H. Harb</u> and H. P. Hratchian, "Anisotropy Parameter and Photoelectron Angular Distribution at Near-threshold from Natural Ionization Orbitals", *in prep*.

14. <u>H. Harb</u>, L. M. Thompson, and H. P. Hratchian, "Resolving the EuO^- Photoelectron Spectrum", *in prep*.

13. <u>H. Harb</u>, B. Fairless, and H. P. Hratchian, "A Cluster of Clusters: *Ab initio* Calculations Indicate Contributions From Multiple Isomers in the Photoelectron Spectrum of LiB_6^-", *to be submitted*.

12. <u>H. Harb</u> and H. P. Hratchian, "A Density Functional Theory Investigation of the Mechanism of Water Reactivity with Ce_2O^- Clusters", *in press*.

11. J. L. Mason, <u>H. Harb</u>, A. Abou Taka, C. D. Huizenga, A. J. McMahon, H. P. Hratchian, and C. C. Jarrold, "Photoelectron-Valence Electron Interactions Facilitate Two-Electron Transitions in the Photoelectron Spectra of Gd_2O^-", *in prep*

10. R. Brisbin, <u>H. Harb</u>, J. Debow, J. Fettinger, H. P. Hratchian, and R. Baxter, "The Effect of Torsional Angle on Reversible Electron Transfer in Donor-Acceptor Frameworks Using Bis(imino)pyridines As a Proxy", *to be submitted*.

9. <u>H. Harb</u> and H. P. Hratchian, "ΔSCF Dyson Orbitals and Pole Strengths from Natural Ionization Orbitals", *J. Chem. Phys.*, **2021**, 154, 084104.

8. J. L. Mason, <u>H. Harb</u>, A. Abou Taka, A. J. McMahon, C. D. Huizenga, H. Corzo, H. P. Hratchian, and C. C. Jarrold, "Photoelectron spectra of $Gd_2O_2^-$ and non-monotonic photon-energy dependent variations in populations of close-lying neutral states", *J. Phys. Chem. A*, **2021**, 125, 3, 857–866.

7. J. L. Mason, <u>H. Harb</u>, J. E. Topolski, H. P. Hratchian, and C. C. Jarrold, "Exceptionally Complex Electronic Structures of Lanthanide Oxide and Small Molecules", *Acc. Chem Res*, **2019**, 52, 11, 3265-3273.

6. <u>H. Harb</u>, L. M. Thompson, and H. P. Hratchian, "On the Linear Geometry of Lanthanide Hydroxides (Ln−OH, Ln=La-Lu)", *Phys. Chem. Chem. Phys*, **2019**, 21, 21890-21897.

5. X. Cai, A. Tohti, C. Ramirez, <u>H. Harb</u>, J. Fettinger, H. P. Hratchian, and B. Stokes, "Dispersion-Controlled Regioselective Acid-Catalyzed Intramolecular Hydroindolation of cis-Methindolylstyrenes to Access Tetrahydrobenzo[cd]indoles", *Org. Lett.*, **2019**, 21, 6, 1574-1577.

4. J. L. Mason, <u>H. Harb</u>, C. D. Huizenga, J. Ewigleben, J. E. Topolski, H. P. Hratchian, and C. C. Jarrold, "Electronic and Molecular Structures of the CeB_6 Monomer", *J. Phys. Chem. A*, **2019**, 123, 10, 2040-2048.

3. J. L. Mason, <u>H. Harb</u>, J. E. Topolski, H. P. Hratchian, and C. C. Jarrold, "A Tale of Two Stabilities: How One Boron Atom Affects a Switch in Bonding Motifs", *J. Phys. Chem. A*, **2018**, 122, 9879.

2. L. M. Thompson, <u>H. Harb</u>, and H. P. Hratchian, "Natural Ionization Orbitals for Interpreting Electron Detachment Processes", *J. Chem. Phys.*, **2016**, 144, 204117.

1. F. Hasanayn, and <u>H. Harb</u>, "A Metathesis Model for Dehydrogenative Coupling of Amines With Alcohols and Esters Into Carboxamides by Milstein's [Ru(PNN)(CO)(H)] Catalyst", *Inorg. Chem.*, **2014**, 53, 8334.

Contents

xii

List of Figures

List of Tables

Abstract

Fantastic Lanthanides and Methods to Model their Photodetachment

by

Hassan Harb

Doctor of Philosophy

in

Chemistry

University of California, Merced

Professor Christine Isborn, Chair

Modeling the photoelectron spectra of lanthanide-based clusters provides unprecedent insight on the complex electronic structures of these clusters. To provide a compact orbital representation of the ionization process, the natural ionization orbitals (NIO) model, developed by our group, allows the differentiation between pure one-electron detachments and detachments that involve shake-up/shake-off transitions. From that, we also established a direct relationship between Δ-SCF Dyson orbitals and NIOs. We formulated pole strength calculations from the NIO model. These pole strengths are directly related to experimental cross-sections observed in photoelectron spectroscopy. Results from photoelectron spectroscopy allows us to further investigate the structure, bonding, and reactivity of these clusters, these include non-trivial bonding motifs, insights into the reactivity of these clusters, and probing photoelectron – neutral interactions. Studying lanthanide-based clusters provide useful insight to the electronic structure of bulk materials with unique magnetic, electronic, and optical properties.

Chapter 1

Introduction

"In describing the effect of the electric spark in chemical decomposition and synthesis, Wiedemann declares that this is more the concern of chemistry. In the same case the chemists declare that it is rather a matter which concerns physics. Thus at the point of contact of molecular and atomic science, both declare themselves incompetent, while it is precisely at this point that the greatest results are to be expected"

— Dialectics of Nature, Friedrich Engels (1883).

The discovery of quantum mechanics marked a turning point when the classical laws of physics catastrophically failed at interpreting molecular and atomic level experimental observations (e.g. Blackbody Radiation, Double-Slit experiments, Photoelectric Effect). Richard Feynman defines quantum mechanics as the "behavior of matter and light in all its details and, in particular, of the happenings on an atomic scale." [1] In his lectures on physics, Feynmann added that "Things on a very small scale behave like nothing that you have any direct experience about. They do not behave like waves, they do not behave like particles, they do not behave like clouds, or billiard balls, or weights on springs, or like anything that you have ever seen." [1] Rather than a continuous description of position and momentum, quantum mechanics restricts those values to discrete packets, or *quanta*. In addition, quantum mechanics presents a description of objects in the framework involving both particle and wave natures. Quantum mechanics also sets a fundamental limit to the precision of measurements of the position and momentum of particles, a principle that is known as the *Uncertainity Principle*. [2]

1.1 The Birth of Quantum Chemistry

Inspired by the work of Max Planck, Albert Einstein, Neils Bohr, Louis de Broglie and many others, Erwin Schrodinger proposed a linear partial differential equation that describes a quantum mechanical system. [3,4]

$$-\frac{\hbar}{i}\frac{\partial \Psi(x,t)}{\partial t} = -\frac{\hbar^2}{2m}\frac{\partial^2 \Psi(x,t)}{\partial^2 x} + V(x)\Psi(x,t) \tag{1.1}$$

The wavefunction $\Psi(x, t)$ can be separated into a time-dependent and a position dependent part:

$$\Psi(x, t) = f(t)\psi(x) \tag{1.2}$$

where x denotes the spatial coordinates of the electrons and t represents time. Plugging eq. 1.2 into eq. 1.1, one can derive the time-dependent component of the wavefunction:

$$f(t) = e^{\frac{-iEt}{\hbar}} \tag{1.3}$$

Separating the time component of the Schrodinger Equation, we can derive the time-independent Schrodinger Equation:

$$\hat{H}|\psi\rangle = E|\psi\rangle \tag{1.4}$$

where $\hat{H}$ is the Hamiltonian operator, E is the total energy of the system and $|\psi\rangle$ is the wave function that contains all information about the system under interest. Solving the Schrodinger Equation is the key to obtain the total energy and all properties of a molecule. The Hamiltonian operator in atomic units[1] for a many-body (molecular) system is given by

$$\hat{H} = -\sum_{i=1}^{N} \frac{1}{2}\nabla_i^2 - \sum_{A=1}^{M} \frac{1}{2M_A}\nabla_A^2 - \sum_{i=1}^{N}\sum_{A=1}^{M} \frac{Z_A}{r_{iA}} + \sum_{i=1}^{N}\sum_{j>i}^{N} \frac{1}{r_{ij}} + \sum_{A=1}^{M}\sum_{B>A}^{M} \frac{Z_A Z_B}{R_{AB}} \tag{1.5}$$

where the first two terms describe the kinetic energies of the electrons and the nucleus, respectively. The third, fourth, and fifth terms represent the potential energies of the system: Coulombic electron-nuclear attraction, Coulombic electron-electron repulsion, and Coulombic nuclear-nuclear repulsion, respectively. The Laplacian operators ∇_i^2 and ∇_A^2 are constituted of terms that involve second-order differentiation with respect to the coordinates of electron i and nucleus A. Z_A is the atomic number of nucleus A and M_A is the relative mass of nucleus A with respect to the mass of one electron. R_{AB}, r_{iA}, and r_{ij} represent the relative positions of nuclei A and B, electron i and nucleus A, and electrons i and j, respectively.

In order to simplify the Schrodinger equation, the Born-Oppenheimer approximation is commonly used to separate the electronic and the nuclear components of the Hamiltonian. [5] Since nuclei are much heavier than electrons, the Born-Oppenheimer approximation assumes that the motions of electrons are much faster than those of the nuclei. Hence, electronic and nuclear motions are separable. The Born-Oppenheimer approximation can be invoked to obtain an electronic solution to the Schrodinger equation at fixed nuclear coordinates. In the Born-Oppenheimer approximation, the electronic Hamiltonian can be written as:

$$\hat{H}_e = -\sum_{i=1}^{N} \frac{1}{2}\nabla_i^2 - \sum_{i=1}^{N}\sum_{A=1}^{M} \frac{Z_A}{r_{iA}} + \sum_{i=1}^{N}\sum_{j>i}^{N} \frac{1}{r_{ij}} + \sum_{A=1}^{M}\sum_{B>A}^{M} \frac{Z_A Z_B}{R_{AB}} \tag{1.6}$$

Since the nuclear coordinates are fixed, the fourth term in the above equation reduces into a parameter that solely depends on the fixed inter-nuclear distances R_{AB}. Thus, we can rewrite

---

[1]In atomic units, electron rest-mass (m_e), elementary charge (e), and reduced plank's constant ($\hbar$) are set to 1.

equation 1.6 as follows:

$$\hat{H}_e = -\sum_{i=1}^{N} \frac{1}{2}\nabla_i^2 - \sum_{i=1}^{N}\sum_{A=1}^{M} \frac{Z_A}{r_{iA}} + \sum_{i=1}^{N}\sum_{j>i}^{N} \frac{1}{r_{ij}} + \hat{V}_{NN}(R). \tag{1.7}$$

Equation 1.7 can be separated into one-electron components (first and second terms in the equation) and two-electron components (third term in the equation). Solutions to the one-electron term have been analytically obtained as solutions of the Hydrogen atom wavefunction. However, when the number of electrons in a system is larger than one, the partial differential equation (1.4) has no analytic solution. This "failure" to solve the multi-electronic Schrodinger equation arises from the inability to separate the variables in the third term of equation 1.7. Hence, various methods have been implemented in order to obtain an approximate solution to the Schrodinger Equation of a many-body system.

1.2 The Hartree-Fock Approximation

One method to solve the Schrodinger equation for molecular systems is the Hartree-Fock method. [6–12]. This method assumes that the many-body problem can be reduced into a system of effective one-body problems. In other words, the molecular wavefunction is approximated as an anti-symmetrized Slater determinant of one-particle molecular orbital (MO) wavefunctions:

$$|\Psi_0\rangle = |\psi_1\psi_2\ldots\psi_N| \tag{1.8}$$

where each ψ_i can be written as a linear combination of atomic orbitals (basis functions) χ_μ:

$$\psi_i = \sum_{\mu=1}^{N_{basis}} C_{\mu i}\chi_\mu \tag{1.9}$$

The Fock operator, f is defined as

$$f(1) = h(1) + \sum_{j}^{N/2} 2(J_j(1) - K_j(1)) \tag{1.10}$$

where $h(1)$ is the one electron term that provides information about the electron kinetic energy and the electron-nuclear attraction

$$h(1) = -\frac{1}{2}\nabla_1^2 - \sum_{A=1}^{M} \frac{Z_A}{r_{1A}} \tag{1.11}$$

$J_j(1)$ and $K_j(1)$ are the coulomb and exchange components of the Fock-operator:

$$J_j(1) = \sum_{j} \int \psi_j^*(2) \frac{1}{r_{12}} \psi_j(2)\, dr_2 \tag{1.12}$$

4

$$K_j(1) = \sum_j \int \psi_j^*(2) \frac{1}{r_{12}} \psi_i(2) \, dr_2 \tag{1.13}$$

The variational principle is used to minimize the total energy with respect to the MO coefficients, (shown in eq. 1.9) which provide an upper-bound to the true energy of the system. This transforms the Hartree-Fock equations into a pseudo-eigenvalue problem:

$$FC = SC\epsilon \tag{1.14}$$

C is the molecular orbitals coefficients matrix. The elements of **F** (Fock-matrix) and **S** (overlap matrix) are given by

$$F_{\mu\nu} = \langle \psi_\mu | \hat{f} | \psi_\nu \rangle \tag{1.15}$$

$$S_{\mu\nu} = \langle \psi_\mu | \psi_\nu \rangle \tag{1.16}$$

Equation 1.14 was developed by Roothan and is often referred to as the Hartree-Fock-Roothan equation. The nonorthogonal nature of the basis sets in the Roothan equation gives rise to the overlap matrix. In order to transform the above equation into an eigenvalue equation, one needs to consider a process to orthogonalize the basis functions. Lowdin's symmetric orthogonalization is used here to overcome the nonorthogonality problem. It involves using inverse square root of the overlap matrix, $S^{-\frac{1}{2}}$, as the orthogonalizing transformation matrix. We then define an auxiliary coefficient matrix, C' and its relationship to C as

$$C' = S^{\frac{1}{2}} C \tag{1.17}$$

$$C = S^{-\frac{1}{2}} C' \tag{1.18}$$

Substituting C in the Hartree-Fock-Roothan equation, we obtain

$$F' C' = C' \epsilon \tag{1.19}$$

where $F' = (S^{-\frac{1}{2}})^\dagger F S^{-\frac{1}{2}}$. The transformed coefficients, C' can be solved by diagonalizing F' and then C can be obtained from equation 1.18.

Hartree-Fock Energy

The restricted close-shell Hartree-Fock energy given by

$$E_{HF} = \frac{1}{2} \sum_{\mu\nu} P_{\mu\nu}(H_{\mu\nu}^{core} + F_{\mu\nu}) \tag{1.20}$$

Where $P_{\mu\nu}$ is the density matrix defined in terms of the MO coefficients (equation 1.9) as

$$P_{\mu\nu} = 2 \sum_{i=1} C_{\mu i}^* C_{\nu i} \tag{1.21}$$

In the unrestricted framework, and after employing the Pople-Nesbet equations [13], the unrestricted

Hartree-Fock energy becomes

$$E_{UHF} = \frac{1}{2} \sum_{\mu\nu}^{k} (P_{\mu\nu}^T H_{\mu\nu}^{core} + P_{\mu\nu}^\alpha F_{\mu\nu}^\alpha + P_{\mu\nu}^\beta F_{\mu\nu}^\beta) \qquad (1.22)$$

1.2.1   Correlation Energy

Hartree-Fock theory provides an independent particle model framework to solve the Schrodinger equation. Hartree-Fock theory replaces the instantaneous electron-electron coulomb repulsion with the individual interaction of one electron with an average of the remaining electrons. This approach is usually referred to as the mean-field approach. This approximation introduces errors in the calculated energies and wavefunctions, which is referred to as *Correlation Energy* [14] The *correlation energy* is defined as the difference between the exact non-relativistic energy and the Hartree-Fock energy:

$$E_{corr} = E_{exact} - E_{HF} \qquad (1.23)$$

While Hartree-Fock theory is able to retrieve up 99% of the total energy, the remaining 1% (correlation energy) remains vital for proper description of chemical processes.

Correlation energy is of two types: *dynamic* and *static*. Dynamic correlation arises from the instantaneous movement of electrons with respect to each other. On the other hand, static correlation (sometimes referred to as non-dynamic correlation) occurs when the single Slater determinant framework fails to describe the system under study, i.e. there exists one or more degenerate or near-degenerate states.

In order to account for electron correlation, several approaches have been made. (CI, CC, MBPT,...) These methods start with a reference Hartree-Fock determinant then "correct" its energy and wavefunction to include higher order forms of the energy and/or the wavefunction. Theoretically, implementation of these methods to infinite order gives rise to the "exact" solution of the Schrodinger equation within the given basis. Yet, the major drawback of these methods is their high computational cost relative to the Hartree-Fock calculations. For example, performing a Full Configurational Interaction (Full-CI) calculation allows us to calculate the exact energy by employing an N-electron basis. This is different than Hartree-Fock, where 1-electron basis is used. In Full-CI, the N-electron basis is determined by using substituted determinants from Hartree-Fock reference (equation 1.24. Yet Full-CI calculations scale as $O(N!)$ (where N is the number of basis functions) which makes it quite impractical for use within our current computational resources.

$$|\Phi_0\rangle = |\Psi\rangle + \sum_{ia} C_i^a |\Psi_i^a\rangle + \sum_{ij\,ab} C_{ij}^{ab} |\Psi_{ij}^{ab}\rangle + \sum_{ijk\,abc} C_{ijk}^{abc} |\Psi_{ijk}^{abc}\rangle + ... \qquad (1.24)$$

1.3   Density-Functional Theory

A different approach to solving the many-body problem was introduced first by Hoenberg and Kohn and later by Kohn and Sham, known as Density Functional Theory (DFT). DFT states that the ground-state energy of a particular system can be defined in terms of electron density, $\rho(r)$. In addition, DFT proposes that the energy can be written as a function of density, which in turn is a function of electron position. Hence, energy can be referred to as a functional of density, $E[\rho(r)]$.

The main challenge of DFT is to find the exact, universal, functional that can precisely determine the energy and consequently calculate all molecular and electronic properties. [15] While, in principle, DFT is exact, the true functional is yet to be discovered. The general form of a density functional is given in eq. 1.25. The first term is the kinetic energy of the electrons, the second term is the external potential, the third term is the coulombic repulsion energy, and the fourth term is the exchange-correlation term. [16–18]

$$E[\rho(r)] = T_0[\rho(\mathbf{r})] + \int d\mathbf{r}\rho[\mathbf{r}]\nu_{ext}(\mathbf{r}) + E_H[\rho(\mathbf{r})] + E_{xc}(\mathbf{r}) \tag{1.25}$$

Various approximations have been made to determine an approximate functional that can better incorporate correlation effects. Some of these functionals incorporated the density as well as its gradients into the formulation of the functionals. In addition, different forms of approximate DFT functionals have also introduced a number of empirical parameters. [18–21] Density functional approximations can be classified into several families(figure 1.1) [22]:

- The Local Density Approximation (LDA) [23], which was initially formulated by Kohn and Sham. This method depends solely on electron density. It also implements the exchange-correlation energy term of a uniform electron gas.

- The Generalized Gradient Approximation (GGA). This approach aims at correcting the errors in LDA approaches by including gradient corrections. [24, 25]

- The Meta-Generalized Gradient Approximation. These functionals make use of higher order density gradients, namely Kohn-Sham kinetic energies. [26]

- Hybrid Density functionals, which combine the exchange-correlation from GGA and a percentage or all (exact) of Hartree-Fock exchange. [26, 27]

- Radom Phase Approximation (RPA), this method is described as a many-body approach that is extended to involve the unoccupied Kohn-Sham orbitals. [28, 29]

1.4   Methods for Simulating Electron Detachment Processes

Theoretical simulations of electron detachment processes is widely used to interpret and understand experiment in a diverse range of chemistry and physics applications. [30–42] In order to understand how the wavefunction changes upon ionization, two families of methods exist. The first is based on Koopmans' approach [43] in which the hole is described by an orbital in the N electron calculation. The second is based on a delta self-consistent field (ΔSCF) between an N and N − 1 electron calculation. According to Koopmans' theorem, the ionization energy is equal to the negative of the orbital energy of the ionized electron in both a restricted (open-shell) Hartree-Fock (HF) and Density Functional Theory (DFT) calculations, [44] although in DFT calculations this value is highly dependent on the functional used and is often significantly incorrect. [45] ΔSCF methods typically calculate the ionization potential by removing the ionized electron excited into a continuum state and explicitly calculating the N − 1 electron system. Such simulations usually employ DFT, owing to the excellent balance of simplicity, cost, and accuracy. However, the generality of the

Utopia of Chemical Accuracy

$$E_c^{MP2-like} \qquad \text{RPA}$$
$$E_x^{HF} \qquad \text{Hybrid Functionals}$$
$$\nabla^2\rho(r) \qquad \text{Meta-GGA}$$
$$\nabla\rho(r) \qquad \text{GGA}$$
$$\rho(r) \qquad \text{LDA}$$
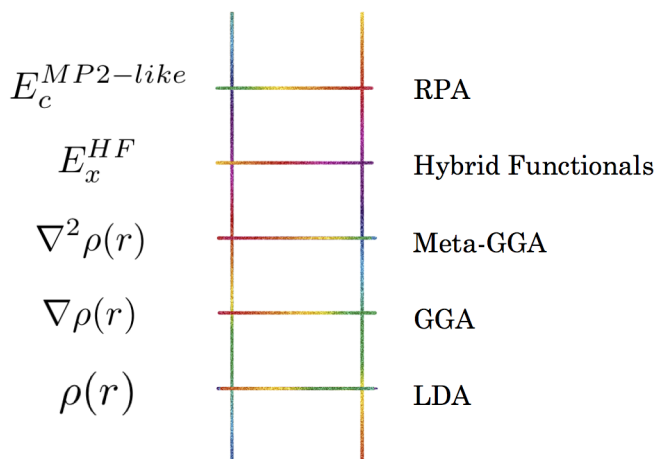
Figure 1.1: Jacob's Ladder of density functional approximations

approach enables any ground state (GS) method to be employed including post-self-consistent field (SCF) methods. Analysis of the wavefunction response to ionization in the Koopmans method and models derived from it is simple. Yet, in studies that employ ΔSCF inclusion of relaxation effects accompanying ionization mean that the resulting canonical orbitals are usually difficult to interpret as they are often spatially diffuse and may not easily map directly to the ionization event.

In order to better interpret and understand the nature of electronic transitions, unitary transformations of the orbital space to which the energy is invariant can be applied. Prior approaches based on such transformations have been reported for analyzing simulations of electron transitions. In the limiting case of electronic excitation to a non-continuum state, Martin's Natural Transition Orbitals (NTO) [46] and the attachment-detachment density analysis of Head-Gordon et al. [47] have been proposed. Ziegler et al. have developed the natural orbitals for chemical valence (NOCV) scheme for analysis of chemical bonding which, in a similar approach to this work, utilizes a natural orbital (NO) orbital transformation of a difference density, ΔP. [48] The NOCV approach constructs ΔP from the difference of total and fragment (promolecular) densities while this study uses a ΔP constructed from the density of initial and final states of an electronic transition.

Methodologies with specific application to ionization calculations in which the size of the occupied-virtual (ov) orbital space changes include the ΔSCF method of Martin and Davidson. [49] This approach, which is directly analogous to the NTO scheme, constructs an N_{elec} by $N_{elec—1}$ overlap matrix between molecular orbitals (MOs) in the ground and ionized states, where Nelec is the number of electrons in the ground state. Singular value decomposition of this matrix accomplishes a corresponding orbital transformation [50] with eigenvalues identifying the overlap between MOs in the ground and excited states. The ground state orbital without a corresponding excited state occupied orbital can be labeled the orbital from which the ionized electron originated.

The study of excitations beyond single reference wavefunctions can be achieved through

8

calculation of Dyson orbitals. [51–54] Dyson orbitals (eq. 1.26) are calculated from the overlap between the N electron wavefunction and the N − 1 electron wavefunction of the ionized state and generalize Koopmans' theorem to correlated wavefunctions obtained through post-SCF methods.

$$\phi_{IF}^d = \sqrt{N} \int \Psi_I^N(1, 2, ..., n) \Psi_F^{N-1}(2, ..., n) d2..dn \tag{1.26}$$

While the Dyson orbital approaches are incredibly powerful, they exist within a wavefunction framework and cannot be easily extended to DFT. Furthermore, the requirement for a correlated wavefunction limits the size of system that can be tackled. Approaches for approximating Dyson orbitals from DFT calculations to reduce computational scaling have been proposed by Dauth et al. [52] However, beyond wavefunction analysis, Dyson orbitals have had particular application in electron propagator theories (EPTs), the formally equivalent one-electron Green's function, and equation-of-motion (EOM) approaches to obtain accurate ionization energies. Most closely related in scope to this work are the developments of EOM-coupled cluster (CC) by Krylov et al. on the study of ionization processes [55–60] and the electron propagator theory (EPT) work of Ortiz et al. [61–67]

Experimentally, electron momentum spectroscopy (EMS) provides the ability to probe the electron density of individual orbitals during ionization events. [68–76] Although EMS can access the complete valence shell, it does this with lower resolution than more widely used photoelectron spectroscopy (PES). However, the EMS cross section is proportional to the square of the Dyson orbital associated with the transition and in this regard has the potential to image the electron/hole density of individual orbitals.

1.5 Motivation: Modeling the Photodetachments of Lanthanide-based Clusters

The work discussed here has appeared as a part of a paper published in 2019 by Accounts of Chemical Research. [77]

The lanthanide series, situated at the bottom end of the periodic table, is a family of "rare earth" metals that are characterized by close-lying 6s, 5d, and 4f subshells. [77]. The lanthanides start at Lanthanum ($4f^0 5d^1 6s^2$) and end at Lutetium ($4f^{14} 5d^1 6s^2$) and the general trend is an increase in 4f subshell occupancy as atomic numbers increase. Electrons occupying the 4f orbitals in lanthanides are considered core-like. This core-like feature of the 4f orbitals results in very similar properties for near-neighbors in the series. [78] Yet it is noteworthy to mention that the partially filled 4f subshells give rise to complex electronic and magnetic properties of lanthanide-based materials. [79–83]

Developing new materials and enhancing the usage and activity of existing ones necessitates the determination of how different types of surface defects enhance particular reactions alongside the mechanism that affects chemical activity. [84,85] In order to avoid direct experimental interrogations of surfaces, which is complicated by low defect concentration and dynamic nature of the surface [84–86], small gas-phase clusters are studied. This alternative approach has been verified by the localized nature of the electronic structures of surface defects. [87–95]

To set the starting point for our theoretical studies, we adapt a useful construct by Bob Field: the term "*superconfiguration*". This term, which was used by Field to provide details onto the ligand field theory treatment of LnO⁻, [96] is considered to be a general characterization of orbital occupancy shared by the constellation of close-lying electronic states in these systems. To better illustrate the term, consider Ce^{2+} center in the ground state of the CeO molecule. The CeO molecule has been a subject of numerous experimental [97–100] and theoretical [101, 102] studies, and all have shown that the Ce^{2+} center exhibits a singly occupied 4f orbital and a singly occupied diffuse 6s-like orbital, thus its superconfiguration is $4f6s$. Many other highly-oxidized lanthanides exhibit 4f and 6s subshells. [103–108]

Theoretical simulations of photodetachments of lanthanide-based clusters give rise to two main complications:

a. The existence of a constellation of close-lying electronic states of anions and neutrals raises the concern of the multireference nature of the target states. However, with increasing size of the cluster, multireference methods tend to get more complicated, and, in many cases, adopting these methods is impractical within the current computational resources. Thus, in lieu of using a multireference approach, we have used DFT calculations. Although their limitations must be recognized, DFT calculations provide useful qualitative insights into the leading superconfiguration description of the electronic structures of small lanthanide-based clusters. [77]

b. The high atomic number of lanthanides gives rise to increased and significant contributions from relativistic effects. Although various methods to treat relativistic effects have been implemented, our aim is to adapt a model chemistry that can provide a decent recovery of relativistic contributions to energy and properties while maintaining a near mean-field cost.

In order to simulate the photoelectron spectra of lanthanide-based molecules and perform spectral assignments, Franck-Condon [109–111] progressions were calculated between the vibronic states of the anion and those of the corresponding neutral. While different approaches rely on calculating the adiabatic and vertical detachment energies, we point out that, in principle, this approach is useful. Yet, in practice, complications arise due to unclear spectral signals which could be attributed to several competing detachments or could be due to significant changes in geometries between the anion and the neutral. [112]

1.6   Dissertation Overview

This dissertation provides a thorough and compact approach to ionization processes within the ΔSCF approach. We use this approach to study the detachment processes of several lanthanide-based clusters in order to determine the molecular and electronic structures of such clusters. Moreover, we utilize the results from the photodetachment studies to provide an enhanced description on the structure, bonding, and reactivity of these clusters.

In chapter 2 we present a new and compact orbital representation of the ionization process and its application in photodetachment calculating cross-sections. This new model enhances spectral assignments by providing orbital-based tools to determine the nature of the electronic detachments,

in addition to provide metrics to distinguish between multiple competitive detachments. We have shown that DFT calculations can provide adequate results that can provide a qualitative description of the electronic and molecular properties of small lanthanide clusters. (Chapters 6 and 7) Furthermore, we use a comparable approach to extend our studies to cover similar clusters. Following up on a similar approach, our calculations have resulted in more enhanced and detailed spectral assignments for the previously published LiB_6^- photoelectron spectrum. [113] (Chapter 3) The work described in chapters 4 and 5 highlights significant outcomes of studying the photoelectron spectra of these molecules. Motivated by the work done by Kafader and coworkers on EuOH [114], chapter 4 provides an in-depth description of the covalent triple bond that governs the structure and bonding of not only EuOH, but also the complete LnOH (Ln = La – Lu) series. In a similar manner, the mixed experimental and computational study on water reactivity with cerium clusters by Topolski [115] and Felton [116], we provide a mechanistic study on the reactivity of the smallest identified cluster, i.e. Ce_2O^-, with water, as an approach to fully understand the reactivity of these clusters with water from the molecular perspective. The final chapter (chapter 2) presents new theory of calculating photoelectron angular distributions and cross-sections using the natural ionization orbital model presented earlier in this chapter. This new model will better enhance spectral assignments by providing orbital-based tools to determine the angular momentum of the orbital from which the electron was detached, in addition to provide metrics to distinguish between multiple competitive detachments.

Chapter 2

∆ SCF Dyson Orbitals and Pole Strengths from Natural Ionization Orbitals

"If you beat your head against the wall, it is your head that breaks and not the wall."

— Antonio Gramsci.

The work described here has appeared in two papers published in 2016 and 2021 by the Journal of Chemical Physics. [117, 118]
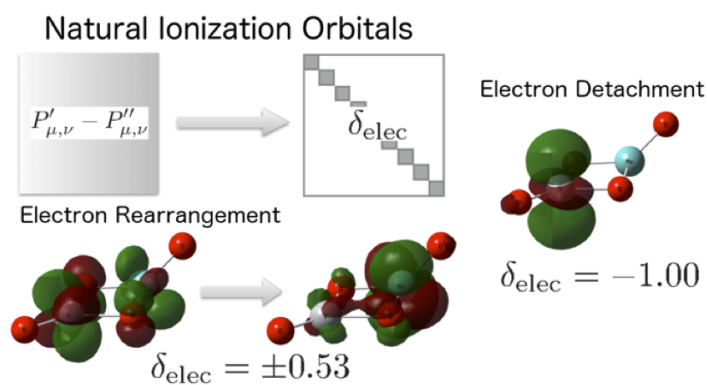
Abstract

The calculation of photoionization cross-sections can play a key role in spectral assignments using modeling and simulation. In this work, we provide formal relationships between pole strengths, which are proportional to the photoionization cross-section, and terms related to the Natural Ionization Orbital model for ∆SCF calculations. A set of numerical calculations using the developed

models is carried out. Pole strength values computed using the two approaches developed for ΔSCF calculations demonstrate excellent agreement with an electron propagator theory model.

2.1 Introduction

The study of electron detachment provides a rich space for interrogating the structure of atomic and molecular systems. [30–41] Indeed, modern applications of photodetachment methods such as cryo-SEVI have been used to provide exceptional insight to structure, bonding, and reactivity in an array of molecular systems. [119–124] Modeling electron detachment processes with electronic structure theory is often essential to interpret experimental results and make definitive spectral assignments. Work from our lab in collaboration with experimental colleagues considering such experiments, for example, has led to detailed understanding of a number of transition metal and inner-transition metal containing systems. [42, 77, 112, 125–128]

Particularly because electron number changes in electron detachment and electron attachment, the quality of electronic structure theory studies of such processes can be quite sensitive to electron correlation treatment. [129–131] Early approaches specifically designed to address this concern implemented wave function models beyond the Hartree-Fock (HF) self–consistent field (SCF) model. These included the Equations of Motion (EOM) approach of Simons [132–137] and the electron propagator theory (EPT) scheme of Cederbaum. [138–141] Those pioneering theory advances subsequently led to two families of modern post-SCF theories: The EOM approach developed ionization potential (IP) and electron affinity (EA) EOM coupled cluster models by Krylov, [55–60, 142, 143] Piecuch, [144–150] and Bartlett. [151–153] Recent advances in EPT include the hierarchy of schemes by Ortiz and co-workers. [61–67, 154–158]

An alternative approach to computing electron detachment/attachment energies is to straightforwardly evaluate the difference between two independent calculations – one for the initial state and one for the final state. At the SCF level this gives the Δ-Self–Consistent–Field (ΔSCF) approach. At times, the ΔSCF scheme has been used to specifically refer to energy differences calculated at the HF level of theory. In recognition of the common application of such schemes in the literature, this work employs a broader definition that includes energy differences from Kohn-Sham Density Functional Theory (DFT), as well as HF, calculations. The ΔSCF approach is subject to the inherent limitations of the underlying SCF model chemistries. Nevertheless, for systems with bound initial and final detachment/attachment electronic structures, ΔSCF is the workhorse approach for studying electron detachment/attachment. Owing to the inclusion of dynamic electron correlation in approximate functionals, DFT calculations have been especially successfully used in a number of such studies and often yield reasonably good agreement with experimental and high-level computational results.

The ΔDFT scheme has a few key additional advantages over post-SCF models. First, the affordability and wide availability of analytic DFT gradient theory readily allows researchers to include geometric relaxation effects to evaluate both vertical and adiabatic detachment/attachment energies. Furthermore, efficient analytic DFT second-derivative codes provide a direct and simple means for including vibrational structure in simulated spectra. As our own work has shown, access to these additional handles is critical for discriminating between spectral candidates and making

definitive spectral assignments. [42, 112, 125–128]

A particular advantage of EPT models in electron detachment/attachment studies has been their direct relationship to the Dyson orbital framework. Dyson orbitals, also referred to as generalized overlap amplitudes, are defined as the overlap between n_{el} and $n'_{el} = (n_{el} - 1)$ wave functions. [55, 58, 159–163] The Dyson orbital ϕ^d is defined by

$$\phi^d = \sqrt{N} \int \Psi^i_{n_{el}}(\mathbf{x}_1, \mathbf{x}_2, ..., \mathbf{x}_{n_{el}}) \Psi^f_{n'_{el}}(\mathbf{x}_2, ..., \mathbf{x}_{n_{el}}) d\mathbf{x}_2...d\mathbf{x}_{n_{el}} \tag{2.1}$$

where the initial and final states are given by $\Psi^i_{n_{el}}$ and $\Psi^f_{n'_{el}}$, respectively. (For the purposes of this work, the wave functions are taken to be real.) The Dyson orbital provides a one-electron orbital description of the source of electron loss/gain. The Dyson picture also provides a formal relationship between theory and observed experimental cross-sections (*vide infra*). [154, 164] Namely, the norm of the resulting Dyson orbital of Eq. (2.1), the pole strength P_n, is proportional to the likelihood of transition from a particular orbital and is given by [165]

$$P_n = \int |\phi^d|^2 dx \tag{2.2}$$

Evaluation of the Dyson orbital from a ΔSCF pair of calculations can be carried out using a corresponding orbital based approach. [50, 161, 164, 166] However, in practice ΔSCF based investigations typically employ Koopmans' theorem when interpreting the electron loss or gain being simulated. [43, 167–169] Critically, the Koopmans' approach ignores electron density relaxation in response to ionization.

A few years ago, our lab proposed the natural ionization orbital (NIO) model to provide such an interpretive tool for use with ΔSCF calculations. [117] The NIO model utilizes a natural orbital transformation of the difference density formed from the initial (with N electrons) and final (with $N \pm 1$ electrons) SCF solutions. The NIO model has been instrumental in making photodetachment spectral assignments and developing an orbital description of the ionization process that would not have been correct using the Koopmans' theorem framework. Indeed, over the last few years we have employed NIO analysis in studies of complicated photoelectron spectra of transition metal and lanthanide containing clusters. [77, 112, 125, 127, 128, 170, 171]

In this report, we develop a formal relationship between the NIO model and the Dyson orbital theory. Importantly, this work establishes a clear and concise connection between the non-zero NIO singular-values – which we term *relaxation NIOs* – and the formal Dyson orbital pole strength. After providing two different derivations of this relationship, the method is numerically demonstrated on a set of seven small molecule electron detachment processes. Comparisons are made between EPT and NIO based Dyson orbitals and pole strengths.

2.2 Methods

As mentioned, the evaluation of a Dyson orbital in the ΔSCF model can be readily determined using the corresponding orbital approach between occupied one-electron molecular orbitals (MOs) of n_{el} electron and $n_{el} - 1$ electron Slater determinants. That framework was used by Martin and Davidson in 1977 to develop their *corresponding ionization orbitals* model. [46, 161] More

14

recently, our lab proposed an orbital description for electron detachment processes studied with ΔSCF approaches based on a natural orbital transformation of the difference density from initial and final states, which we named the NIO model. [117]

While it is a relatively straightforward exercise to show that the corresponding ionization orbital and NIO models both yield a one-electron orbital that is proportional to the ΔSCF Dyson orbital, evaluation of the Dyson orbital pole strength using the NIO model is less clear. With this in mind, this section begins by briefly defining the NIO model. Then, we develop two different derivations for evaluating pole strengths in terms of the NIO model. We note that the remainder of this discussion focuses on electron detachment; analogous expressions can be derived for electron attachment processes.

2.2.1   Natural Ionization Orbitals

The NIO model provides a compact orbital representation of ionization processes by using the difference of one-particle density matrices and provides a means for interpreting and characterizing electronic detachment processes, including distinguishing between one-electron transitions and shake-up/shake-off transitions. [77, 112, 125, 127, 128] In the case of electron detachment, the difference density matrix, $\mathbf{\Delta}_P$, can be calculated for a vertical detachment according to

$$\mathbf{\Delta}_P = \mathbf{P}^f - \mathbf{P}^i \tag{2.3}$$

where $\mathbf{P}^i$ and $\mathbf{P}^f$ are *initial* ground state and *final* ionized state density matrices (which are in the atomic orbital (AO) basis in our implementation). The change in the number of electrons, Δn_{el}, can be given in terms of the difference density matrix and the AO overlap matrix, $\mathbf{S}$, according to

$$\Delta_{el} = \mathrm{tr}(\mathbf{\Delta}_P \mathbf{S}) \tag{2.4}$$

where $\mathrm{tr}(\mathbf{X})$ denotes the trace of matrix $\mathbf{X}$.

A set of orbitals, ϕ_P, can be constructed in the occupation number basis from the canonical MO, $\{\psi_p\}$, according to

$$(\phi_1, \phi_2, ..., \phi_{N_{basis}}) = (\psi_1, \psi_2, ..., \psi_{N_{basis}})\mathbf{U} \tag{2.5}$$

where the rotation matrix $\mathbf{U}$ can be determined by solving the eigenvalue equation

$$\mathbf{U}^T \mathbf{S}^{1/2} \mathbf{\Delta}_P \mathbf{S}^{1/2} \mathbf{U} = \delta_{elec} \tag{2.6}$$

In Eq. (2.6), δ_{elec} is a diagonal matrix containing the occupation change number for each NIO. The eigenvectors $\mathbf{U}$ can be back-transformed to the AO basis to give the NIO coefficients $\mathbf{V}$ according to

$$\mathbf{V} = \mathbf{S}^{-1/2} \mathbf{U} \tag{2.7}$$

15

2.2.2 NIO Pole Strength Model A: Determinant Approach

Following King et al., [166] we define $\mathbf{D}$ to be the overlap matrix between occupied MOs of the initial and final SCF solutions,

$$\mathbf{D} = \left(\mathbf{C}^f_{(\text{occ})}\right)^T \mathbf{S}\mathbf{C}^i_{(\text{occ})} \tag{2.8}$$

where $\mathbf{C}^i_{(\text{occ})}$ and $\mathbf{C}^f_{(\text{occ})}$ are the occupied MO coefficients of initial and final states, respectively. Singular-value decomposition of $\mathbf{D}$ yields

$$\mathbf{D} = \mathbf{Q}\boldsymbol{\Sigma}\mathbf{R}^T \tag{2.9}$$

The eigenvectors and eigenvalues of the product $\mathbf{D}\mathbf{D}^T$ are given by $\mathbf{Q}$ and $\boldsymbol{\Sigma}^2$,

$$\begin{aligned}
\mathbf{D}\mathbf{D}^T &= \left(\mathbf{C}^f_{(\text{occ})}\right)^T \mathbf{S}\mathbf{C}^i_{(\text{occ})} \left(\mathbf{C}^i_{(\text{occ})}\right)^T \mathbf{S}\mathbf{C}^f_{(\text{occ})} \\
&= \mathbf{Q}\boldsymbol{\Sigma}\mathbf{R}^T\mathbf{R}\boldsymbol{\Sigma}^T\mathbf{Q}^T = \mathbf{Q}\boldsymbol{\Sigma}^2\mathbf{Q}^T
\end{aligned} \tag{2.10}$$

where $\boldsymbol{\Sigma}^2$ is used to denote $\boldsymbol{\Sigma}\boldsymbol{\Sigma}^T$. Whereas the diagonal matrix of singular values $\boldsymbol{\Sigma}$ is rectangular, $\boldsymbol{\Sigma}^2$ is a square diagonal matrix. In the case of electron detachment, the common application of the NIO model used by our lab, the dimension of $\boldsymbol{\Sigma}^2$ is $n'_{el} = (n_{el} - 1)$.

We note that the initial and final state density matrices are given by

$$\mathbf{P}^i = \mathbf{C}^i_{(\text{occ})} \left(\mathbf{C}^i_{(\text{occ})}\right)^T \tag{2.11}$$

$$\mathbf{P}^f = \mathbf{C}^f_{(\text{occ})} \left(\mathbf{C}^f_{(\text{occ})}\right)^T \tag{2.12}$$

Eq. (2.10) can be rewritten as

$$\mathbf{D}\mathbf{D}^T = \left(\mathbf{C}^f_{(\text{occ})}\right)^T \mathbf{S}\mathbf{P}^i\mathbf{S}\mathbf{C}^f_{(\text{occ})} = \mathbf{Q}\boldsymbol{\Sigma}^2\mathbf{Q}^T \tag{2.13}$$

Using Eq. (2.3) gives

$$\left(\mathbf{C}^f_{(\text{occ})}\right)^T \mathbf{S}\left(\mathbf{P}^f - \boldsymbol{\Delta}_P\right)\mathbf{S}\mathbf{C}^f_{(\text{occ})} = \mathbf{Q}\boldsymbol{\Sigma}^2\mathbf{Q}^T \tag{2.14}$$

and

$$\begin{aligned}
&\left(\mathbf{C}^f_{(\text{occ})}\right)^T \mathbf{S}\mathbf{C}^f_{(\text{occ})} \left(\mathbf{C}^f_{(\text{occ})}\right)^T \mathbf{S}\mathbf{C}^f_{(\text{occ})} - \\
&\left(\mathbf{C}^f_{(\text{occ})}\right)^T \mathbf{S}\boldsymbol{\Delta}_P\mathbf{S}\mathbf{C}^f_{(\text{occ})} = \mathbf{Q}\boldsymbol{\Sigma}^2\mathbf{Q}^T
\end{aligned} \tag{2.15}$$

Given that the occupied canonical MOs form an orthonormal set, Eq. (2.15) becomes

$$\mathbf{I}_{n'_{el}} - \left(\mathbf{C}^f_{(\text{occ})}\right)^T \mathbf{S}\boldsymbol{\Delta}_P\mathbf{S}\mathbf{C}^f_{(\text{occ})} = \mathbf{Q}\boldsymbol{\Sigma}^2\mathbf{Q}^T \tag{2.16}$$

16

where $\mathbf{I}_{n'_{el}}$ is the identity matrix with dimension $(n'_{el} \times n'_{el})$.

Given that $\mathbf{U}$ is unitary, Eq. (2.6) can be used to write Eq. (2.16) as

$$\mathbf{I}_{n'_{el}} - \left(\mathbf{C}^f_{(occ)}\right)^T \mathbf{S}^{1/2} \mathbf{U} \delta_{elec} \mathbf{U}^T \mathbf{S}^{1/2} \mathbf{C}^f_{(occ)} = \mathbf{Q}\mathbf{\Sigma}^2\mathbf{Q}^T \tag{2.17}$$

Using Eq. (2.7) gives

$$\mathbf{I}_{n'_{el}} - \left(\mathbf{C}^f_{(occ)}\right)^T \mathbf{S}\mathbf{V} \delta_{elec} \mathbf{V}^T \mathbf{S}\mathbf{C}^f_{(occ)} = \mathbf{Q}\mathbf{\Sigma}^2\mathbf{Q}^T \tag{2.18}$$

which we rewrite as

$$\mathbf{T}_{(occ)} \delta_{elec} \mathbf{T}^T_{(occ)} = \mathbf{I}_{n'_{el}} - \mathbf{Q}\mathbf{\Sigma}^2\mathbf{Q}^T \tag{2.19}$$

Elements of $\mathbf{T}$ expand the NIOs in the final state MO basis,

$$T_{p\alpha} = \sum_{\mu\nu} C^f_{\mu p} S_{\mu\nu} V_{\nu\alpha} \tag{2.20}$$

where $\{\mu, \nu, \cdots\}$ denote atomic orbital basis functions, $\{p, q, \cdots\}$ denote molecular orbitals, and $\{\alpha, \beta, \cdots\}$ denote NIOs. Note that the rectangular matrix $\mathbf{T}_{(occ)}$ in Eq. (2.19) only includes expansion coefficients of Eq. (2.20) in the final state *occupied* MO sub-space.

Multiplying Eq. (2.19) on the left by $\mathbf{Q}^T$ and on the right by $\mathbf{Q}$ gives

$$\mathbf{Q}^T \mathbf{T}_{(occ)} \delta_{elec} \mathbf{T}^T_{(occ)} \mathbf{Q} = \mathbf{Q}^T \mathbf{I}_{n'_{el}} \mathbf{Q} - \mathbf{Q}^T \mathbf{Q}\mathbf{\Sigma}^2\mathbf{Q}^T\mathbf{Q} \tag{2.21}$$

Given that $\mathbf{Q}$ is unitary, Eq. (2.21) simplifies to

$$\mathbf{\Sigma}^2 = \mathbf{I}_{n'_{el}} - \mathbf{Q}^T \mathbf{T}_{(occ)} \delta_{elec} \mathbf{T}^T_{(occ)} \mathbf{Q} \tag{2.22}$$

Following King et al., [166] the square of the overlap of the initial and final state Slater determinants, i.e. the pole strength, is given by $\det\left(\mathbf{\Sigma}^2\right)$. Thus,

$$\det\left(\mathbf{\Sigma}^2\right) = \det\left(\mathbf{I}_{n'_{el}} - \mathbf{Q}^T \mathbf{T}_{(occ)} \delta_{elec} \mathbf{T}^T_{(occ)} \mathbf{Q}\right) \tag{2.23}$$

Therefore, the right-hand side of Eq. (2.23) also gives the overlap of these two Slater determinants, which will ultimately provide a means to calculate the pole strength associated with the Dyson orbital. Using Sylvester's determinant theorem, [172–175] Eq. (2.23) can be rewritten as

$$\det\left(\mathbf{\Sigma}^2\right) = \det\left(\mathbf{I}_{N_{basis}} - \mathbf{T}^T_{(occ)} \mathbf{T}_{(occ)} \delta_{elec}\right) \tag{2.24}$$

which provides a form for the pole strength that can be directly evaluated using terms formed in the NIO model according to

$$P_n = \det\left(\mathbf{I}_{N_{basis}} - \mathbf{T}^T_{(occ)} \mathbf{T}_{(occ)} \delta_{elec}\right) \tag{2.25}$$

2.2.3 NIO Pole Strength Model B: Trace Approach

The NIO model often yields only one non-zero eigenvalue corresponding to the one-electron Dyson orbital. However, in many cases the SCF determinant undergoes relaxation upon ionization relative to the converged initial state determinant. Under such conditions, the NIO analysis yields one or more pairs of fractional occupation change eigenvalues. Most common are cases with only one fractional NIO eigenvalue pair with appreciable magnitudes. Under such conditions, an approximate second approach for computing pole strengths from the NIO model can be developed.

The development of this approximate second model begins by taking the trace of Eq. (2.19) to give

$$\text{tr}\Big(\mathbf{T}_{(\text{occ})}\delta_{elec}\mathbf{T}^T_{(\text{occ})}\Big) = \text{tr}\Big(\mathbf{I}_{n'_{el}} - \mathbf{Q}\boldsymbol{\Sigma}^2\mathbf{Q}^T\Big) \tag{2.26}$$

Applying the cyclic rule of traces $\text{tr}(\mathbf{ABC}) = \text{tr}(\mathbf{BCA}) = \text{tr}(\mathbf{CAB})$, recalling that $\mathbf{QQ}^T = \mathbf{I}_{n'_{el}}$, and noting $\text{tr}(\mathbf{I}_{n'_{el}}) = n'_{el} = n_{el} - 1$ yield

$$\text{tr}\big(\boldsymbol{\Sigma}^2\big) = n_{el} - 1 - \text{tr}\Big(\delta_{elec}\mathbf{T}^T_{(\text{occ})}\mathbf{T}_{(\text{occ})}\Big) \tag{2.27}$$

Assuming no more than one corresponding orbital pair has an overlap less than 1, the trace of $\boldsymbol{\Sigma}^2$ is given by

$$\text{tr}\big(\boldsymbol{\Sigma}^2\big) = n_{el} - 2 + \sigma^2 \tag{2.28}$$

where σ^2 is the diagonal element of $\boldsymbol{\Sigma}^2$ associated with the single fractional-overlap corresponding orbital. Since $\boldsymbol{\Sigma}^2$ is diagonal and all other elements are equal to 1, the pole strength under this condition is equal to σ^2. Using Eqs. (2.27) and (2.28) gives an alternative and approximate expression for the ΔSCF pole strength using the NIO model as

$$P_n = \sigma^2 = 1 - \text{tr}\Big(\delta_{elec}\mathbf{T}^T_{(\text{occ})}\mathbf{T}_{(\text{occ})}\Big) \tag{2.29}$$

2.3 Numerical Tests

Numerical tests of NIO based pole strengths have been carried out on a set of seven vertical electron detachment processes. Electronic structure calculations were performed using a local development version of the Gaussian suite of programs. [176] The unrestricted HF method was used in all cases and the stability of all HF determinants was verified. [177, 178] All orbital surfaces shown in this work were generated using an outermost contour value of 0.02 a.u. Initial state geometries were optimized using standard methods. [179] Ionization energies calculated from ΔSCF and EPT methods are shown in the supporting information. While ionization potentials obtained with ΔSCF are lower than those obtained using EPT, we highlight that the aim of this study focuses on presenting the relationship between NIOs and Dyson orbitals rather than assessing the validities of ionization energies obtained using ΔSCF and EPT.

NIO analyses were performed using an open source code. [180] For each studied detachment, orbital occupation change numbers are reported (δ_{elec}). In the cases where reasonable orbital relaxation is observed, the projection of the orbitals onto the occupied manifold of the initial state (%occ) is also reported. We note that % occ is calculated using an approach similar to Eq. 2.20. In lieu of

Table 2.1: Pole strengths calculated using EPT, NIO trace, and NIO Determinant methods.

Molecule	NIO (Determinant)	NIO (Trace)	EPT
Formaldehyde	0.907	0.906	0.925
Nitromethyl Radical	0.847	0.845	0.911
H_2O	0.948	0.948	0.933
Chlorobenzene	0.897	0.895	0.901
CCl_4	0.933	0.933	0.913
NH_3	0.947	0.946	0.927
Ethanol	0.929	0.927	0.922

projecting the NIOs onto the final occupied state manifold, we project the NIO coefficients onto the *initial state* MOs followed by considering the subspace that maps onto the *occupied* manifold of the initial state.

NIO based pole strengths from ΔSCF calculations were compared to results from EPT outer-valence Green's function (OVGF) calculations. [138, 140, 165] Table 2.1 provides a comparison of pole strengths obtained from both the ΔSCF/NIO and EPT approaches. Tables S2 and S3 report $\langle S^2 \rangle$ and detachment energies for the HF and EPT calculations used in this work. Consistent with previous reports, HF theory with a modest basis set yields only modest agreement between vertical detachment energies evaluated using the ΔSCF approach and higher levels of theory. [181, 182] Nitromethyl radical exhibits a high degree of spin contamination and correspondingly poor ΔSCF vertical detachment energy. Nevertheless, as shown below, the chosen model chemistries are adequate for demonstrating the formal relationships for evaluating pole strengths developed above.

2.3.1 Formaldehyde

The first system considered is the valence electron detachment from the $^1A_1$ ground state of formaldehyde. The result is the $^2B_2$ state. The NIO analysis was carried out using a ΔSCF calculation performed at the UHF/6-311++G level of theory. Figure 2.1 shows the ΔSCF Dyson orbtial (the NIO with eigenvalue –1.0, depicting the electron hole) on the left and the Dyson orbital calculated using the EPT diagonal self-energy approximation on the right. In this case, it is clear that the ΔSCF and EPT based Dyson orbitals are qualitatively the same.

This first numerical example shows very good agreement between the NIO and EPT approaches for calculating Dyson orbital pole strength. The NIO model suggests minimal electron relaxation with small pairs of occupation change numbers ($|\delta_{elec}| < 0.2$), which yields a large pole strength. Using the NIO analysis yields ΔSCF pole strengths of 0.907 and 0.906 from the determinant and trace approaches, respectively. The EPT pole strength, P_n, is 0.925. The difference between the ΔSCF and EPT based values is roughly 2%.

2.3.2 Nitromethyl Radical

Calculations on the nitromethyl radical were carried out using the UHF/6-31g(3d,3p) model chemistry. Electron detachment from the ground state of the nitromethyl radical ($^1A' \leftarrow {}^2A''$) involves a meaningful degree of accompanying electron relaxation. As shown in the top panel of Fig. 2.2, the ΔSCF and EPT Dyson orbitals are essentially the same. Unlike the previous example
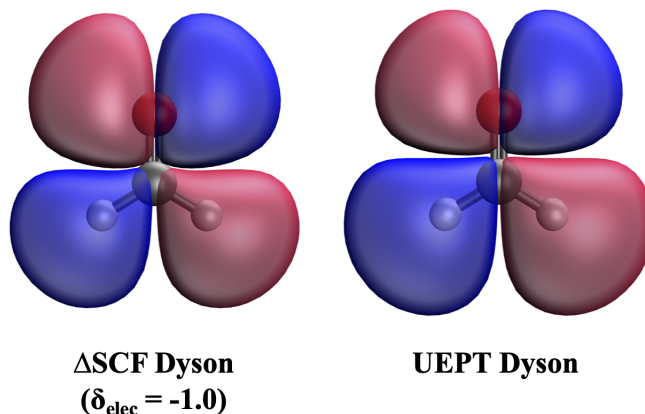
ΔSCF Dyson
(δ_{elec} = -1.0)

UEPT Dyson

Figure 2.1: ΔSCF (left) and EPT (right) Dyson orbitals associated with electron detachment of $^1A_1$ ground-state of formaldehyde.

case (formaldehyde), detachment from the nitromethyl radical results in meaningful orbital relaxation. As shown in in the boxed bottom panel of Fig. 2.2, there are two pairs of relaxation NIOs (one α pair and one β pair).

Projections onto the initial state occupied and virtual MO sub-spaces (or, equivalently, final state virtual and occupied MO sub-spaces) of relaxation NIO pairs show complementarity in their occupied/virtual decomposition. For example, the α relaxation NIO pair has initial state occupied MO projections of 62.3% and 37.8%. The β relaxation NIO pair has initial state occupied MO projections of 63.0% and 36.0%. The negative α relaxation NIO is 62.25% occupied in the initial state and the positive eigenvalue NIO constitutes of 37.75% of the initial occupied manifold. Similarly, the β relaxation NIO pair is associated with eigenvalues of $\delta_{elec} = \pm 0.26$. The positive eigenvalue NIO has a 63.01% occupied character and the negative-eigenvalue NIO has a 36.00% occupied character.

In previous work, we hypothesized that non-zero fractional change eigenvalues in the NIO analysis correspond to decreased pole strengths. [112] This work quantifies that relationship though Eqs. (2.25) and (2.29). Indeed, as shown in Table 2.1 the relaxation NIOs decrease the pole strength to ~ 0.85 in the ΔSCF model and ~ 0.91 in the EPT diagonal self-energy approximation. Notably, the approximate trace method of Eq. (2.29) is quite close to the exact ΔSCF pole strength result. The difference between the two ΔSCF methods is less than 0.5%. This test case presents the largest disagreement in calculated pole strengths between ΔSCF and EPT models. As noted previously, NIOs based on spin-unrestricted calculations do account for both orbital relaxation and some electron correlation contributions, but the unrestricted framework does introduce spin contamination. [117] In this particular case, the values of $\left\langle S^2 \right\rangle$ are 1.17 and 0.92 for the doublet and singlet states, respectively.

2.3.3 Water

The third system included in the test set is the electron detachment from the $^1A_1$ ground-state of water using the UHF/6-311G** model chemistry. Figure 2.3 shows the ΔSCF (left) and EPT (right) Dyson orbitals for $^1A_1 \rightarrow\ ^2B_1 + e^-$ detachment of water. As shown, these two approaches for evaluating electron detachment result in similar Dyson orbitals. NIO analysis shows three pairs of relaxation NIOs orbitals with very small electron change eigenvalues ($\left|\delta_{elec}\right| < 0.1$). The calculated ΔSCF pole strength using the NIO determinant and trace approaches is 0.948, which is only 1.68% different from the EPT OVGF pole strength.

2.3.4 Chlorobenzene

A second case in the test set exhibiting significant orbital relaxation with electronic detachment is the ionization of chlorobenzene. The ΔSCF and EPT calculations were run using the UHF/6-311G(d,p) level of theory. Figure 2.4 shows the computed Dyson orbitals associated with the $^2B_1 \leftarrow\ ^1A_1$ detachment of C_6H_5Cl. As with the previous examples, the ΔSCF and EPT Dyson orbitals closely resemble each other, describing electron detachment from a delocalized π^* orbital.

The NIO analysis shows a relaxation pair with electron occupation change eigenvalues of ±0.21, as shown in the bottom panel of Fig. 2.4. The orbital with a negative fractional occupation change has a 60.75% contribution from the initial state occupied MOs, while its complimentary relaxation NIO has a 39.25% contribution from the initial state occupied MOs. Two additional minor relaxation NIO pairs (not shown in Fig. 2.4) were found with occupation change values of ±0.12. As discussed above for the nitromethyl radical case, relaxation NIOs correspond to decreased pole strengths. Using the determinant and trace approaches, the calculated ΔSCF pole strengths are 0.895 and 0.897, respectively. Both values agree well with the EPT pole strength of 0.901.

2.3.5 Tetrachloromethane

Calculations on the vertical electron detachment energy for tetrachloromethane were carried out using the UHF/6-311G(d,p) level of theory. The ΔSCF and EPT Dyson orbitals corresponding to detachment from the ^1A ground state to the ^2A cation are shown in Fig. 2.5. Unlike the previous cases, there is a noticeable difference between the ΔSCF an EPT Dyson orbitals. This difference is due to the lack of symmetry in the cation SCF wave function. Neutral tetrachloromethane features a triply-degenerate highest-occupied molecular orbital (HOMO). The EPT method is able to correctly predict a symmetric description of the Dyson orbtial due to symmetry adaptation, which the ΔSCF model does not include. Notably, the degree of spin contamination in the cation – which one might expect to be meaningful – is quite modest with $\left\langle S^2 \right\rangle = 0.76$. As shown in Fig. 2.5, the ΔSCF Dyson orbital does share key features with the EPT Dyson orbital. The Dyson orbitals for each model are similarly delocalized and have the same general nodal structure. NIO analysis showed minor electron relaxation with two non-trivial relaxation NIO pairs with $\delta_{elec} = \pm 0.11$ and ±0.13. The resulting ΔSCF pole strength is 0.933 using both determinant and trace NIO approaches. The value is in very good agreement with the EPT pole strength of the detachment (0.913).

2.3.6 Ammonia

The detachment from ground state of ammonia ($^1A_1$) shows a Koopmans-like behavior. Both ΔSCF and EPT Dyson orbitals (Fig. 2.6) show that the detached electron originates from the $2a_1$ nitrogen lone pair orbital. In addition, NIO analysis showed only very slight orbital relaxation, with the most meaningful relaxation NIO pairs given by $\delta_{elec} \pm 0.11$. Calculations of pole strengths using the determinant and trace approaches yield values of 0.947 and 0.946, respectively. These values are very close to the EPT pole strength (0.927), with a difference of only 2%.

2.3.7 Ethanol

The final case considered in the test set electron detachment from the ground state of ethanol to form the ^2A radical cation. For this test, the UHF/6-311G** level of theory was employed. The ΔSCF and EPT Dyson orbitals are shown in Fig. 2.7. Both orbitals indicate electron detachment from a non-bonding MO. However, the ΔSCF Dyson orbital is more localized on the C–O bond, while the EPT Dyson orbital is delocalized over the whole molecule. The ΔSCF pole strengths calculated using determinant (0.929) and trace (0.927) approaches are in excellent agreement with the EPT pole strength (0.922).

2.4 Summary

This work presented two formulations relating Dyson orbital pole strength in ΔSCF calculations using the NIO model. The relationships described in Eqs. (2.25) and (2.29) show that the occupation change numbers obtained from an NIO analysis relate to the overlap of the initial and final SCF states of electron detachment. Comparisons of Dyson orbitals and their pole strengths calculated using ΔSCF and EPT approaches were also presented. It was shown that using the NIO model, ΔSCF Dyson orbitals and pole strengths are often in excellent agreement with EPT results.

Interestingly, the use of relaxation NIO pairs to evaluate ΔSCF pole strengths and the demonstrated agreement between ΔSCF and EPT pole strengths further suggests some connection with orbital relaxation and other correlation effects included in models such as EPT. As shown in previous work, one can attribute specific components of, for instance, the second-order diagonal self-energy expression in EPT to orbital relaxation effects. [183, 184] Indeed, relaxation NIO pairs correspond to occupied-virtual rotations in a framework where the final SCF determinant is written in terms of the initial SCF determinant molecular orbitals. Such relationships are currently being explored by our group and will be reported in future work.
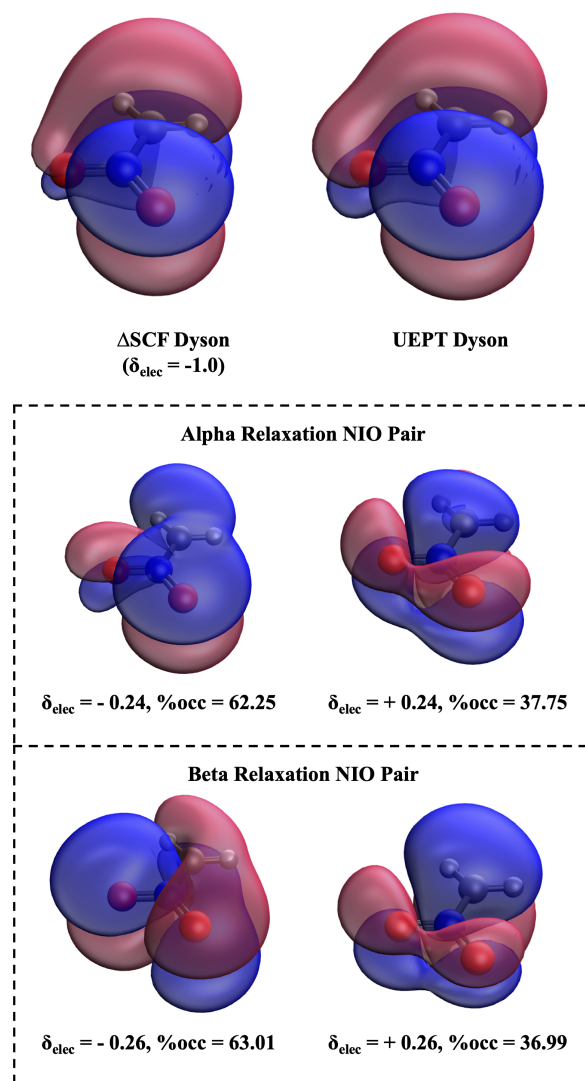
ΔSCF Dyson
(δ_{elec} = -1.0)

UEPT Dyson

Alpha Relaxation NIO Pair

δ_{elec} = - 0.24, %occ = 62.25 δ_{elec} = + 0.24, %occ = 37.75

Beta Relaxation NIO Pair

δ_{elec} = - 0.26, %occ = 63.01 δ_{elec} = + 0.26, %occ = 36.99

Figure 2.2: ΔSCF (top left) and EPT (top right) Dyson orbitals associated with electron detachment from ground state nitromethyl radical. Dashed boxes present the relaxation NIO pairs.
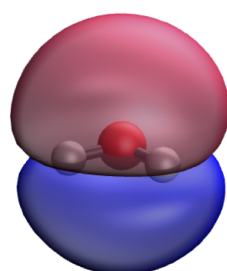
ΔSCF Dyson
($δ_{elec}$ = -1.0)
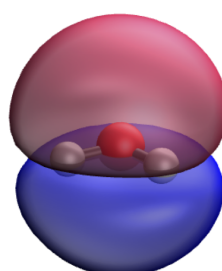
UEPT Dyson

Figure 2.3: ΔSCF (left) and EPT (right) Dyson orbitals associated with electron detachment of $^1A_1$ ground state of water.

ΔSCF Dyson
($δ_{elec}$ = -1.0)

UEPT Dyson

Alpha Relaxation NIO Pair

$δ_{elec}$ = - 0.21, %occ = 60.75 $δ_{elec}$ = + 0.21, %occ = 39.25
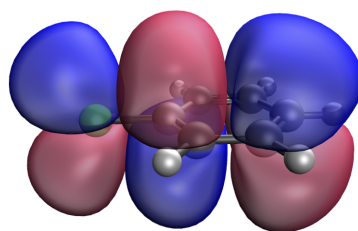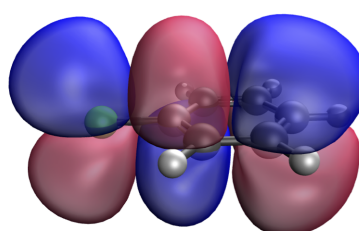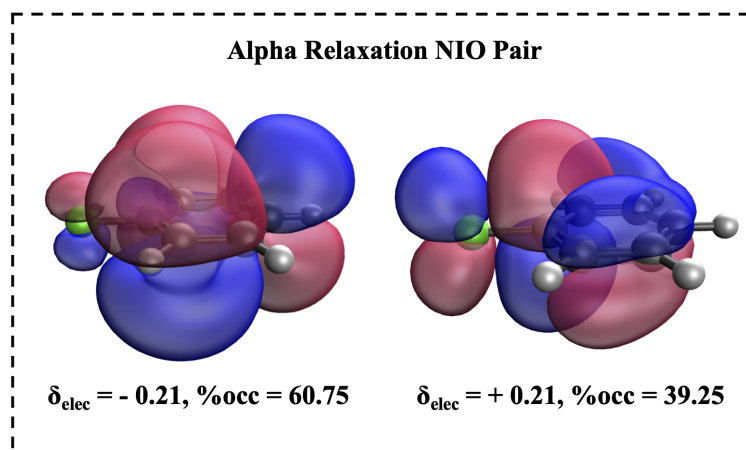
Figure 2.4: ΔSCF (top left) and EPT (top right) Dyson orbitals associated with electron detachment from chlorobenzene. The dashed box presents the relaxation NIO pair.
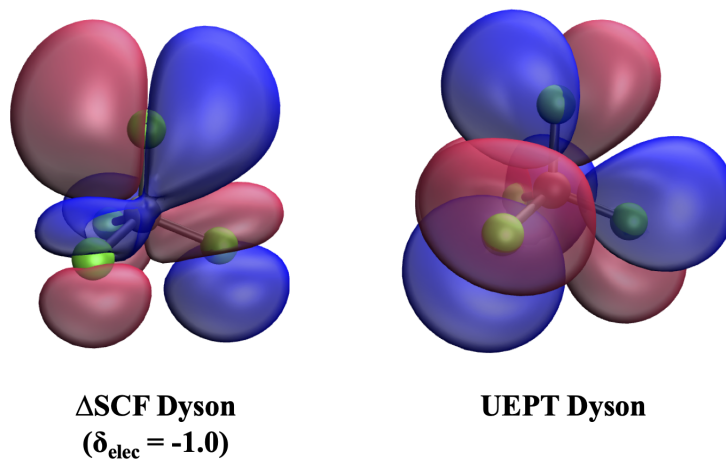
24

ΔSCF Dyson
(δ_elec = -1.0)

UEPT Dyson

Figure 2.5: ΔSCF (left) and EPT (right) Dyson orbitals associated with electron detachment from the ground state of tetrachloromethane.
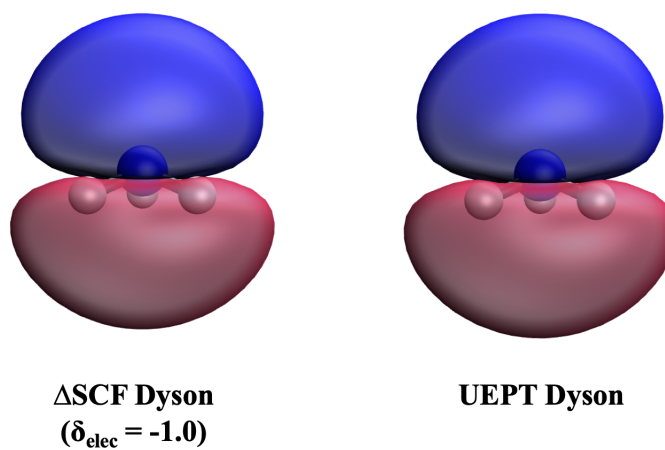
ΔSCF Dyson
(δ_elec = -1.0)

UEPT Dyson

Figure 2.6: ΔSCF (left) and EPT (right) Dyson orbitals associated with electron detachment from the ground state of NH_3.

ΔSCF Dyson
(δ_{elec} = -1.0)

UEPT Dyson
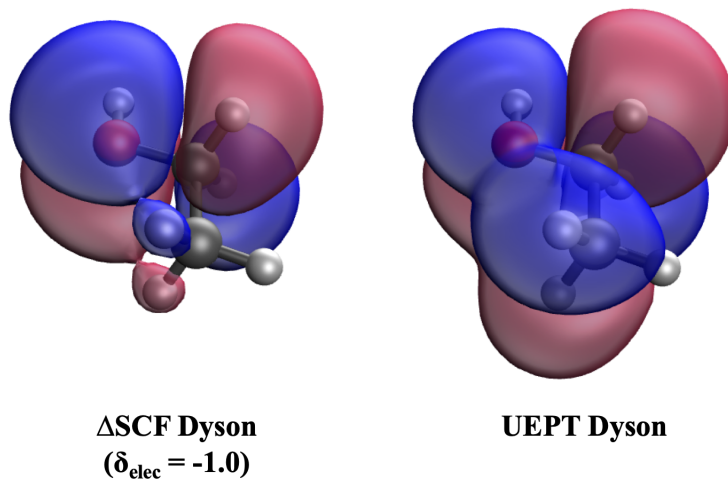
Figure 2.7: ΔSCF (left) and EPT (right) Dyson orbitals associated with electron detachment from the ground state of ethanol.

Chapter 3

A cluster of clusters: *Ab initio* calculations indicate contributions from multiple isomers in the photoelectron spectrum of LiB$_6^-$

"We don't need no education
We don't need no thought control
No dark sarcasm in the classroom
Teachers leave those kids alone"

— *The Wall*, Pink Floyd.

In this paper, we revisit the previously published experimental photoelectron spectrum of LiB$_6^-$. [*J. Chem. Phys.* **122**, 054313 (2005)] Alexandrova and coworkers point out that "*Comparisons of the calculated electronic transitions and experimental phtoelectron spectra showed distinctly the presence of the pyramidal species in the cluster beam*". Our results also predicted that the pyramidal structure to be the ground-state anion conformation of LiB$_6^-$, but computational data also suggest that other low-lying isomers and higher-order spin states significantly contribute to the experimental photoelectron spectrum. The ability to identify additional states is based on the proper analysis of wavefunction stability and performance of Franck-Condon progressions between the ground-state anion(s) and their corresponding neutral(s). However, we also note the necessity to perform additional experimental results is needed to perform definite spectral assignments.
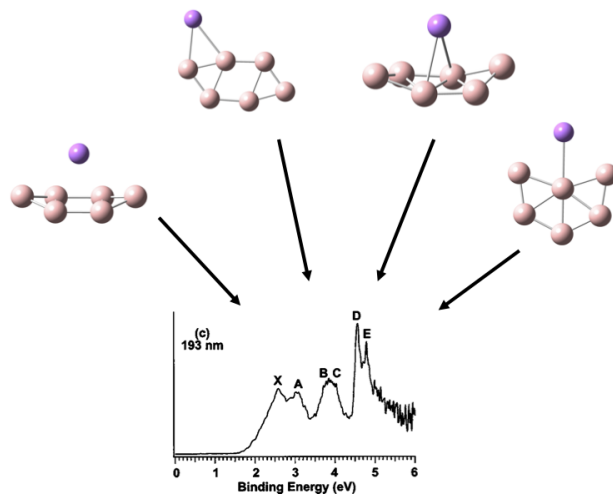
3.1 Introduction

The unique and intriguing properties of boron and boron clusters and their chemical applications have been subject to various experimental and theoretical studies. [113, 185–193] With only one fewer electron than carbon, the chemistry of boron has shown to be vastly different from that of its neighboring element. This electron deficiency provokes boron to form aggregate structures and create clusters with high electron delocalizations. [193–198] One interesting feature about boron clusters is their unique bonding motifs. Studies on $B_n{}^-$ show that most structures exhibit a 2D planar or a quasi-planar conformation which are accompanied by several types of vacancies. [196–211] . In various studies, Wang and co workers report those structures as joint B_3 triangles that contain several types of vacancies which the authors describe as tetragonal, pentagonal, and hexagonal vacancies. [113, 185–194, 196–210, 212–222] Those vacancies play a critical role in the stabilization of the planar structure of $B_n{}^-$ and suggest broad scope for various current and potential applications.

Electronic structure calculations can be efficient in predicting the ground-state configuration(s) of molecules, along with various properties such as ionization energies and harmonic frequencies, both of which are essential to modeling the photodetachments of molecules. [223–226] However, the current widely-used electronic structure methods, including various hybrid density functionals, should be handled with caution in order to avoid inaccuracies in computational results. [227, 228] Specifically, the stability of the reference Hartree-Fock (HF) or Kohn-Sham (KS) determinant is crucial to all analyses that follow. Wavefunction stability analysis proceeds by relaxing various constrains, one of which affects the final computational result is the reduction of orbital spin and spatial symmetries. Various previous studies on wavefunction stability and its effect on molecular properties have been discussed [177, 178]. A key effect of internal wavefunction instability is the invalidity of analytic frequency calculations, which is critical to performing the Franck-Condon progressions. [229] Thus, testing and validating the stability of the HF or KS determinant is an essential step prior to performing vibrational analysis calculations.

Another challenge that arises when modeling photodetachments of molecules lies in providing an orbital description of the ionization process. This allows identifying the orbital from which the electron was ejected and probe any electron rearrangements (wavefunction relaxations) that accompany the ionization event. To do so, our group recently developed the natural ionization orbital (NIO) model. [117, 118] The NIO model utilizes the difference density matrices of the ground-state and detached-state and allows for the representation of the ionization process from the standppint of orbital occupation change numbers. We applied the NIO model onto various studies [77, 112, 125–128] and we were able to identify differences between one-electron transitions and shake up/shake-off states and compare to experimental photoelectron spectra.

A recent study by Wang and co-workers reported the photoelectron spectrum of $LiB_6{}^-$ along with computational data followed by peak assignments. [113] The authors report several close-lying structures identified using gradient embedded genetic algorithm. Further geometry optimization was performed at the B3LYP/6-311G* and CCSD(T) levels of theory. Outer-Valence Green's Function (OVGF), time-dependent DFT, and CCSD(T) calculations were performed to calculate vertical detachment energies. They conclude that a symmetric boat-like structure is the sole contributor to the experimental photoelectron spectrum. Spectral assignments were based on calculated

adiabatic and vertical detachment energies. This approach can be useful, yet the photoelectron spectra, in practice, can exhibit unclear signals, especially if more than one transition contributes to the experimental peak(s) or a significant change in the geometry is observed. [42] For this reason, rather than just computing the detachment energies, a complete simulation of the experimental spectrum may provide further and more definite insight on the structure(s) responsible for the observed peaks. [109–111] Moreover, further inspections of the published results, we find out that several of the reported close-lying structures' wavefunctions exhibit internal instabilities. This raises the question on the accuracy of the molecular properties reported and analyzed which in turn lies as a barrier in performing proper spectral assignments of low-energy spin states and corresponding structures. The reported photoelectron spectrum (PES) by Alexandrova and coworkers exhibit two diffuse bands (labeled as X and A) at 2.60 and 2.97 eV, respectively. Reproducing the (PES) with higher photon energy gave rise to four more bands: B, C, D, and E, at 3.76, 4.00, 4.56, and 4.79 eV, respectively. While the authors conclude that the sole contributor to the experimental PES is a pyramidal C_{2v} structure with a $^1A_1$ electronic state, we show that, once we use proper computational tools with focus on reoptimizing the SCF determinant and verifying that we land at a stable wavefunction, we suggest that multiple isomers and electronic states contribute to the peaks observed in the experiment.

3.2 Computational Methods

All calculations were done using a local development version of the Gaussian suite of electronic structure programs. [176] Calculations were done using the B3LYP hybrid density functional [26, 27, 230, 231] with the 6-311+G* basis set. [232] The unrestricted spin formalism was used for all open-shell calculations. Geometry optimizations were carried out using standard methods and vibrational frequencies were calculated to ensure that minimum energy structures correspond to stationary points on the potential energy surface. [179, 233, 234] All relative energies of anions and neutrals reported include zero-point energy corrections. In all cases, the stability of the Kohn-Sham determinants was verified. [177, 178, 229] Franck-Condon progressions were generated for all possible transitions and their profiles were compared to the previously published experimental photoelectron spectrum. [109–111, 235] The natural ionization orbital (NIO) analysis has been used to provide an orbital description of the electron detachment process. [117, 118] Calculations of the excited states were performed using the linear response form of the time dependent density functional theory (TD-DFT). [236, 237] The nature of each of the identified electronic state transitions were characterized using the natural transition orbitals (NTO) model. [46] In all what follows, we use uppercase letters (A, B, C..) to represent the different identified anions and lowercase letters (a, b, c ...) to represent neutrals.

3.3 Results

In order to determine the proper electronic and molecular states that contribute to the photoelectron spectrum of lithium hexaborinde, we re-optimize the previously-reported close-lying structures of LiB_6^-. Additionally, we probe the presence of higher-order spin states and investigate their contribution to the experimental photoelectron spectrum through performing vibrational analysis and comparing the simulated peaks with experimental results.
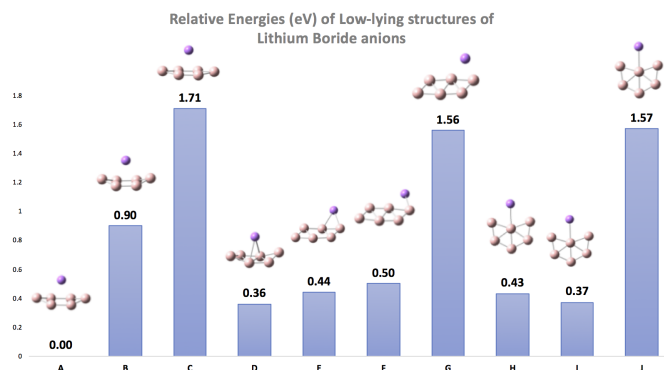
Figure 3.1: Relative energies of various close-lying states of LiB_6^-

Figure 3.1 and tables 3.1 and 3.2 show the various low-lying anions and neutrals of lithium hexaborides. While geometries of the ten structures shown have conformations similar to the previously reported structures, the electronic states are further explored here. Higher-order spin-states were explored and singlets, triplets, and quintet states of each of the structures are reported here. All of the structures lie within 1.7 eV higher than the ground-state anion. It is also noteworthy that all the structures presented in fig. 3.1 exhibit a planar or near-planar B_6 structure, which has been previously reported as a common feature for B_n clusters [113, 185–194, 196–210, 212–222]. The ground-state anion structure is a symmetric boat-like B_6 structure with lithium lying outside the hexaboride moiety. Five other structures were identified that lie 0.36 - 0.50 eV higher in energy than the ground state structures. Despite the small differences in their relative energies, these isomers can be grouped into three families of structures, the first is a pyramidal structure with a relative energy of 0.36 eV. Two structures identified at 0.44 eV (singlet) and 0.50 eV (triplet) exhibit a planar B_6 conformation that is composed of two B_3 triangles fused together. The third family of structures resemble the planar CeB_6^- teardrop structures we described in a previous study [128]. Two electronic states were identified at the teardrop structure, a triplet at 0.37 eV and a singlet at 0.43 eV, both of which exhibit a planar conformation. Higher spin-states for the described structures were also identified and are shown in fig. 3.1. It is important to highlight that in several cases, the idetified higher-spin electronic state is of comparable energy relative to its respective lower-spin state, which serves as a key feature in identifying additional contributors to the experimental photoelectron spectrum. Comparing structures E and F serves as a good example to the discussed point. We identified the triplet state **F** that is 0.06 eV higher in energy than its corresponding singlet (**E**). In addition, structure I, described as a triplet teardrop structure, was found to be 0.06 eV lower in energy than its analogous singlet state, H. A summary of all the structure labels, electronic states, point groups, relative energies and <S^2> expectation values are given in table 3.1 (anions) and table 3.2 (neutrals).

Figure 3.2 shows the convolution of the various simulated Franck-Condon progressions (colored) with the previously published photoelectron spectrum [113] (black). From the alignments of the several simulated peaks, we can clearly say that several of the reported isomers of lithium hexaboride contribute to the experimental photoelectron spectrum. The shown A $\rightarrow$ a simulation corresponds to the detachment of a beta electron from the ground state anion. While the Franck-Condon simulation aligns with the experiment, our calculations also show that F $\rightarrow$ e also contributes to

31

Label	Electronic State	Nuclear Symmetry	Relative Energy (eV)	$<S^2>$
A	^{1}A	C_1	0.00	0.1247
B	^{3}A	C_1	0.90	2.0284
C	^{5}A	C_1	1.71	6.0094
D	^{3}B	C_2	0.36	2.0209
E	^{1}A	C_1	0.44	0.4893
F	^{3}A	C_1	0.50	2.0217
G	^{5}A"	C_s	1.56	6.0255
H	^{1}A	C_2	0.43	1.0250
I	^{3}A	C_2	0.37	2.0250
J	^{5}A	C_2	1.57	6.0237

Table 3.1: Electronic states, nuclear symmetries, relative energies, and $<S^2>$ values of low-lying LiB_6^- anions.

Label	Electronic State	Nuclear Symmetry	Anionic Structure Resemblance	Relative Energy (eV)	$<S^2>$
a	^{2}A	C_1	A	2.21	0.8021
b	^{4}A	C_1	A	3.15	3.8240
c	^{6}A	C_1	A	5.22	8.7646
d	^{2}A	C_1	E	2.27	1.1363
e	^{4}A	C_1	E	2.54	3.7756
f	^{6}A"	C_s	E	5.17	8.7795
g	^{2}A	C_1	H	2.37	1.3935
h	^{4}B	C_2	H	2.62	3.7741
i	^{6}B	C_2	H	4.83	8.7694
j	^{4}A	C_2	D	3.91	3.7743

Table 3.2: Electronic states, nuclear symmetries, relative energies, and $<S^2>$ values of low-lying LiB_6 neutrals. Relative energies are given in eV and are calculated relative to the ground state anion **A**
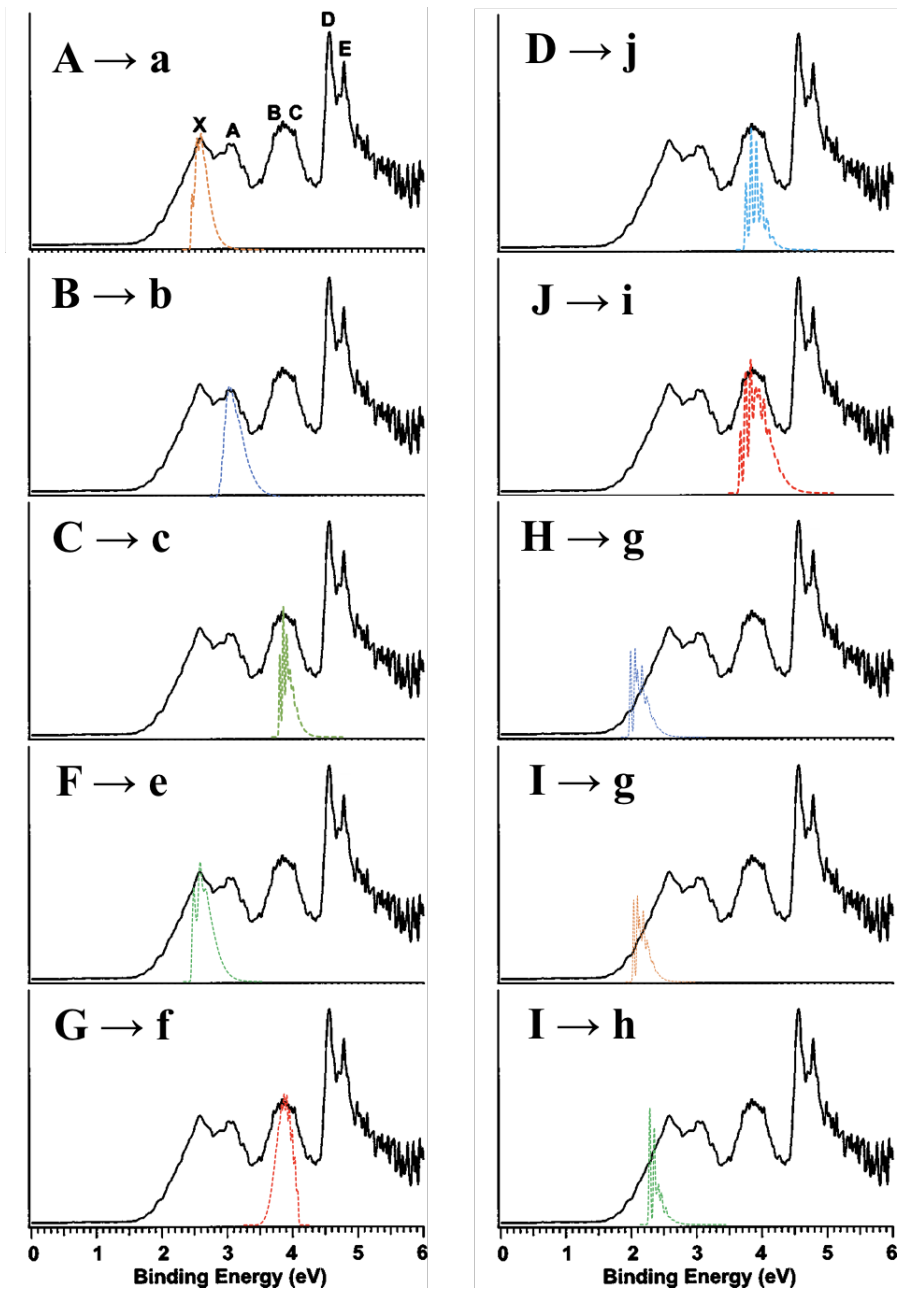
Figure 3.2: Franck-Condon simulations of the electronic detachments of low-lying LiB$_6{}^-$ anions.

the spectrum. This progression is best described as a detachment of a beta electron from ^{3}A LiB$_6^-$ into a ^{4}A neutral that bears a structure similar to its relative anion. It is noteworthy to mention that structure A exhibits a B$_6$ moeity that lies in a boat-like conformation and lithium lies on top of the conformation. On the other hand, structure F has a planar B$_6$ structure with lithium bounded to one side of the B$_6$ structure and lies outside the boride plane.

While our calculations showed that two detachments contribute to peak **X**, we have found one transition corresponding to peak **A**, namely **B → b** detachment (fig. 3.2). This peak is associated with a detachment of a beta electron from ^{3}A anion. The anion's geometry is analogous to the boat-like ground state anion (Structure A). However, identification of only one transition associated with peak **A** does not rule out the possible contributions from other states (isomers, electronic states, excited states...). Yet the limited availability of current experimental results prevents the accurate spectral peak assignments. As shown in figure 3.2, peaks B and C potentially correspond to multiple detachment processes. Our calculations show that detachments from several molecular and electronic states contribute to the broad peak that appears at in the range of 3.5 - 4 eV. Although their detachments originated from different structural isomers, **C → c**, **G → f**, and **J → i** exhibit one common feature concerning the detachment process: In all three cases, the initial anion bears a quintet state and, upon the detachment of a β electron, the resulting neutrals bear a sextet state.

In order to better understand the electron detachment process, we inspect the NIOs of the three transitions. Figure 3.3 shows the NIOs for each of the three detachments, along with the occupation change numbers of the orbitals. Three different behaviors are shown in fig. 3.3: (1) C → c exhibits one B$_6^-$-delocalized NIO of with a -1 eigenvalue, indicating the site of electron detachment. (2) G → f also shows that the detached electron originates from B$_6^-$-delocalized orbital. However, in this case, the detachment of the β electron is accompanied by a promotion of an α electron from lithium's s orbital onto the diffuse B$_6^-$-based orbital. ($\delta_{electron} = \pm 0.95$). Due to the two-electron process nature of this detachment, its contribution to the experimental photoelectron spectrum can be ruled out. (3) Electron detachment from J → i occurs at the B$_6$ moiety. This detachment is followed by a slight rearrangement of two sets of partial electron densities ($\delta_{electron} = \pm 0.19$ and ± 0.17).

The broad tail appearing to the left of peak **X** shows contributions from low-lying isomers of LiB$_6^-$. In particular, our calculations have shown that the experimental photoelectron spectrum exhibits minor contributions from a teardrop-like structure. H → g, I → g, and I → h transitions (shown in fig. 3.2) all refer to detachments from triplet and singlet teardrop anions to doublet and quartet neutrals. The anionic structures **H** and **I** both represent the singlet and triplet teardrop structure, with energies of 0.43 and 0.37 eV relative to the ground-state anion. The adiabatic detachment energies, along with the Franck-Condon progressions shown in fig. 3.2, suggest that detachments from **H** and **I** contribute to the broad, relatively lower intensity peak that appears at around 1.5 eV. By inspecting the NIOs of these two detachment, we can see that accessing the doublet neutral by either an alpha electron detachment from the triplet or a beta electron detachment from the singlet is accompanied by a significant occupation change number of the remaining electrons. NIOs for both detachment show a relaxation of around 0.5 electron into the virtual space, which makes the detachment an effective 1.5 electron process. In addition, a fourth detachment has been identified, **D → j**, that corresponds to a detachment from the boat-like triplet into an excited state doublet. TD-DFT calculations identified an excited state triplet that lies at around 3.55 eV higher in energy than its corresponding triplet anion. The presence and the accessibility of this state via a one-electron process has been confirmed by both NIO and NTO analyses. A summary of all the detachments is

C → c

β detachment

δelec = -1.00

G → f

β detachment

δelec = -1.00

α relaxation

δelec = -0.95   δelec = +0.95

J → i

β detachment

δelec = -1.00

α relaxation

δelec = -0.19   δelec = +0.19

α relaxation

δelec = -0.17   δelec = +0.17
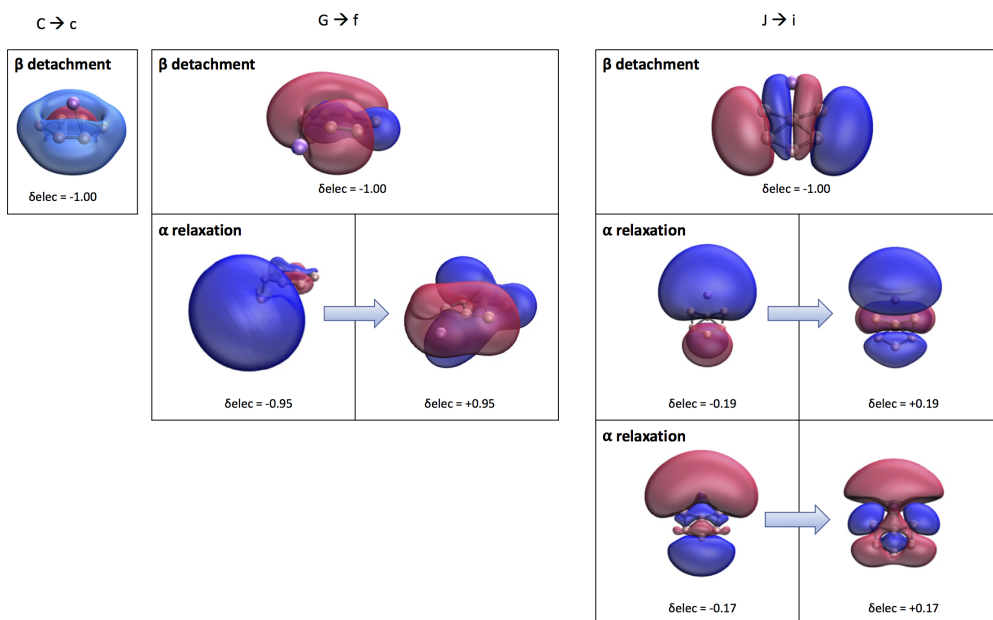
Figure 3.3: Natural ionization orbitals that correspond to the C → c, G → f, and J → i detachments

H → g

β detachment

δelec = -1.00

α relaxation

δelec = -0.48   δelec = +0.48

I → g

α detachment

δelec = -1.00

β relaxation

δelec = -0.51   δelec = +0.51
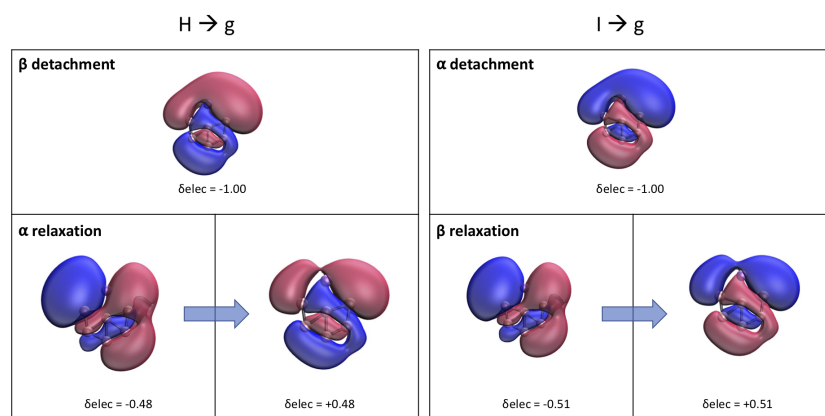
Figure 3.4: Natural ionization orbitals that correspond to the H → g, and I → g detachments

presented in table 3.3.

3.4 Discussion

The goals of this study can be summarized in two points: determination of the anionic LiB_6 structures that contribute to the previously-published photoelectron spectrum, and address the issue regarding proper treatment of results from electronic-structure calculations. Previous studies by our group [42, 77, 112, 125–128] have shown that clusters involving transition or heavy metals might exhibit photoelectron spectra that arise from contributions from several electronic states and molecular structures. This phoenomena is observed due to the existence of a constellation of close-lying anionic states, in addition to one-electron, close-lying accessible neutral excited states. It is noteworthy to mention that in the cases of lanthanides and transition metal based clusters, the existence of a manifold of close-lying states is attributed to the partially filled 3d, 4s orbitals in transition metals and 4f, 5d, and 6s in lanthanides. While this is not the case for lithium in LiB_6^-, yet the expected existence of a manifold of close-lying anionic and neutral states in LiB_6^- is due to the nature of the boron moiety, which has been shown by various studies to exhibit significant delocalization over the entire ring. Such delocalization drives the borons to form diverse forms of planar or near-planar structures. In such cases, the self-consistent field (SCF) energy surface exhibits multiple stable electronic structures that can be accessible with the SCF approaches. Particularly, we are interested in states that ensure anion/neutral pairing that corresponds to allowed one-electron transitions. In addition to manually inspect each SCF solution, Franck-Condon simulations, the NIO model [117, 118] and the NTO model [46] were helpful in determining the desired and allowed one-electron transitions.

In three studied MB_6^- clusters (M= Li, Sm, Ce), the boron moeity has shown intriguing electronic and molecular structures. The electron deficiency of each individual boron atom, alongside the electron delocalization provided a structural motif for the formation of planar or quasi-planar structures. The the chemical bonding between the B_6^{2-} entity and the metal center is shown to be also driven by the nature of the metal, which in turn dictates the nature of the detached electrons in experimental photoelectron spectroscopy. In both studies on SmB_6^- [238] and CeB_6^- [128], two energetically competitive structures were determined: a C_{2v} teardrop planar structure and a C_s puckered boat structure, with energy gaps between them as low as 0.1 eV for SmB_6^- and 0.01 eV for CeB_6^-. While the two studies argue that the teardrop structures are more consistent with experimental results, the main difference lies in the site of electron detachment. SmB_6^- photoelectron spectroscopy shows that photoelectrons originated from 2p-based orbitals localized on the B_6 entity, while detachments from CeB_6^- clusters occurred at 6s-like molecular orbitals that are cerium-centered. This difference can be attributed to the difference in 4f, 5d, and 6s occupations between both cerium and samarium. However, in the case of neutral lithium atom, the only occupied orbitals at the metal are the 1s and 2s orbitals. This yields a different type of interaction between the B_6 cluster and the lithium center, and therefore one would expect an electron detachment behavior to be different from that observed in CeB_6^- or SmB_6^-.

A particular interesting experimental observable that has been widely used to obtain additional information on the photodetachment process is utilizing angle-resolved photoelectron spectroscopy, which provides information regarding photoelectron angular distribution (PAD). PADs that result from one-photon ionization provide a useful picture about the properties of the orbital

36
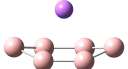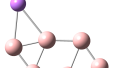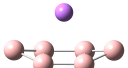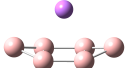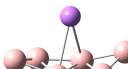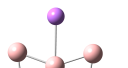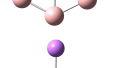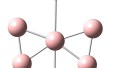
Transition	Anion Geometry	Anion Spin	Neutral Spin	Tentative Assignment	NIO Notes	NIO angular momentum
A → a		^{1}A	^{2}A	Peak **X**	rearrangement $\delta_{elec} = \pm 0.27$	0.73
F → e		^{3}A	^{4}A	Peak **X**	rearrangement $\delta_{elec} = \pm 0.21$	0.32
B → b		^{3}A	^{4}A	Peak **A**	no rearrangement	1.02
C → c		^{5}A	^{6}A	Peaks **B & C**	no rearrangement	0.74
G → f		^{5}A"	^{6}A"	Peaks **B & C**	rearrangement $\delta_{elec} = \pm 0.95$	0.88
D → j		^{3}B	^{4}A	Peaks **B & C**	NTO show one-electron process	0.80
J → i		^{5}A	^{6}B	Peaks **B & C**	Two rearrangements $\delta_{elec} = \pm 0.19, \pm 0.17$	1.21
H → g		^{1}A	^{2}A	Tail to right of **X**	rearrangement $\delta_{elec} = \pm 0.48$	0.67
I → g		^{3}A	^{2}A	Tail to right of **X**	rearrangement $\delta_{elec} = \pm 0.51$	0.66
I → h		^{3}A	^{4}B	Tail to right of **X**	rearrangement $\delta_{elec} = \pm 0.18$	0.47

Table 3.3: Summary of all reported detachments alongside relevant data from their respective NIO analyses.

Detachment	Pole Strength
A → a	0.877
F → e	0.907
B → b	0.929
C → c	0.936
G → f	0.087
D → j	—[1]
J → i	0.899
H → g	0.728
I → g	0.703
I → h	0.920

Table 3.4: Pole strengths of the studied candidate detachments. [1] Detachment into an excited state.

in which the electron was detached from. PADs are characterized by the anisotropy parameter, β, which is an experimental observable that ranges from -1 to +2 and is dependent on the angular momentum of the detached electron. While our NIO model presents a compact orbital picture of the detachment process rather than providing a quantitative value for the anisotropy parameter, we report the angular momentum of the NIO of each detachment in table 3.3. The values of the angular momenta range from 0.47 to 1.21 and NIOs of different calculated detachments show significant difference in s and p characters, indicating the difference in nature of the angular momenta of the studied detachments. This indicates that the detached electrons originate from molecular orbitals that are formed from atomic orbitals with different flavors of angular momenta. Such differences in angular momenta further supports the requirements for additional experimental parameters in order to distinctly perform spectral assignments. This is also shown in figures 3.3 and 3.4

In order to precisely perform spectral analysis and determine the structures and electronic states that contribute to the experimental photoelectron spectrum, our future work focuses on using the NIO model to calculate experimental cross-sections and photoelectron angular distributions. This approach is based on utilizing the angular momentum of the NIOs and their respective partial occupation change numbers in order to estimate the experimental photodetachment cross-sections and the photoelectron angular distributions.

$$P_{IF} = det(\delta_{elec} T_{occ}^{\dagger} T_{occ} + I_N) \tag{3.1}$$

To partially address this issue, our recent work focused on deriving a formal relationship between pole strengths and terms arising from NIO analysis. [117, 118] Calculated pole strengths are related to the experimental cross sections, i.e. the likely-hood of the occurrence of a particular electronic detachment. Equation 3.1 shows the relationship between the pole strength (P_{IF}), the occupation change numbers of the NIOs (δ_{elec}) and their projections onto the initial occupied manifold (T_{occ}). As we have shown [118], equation 3.1 enables us to calculate the overlap between the initial and final states using data from the NIO analysis.

Table 3.4 shows the pole strengths of the different explored detachments. While the values given lack the angular dependence contribution, they would still serve as qualitative metrics to describe experimental cross sections. The calculated pole strengths vary from 0.087 to 0.936, indi-

cating that the studied detachments exhibit different cross sections. Six of the detachments reported in this study show pole strengths that are close to 1, with values that are between 0.877 and 0.936. These detachments are predicted to be the major contributors to the observed experimental peaks. Another set of pole strength values, namely $\mathbf{H} \rightarrow \mathbf{g}$ and $\mathbf{I} \rightarrow \mathbf{g}$, have pole strengths of 0.728 and 0.703. These pole strengths contribute to the detachments of the triplet and singlet tear-drop LiB_6^- into the doublet structure. Their detachment energies and their Franck-Condon profiles fit with the tail observed at the right of peak $\mathbf{X}$, and their calculated pole strengths predict peaks with lower relative intensities. While a third detachment corresponding to the tear-drop structure ($\mathbf{I} \rightarrow \mathbf{h}$) was also identified, its calculated pole strength shows a higher cross-section, which makes it unlikely to contribute to the tail observed to the right of peak $\mathbf{X}$. Additionally, while the Franck-Condon progressions corresponding to $\mathbf{G} \rightarrow \mathbf{f}$ shows good agreement with peaks B and C in the experimental spectrum, the calculated pole strength of this detachment is 0.087, indicating a very low cross-section, which also allows us to eliminate its contribution to the experimental photoelectron spectrum.

Revisiting the photoelectron spectrum presented by Lai-Sheng Wang and coworkers [113], we observe a manifold of peaks that appear in the range of 2-5 eV. The authors distinctively attribute the six observed peaks to detachments from a pyramidal C_{2v} structure. Our calculations confirm the previously reported structure as the ground-state structure of LiB_6^- (structure $\mathbf{A}$ in figure 3.1). However, upon employing stability analysis tests on the resulting Kohn-Sham determinants, followed by performing Franck-Condon simulations between anions and their respective, symmetry-allowed, one-electron accessible neutrals, our calculations provide evidence of the presence of multiple close-lying anions and neutrals that pose as potential contributors to the photoelectron spectrum. NIO analysis and pole strength calculations gave further insight onto the nature of each of the studied detachments and allowed the inspection of the orbital(s) that is(are) directly involved in the ionization processes. Our calculations identified ten low-lying states of LiB_6^- that lie within an energy window of 1.6 eV. The calculated energy gap between the three lowest-lying structures of LiB_6^- (Structures $\mathbf{A}$, $\mathbf{D}$, and $\mathbf{I}$) is only 0.37 eV. Franck-Condon simulations of detachments from several structures have shown good agreement with the higher energy peaks present in the photoelectron spectrum. These include structural isomers that are significantly different from the ground-state singlet LiB_6^- as well as a manifold of higher spin-states (Figure 3.2).

Vibrational analysis calculations have identified the potential contributions from several isomers to the experimental photoelectron spectrum. However, in order to distinctively determine the appropriate isomers contributing to the experimental photoelectron spectrum collected. One experimental technique that has been discussed by Trommsdorf, Corval, and Von Laue, [239] is spectral hole-burning. This technique's main aspect is performing frequency-selective bleaching of the spectrum, which in turn leads to an increased transmission at the selected frequency and allows to distinctively characterize any present isomers.

3.5 Conclusion

In this paper, we have performed density-functional theory calculations on several low-lying electronic and molecular states of LiB_6^- in order to determine the species contributing to the experimental photoelectron spectrum. Our results reaffirm the existence of structure $\mathbf{A}$ as the ground-state anion (pyramidal structure with ^1A electronic state). Yet, we have shown that in order to defini-

tively assign spectral peaks, calculations of detachment energies is necessary but not sufficient. Franck-Condon progressions, which serve as the theoretical equivalent of photoelectron spectra, were performed and the profiles of the simulated progressions were then compared to experiment. In addition, the natural ionization orbital analysis and the pole strength calculations further helps in identifying the nature of each detachment and its interpretation of electronic detachments allows us to distinguish between one- and two-electron processes. Moreover, an additional key point in this study is to shed light on the importance of achieving wavefunction stability. In order to do so, we have confirmed the stability of all the calculated structures by searching for a lower-energy wavefunction that could exhibit reduced orbital and spin-symmetry.

Chapter 4

On the Linear Geometry of Lanthanide Hydroxides (LnOH, Ln = La–Lu)

"What in this context do we mean by "laws"? What exactly is the materialist conception of "laws", whether it be laws of nature or of social processes?"

— *Historical Materialism*, Maurice Cornforth (1954).

The work described here has appeared in a paper published in 2019 in Physical Chemistry Chemical Physics. [240]
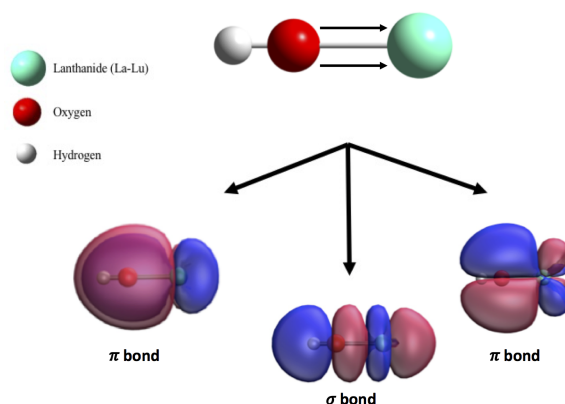
Figure 4.1: A simplified diagram explaining the nature of the Ln–OH bond.

Abstract

Lanthanide hydroxides are key species in a variety of catalytic processes and in the preparation of corresponding oxides. This work explores the fundamental structure and bonding of the simplest lanthanide hydroxide, LnOH (Ln = La–Lu), using density functional theory calculations. Interestingly, the calculations predict that all structures of this series will be linear. Furthermore, these results indicate a valence electron configuration of $\sigma^2\pi^4$ for all LnOH compounds, suggesting that the lanthanide-hydroxide bond is best characterized as a covalent triple bond.

4.1   Introduction

Lanthanide compounds exhibit unique electronic and magnetic properties yielding a wide diversity of high-impact applications. [114, 241–244] Lanthanides and, in particular, their corresponding hydrides, oxides, and hydroxides are known to efficiently facilitate important fundamental chemical transformations. Specific reactions catalyzed by such lanthanide species include oxidative dehydrogenation of alkenes, exchange of deuterium, and oxygen exchange. [114–116, 241–251]

While the unique magnetic and optical properties of lanthanides have been attributed to partially filled 4f shells, it has been shown that these metal orbitals are essentially unaffected in ligand bonding and are, at most, weakly involved in chemical bonding. Indeed, their poor overlap with ligand orbitals results in very little energy stabilization. [252–254] Instead, bonding in such species is driven by 6s and 5d orbitals. [255] The question of covalent bonding in f element complexes has been an active research area for some time. [256–261] Work by B. Roos and P. Pyykkö suggested lanthanide carbene ($LnCH_2^+$) compounds exhibit double bond character. [262] Bonding was found to involve 5d lanthanide orbitals while the 4f orbitals serve as spin counterweights and as an electron reservoir. Interestingly, studies on small actinide molecules have shown different bonding behavior, where, unlike lanthanides, 5f orbitals can significantly contribute to bonding. For instance, Kovacs has shown that AnO_3 exhibits actinide–oxygen bonds include contributions from actinide 5f orbitals. [263] Similar studies performed on AnC_2 and $AnCl_3$ have also implicated actinide 5f orbitals in bond formation. [263–269]

Motivated by our lab's previous work on metal oxide clusters, [42, 112, 125–128] we were intrigued by an apparent dearth of literature exploring the structure and bonding of lanthanide hydroxides. With the goal of exploring the full series, we note the inclusion of PmOH; while included here for completeness, Pm is unstable and thus PmOH is not likely to be experimentally studied. Hydroxide complexes play an important role in catalysis, biological systems, and in materials science. [243, 244, 250] Thus, knowledge of bonding in such complexes will provide a more complete understanding of reaction mechanisms and enhance the development of new catalysts and new materials. [270] Of particular interest here is the series of LnOH complexes, which allows for the study of the fundamental aspects of hydroxide bonding with lanthanide metals. Furthermore, such cluster species serve as models for electronically strained defect sites on surfaces. [271] In support of this use of small molecules and clusters as models for such sites, Baker and coworkers recently demonstrated the highly localized nature of the electronic structure of metal oxides. [87]

In this chapter, density functional theory (DFT) is used to examine the electronic structure of lanthanide hydroxides. In particular, this study examines the ground state of each Ln-OH (Ln = La–Lu) followed by an in-depth investigation of the nature of the lanthanide-hydroxide bond. Relating this result to the well-studied structure and bonding of transition metal hydroxides, [272–280] we observe a similarity with early transition metal hydroxide bonding. Specifically, we show that the nature of the lanthanide hydroxide bond involves important π-bonding.

4.2   Computational Details

Calculations were carried out using a local development version of the Gaussian suite of electronic structure programs. [176] The B3PW91 functional was employed [24, 26, 27, 230, 231, 281] using the unrestricted spin formalism for open shell cases. The segmented all-electron relativis-

tically contracted zeroth-order regular approximation (SARC-ZORA) basis set was used for all lanthanide centers. [282] This basis set provides an efficient alternative to effective core potentials in many routine DFT studies of similar species. Moreover, the SARC-ZORA basis set provides a balanced treatment of different electronic configurations of lanthanides. [282–284] The Dunning-style correlation consistent basis set, aug-cc-pVTZ, was used for both hydrogen and oxygen centers. [285, 286] To account for relativistic effects, the second-order Douglass–Kroll–Hess scalar relativistic correction was employed during geometry optimizations and frequency calculations. [287] Geometry optimizations were carried out using standard methods and all nature of all potential energy surface stationary points was confirmed by second-derivative calculations. [179] In all cases, the stability of converged Kohn–Sham determinants was verified. [177, 178] Fragment-based orbital perturbation theory analysis was performed on all molecules using the Natural Bond Orbital program (NBO6). [288]

4.3 Results and Discussion

To explore the structure and bonding of LnOH, we began by calculating minimum energy structures for each member of the series. Table 4.1 presents the geometric parameters of optimized LnOH structures. The lanthanide–oxygen bond lengths range from 1.90 to 2.09 Å and the O–H bond is consistently around 0.95 Å through the series. For all species, the Ln–O–H bond angle is linear, suggesting two possible bonding descriptions. Either the compounds are covalently bound with the oxygen center adopting a sp hybridization and the Ln-OH bond featuring π-bonding character, or the system is best described as ionic and bound by a charge/dipole interaction. In an effort to fully characterize the Ln-hydroxide bond and understand the observed linear structure, three analyses have been carried out. Specifically, this study examines the canonical molecular orbitals (MOs) predicted by DFT, considers an analysis of ionic bond character, and employs a perturbational fragment MO analysis. [289, 290]

Figure 4.2 shows the MO diagram of europium hydroxide, which is shown as a representative case for the LnOH series. The MO diagrams for the 14 other members of this series are substantially the same, with changes in the number of valence electrons resulting in a change of electron count in 4f, 5d, and 6s based non-bonding orbitals. In addition to the differences in 4f occupations, GdOH and LuOH exhibit doubly-occupied 6s based non-bonding MOs. LaOH also has a doubly occupied 6s metal-based MO and an empty 4f manifold unlike the other LnOH species. The MO diagrams of CeOH, PrOH, NdOH, and PmOH share the common feature of a singly-occupied 5d orbital as the highest occupied MO (HOMO). Importantly, the relative energetic ordering of bonding and antibonding orbitals is unchanged across the full Ln series and, consequently, the Ln-(OH) bond order remains constant. Noteworthy are additional nearby low-energy states located for CeOH, NdOH, and PmOH. Indeed, multiple states for these species lie within a window of roughly 0.1 eV, which underscores how close-lying the 4f, 5d and 6s orbitals are in these molecules. In all cases, though, the minimum energy structure remains linear and the Ln–(OH) bond order is unchanged (vide infra). Full details regarding such states are provided in appendix C. [240]

Examination of the bonding orbitals supports assignment of the Ln-OH bond order as 3. Specifically, the MO diagram includes an occupied σ bonding orbital and two degenerate doubly-occupied π. The metal-based 4f and 6s orbitals are predominantly non-bonding. The 6s orbital is singly-occupied across the lanthanide hydroxide series except for LaOH, GdOH, and LuOH where

Species	Ln—OH bond length (Å)	LnOH angle (degree)	O–H bond length (Å)
LaOH	2.04	180.0	0.96
CeOH	2.05	180.0	0.96
PrOH	2.05	180.0	0.95
NdOH	2.01	180.0	0.95
PmOH	2.03	180.0	0.95
SmOH	2.09	180.0	0.95
EuOH	2.08	180.0	0.95
GdOH	1.96	180.0	0.95
TbOH	2.01	180.0	0.95
DyOH	2.06	180.0	0.95
HoOH	2.05	180.0	0.95
ErOH	2.04	180.0	0.95
TmOH	2.03	180.0	0.95
YbOH	2.02	180.0	0.95
LuOH	1.90	180.0	0.95

Table 4.1: Optimized geometries of lanthanide hydroxides.
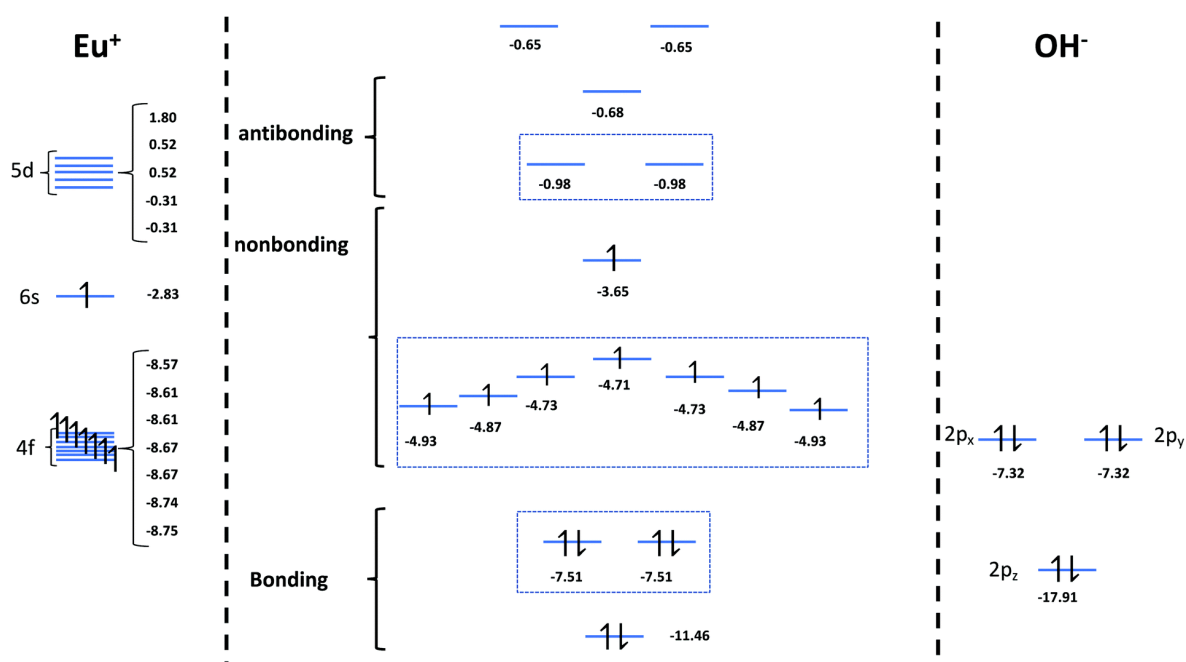
Figure 4.2: Orbital energies of the fragment Eu$^+$, OH$^-$, and the molecular orbital diagram of EuOH Orbital energies are given in eV

Species	Ln—OH Bond Length at 109°	Ln—OH Bond Length at 120°	Ln—OH Bond Length 180°	%Difference from 109°	%Difference from 120°
CeOH	2.138	2.132	2.055	3.88	3.61
EuOH	2.153	2.143	2.084	3.20	2.75
YbOH	2.0746	2.0646	2.019	2.68	2.21

Table 4.2: Variation in the bond length of some lanthanides at different Ln–O–H angles. Bond lengths are given in units of Angstroms.

the 6s based MO is doubly occupied as stated earlier, while 4f occupation changes with the atomic number of the lanthanide. A Mulliken population analysis (appendix C) shows, as might be expected, that the bonding orbitals are mostly ligand based. Indeed, in both σ and π bonds the contribution from Ln centered atomic orbital basis functions can be as small as 3%. The Mulliken analysis further shows that metal participation in bonding primarily involves p and d Ln atomic orbitals, though the bonding in some members of the series includes some metal f-orbital character.

In order to explore the strength of the LnOH π MOs (Fig. 1), we investigated the dependence of the Ln-OH bond length with respect to changes in the Ln–O–H angle. Three specific LnOH cases were chosen: CeOH, EuOH, and YbOH. The bond lengths were relaxed while constraining the Ln–O–H angle to 109.5° and 120°. Table 4.2 shows the results of these calculations. For these three specific lanthanide hydroxides, the bond length decreases as the angle increases from 109° to the equilibrium value of 180°. This indicates that as the bond angle relaxes towards the linear minimum energy geometry, the sum of the covalent radii of the atoms decrease. Following Pyykko, [291–293] we interpret a decrease in the additive covalent radii as an indirect measure of an increase in bond order. Thus, the results of Table 4.2 indicate the bond order in the optimized linear structures is higher than in the bent structures.

As mentioned above, the lanthanide-hydroxide linear geometry also could be due to electrostatic charge-dipole interactions. To explore this possibility, we compared optimized Ln–OH bond lengths with sums of Ln^+ and OH^- ionic radii. [294] An ideal ionic bond length is the sum of ionic radii of the two ions, and this value is expected to be appreciably larger than the associated covalent bond length. For the lanthanide ionic radii, where multiple radii are reported, we consider the smallest ionic radii for each lanthanide given by Shannon. [295] The reported ionic radii by Shannon correspond to higher oxidation states (+2, +3, and +4) of the studied lanthanides. While the required Ln^+ and OH^- are missing, we can estimate their values by considering changes in ionic radii of ions as their oxidation states and coordination numbers change. A detailed description of the determination of the proper values of ionic radii for Ln^+ and OH^- is provided in appendix C. Table 4.3 gives effective ionic radii and optimized bond lengths given by our DFT calculations for the LnOH series. In all cases, the optimized bond lengths are much shorter than the corresponding (ideal) LnOH ionic bond length. These results suggest Ln-OH bonding is not predominantly ionic in nature.

To more fully quantify the ionic character of the Ln-OH bond, we calculated the percent ionic character of the bond for each member in the series. [294] Specifically, dipole moments evaluated as part of our DFT calculations have been compared with dipoles evaluated classically between Ln cations and the hydroxide anion. For purely ionic systems, one would expect the ions to be Ln^+ and

Species	R(Ln$^+$)	R(OH$^-$)	R(Ln$^+$) +R(OH$^-$)	Bond Length	%Difference
LaOH	0.88	1.31	2.19	2.04	7.13
CeOH	0.86	1.31	2.17	2.05	5.78
PrOH	0.84	1.31	2.15	2.05	4.95
NdOH	0.84	1.31	2.15	2.01	6.74
PmOH	0.82	1.31	2.13	2.03	5.15
SmOH	0.81	1.31	2.12	2.09	1.64
EuOH	0.80	1.31	2.11	2.08	1.68
GdOH	0.79	1.31	2.10	1.96	7.39
TbOH	0.78	1.31	2.09	2.01	4.21
DyOH	0.78	1.31	2.09	2.06	1.22
HoOH	0.77	1.31	2.08	2.05	1.26
ErOH	0.76	1.31	2.07	2.04	1.30
TmOH	0.75	1.31	2.06	2.03	1.38
YbOH	0.74	1.31	2.05	2.02	1.38
LuOH	0.73	1.31	2.04	1.90	7.47

Table 4.3: Comparison of the ionic radii with the optimized bond lengths for Ln—OH. Distances are given in units of Angstroms.

OH$^-$.

As shown in Table 4.4, the ionic character of the Ln–(OH) bond varies with the lanthanide. For LaOH, which has zero f orbital population, the ionic character of the metal–hydroxide bond is essentially zero, suggesting the metal–hydroxide bond is purely covalent. The metal–hydroxide ionic bond character for the rest of the series varies from 5% at LuOH to 17% at YbOH. Stepping across the period from Ce to Eu, with a half-filled f shell, the ionic character of this bond increases. Another periodic trend of increasing ionic character is also observed as one moves across the series from Gd to Yb. These trends may be understood by considering the occupation of f-based non-bonding MOs. In addition, the classical idealized dipole moment was calculated at two other cases (shown in table 4.4). Specifically, in one case the center of the OH dipole fragment was taken to be at the midpoint of the O–H bond and in the other case the charge center was placed at the hydrogen nucleus. In both cases, the calculated dipole moment was larger than the dipole moment obtained from DFT calculations. The dipole moments resulting from these additional cases also resulted in a small percent ionic character (see appendix C).

To consider the extent of Ln–(OH) bond covalency, we performed a fragment based orbital perturbation study based on the Natural Bonding Orbital (NBO) model. [296] Specifically, the metal center (in the +1 oxidation state) and hydroxide ligand (1 charge) were defined as separate fragments for the NBO fragment orbital second-order perturbation model. Table 4.5 reports NBO based second-order perturbation stabilization energies arising from inter-fragment occupied-unoccupied interactions. [288–290, 296] As seen in the MO diagram discussed above (Fig. 4.2), the LnOH series shows both σ and π bonding interactions. The NBO analysis (Fig. 4.3 and Table 4.5) supports this characterization. Indeed, the NBO study indicates that the σ bond is formed from hydroxide lone pair donation into the empty lanthanide $5d_{z^2}$. In the second-order treatment of the model the stabilization energies from this bonding interaction are 11.2–25.4 kcal/mol. The NBO analysis

Species	Calculated Bond Length	Calculated Dipole Moment (DFT)	Idealized Dipole Moment (Placed at O)	Percent Ionic Character
LaOH	2.04	0.04	9.76	0.4
CeOH	2.05	0.74	9.81	7.5
PrOH	2.05	0.87	9.77	8.9
NdOH	2.01	1.05	9.62	10.9
PmOH	2.03	1.15	9.68	11.9
SmOH	2.09	1.24	9.97	12.4
EuOH	2.08	1.42	9.95	14.3
GdOH	1.96	0.51	9.39	5.4
TbOH	2.01	0.60	9.61	6.2
DyOH	2.06	1.39	9.82	14.1
HoOH	2.05	1.52	9.79	15.5
ErOH	2.04	1.51	9.73	15.5
TmOH	2.03	1.60	9.69	16.5
YbOH	2.02	1.66	9.64	17.2
LuOH	1.9	0.47	9.05	5.2

Table 4.4: Comparison of the dipole moments of ideal ionic LnOH and optimized species. Dipoles are given in units of Debye

also shows two significant interactions corresponding to π bonding between the lanthanides and hydroxide ligand. Such interactions result from lanthanide $5d_{xz}$ and $5d_{yz}$ orbitals interacting with hydroxide $2p_x$ and $2p_y$ orbitals. The calculated stabilization energies due to these π interactions range from 6.0 to 11.0 kcal/mol.

The σ and π stabilization energies increase with deceasing Ln–OH bond lengths (Table 4.1). However, rather than a single periodic trend being observed as one moves across the Ln series, our results show bimodal behavior. Moving across the series from Ce to Eu, results in decreasing stabilization energies. A second decreasing trend begins at Gd and continues to Yb. Both La and Lu, the two extremes of the lanthanide series, are outliers. Similar to the discussion above regarding the ionic character of Ln-(OH) bonds, Ce–Eu/Gd–Yb trends can be understood by considering 6s5d4f occupations. Table 4.5 includes the known electron configurations for the lanthanide metals (in oxidation state I). The increase in f orbital occupation from Ce to Eu corresponds to the observed decrease in NBO stabilization energies for both σ and π bonds. Going from Eu to Gd, the increase in stabilization energies is due to occupation of the Gd 5d orbital, which is not common among the series (except for La and Ce). Stabilization energy decreases again to around 11 kcal/mol for the series Dy–Yb.

Linear metal–hydroxide compounds are not unique to the lanthanide species described in this work. Early first row transition metal hydroxides, ScOH, TiOH, and VOH, are also known to exhibit a linear conformation. Those systems feature σ bond donation from an oxygen lone pair to the empty metal $3d_{z^2}$ orbital, as well as donation of two additional oxygen lone pairs to metal $3d_{xz}$ and $3d_{yz}$ orbitals. Thus, the bond order in those systems is 3, [272–274] just as our results suggest for LnOH.

Interestingly, the bonding changes as one moves from early to late transition metals. Various

47

Species	σ (Ln–OH) NBO stabilization energy (kcal/mol)	π (Ln–OH) NBO stabilization energies (kcal/mol)	Molecular Term Symbol	Orbital Occupation	Ln(I) electron configuration
LaOH	23.8	10.4, 10.4	$^1\Sigma^+$	$4f^06s^2$	[Xe] $5d^2$
CeOH	18.3	9.3, 9.3	^{4}H	$4f^16s^15d^1$	[Xe] $4f^15d^2$
PrOH	17.0	9.2, 9.2	^{5}K	$4f^26s^15d^1$	[Xe] $4f^36s^1$
NdOH	18.2	10.2, 8.7	^{6}L	$4f^36s^15d^1$	[Xe] $4f^46s^1$
PmOH	17.0	8.8, 7.9	^{7}L	$4f^46s^15d^1$	[Xe] $4f^56s^1$
SmOH	14.6	6.6, 6.6	$^8\Phi$	$4f^66s^1$	[Xe] $4f^66s^1$
EuOH	12.5	6.9, 6.9	$^9\Sigma^-$	$4f^76s^1$	[Xe] $4f^76s^1$
GdOH	14.1	7.2, 7.2	$^8\Sigma^-$	$4f^76s^2$	[Xe] $4f^75d^16s^1$
TbOH	14.2	7.6, 7.3	^{7}K	$4f^96s^1$	[Xe] $4f^96s^1$
DyOH	11.7	6.4, 6.3	^{6}I	$4f^{10}6s^1$	[Xe] $4f^{10}6s^1$
HoOH	11.6	6.2, 6.2	^{5}I	$4f^{11}6s^1$	[Xe] $4f^{11}6s^1$
ErOH	11.2	6.0, 6.0	^{4}H	$4f^{12}6s^1$	[Xe] $4f^{12}6s^1$
TmOH	11.2	6.1, 5.8	$^3\Phi$	$4f^{13}6s^1$	[Xe] $4f^{13}6s^1$
YbOH	11.2	6.0, 6.0	$^2\Sigma^-$	$4f^{14}6s^1$	[Xe] $4f^{14}6s^1$
LuOH	25.4	11.0, 11.0	$^1\Sigma^-$	$4f^{14}6s^2$	[Xe] $4f^{14}6s^2$

Table 4.5: Stabilization energies from Natural Bond Orbital analysis (NBO) along with the molecular term symbols and the orbital occupation of each species.
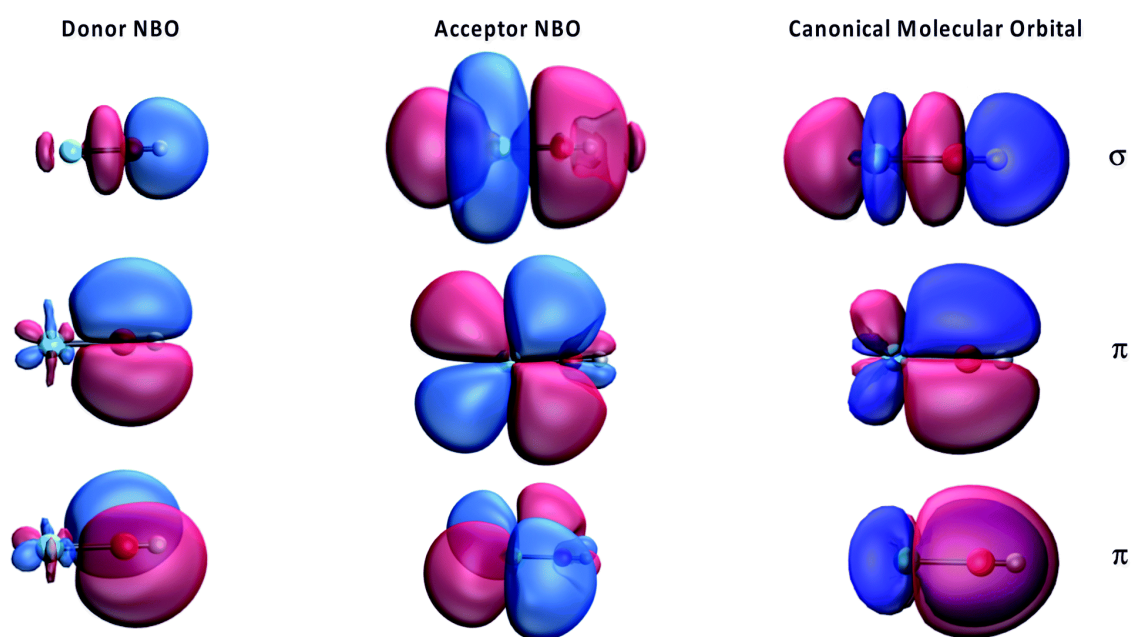
Figure 4.3: Natural Bond Orbitals of EuOH showing the donor and acceptor Natural Bond Orbitals (left and center columns) from metal(I) and OH⁻ fragments and corresponding resultant canonical molecular orbitals (right).

studies on CuOH report weaker Cu–OH bonding than for the early transition metals. [275–278] Previous studies, supported by both experimental and DFT calculations, have also shown that CuOH exhibits a bent geometry, unlike ScOH, TiOH or VOH. [276, 277] For example, Karzhavyi et al. reported a bent CuOH structure with a Cu–O–H angle of 107–110° in both a solid and a molecular calculation of CuOH. [278] Other previous work also suggest that zinc hydroxide exhibits a bent structure. [279, 280] This difference in bonding trends between early and late transition metal hydroxides is due to differences in 5d occupation. As the d-orbital occupation increases, π-donation from the hydroxide lone pair orbitals becomes less favorable.

As mentioned, the LnOH species considered in this work have been motivated by recent fundamental bonding studies on gas phase lanthanide molecules and clusters. The analysis presented above suggests that in the case of multiple hydroxyl and oxo ligands coordination, one would expect a distortion of the Ln–O–H bond from its linear structure due to the inaccessibility of the lanthanide 5d orbitals. In recent studies, Chick Jarrold and coworkers presented the structure and bonding of various lanthanide oxides and hydroxides, some of which involve multiple lanthanide–oxygen bonds. [103, 114, 115, 297] In agreement with our results, their experimental photoelectron spectroscopic studies and supporting DFT calculations have shown that Ln(I) complexes (e.g. EuOH [114]) favor a linear geometry, while lanthanide complexes with a higher coordination number (two or more hydroxide ligands coordinated to the lanthanide center) and corresponding higher lanthanide oxidation state (+2, +3, etc.) yield bent Ln–O–H angles between 140° and 160°. [103, 115]

4.4 Summary

In this chapter, DFT calculations have been used to explore the fundamental structure and bonding of lanthanide hydroxide complexes. For all members of this series, the minimum energy structure is a linear. An analysis of the canonical MOs establishes a metal–hydroxide bond order of 3, involving one σ- and two π-bonding MOs. Additional analysis suggests that the percent ionic character of the bond varies with the lanthanide metal. Interestingly, the degree of ionic character is relatively small in all cases (ranging from < 1% to 17%). A fragment based orbital perturbation study using the NBO model was employed to examine the strength of covalent bonding in the LnOH series. In agreement with the qualitative features of the canonical MOs, the NBO fragment orbital analysis identifies meaningful σ- and π-bonding interactions. Taken together, this work supports the assignment of the lanthanide-hydroxide bond as a triple bond.

Chapter 5

A Density Functional Theory Investigation of the Reaction of Water with Ce$_2$O$^-$

"Radical simply means 'grasping things at the root'."

— Angela Davis

Cerium

Oxygen

Hydrogen
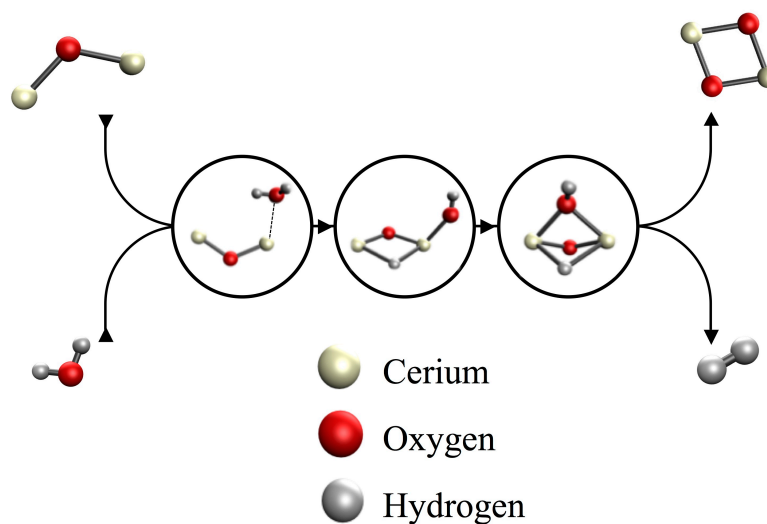
Abstract

Cerium suboxide clusters have been shown to react with water to yield H_2. Since reactions of metal oxides with water are of great fundamental and practical importance in energy science, detailed study of this reaction can provide new key knowledge for future catalyst design. Using density function theory calculations, we identified and report complete reaction pathways for two spin-states of Ce_2O^- reacting with H_2O. Additionally, examining the molecular orbitals of initial and final cerium oxide clusters, we found that metal d electrons facilitate the reduction of water. The work in this chapter provides new understanding of this reaction and insights to the reactivity enhancements for cerium-doped surfaces.

5.1 Introduction

Water, being one of the most abundant substances in nature, has been the subject of intense interest for scientists to study its physical and chemical properties. [298–308] In addition to the various roles water plays in different families of chemical reactions and biological systems, H_2O has been a key focus in energy related research. Of particular interest are catalysts facilitating the four-electron $2H_2O \longrightarrow 2H_2 + O_2$ reaction. [116, 309–313] Cerium oxides attracted special interest recently due to their ability to efficiently catalyze a wide range of oxidation and reduction reactions, including water-gas shifting reactions. [314–318] Several studies have also shown that cerium oxide-supported metal surfaces exhibit increased catalytic activity relative to their non-cerium oxide supported analogues. [80–82, 319–328]

Surface defects due to metal or oxide deficiencies possess unique electronic properties and facilitate increased reactivity. As with other metal oxides, the catalytic activity of lanthanide oxide surfaces is most active at surface defect sites. However, studying extended surfaces is complicated by the low concentration of surface defects and the continuous structural changes along the surfaces. Defect sites exhibit incomplete valencies and localized electronic structures, [87] thus they pose as model systems to study reactivity on surface defects on catalytic surfaces.

While the partially filled f-manifold in most lanthanide complexes lies close to the 5d and 6s orbitals of the lanthanide centers, it is non-bonding in nature and exhibits core-like behavior. Several studies have shown that the orbitals involved in chemical processes on lanthanides and lanthanide-based clusters involve 6s and 5p orbitals, while the occupation number of 4f orbitals remains intact. [77, 240, 255, 262, 329–331].

Several experimental and computational studies have been performed on cerium oxide clusters in order to better understand the electronic structure features that pave the way to a thorough understanding of their reactivity and catalytic activity. In addition, various experimental and theoretical studies have explored the reactivity of classes of cerium-based clusters with various gas-phase small molecules. [103, 114–116, 126, 315, 329, 331–340] Of particular interest here are computational studies conducted by Zhou and co-workers on the reactivity of Ce_n (n=1-3) with up to six water molecules. [332, 333] Their results indicate high reactivity of these cerium clusters and their efficiency in decomposing multiple water molecules. Recently, Jarrold and co-workers reported mass spectra of $Ce_xO_y^-$ systems (x= 2,3 ,y= 1-4) and their respective products of the clusters and water. [116] Their results indicate that cerium oxide clusters undergo three types of reactions: hydrogen gas production, water abstraction, and hydroxide abstraction. The relative selectivity of one

reaction type over the others is highly dependent on the stoichiometry of the cluster. For example, Ce_2O^-, Ce_3^-, $Ce_3O_2^-$, and $Ce_3O_2^-$ preferentially produce H_2 gas, while clusters with equal stoichiometric ratios of Ce and O undergo –OH abstraction, and clusters bearing more oxygens than ceriums undergo water abstraction.

In order to investigate the mechanism of water reactivity with cerium oxide clusters, we consider the simplest stoichiometric cluster that is capable of efficiently producing H_2 gas, namely Ce_2O^-. We first examine the geometric and electronic structure of different gas-phase clusters potentially involved in the reaction. Obtained experimental results include data from mass-spectrometry and photoelectron spectroscopy which supply us with valuable information on the geometric and electronic structures of the studied molecules. To this extent, we map the potential energy surface of the studied reaction by altering the relative positions of cerium, oxygen, and, when necessary, hydrogen atoms as well. In addition, for each conformation, we optimize the geometry under several spin-states and investigate the relative stabilities of these states. In this paper we present an exploration of the reaction of Ce_2O^- with water to provide a clear mechanistic explanation of the overall chemical process.

5.2 Computational Methods

Calculations were performed using a development version of the GAUSSIAN suite of electronic structure programs. [176] The B3PW91 density functional was employed. [24, 26, 27, 230, 281] The unrestricted formalism was used for all calculations. [13] The Stuttgart relativistic small core atomic natural orbital basis set and corresponding effective core potential (ANO/ECP) basis set with 28 core electrons and a contracted valence basis set (14s13p10d8f6g)[6s6p5d4f3g] for cerium center. [341] The Dunning style correlation-consistent basis set aug-cc-pVTZ was used for oxygen and hydrogen centers. [285, 286] Geometry optimizations were carried out using standard methods and the nature of all located potential energy surface stationary points were confirmed by vibrational frequency analysis. [179] Intrinsic reaction coordinate (IRC) calculations were performed to ensure that optimized transition structures connect appropriate potential energy surface minima. [233, 234] For all stationary points along the reaction pathways, all reasonable spin-states were calculated. The stability of all calculated Kohn-Sham determinants was verified. [177, 178, 227] Reported enthalpies of reactions were calculated at 298 K. Relative energies including zero-point corrections at 0 K are reported in the supporting information appendix.

5.3 Results and Discussion

In what follows, structures are labeled as *X-n*, where *X=A,B,C...* represents a particular molecular structure, and the value of n indicates the multiplicity of the cluster. Transition structures are labeled as TS1-*n* and TS2-*n*, where *n* also represents the spin multiplicity of the transition structure. As shown in figure 5.1, the reaction proceeds via the addition of water to a cerium center (**A** $\longrightarrow$ **G**), followed by formation of a hydride bridge between cerium atoms (**G** $\longrightarrow$ **H**). This is followed by formation of complex **I**, which features a bridging hydroxide ligand. The last step yields evolution of H_2 and formation of $Ce_2O_2^-$.
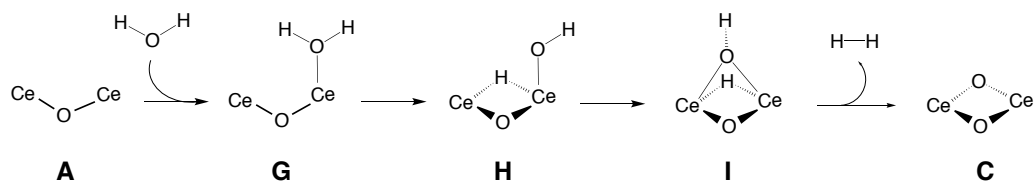
Figure 5.1: Overview of the proposed mechanism

5.3.1 Reactant and Product Cerium Oxide Clusters

The first step of exploring the mechanism of $Ce_2O^- + H_2O \longrightarrow Ce_2O_2^- + H_2$ is to determine the initial structure of Ce_2O^-. In order to do so, various molecular structures and electronic configurations were studied. For a Ce_2O^- molecule, two general structures can be considered: (1) the oxygen atom can bridge the two cerium atoms; or (2) the oxygen can be a terminal and bound to one cerium only. In addition to the molecular structure, we accounted for the possible existence of several spin-states. We performed our calculations on the ground-state quartet in addition to doublet and the sextet multiplicities.

Our calculations showed that several different structures of Ce_2O^- species exist. Figure 5.2 shows all competitive Ce_2O^- species. The ground state of Ce_2O^-, shown in Fig. 5.2 as **A-4**, is a quartet state featuring a bridging oxide. In this structure, the two Ce–O bonds are equivalent with a bond length of 2.06 Åand a Ce–O–Ce angle of 120.8°. Two other closely lying states, both having bridging oxides were located. The first is the sextet (**A-4**), lying 3.92 kcal/mol higher than **A-4** and the doublet state (**A-2**) which is 9.88 kcal/mol higher in energy than the ground state. These results are in agreement with the anion photoelectron spectroscopy results published by Kafader et al. [329]. Another located structure, **B-6**, features a terminal oxide rather than bridging and has a sextet spin ground state. This structure is much higher in energy than the others; it is 48.40 kcal/mol higher than **A-4**. Quartet and doublet states were not found for this structure. Despite the fact that **B-6** is much higher in energy than the other three structures, we still considered the possibility of its role in the reaction with water and consequent H_2 production. Yet, calculations that considered **B-6** to be the structure for the initial Ce_2O^- reactant did not yield any conclusive results.
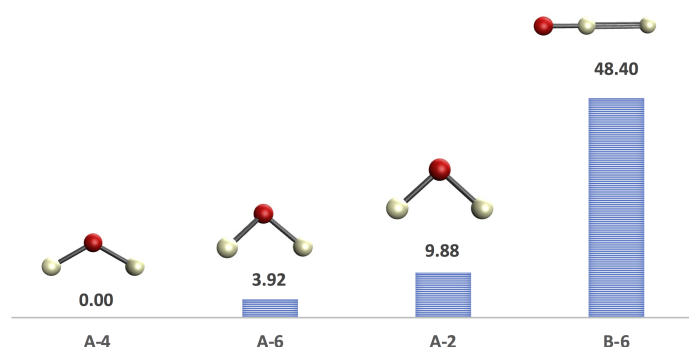
Figure 5.2: Optimized structures of Ce_2O^- and their relative energies given in kcal/mol.

In order to determine the various geometric structures of the product cluster species **C**, $Ce_2O_2^-$, we consider different variations in the positions of oxygens relative to the cerium centers. As for **A** and **B** above, each oxide can either be at terminal positions relative to a cerium atom or bridging the two cerium centers. We have calculated various combinations of terminal and bridging geometric configurations.

Figure 5.3 shows the various identified $Ce_2O_2^-$ structures and their relative energies. The ground-state structure, **C-4**, is a quartet planar structure where both oxygens are bridging the two cerium atoms. Another closely lying state is doublet **C-2**, which has a geometry similar to the ground-state. **C-2** lies only 0.63 kcal/mol higher than **C-4**, and the geometries of the two structures are quite similar.

Compounds **C-6** and **F-2** lie approximately 25 kcal/mol higher in energy than **C-2** and **C-4**. **C-6** is a sextet and is 24.94 kcal/mol higher in energy than **C-4**. Although the structure of **C-6** is similar to **C-4** and **C-2**, **C-6** is not a planar structure. In fact, the Ce–O–Ce–O torsion angle is 20.3°, unlike **C-4** and **C-2**, which have Ce–O–Ce–O torsion angles of 0°.

An additional set of higher energy $Ce_2O_2^-$ isomers have also been found and are labeled **D-*n***, **E-*n***, and **F-*n***. The geometry of **F-2**, which is only 2.2 kcal/mol higher in energy than **C-6**, is quite different. Specifically. one oxide is terminal while the other one is bridging. Given that **D-2**, **D-4**, **D-6**, **E-2**, **E-4**, **E-6**, and **F-6** are all much higher in energy (58.73 - 162.47 kcal/mol) we presume that they do not contribute to the mechanistic study presented in this paper and do not consider them further.
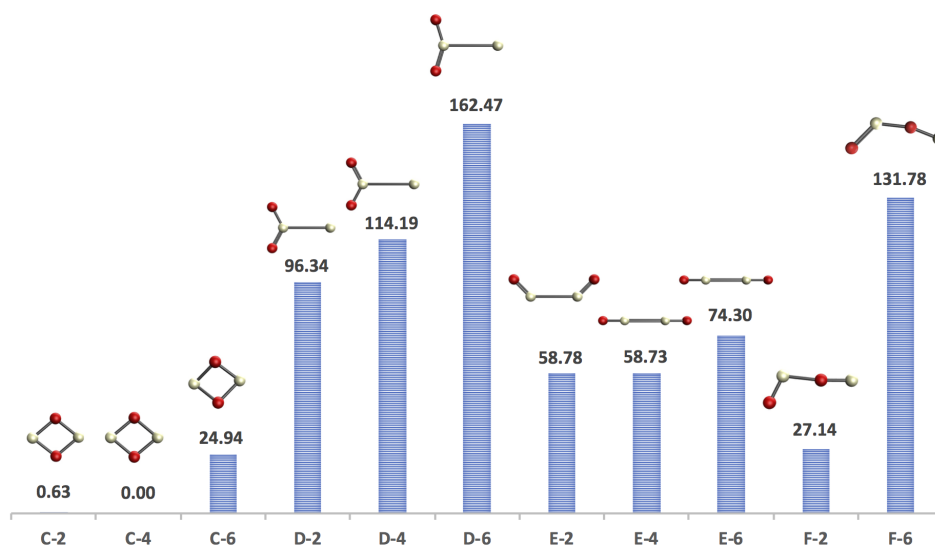
Figure 5.3: Optimized structures of $Ce_2O_2^-$ and their relative energies given in kcal/mol.

In their study, Kafader et al. reported the anion photoelectron spectra of Ce_2O^- and $Ce_2O_2^-$ is reported alongside a computational analysis to fully characterize the observed structures. [329] DFT calculations and Franck-Condon simulations were used to determine that the ground-state configuration of Ce_2O^- is a $^4A_2$ state with the Ce–O–Ce bridge bonding being the favored structural

motif, resulting in C_{2v} symmetry. Another close-lying state was found, a $^2A_2$ with a bonding motif resembling the ground-state quartet. These two structures correspond to **A-2** and **A-4** structures reported in Fig. 5.2. Using the same approach, Kafader et al. determined the ground-state configuration for $Ce_2O_2^-$ to be a ^4A_g state with the ^2A_g state being slightly higher in energy. Both structures exhibit D_{2h} symmetry and Franck-condon simulations confirmed their contributions to the photoelectron spectrum. These two structures resemble **C-4** and **C-2** shown in Fig. 5.3, respectively. As far as the starting materials and the final products are concerned, our computational results are in good agreement with the results reported by Kafader and coworkers. Thus, the two potential energy surfaces to be explored are the $^4A_2$ and $^2A_2$ routes leading to ^4A_g and ^2A_g, respectively. Following up on this, we aim to explore the mechanistic studies of the reactions of **A-2** and **A-4** with water to produce **C-2** and **C-4** alongside H_2.

5.3.2 Water Addition

We have identified one unique mode for water addition to **A-2** and **A-4** clusters. This mode is best described as an interaction between the water oxygen and a terminal cerium atom, while the second cerium atom does not directly engage in this step. Water addition to the Ce_2O^- clusters forms structures **G-2** and **G-4**. A distinctive feature about both adduct structures is that a water hydrogen is oriented towards the distant cerium, suggesting the feasibility of proton transfer to the remote cerium center.

G-4   G-2

ΔH = -12.2   ΔH = -23.3
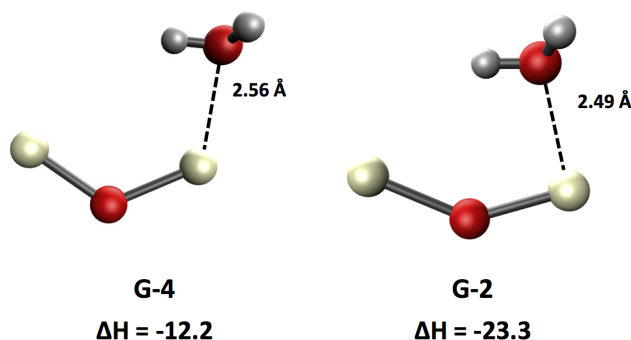
Figure 5.4: Quartet G-4 (left) and doublet G-2 (right) with intermolecular distances given in Angstroms and relative energies given in kcal/mol.

The relative heats of reactions of the water adducts are also shown in Fig. 5.4. Formations of both adducts resulting from water addition to Ce_2O^- are exothermic, with ΔH values of -23.3 and -12.2 kcal/mol for the doublet and quartet states, respectively. For the two formed intermediates the distance between the water oxygen center and the cerium atom is 2.56 Å (**G-4**) and 2.49 Å (**G-2**). Moreover, as the oxygen approaches Ce_2O^-, one of the hydrogens from the water molecule orients towards the position of the cerium atoms, indicating the first step towards breaking the O–H bond and consequent formation of a new Ce–H bond. An interesting aspect of water addition to the cerium oxide cluster is the activation of the aqua-oxygen by the Ce center, which precedes O–H bond cleavage. Instead, the interaction of the lone pairs on the oxygen of the water with the electron-deficient cerium center provides an incentive to proceed with an energetically-favored

water addition to Ce_2O^- through direct addition via the water oxygen onto the cluster. Unlike the behavior of transition metal oxides and their reactions with water [342], the mode of water addition in Ce_2O^- does not involve initial interaction between the water hydrogens and a cluster oxide site. Instead, the interaction of the water lone pairs with the electron deficient cerium center initiates an energetically favorable water addition to Ce_2O^- through direct addition via the water oxygen to the cluster.

5.3.3 Hydride Bridge Formation

Following water addition, the reaction undergoes Ce oxidation as a water O–H bond is cleaved and leads to formation of a bridging hydride. Structures **H-2** and **H-4** correspond to these intermediates, $Ce_2HO(OH)^-$ that form from O–H bond cleavage in **G-2** and **G-4**, respectively. Figure 5.5 shows the structure and relative energies of two identified spin states that correspond structure H. Both doublet and quartet states of structure H bear the same geometry. The oxygen and hydrogen centers in the ring are both in bridging positions relative to the two cerium atoms. The bridging hydride binds to the Ce centers with bond lengths of 2.29 Å and 2.30 Å for both the doublet and quartet species. The structure of **H-2** and **H-4** is best described as a four-membered planar ring consisting of two cerium atoms, an oxygen, and a hydrogen, with a bound hydroxide ligand. The O–H bond cleavage in both the quartet and doublet states is exothermic with heats of reaction of -73.0 kcal/mol (quartet state) and -81.6 kcal/mol (doublet) relative to their respective starting materials. Such exothermicity suggests the formation of each of **H-2** and **H-4** is highly favorable.

H-4

ΔH = -73.0

H-2

ΔH = -81.6
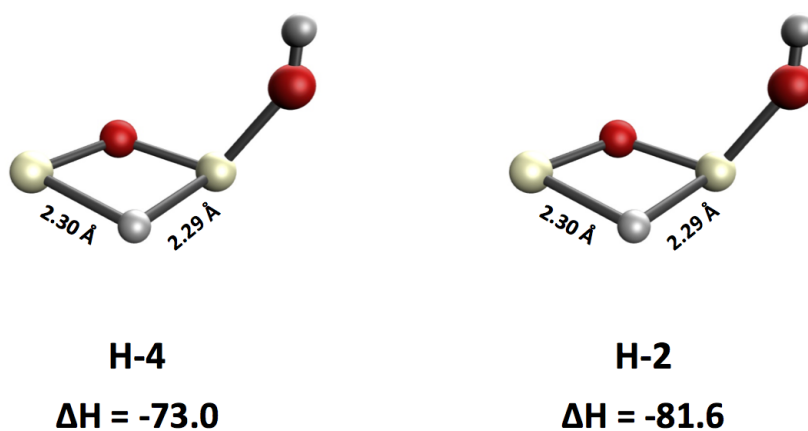
Figure 5.5: Structures of quartet H-4 and doublet H-2, Ce–O distances are shown in units of Angstroms and relative energies are shown in kcal/mol.

Transition structures connecting **G-2** to **H-2** and **G-4** to **H-4** have been identified and verified by calculating analytic frequencies and intrinsic reaction coordinates. These transition structures are shown in Fig. 5.6. The identified transition structures are geometrically similar to their respective precursors, **G-4** and **G-2**, with the water hydrogen oriented towards the two cerium centers. The Ce–H bond distances are 2.34 and 2.80 Å (quartet) and 2.38 Å and 2.79 Å (doublet), respectively.

TS1-4

ΔH = -11.6

TS1-2

ΔH = -21.0
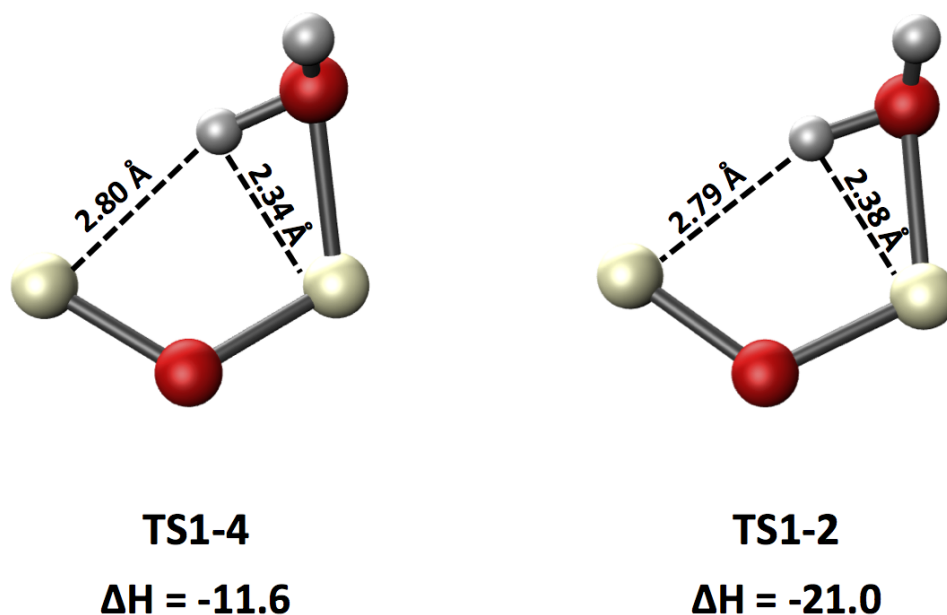
Figure 5.6: Structure TS1-4 that connects G-4 and H-4 (left) and TS1-2 that connects G-2 and H-2 (right) with relative energies given in units of kcal/mol.

The transition state between structures **G-2** and **G-4** on one side and **H-2** and **H-4** on the other side is essentially barrierless, with a calculated activation energy of only 0.6 kcal/mol (quartet) and 1.3 kcal/mol (doublet) and relative enthalpies of reaction of -11.6 kcal/mol (quartet) and -21.0 kcal/mol (doublet).

5.3.4 H$_2$ Production

The relative positions of the two hydrogen centers is critical for the final H$_2$ formation step. For this reason, we explored a series of possible rearrangement steps. Of the identified structures, **I-2** and **I-4** feature molecular orientations that act as reasonable precursors to the formation of H$_2$ (Fig. 5.7). Structures **I-2** and **I-4** include a new hydroxide bridge between the cerium centers, resulting in the two hydrogens being in close proximity to one another (H–H distance is ∼ 3 Å). These structures directly lead to subsequent release of H$_2$ and formation of product clusters **C-2** and **C-4**. By comparing the Ce–H bond lengths of structures **H-2** and **H-4** with **I-2** and **I-4**, we observe a decrease in bond distance as the hydroxide binds to the second cerium atom. Thus the bond formation between the hydroxide and cerium plays a role in decreasing the bond distance between one of the cerium atoms and the other hydrogen center.

Our calculations identified transition structures connecting **H-2** and **H-4** to **I-2** and **I-4**, shown in Fig. 5.8. These transition structures lead to bond formation between the hydroxide and a cerium center. Both doublet and quartet transition structures were confirmed as first-order saddle points by identifying one imaginary frequency. Further confirmation of the nature of the potential energy surface was done using IRC calculations (see appendix C for more details). In both cases, the

58
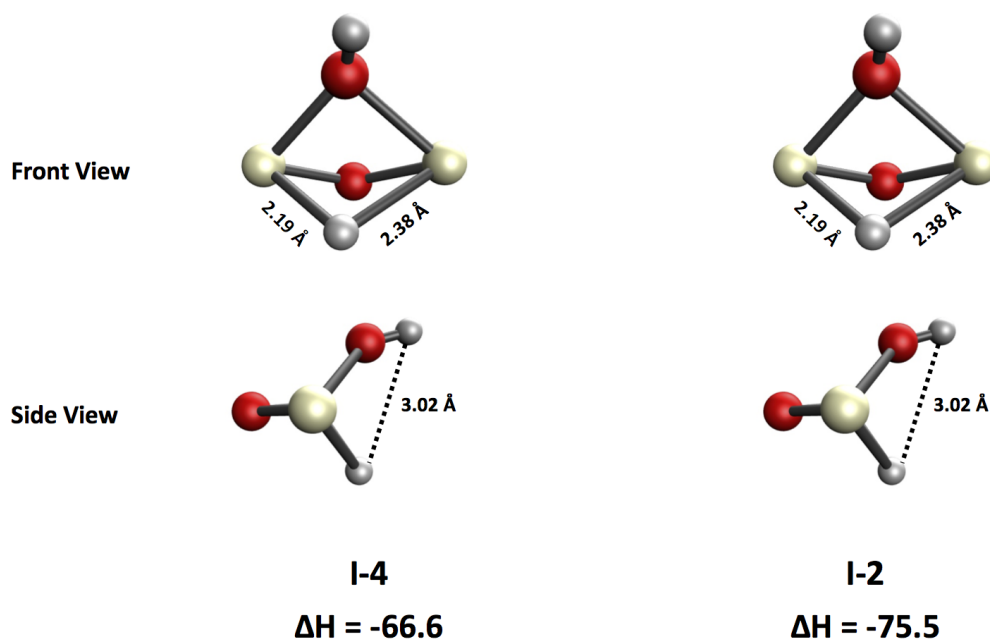
Figure 5.7: Front and side view of the geometry of structures quartet I-4 (left) and doublet I-2 (right) with relative energies given in kcal/mol.

transition structures present small reaction barriers (7.6 kcal/mol for the quartet and 6.5 kcal/mol for the doublet). In support of experimental interpretations, [115, 329] these transition structures feature an electron rich hydroxide attracted by the electron-poor cerium center resulting in diffuse multi-centered bonds involving the hydroxide and both cerium atoms.

Figure 5.9 shows structures of the last step of the mechanism, which involves H_2 production and formation of **C-2** and **C-4**. The relative energies of the separated products (shown in Fig. 5.9) indicate the exothermic nature of the last step as well as the overall reaction. The enthalpy of reaction for hydrogen gas evolution via a quartet starting material is -91.3 kcal/mol, while ΔH calculated for the doublet is -100.5 kcal/mol. Moreover, the relative energies of the separated products with respect to their precursors, structures **I-4** and **I-2**, are -24.7 kcal/mol and -25.0 kcal/mol, respectively.

5.3.5 Reaction Profiles

Figure 5.10 shows the full energy profile of the doublet and quartet mechanistic routes. In both cases the overall reactions are barrierless, in agreement with the experimental data provided by Jarrold and coworkers. [115, 329] Again, the reaction can be summarized by four steps: (1) addition of water onto a cerium center of Ce_2O^-; (2) hydride transfer from water into a bridging position between the two cerium atoms; (3) bond formation between hydroxide and the far cerium atom; and (4) evolution of H_2.

59

TS2-4

ΔH = -65.4
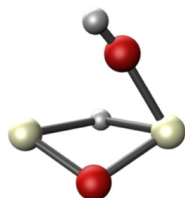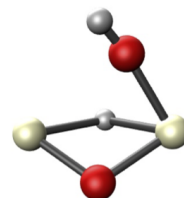
TS2-2

ΔH = -75.1

Figure 5.8: Structures of TS2-2 and TS2-4 that connect H-2 and H-4 to I-2 and I-4, respectively and their relative energies (in kcal/mol).

I-4

C-4 + H$_2$

I-2

C-2 + H$_2$

ΔH = -91.3
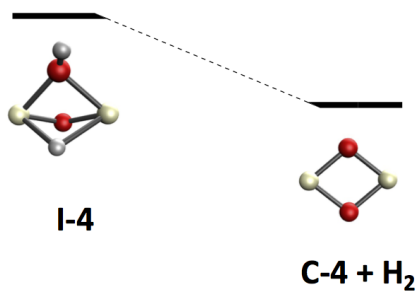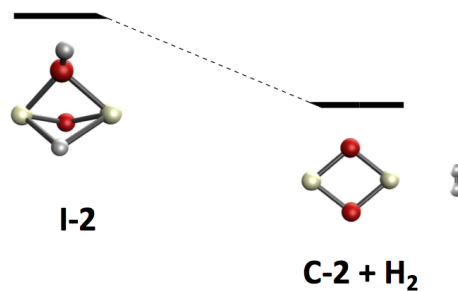
ΔH = -100.5

Figure 5.9: Structures and relative energies (in kcal/mol) of I-4 and C-4 (left) and I-2 and C-2 (right).

9.8
0.0

A-2 + H₂O
A-4 + H₂O

-12.5
-12.2

G-2
G-4

-11.2
-11.6

TS1-2
TS1-4

-71.8
-73.0

H-2
H-4

-65.4
-65.4

TS2-2
TS2-4

-65.7
-66.6

I-2
I-4

-90.7
-91.3

C-2 + H₂
C-4 + H₂
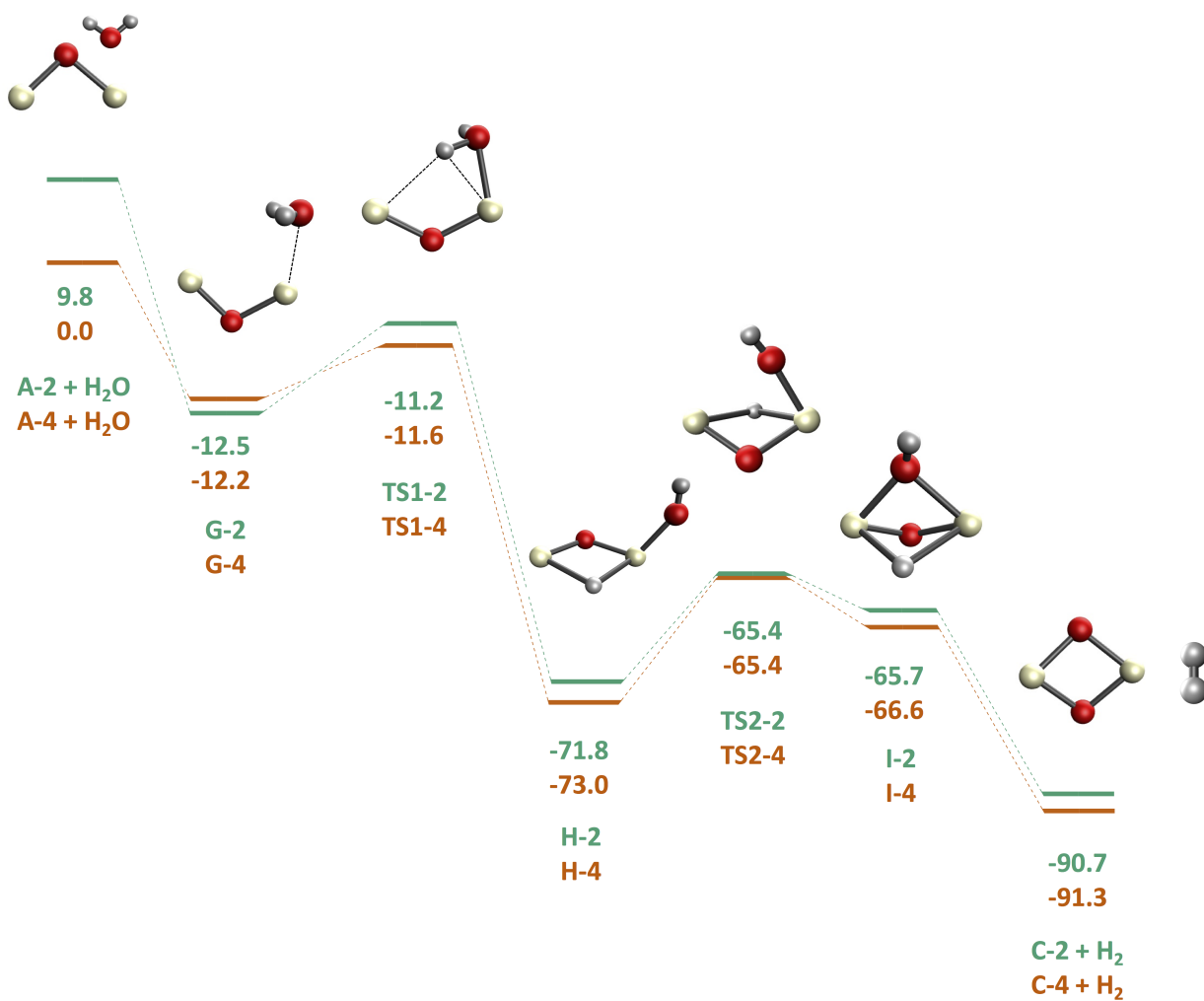
Figure 5.10: Energy profile for the proposed Ce_2O^- + H_2O $\longrightarrow$ $Ce_2O_2^-$ + H_2 quartet (orange) and doublet (green) mechanisms
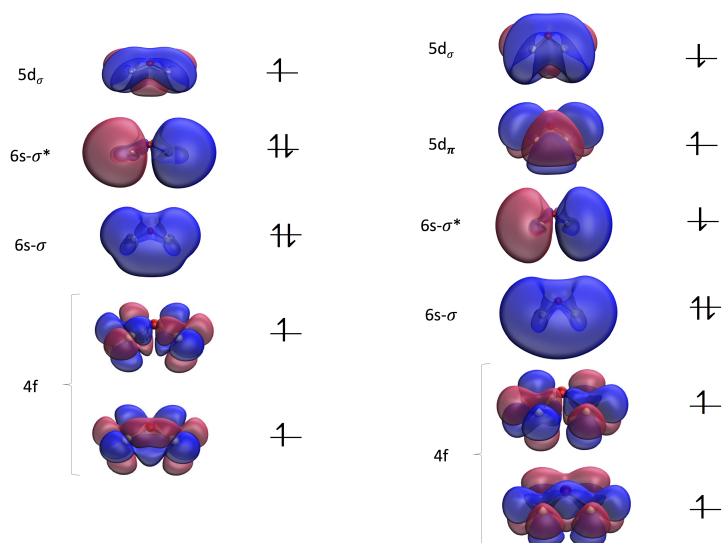
Figure 5.11: Valence molecular orbitals of quartet (left) and doublet (right) Ce_2O^-

There are features of the Ce_2O^- catalyzed reaction that are different from reports published for transition metal oxide cluster analogues. Three such examples include tungsten oxide, molybdenum oxide, and mixed manganese-molybdenum oxides. [32, 342–344] The overall reaction barriers for those cases is similar to the case reported in this work, but a key difference lies in the mode of addition of water to the clusters. Indeed, previous reports found that the initial steps of water addition occur via a concerted step involving simultaneous addition of hydroxide (from water) to the metal center and O–H formation at an oxo site. As discussed above, our calculations identified a different pathway for the reaction with cerium oxide that occurs via a two-step process: water adds to the cerium center to form structures **G-2** and **G-4** (Fig. 5.4), then the hydrogen transfers to a bridging position between the two cerium centers.

In the reaction of Mn_xMoO_y anions with water, both Mn and Mo are involved in the initial cluster-water formation. [344] However, only the Mo center undergoes oxidation. In fact, the reactivity of the Mn_xMoO_y anion clusters with water depends on the oxidation state only of the molybdenum center. Once the Mo center reaches its highest oxidation state (VI), reaction with additional water molecules ends.

5.3.6 Electronic Structures of Cerium Oxide Clusters

Figure 5.11 shows the frontier molecular orbitals (MOs) of **A-2** and **A-4**. The MO diagram of **A-4** is comprised of three general manifolds: 4f orbitals, σ and σ^*, and 5d orbitals. The first frontier orbital group includes two singly occupied 4f orbitals localized on the cerium centers. The σ and σ^* orbitals are doubly occupied and are predominantly Ce 6s-based. Finally, the (α) highest occupied MO (HOMO) of quartet Ce_2O^-, is a 5d-based singly occupied orbital with the electron delocalized over the space spanning the two cerium centers. The shown doublet Ce_2O^- MOs include occupied 4f orbitals localized on the cerium centers and the doubly occupied σ orbital. The main difference between **A-2** and **A-4** MOs lies in the manifold of singly occupied orbitals. Unlike its quartet

analogue, the doublet Ce_2O^- exhibits three singly occupied orbitals: one $5d_\pi$ α orbital; one σ^* β orbital; and one $5d_\sigma$ β orbital.

MO diagrams for **C-2** and **C-4** (shown in Fig. 5.12) exhibit more similarity to each other than **A-2** and **A-4**. Both spin states of structure **C** include the two singly occupied 4f orbitals present in their respective starting **A** clusters. In addition, both doublet and quartet spin states have a doubly occupied 6s-based σ orbital and a singly occupied σ^* orbital. The only difference is the spin of the electron occupying the σ^* orbital. The quartet has an α electron in the σ^* orbital, while that same orbital is occupied by a β electron in the doublet **C-2**.
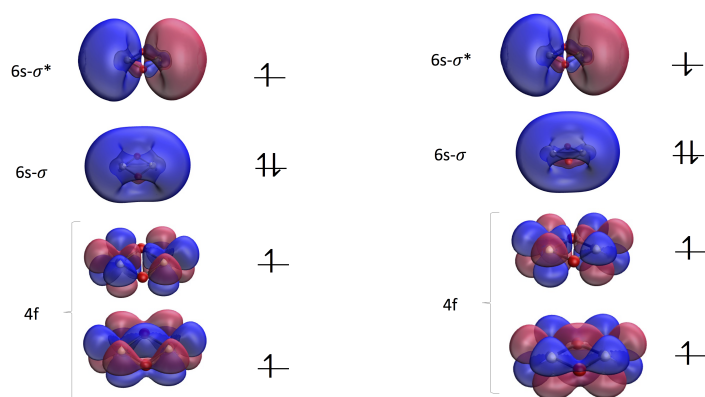
Figure 5.12: Valence molecular orbitals of quartet (left) and doublet (right) $Ce_2O_2^-$

The combined oxidation state of the two cerium centers is (+I) in Ce_2O^- and (+III) in $Ce_2O_2^-$. Figures 5.11 and 5.12 show that the frontier molecular orbitals of both Ce_2O^- and $Ce_2O_2^-$ exhibit delocalization of electrons over the two cerium metals. In addition, as discussed in the previous sections, all Ce–O bonds are equivalent within the same molecule in both the Ce_2O^- and $Ce_2O_2^-$. For these reasons, the oxidation states of the cerium centers should also be equal. In addition, given the delocalized nature of the frontier orbitals over the two cerium centers, these species can be described by two resonance structures that have cerium centers with unequal oxidation states. For Ce_2O^-, the studied structure can be described by two resonance structures of Ce_2O^-, with each resonance form featuring one Ce(0) and one Ce(I) center. In a similar manner, the final $Ce_2O_2^-$ structures are described by two Ce(I)/Ce(II) resonance structures.

While the cerium-based 6s orbitals have been previously determined to be the sites of electron detachments in various cerium and cerium suboxide clusters (including Ce_2O^- and $Ce_2O_2^-$), we notice here that both σ and σ^* orbitals retain all or most of their electron occupations as the reaction proceeds. This shows that σ and σ^* electrons are not the source of metal facilitated reduction of water. Instead, the electron source in the studied reaction is the set of singly occupied 5d orbitals. This observation is consistent with the reported experimental result that reaction of $Ce_2O_2^-$ with water yields H-radical rather than H_2. The reaction of water with Ce_2O^- depletes the metal centers of their d electrons and prevents further H_2 production. [116]

5.4 Summary

The work in this chapter studied the reaction of water with Ce_2O^- clusters to produce $Ce_2O_2^-$ and H_2. Density functional theory calculations have been used to map out the full reaction pathway for hydrogen production. A thorough search for candidate intermediates and transition structures has shown that a key point in the progression of the reaction is the formation of successive bridging bonds that place the two hydrogen atoms in close proximity and eventually facilitates the production of H_2. We have also shown that it is energetically possible for both experimentally identified electronic states of Ce_2O^- to react with water and eliminate molecular hydrogen with low energy barriers relative to the starting materials. Finally, while the valence molecular orbitals of the studied cerium oxide clusters consist of 4f, 5d, and 6s metal-centered orbitals, an examination of the molecular orbitals of initial and final cerium oxide clusters clearly indicates that the metal 5d electrons provide the means for water reduction. This work provides new insight to the reactivity of small lanthanide-based clusters with water.

Chapter 6

Modeling the Photoelectron Spectra of $CeO_2B_x^-$ (x = 2, 3) and CeB_6^- Clusters

"Our scribblings are usually not lyrics but whirrings, without colour or resonance, like the tone of an engine-wheel. I believe that the cause lies in the fact that when people write, they forget for the most part to dig deeply into themselves and to feel the whole import and truth of what they are writing."

— Rosa Luxemburg (1898).

The work described here has appeared in two papers published in Journal of Physical Chemistry A. [127, 128] This work is part of a collaboration between the Hratchian group at UC Merced and Chick-Jarrold group at Indiana University. All reported experimental procedures and results were performed by our collaborators. Further experimental details can be found in references [127, 128].

Abstract

Density functional theory calculations were employed to model the anion photoelectron spectra of small $CeO_2B_x^-$ (x = 2, 3) and CeB_6^- complexes. A comparison of the results of the $CeO_2B_x^-$ (x = 2, 3) clusters, we observe that their spectra reveal markedly different bonding upon incorporation of an additional B atom. Most interestingly, $CeO_2B_2^-$ was found to have a Ce(I) center coordinated to two monoanionic boronyl ligands in a bent geometry. This result was unexpected as previous studies suggest electron-rich metals are most suitable for stabilizing such ligands; furthermore, it is one of the first examples of an experimental metal-polyboronyl complex. Introducing another boron atom, however, favors a much different geometry in which Ce(II) coordinates an $O_2B_3^{3-}$ unit through both the O and B atoms, which was evident in the markedly different photoelectron spectra. As for CeB_6^-, two competitive molecular structures were identified for the anion and neutral species, which include a boat-like structure and a planar or near-planar teardrop structure. Ce adopts different orbital occupancies in the two isomers; the boat-like structure has a 4f superconfiguration while the teardrop favors a 4f 6s occupancy. The B_6 ligand in these structures carries a charge of -4 and -3, respectively. The teardrop structure, which was calculated to be isoenergetic with the boat structure,

65

was most consistent with the experimental spectrum. B_6-local orbitals crowd the energy window between the Ce 4f and 6s (HOMO) orbitals. A low-lying transition from the B-based orbitals is observed slightly less than 1 eV above the ground state. The results suggest that edge and corner conductivity involves stabilized, highly diffuse 6s orbitals or bands rather than the bulk-favored 5d band. High-spin and open-shell low-spin states were calculated to be very close in energy for both the anion and neutral, a characteristic that reflects how decoupled the 4f electron is from the B_6 2p- and Ce 6s-based molecular orbitals.

6.1   Introduction

Lanthanide borides possess a range of interesting electronic and magnetic properties, [345] beyond the common usage of LaB_6 as an emitter used in electron guns. CeB_6 in particular, which is also used as an emitter, is a heavy fermion material and has temperature-dependent and "hidden" magnetic phases. Structurally, these materials are cluster compounds, in which boron units assume the form of B_6^{3-} octahedral with the Ln^{3+} cations arranging in CsCl-like packing (figure 6.1). [346, 347] In tetraboride crystals, the octahedra are connected by boron dimers and form channels filled by Ce atoms.
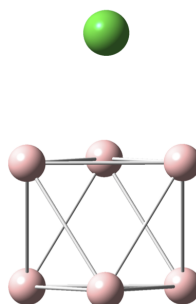
Figure 6.1: Structure of Bulk LnB_6

With the ubiquity of carbon monoxide in organometallic compounds, integral in both catalysis and synthesis, there have been significant efforts to expand the breadth and specificity of their chemical reaches using isolobal and isoelectronic CO analogues. [348–351] Boronyl (BO^-) is one such example, [349, 352, 353] yet metal$-$(BO)$_n$ complexes have been largely elusive in non-gas-phase experiments, unlike other main group elements multiply bound to boron, for example, BN. [352, 353] The highly polarized BO ligand acts as a strong nucleophile due to the electron density localized on the O atom, with a tendency for cyclo-oligomerization with any nearby BO units. [354–356] Transition metals do stabilize small reactive functionalities like carbenes through electronic and steric effects, [357] but only recently did Braunschweig and co-workers [358] synthesize the first metal-BO complex, trans$-[(Cy_3P)_2BrPtBO]$, in which the boronyl moiety is stabilized by a Pt(II) center. This work inspired both experimentalists and theorists to explore several derivatives of trans$-[(Cy_3P)_2BrPtBO]$ [359–361] as well as the potential stabilization of boronyls by other metals. [351, 362–368] While some unexpected observations resulted, such as the synthesis of a trinuclear ruthenium complex capped with a BO unit, [369] the general theme that has emerged

is that an electron-rich metal center is necessary to stabilize the polar B≡O bond. And while B-centered polyboronyls have been previously observed and characterized in the gas phase, [370] metal-boronyl complexes have yet to be observed with more than one boronyl ligand.

Fundamentally, the complex electronic and magnetic properties of lanthanide-based materials arise from partially filled but contracted core-like 4f orbitals. While the 4f orbitals are generally considered to be core-like and nonbonding, they lie close in energy to the 5d and 6s valence electrons, giving rise to a constellation of very close-lying electronic states resulting from a single general subshell occupancy, or "superconfiguration", to borrow a term from seminal work on the lanthanide oxide diatomics. [97, 100, 114, 297, 331, 371–380] As an example, the two singly occupied orbitals in CeO can be largely described as Ce-local 4f and 6s orbitals, the latter being very delocalized and therefore modestly antibonding. These contain 16 very close-lying electronic states arising from this 4f 6s superconfiguration. [96] From a molecular standpoint, there have been very few electronic spectroscopic studies on lanthanide oxides larger [381] than diatomic molecules (a sampling is included in the references cited) [97, 100, 114, 297, 331, 371–380] let alone borides, aside from several recent anion photoelectron spectroscopic studies, including new and interesting "inverse-sandwich" complexes consisting of planar boride rings sandwiched by lanthanide cations. [127, 238, 382–385] In particular, the studies by Wang and co-workers on Pr-doped B_x clusters (x = 3, 4, 7) provide a story of structural evolution with increasing B coordination. [382, 386]

Since bonding in ionic systems is localized, and, in the case of lanthanide borides, the material itself is cluster-like, small cluster models provide a particularly powerful platform for probing the electronic and molecular structures, both from an electronic structure theory standpoint and from experiment owing to the accessibility of mass selected clusters of these systems and their spectroscopic characterization. The molecular and electronic structures of clusters are governed by the same attributes that govern bulk properties, as supported by numerous studies on elemental and ionic cluster systems across the periodic table. [32, 387–392]

In the first section of this study, two cerium-based oxoboride complexes $CeO_2B_x^-$ (x = 2, 3) were interrogated with density functional theory calculations. The results indicate that the two species assume very different bonding motifs. $CeO_2B_2^-$ can be described as a diboronyl, $Ce(BO)_2^-$, with the Ce center in a +1 oxidation state in the anion and a +2 oxidation state in the associated neutral. The BO ligands in this particular complex are singlet anions with the same orbital occupancy described by Zhai et al. [393] In contrast, while differing by one B atom, the $CeO_2B_3^-$ complex features the Ce center binding side-on to an $O_2B_3^{3-}$ unit, structurally similar to the $B(BO)_2^-$ molecule previously characterized by Zhai et al., [370] in a fanlike structure. In this case, Ce is in the +2 oxidation state in the anion and +3 in the neutral.

Detachment transitions observed for both $Ce(BO)_2^-$ and $CeB_3O_2^-$ involve nominal one-electron detachment of electrons from Ce 6s-like molecular orbitals. Calculations on both anions and associated neutrals, which predict spectroscopic parameters in very good agreement with observed PE spectra, reveal interesting electronic structures that may advance understanding of oxidized cerium boride surfaces. $Ce(BO)_2^-$ and $Ce(BO)_2$ present particularly challenging systems for study because of the exceptionally flat (OB)−Ce−(BO) bend potential and the low-lying open-shell singlet neutral state that is accessed by one-electron detachment of the anion. In addition, the near degeneracy of states featuring single occupancy of different Ce-local 4f orbitals, the degeneracy of which is broken in the ligand field, often results in challenging SCF convergence cases and requires particular care to ensure meaningful analysis of the computational results.

Recently, Bowen and co-workers reported the anion PE spectrum of SmB_6^-. Electron detachment energies were calculated using the CASPT2 method, and Kohn-Sham orbitals were used to model the detachment process.(21) While they were unable to definitively assign the structure based on the calculations, a near planar C_{2v} structure was consistent with their spectrum. The spectrum appeared to be congested with numerous, overlapping electronic transitions, making assignments particularly challenging. The Sm center in bulk SmB_6 has a $4f^5$ subshell occupancy, and nominally the same was found in calculations on the molecular unit, though there was some delocalization of the 4f electrons into the 2p molecular orbitals predicted, which is contrary to the general viewpoint of the core-like character of the 4f subshell. The near-half-filled subshell does result in exceptionally complex electronic structure. However, a similar study on the LiB_6^- photoelectron spectrum with attending theoretical treatment by Wang and co-workers was similarly complex, with an anion PE spectrum as congested as the SmB_6^- spectrum. Calculations on LiB_6^- suggested a B_6^{2-} ring complexed to the Li^+ cation, with all the detachment transitions being associated with B_6^{2-} orbitals. [113]

CeB_6^- offers a molecule with interactions between the metal center and the boron cluster that is comparable to SmB_6^- but should be simpler from a computational standpoint, since the 4f subshell would at most be singly occupied. On the basis of the comparison of a large number of calculated structures with vibrationally resolved anion photoelectron spectra, the molecular unit assumes a planar C_{2v} or near-planar C_s structure that can be described as $Ce^{2+}(B_6)^{3-}$ for the anion and $Ce^{3+}(B_6)^{3-}$ for the neutral. We compare the relative energy of more bulk-like unit structures to the energey of the planar structure determined from the spectrum and relate the findings to what would likely be structural changes in the bulk $(B_6)^{3-}$ octahedral units located on edges or corners, and we compare the impacts on the electronic structure and emission properties.

6.2   Computational Methods

Release and local development versions of the GAUSSIAN 16 quantum chemistry package were used to test the viability of a plethora of molecular and electronic structures the studied anions and neutrals. [176, 394] The unrestricted B3LYP hybrid density functional method was used. The Stuttgart relativistic small core atomic natural orbital basis set and corresponding effective core potential (ANO/ECP) basis set with 28 core electrons and a contracted Gaussian basis for the valence electrons (14s 13p 10d 8f 6g)/[6s 6p 5d 4f 3g] was used for Ce, [341] and a Dunning-style correlation consistent basis set was used for both B and O. [285, 286, 395] A wide range of isomers in numerous spin states was calculated, and vibrational analyses were performed to ensure structures were at local minima. The relative energies of the plethora of anion and neutral structures and spin states reported are zero-point energy corrected values. The natural ionization orbital (NIO) model has been used to provide an orbital picture of the electron detachment process. [117]

In all cases, the stability of KS determinants has been verified. [177, 178] The electronic structures of all converged Kohn-Sham DFT determinants have been fully characterized as part of our standard analysis. For the systems studied in this work, such a process requires special attention as multiple stable electronic configurations can be optimized with standard SCF optimization approaches. Of particular concern was ensuring that located electronic configurations resulted in anion/neutral electronic structure pairings corresponding to allowed one-electron transitions. In addition to manual inspection of each SCF solution obtained in our calculations, NIO analysis assisted

with such concerns and, in some cases, was used to identify improved sets of orbitals for the SCF engine's initial guess.

The calculation of electronic excited states was carried out using the linear response form of time-dependent DFT. [236,237] Such calculations were carried out using optimized ground state geometries. The nature of each excitation was characterized using the natural transition orbital (NTO) model of Martin. [46] To ensure convergence of the Davidson diagonalization process, TDDFT results reported below requested 30 states. To compare computational and experimental results, the adiabatic and vertical detachment energies (ADE and VDE) of each anion were computed. The ADE is the difference between the zero-point corrected energies of the anion and one-electron accessible neutral with the common structure, and the VDE is the difference between the ground state energy of anion and single-point energy of neutral confined at anion geometry. Franck-Condon progressions were generated for all detachments and their profiles were compared to experimental photoelectron spectra and subsequent spectral assignments were performed. [109–111, 235, 396–398]

6.3   Results and Analysis

6.3.1 $CeO_2B_2^-$ Computational Results

The photoelectron spectrum obtained by the Chick-Jarrold group shows an intense band, **X**, originating at 1.87(5) eV, which is taken to be the electron affinity (EA) of CeO_2B_2, with lower intensity transition, **A**, appearing approximately 0.7 eV higher in binding energy. The vibrational structure in band X is congested and only partially resolved. The asymmetry parameter, $\beta \simeq 0.9(5)$, reflects a parallel transition characteristic of detachment from a Ce-local 6s-like orbital. In order to simulate the experimental photoelectron spectra of the studied clusters, we have invstigated the structures and relative energies of various close-lying isomers and electronic states of both anions and neutrals. Computationally, the lowest energy structure for $CeO_2B_2^-$ was found to be a Ce(I) center bound to two monoanionic boronyl units with C_{2v} symmetry, $Ce(BO)_2^-$ shown in Figure 6.2. Structures in which Ce coordinated the O atoms of the BO units did not converge, and the lowest-lying structure incorporating mixed Ce−O and Ce−B bonding was approximately 0.5 eV higher in energy. The Ce−B−O bond angles in the lowest energy $Ce(BO)_2^-$ geometry are 175°. Notably, the harmonic frequency corresponding to symmetric Ce−B−O bending is only 40 cm^{-1}. Indeed, geometry optimization with constrained linear Ce−B−O angles results in a species lying only 0.1 kcal/mol higher in energy than the lowest energy structure.

	Electronic Etate	$\langle S^2 \rangle$	Electronic Energy (eV)	r_{Ce-B}, r_{B-O} (Å)	$\angle B-Ce-B$, $\angle Ce-B-O$	Totally symmetric vibrational frequencies (cm^{-1})
$Ce(BO)_2$	$^1B_1$	1.003	1.84	2.657, 1.212	116, 175	40, 204, 257, 1903
	$^3B_2$	2.002	1.68	2.688, 1.213	114, 175	39, 193, 259, 1897
$Ce(BO)_2^-$	$^2B_1$	1.1950	0.00	2.760, 1.221	132, 178	39, 186, 243, 1841

Table 6.1: DFT-Calculated Energies, Structural Parameters, and Symmetric Vibrational Frequencies of the $CeO_2B_2^-$ $^2B_1$ State and CeO_2B_2 $^3B_2$ and $^1B_1$ States.

CeO$_2$B$_2$

(1.84 eV)
^{1}B$_1$ C$_{2v}$

(1.68 eV)
^{3}B$_2$ C$_{2v}$

CeO$_2$B$_2^-$

(0.0 eV)
^{2}B$_1$ C$_{2v}$
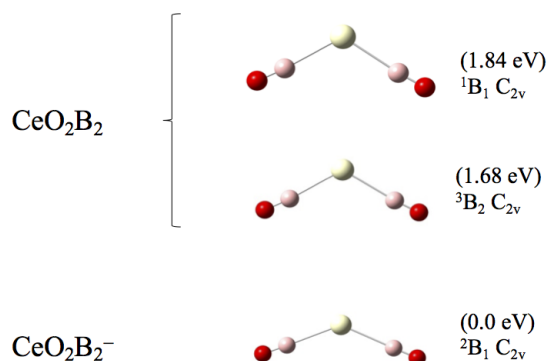
Figure 6.2: Structures of Ce(BO)$_2$ anion and neutrals

Ce(BO)$_2^-$ has a $^2B_1$ ground state, with nominally a $4f6s^2$ Ce superconfiguration (the HOMO is a 6s-5d hybrid). The molecular orbital occupancy is summarized in Figure 6.3. The Ce-local orbital occupancy is similar to that of CeO$^-$, and detachment of an electron from the HOMO can access both the triplet neutral and open-shell singlet neutral state. [297] In neutral CeO, these states are separated by less than 100 cm^{-1}. [98, 100] The lowest energy neutral identified computationally has a $^3B_2$ electronic term, and has the same structure as the $^2B_1$ anion, though with a slightly smaller B−Ce−B angle and slightly shortened Ce−B and B−O bonds lengths. The calculated electron affinity is 1.68 eV, which is in fair agreement with the observed onset of electron signal in the spectrum. The relative energies and several structural parameters are summarized in Table 6.1.

NIO analyses of detachment to both neutral states occurs via the Ce 6s-like molecular orbital, shown in Figure 6.4. NIO analysis [117] of these ionization processes also shows modest orbital rearrangement after electron detachment. This orbital relaxation involves about one-third of an electron and results in modified spin polarization. The open-shell $^1B_1$ state is calculated to be 1.84 eV higher in energy than the anion, which yields a triplet-singlet splitting of 0.16 eV (1300 cm^{-1}), somewhat higher than the analogous splitting in neutral CeO. However, the HOMO of the triplet and singlet neutrals has significantly more 5d character, so the two unpaired electrons are more strongly coupled than the two unpaired electrons in CeO, in which the HOMO is a very diffuse 6s-like orbital.

Clearly, the change in term symbol between anion ($^3B_2$) and neutral ($^2B_1$) is not allowed in a one-electron transition after detachment from the 6s-like HOMO with a_1 symmetry. This discrepancy is the result of differences in the calculated 4f orbital occupation for the lone 4f electron between anion and neutral. Attempts to edit the occupancies to ensure common 4f orbital occupancies in the states for the anion and neutral are identical were unsuccessful. However, on the basis of the current and previous studies, the effect of changing which of the seven nearly degenerate 4f orbitals is occupied has a minor impact on energy and structure.

Despite the minor disparity in the occupied 4f orbital, simulations based on the $^3B_2 - {}^2B_1$ and $1B_1 - {}^2B_1$ transition parameters (normal coordinate displacements, vibrational frequencies) are shown in Figure 6.3 as blue and red traces, respectively. The individual transitions do not account for the full energy span of band **X** on the experimental photoelectron spectrum. However, setting the origin of the $^3B_2 - {}^2B_1$ transition to 1.84 eV and the $^1B_1 - {}^2B_1$ to 1.99 eV (in fair agreement with the calculated values of 1.68 and 1.84 eV, respectively) and summing the two simulations (purple
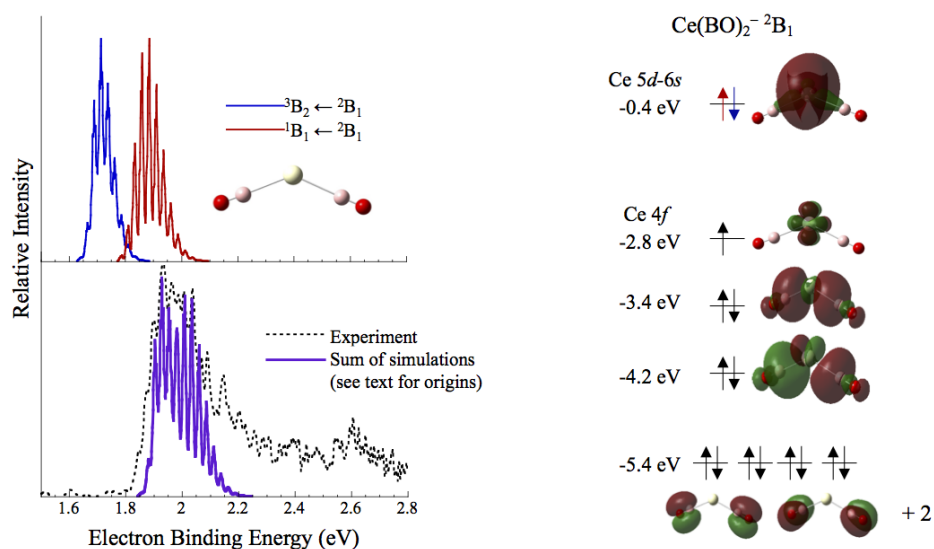
Figure 6.3: Summary of the lowest energy structures that converged for $CeO_2B_2^-$ and CeO_2B_2 as well as the relative orbital occupations of the anion. A simulation of the $^3B_2 - {}^2B_1$ transition is shown above in blue and the $^1B_1 - {}^2B_1$ transition in red with the corresponding detached electrons labeled in blue and red, respectively.
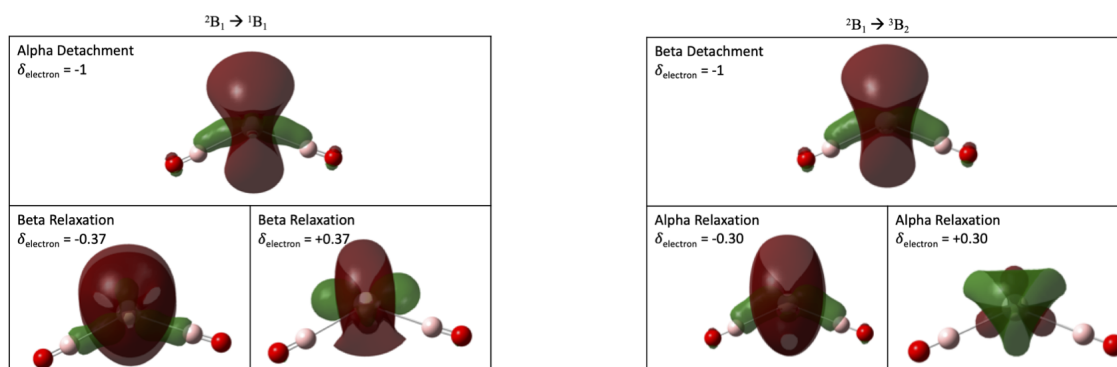
Figure 6.4: Natural ionization orbitals (NIOs) for $CeO_2B_2^-$ / CeO_2B_2 electron detachment. The left panels display NIOs for electron detachment from the $^2B_1$ anion state to a $^3B_2$ neutral state. The right panels display NIOs for electron detachment from the $^2B_1$ anion state to an open-shell $^1B_1$ neutral state.

71

trace) does result in a band profile that is similar to the observed spectrum (black dotted trace). The simulation matches the position of the vibrational fine structure on the low and high binding energy side of band **X**. The agreement supports the assignment of $CeB_2O_2^-$ to the diboronyl structure. The primary active modes are the Ce$-$B symmetric stretch (259/257 cm^{-1}) and symmetric bending (39/40 cm^{-1}, 193/204 cm^{-1}) modes.

6.3.2 $CeO_2B_3^-$ Computational Results

The photoelectron spectrum, also obtained by our collaborators, shows an intense, nearly vertical transition, **X**, is observed at 1.15(2) eV e-BE, which is taken to be the EA. The aniostropy, $\beta = 0.9(2)$, is nearly identical to that of Ce(BO)$^-$, again consistent with detachment from a Ce-local 6s-like orbital. Two lower-intensity transitions, **A** and **B**, emerge around 1.0 and 1.5 eV higher in binding energy. The PE spectrum of $CeO_2B_3^-$ obtained using 2.33 eV photon energy (green trace) exhibits a well-resolved vibrational progression with a 330 cm^{-1} spacing. Furthermore, in the 3.49 eV spectrum, there are regularly spaced low-intensity peaks at energies between **X** and **A**, which may be indicative of vibronic coupling between states. The EA of CeO_2B_3 is similar to cerium oxide clusters that have been studied previously. [329, 399] Indeed, the lowest energy structure of $CeO_2B_3^-$ found computationally, shown in Figure 6.6, at first glance appears to be a borated cerium dioxide molecule. However, compared to CeO_2^-, [103] the Ce$-$O bond is substantially longer for the oxoboryl complex, approximately 2.4 Å compared to 1.9 Å. Numerous additional structures and spin states were explored computationally but were not included in the discussion here. They can be found in the supporting information of reference [127].

CeO_2B_3 (1.25 eV) $^2B_2$ C_{2v}

$CeO_2B_3^-$ (0.04 eV) $^1B_2$ C_1

(0.0 eV) $^3B_2$ C_1
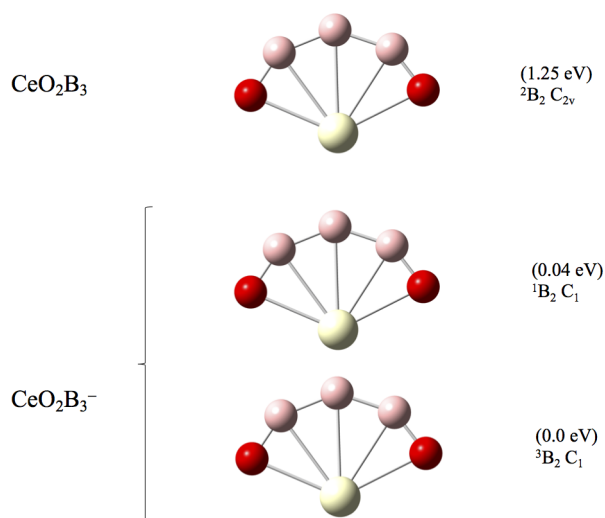
Figure 6.5: Structures of CeO_2B_3 anions and neutral.

$CeO_2B_3^-$ is predicted to have a $^3B_2$ ground electronic state with Ce in the 6s 4f supercon-figuration (+2 oxidation state) (figure 6.5). The 6s-like HOMO is more diffuse than the HOMO of Ce(BO)$_2^-$; Figure 6.6 includes a summary of the orbital occupancy. The lowest-energy neutral structure found computationally is structurally very similar, in agreement with the narrow Franck-Condon manifold observed for band **X**. The Ce$-$O and Ce$-$B bond lengths are modestly shorter

in the neutral, and the O−Ce−O bond angle is marginally larger. The neutral is predicted to have a $^2B_2$ ground state, accessed via detachment of the single 6s-like electron, resulting in a Ce(III) center. The calculated EA, 1.25 eV, is in very good agreement with the observed EA, 1.15 eV. Table 6.2 lists the structural parameters and relative energies calculated for the ground states of the lowest energy structures found for the anion and neutral.

	Electronic State	$\langle S^2 \rangle$	Electronic Energy (eV)	$r_{Ce-B_{1,3}}, r_{Ce-B_2}$ r_{Ce-O}, r_{B-O} r_{B-B} (Å)	$\angle$ O-Ce-O	Totally symmetric vibrational frequencies (cm^{-1})
CeO_2B_3	$^2B_2$	0.756	1.25	2.476, 2.487, 2.349, 1.294, 1.521	133	268, 334, 597, 786, 1549
$CeO_2B_3^-$	$^1B_2$	1.006	0.04	2.509, 2.509, 2.406, 1.295, 1.517	130	229, 301, 584, 778, 1558
	$^3B_2$	2.007	0.00	2.509, 2.589, 2.408, 1.294, 1.517	130	229, 301, 584, 777, 1559

Table 6.2: DFT-Calculated Energies, Structural Parameters, and Symmetric Vibrational Frequencies of the $CeO_2B_3^-$ $^3B_2$ and $^1B_2$ states and CeO_2B_3 $^2B_2$ States

The simulation of the $^2B_2 - {}^3B_2$ transition based on the calculated spectroscopic parameters, also shown in Figure 6.6, is in excellent agreement with the experimental spectrum. The calculated origin is 1.25 eV; the origin of the simulation shown was set to 1.15 eV to highlight the excellent agreement between the calculated vibrational progression and the experimental spectrum. The primary active vibrational mode is the symmetric breathing of Ce and the O_2B_3 unit (334 cm^{-1}), consistent with the overall contraction of bond lengths in the transition (Table 6.2). NIO analysis on both detachments show detachment from Ce-based 6s-like molecular orbital. (Figure 6.7)

The experimental spectrum obtained using 2.330 eV photon energy also exhibits lower-intensity peaks between the peaks in the main vibrational progression which could be attributed to transitions originating from the open-shell singlet state of $CeO_2B_3^-$ in which the electrons singly occupying the Ce 6s and 4f orbitals are antiparallel. An open-shell singlet state was found computationally to be 326 cm^{-1} higher in energy than the triplet, which is certainly within the ballpark of ca. 150 cm^{-1} suggested by the features lying between members of the 334 cm^{-1} vibrational progression not accounted for in the simulation of the $^2B_2 - {}^3B_2$ transition.

On the basis of the orbital occupancy of the anion (Figure 6.6), bands **A** and **B**, which are less intense than band X, very likely involved the detachment of electrons for the MOs that can be described as B 2p π-like orbitals, which would be degenerate in free $B_3O_2^-$, but bound to the Ce center, they have a_1 and b_1 species. These delocalized orbitals lie above the singly occupied 4f orbital energetically, while O 2p-based bonding orbitals in cerium oxide lie energetically below the singly occupied 4f orbital.

6.3.3 CeB$_6^-$ Computational Results

The photoelectron spectrum collected by our collaborators shows an intense band exhibiting partially resolved vibrational structure with irregular spacing in both spectra, with an onset at ap-
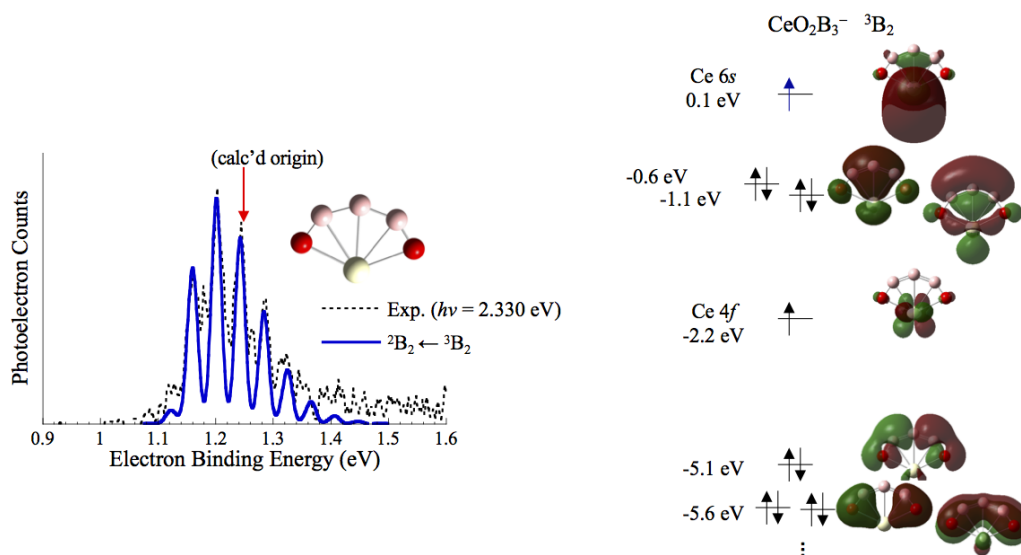
Figure 6.6: Summary of the lowest energy structures that converged for $CeO_2B_3^-$ and CeO_2B_3 as well as the relative orbital occupations of the anion. A simulation of the $^2B_2 - {}^3B_2$ transition is shown above with the corresponding detached electron labeled in blue.

proximately 1.36 eV. The feature is tentatively labeled to indicate two transitions, **x** and **X**, with **x** being much narrower than other features in the 1.3-1.7 eV e-BE range. Both bands **X** and **x** are parallel transitions with $\beta = 1.1(1)$, consistent with detachment from a Ce-local 6s-like molecular orbital. [114, 127, 297, 331] An additional broad feature, labeled **A**, with isotropic photoelectron angular distribution is observed with a vertical detachment energy (VDE) of 2.28 eV. The origin of band **A** is difficult to identify because of the continuum signal observed from band **X** to higher e-BE. This band is assigned to detachment of an electron nominally from the hexaboride unit, since detachment of a 4f electron is expected to have a very small cross section. [107]

Computationally, two general structural isomers were found to be energetically competitive: A planar or near-planar teardrop structure, and a boat-like structures in which the B_6 cluster assumes a structure comparable to the boat conformation of cyclohexane, with the Ce center serving as a mast. Figure 6.8 shows these structures and relative energies of several spin states of anions (bottom half) and neutrals (top half). Table 6.3 summarizes the relative energies, a general description of the electronic structures, and the $\langle S^2 \rangle$ values.

The lowest energy CeB_6^- structure features a distorted boat-like B_6 unit coordinated to a Ce center, in a pure doublet spin state. The geometry of this molecule is trivially distorted from C_2 symmetry. A similar structure with C_{2v} symmetry lies 0.57 eV higher in energy. Within the accepted error of the computational model chemistry, a planar C_{2v} teardrop structure in a quartet spin state was found to be only 0.01 eV above the lowest lying boat structure. Several open-shell anion doublet spin states were also identified within 0.1 eV of the quartet state (*vide infra*). The lowest energy detachment transition associated with the boat structure is 1.74 eV. In better agreement with experimental observation, the lowest energy detachment for the teardrop structure is calculated at 1.52 eV. We note that an anion structure most similar to the bulk, which is a Ce center coordinated to
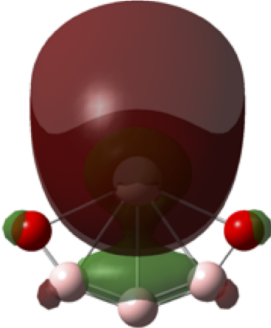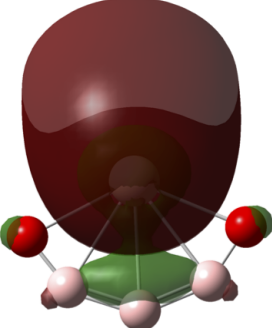
$^1B_2 \rightarrow {}^2B_2$ NIO Beta Detachment	$^3B_2 \rightarrow {}^2B_2$ NIO Alpha Detachment

Figure 6.7: Natural ionization orbitals (NIOs) for $CeO_2B_3^-/CeO_2B_3$ electron detachment. The left panel displays the NIO for electron detachment from the $^3B_2$ anion state to the $^2B_2$ neutral state. The right panel displays the NIO for electron detachment from the open-shell $^1B_2$ anion state to the $^2B_2$ neutral state

the face of a B_6 octahedron, converged over 1.7 eV higher in energy. Isolated B_6 in neutral, anionic, and dianionic charge states are predicted to be planar, with anion PE spectra of B_6^- supporting the computational results for the neutral and anion. [400]

On the basis of the orbital occupancies of the asymmetric boat structure, the anion can be described as $Ce^{3+}(B_6)^{4-}$, with the hexaboride cluster being closed shell and the Ce center having a 4f occupancy. A higher lying quartet state with this structure can be described as $Ce^{2+}(B_6^{3-}$, with the Ce center having 4f 6s occupancy, and the hexaboride cluster in a doublet state. The lowest energy electronic states of the neutral boat structure are accessed from the ground electronic state of the anion by detaching an electron from the hexaboride ligand $Ce^{3+}(B_6)^{3-}$, which can yield open-shell singlet or triplet states, associated with antiparallel and parallel alignment of the two unpaired electrons. The calculations predict the open-shell singlet energy to be only slightly lower than the triplet energy. The proximity of these two states suggests that the unpaired electrons in the Ce-local 4f orbital and the B_6-local orbital are weakly (spin) coupled. Simulations of the $^1A \leftarrow {}^2A$ and $^3A \leftarrow {}^2A$ transitions generated from the computational results are shown in Figure 6.9. Both transitions are fairly vertical, with the short 264 cm^{-1} vibrational progressions associated with the Ce$-B_6$ metal-ligand stretch.

The teardrop structure of the anion has a different occupancy, which can be described as $Ce^{2+}(B_6)^{3-}$, with the Ce center having a 4f 6s orbital occupancy and the hexaboride unit in a $^2A_2$ state. Again, the 4f electron generally is decoupled from the other unpaired electrons, and the anion can assume pure quartet spin and open-shell doublet spin states featuring antiparallel electrons occupying Ce 4f- and 6s-like orbitals. Furthermore, with five nearly degenerate 4f orbitals, calculations on states with the single electron occupying different 4f orbitals (symmetry broken by the B_6 ligand) are very close in energy. Two examples of open-shell doublet states that differ only by the symmetry of the singly occupied 4f orbital are included in table 6.3.

75

2.18 eV $^3B_1$ C_{2v}

1.76 eV ^3A C_1

1.74 eV ^1A C_1

1.57 eV $^3A_1$ C_{2v}
(one i freq)

1.56 eV $^1A_1$ C_{2v}
(one i freq)

1.53 eV $^3A''$ C_s

1.54 eV $^1A''$ C_s

0.73 eV $^2A_1$ C_{2v}

0.57 eV $^4B_1$ C_{2v}

0.51 eV ^4A C_1

0.05 eV $^2B_2$ C_{2v}

0.04 eV $^2A_1$ C_{2v}

0.0 eV ^2A C_1

0.01 eV $^4A_2$ C_{2v}
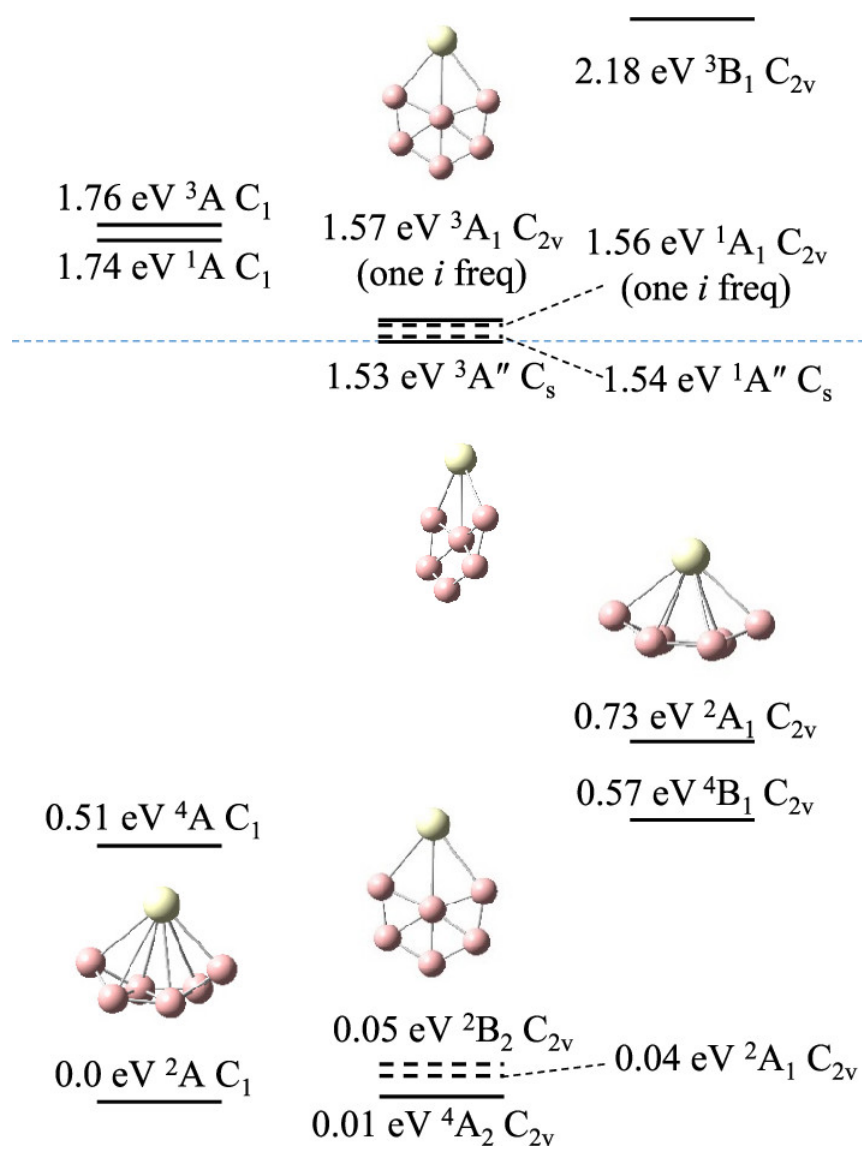
Figure 6.8: Calculated relative energies of anion and neutral CeB$_6$ structures and spin states. Open-shell low-spin states are indicated with dashed lines
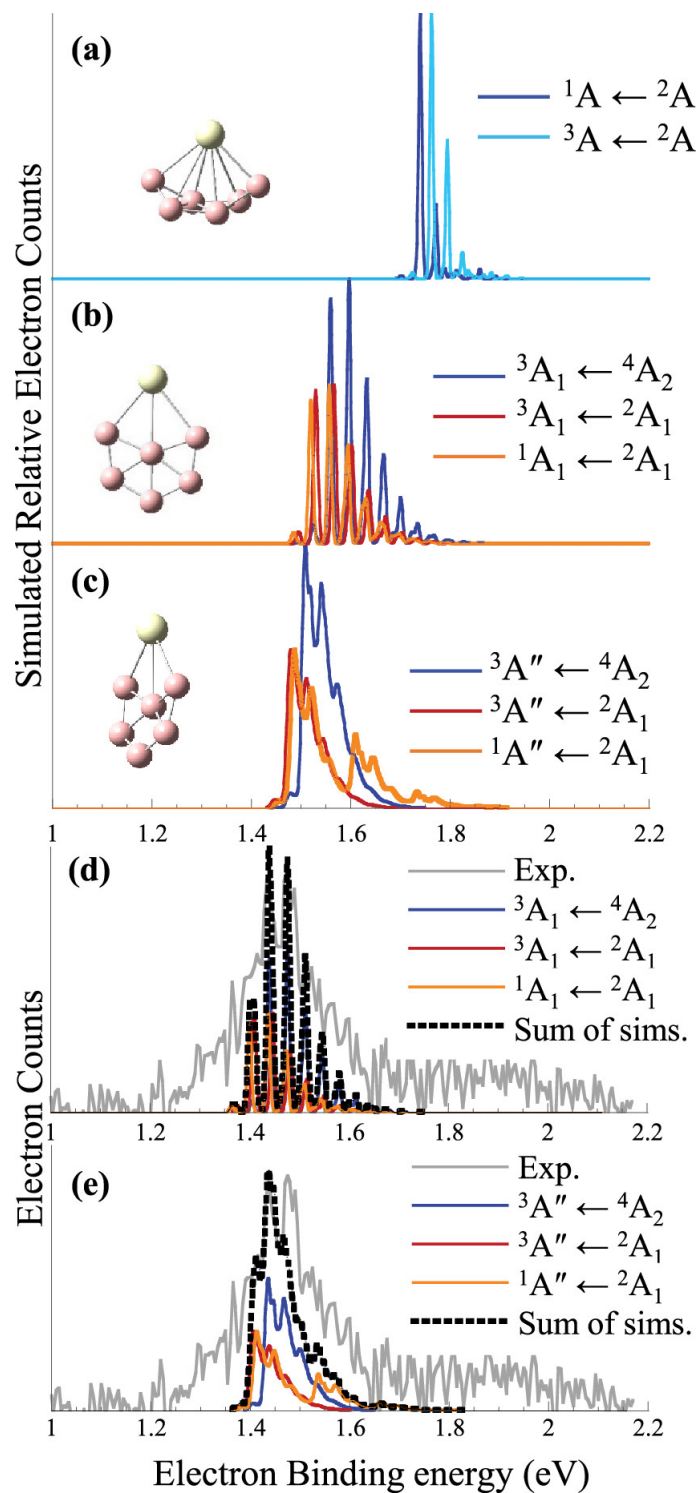
Figure 6.9: (a) Spectral simulations based on the asymmetric boat structure, (b) planar teardrop structure, and (c) buckled (relaxed) teardrop structure. (d) and (e) show the simulated spectra from (b) and (c), respectively, shifted to lower e-BE to overlap with the observed spectra.

77

	Symmetry	General electronic description	$\langle S^2 \rangle$	Relative energy/eV	ADE/eV
CeB_6					
sym boat $^3B_1$	C_{2v}	$Ce^{3+}(4f)[B_6(^2A)]^{3-}$	2.01	2.18	1.61
asym boat ^3A	C_1	$Ce^{3+}(4f)[B_6(^2A)]^{3-}$	2.04	1.76	1.76
asym boat ^1A	C_1	$Ce^{3+}(4f)[B_6(^2A)]^{3-}$	1.03	1.74	1.74
planar teardrop^a 3_1^A	C_{2v}	$Ce^{3+}(4f)[B_6(^2A_2)]^{3-}$	2.01	1.57	1.56 $(1.53)^b$
planar teardrop^a $^1A_1$	C_{2v}	$Ce^{3+}(4f)[B_6(^1A_2)]^{3-}$	0.99	1.56	1.52
buckled teardrop $^1A''$	C_s	$Ce^{3+}(4f)[B_6(^1A_2)]^{3-}$	1.02	1.53	1.49
buckled teardrop $^3A''$	C_s	$Ce^{3+}(4f)[B_6(^2A'')]^{3-}$	2.01	1.53	1.52 $(1.48)^b$
CeB_6^-					
bulk monomer ^4A	C_1	$Ce^{2+}(4f6s)[B_6(^2A)]^{3-}$	3.88	1.96	
sym boat $^2A_1$	C_{2v}	$Ce^{2+}(4f_{b_1}5d_{b_1})[B_6(^2A_1)]^{3-}$	1.77	0.73	
sym boat $^4B_1$	C_{2v}	$Ce^{2+}(4f_{a_1}5d_{b_1})[B_6(^2A_1)]^{3-}$	3.77	0.57	
asym boat ^4A	C_1	$Ce^{2+}(4f6s)[B_6(^2A)]^{3-}$	3.78	0.51	
teardrop $^2B_2$	C_{2v}	$Ce^{2+}(4f6s)[B_6(2A_2)]^{3-}$	1.76	0.05	
teardrop $^2A_1$	C_{2v}	$Ce^{2+}(4f6s)[B_6(^2A_2)]^{3-}$	1.74	0.04	
teardrop $^4A_2$	C_{2v}	$Ce^{2+}(4f6s)[B_6(^2A_2)]^{3-}$	3.76	0.01	
asym boat ^2A	C_1	$Ce^{3+}(4f)[B_6(^1A)]^{4-}$	0.76	0.0	

^{a} One imaginary frequency, ^{b} ADE for transition from the $^2A_1$ excited state.

Table 6.3: Summary of Lowest Energy Structures and Electronic States for CeB_6^- and CeB_6 Presented in Order of Decreasing Energy.

The lowest energy state of the neutral can be described as $Ce^{3+}(B_6)^{3-}$, with the Ce center having 4f orbital occupancy and the hexaboride unit having a singly occupied p_π orbital. Calculations identified both high-spin triplet and low-spin open-shell singlet configurations of the neutral. In both cases, the planar C_{2v} neutral teardrop structures have one imaginary frequency, with the minimum energy puckered teardrop structure with C_s symmetry, similar to the structure of AlB_7^- cluster, [401] lying around 370 cm^{-1} lower in energy. This difference is sufficiently low to raise the possibility that, on average, the neutral geometry could be considered planar.

Notably the spin-squared expectation values for the open-shell singlets were all roughly 1.0, suggesting that the spin contaminated determinants can be characterized as equal admixtures of pure singlet and triplet determinants. [402] Previous work on metal oxides by our laboratories has demonstrated that in some cases spin contaminated results pose significant challenges for spectral analyses and that such cases can be improved using spin-projection methods. [30, 42] With this in mind, geometry optimizations and analytic frequency calculations using the approximate projection (AP) model were carried out on these species. [403–407] The result of these calculations indicated that spin contamination has a small effect on the spectral analysis of the CeB_6 teardrop. AP energy corrections are less than 0.01 eV, and AP calculations provide negligible changes to geometries force constants relative to the open-shell results.

Figure 6.9 includes simulations based on transitions from the quartet (**X**) and open-shell doublet anions (**x**) to the (b) triplet neutral and open-shell singlet confined to the planar structure and (c) the triplet neutral and open-shell singlet allowed to relax. Note that the transition energies in both panels are very similar because of the very small relaxation energy of the neutral. Their profiles

(a) Boat Structure
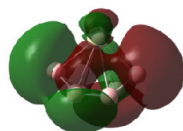
Alpha Detachment	Beta Detachment	Alpha Detachment
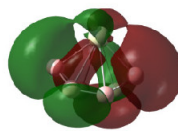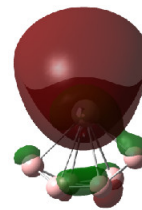
$$^2A \rightarrow {}^1A \qquad {}^2A \rightarrow {}^3A \qquad {}^4A \ (E_{rel} = 0.51 \text{ eV}) \rightarrow {}^3A$$

(b) Teardrop Structure

Alpha Detachment	Alpha Detachment	Alpha Detachment
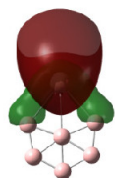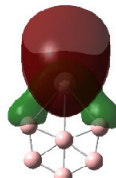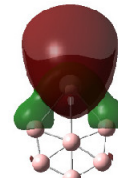
$$^4A_2 \rightarrow {}^3A_2 \qquad {}^2A_1 \ (E_{rel} = 0.04 \text{ eV}) \rightarrow {}^1A_1 \qquad {}^2B_2 \rightarrow {}^1B_2$$

Figure 6.10: NIOs for the one-electron allowed transitions associated with the (a) boat and (b) teardrop structures of CeB_6^-

are slightly different, with the progression in the $Ce-B_6$ stretch (305 cm^{-1} for the planar structure, 309 cm^{-1} for the relaxed structure) being more extended for the planar teardrop structure, and the activation of the 73 cm^{-1} pucker mode adding congestion to the profile for the simulation for the relaxed neutral structure. Parts d and e of Figure 3 show the simulations with all origins shifted to modestly lower electron binding energy (e-BE) to overlay the simulated spectra with the experimental spectrum (0.12 eV for the planar structure simulations, 0.07 eV for the relaxed structure simulations).

While we are unable to definitively assert whether the structure is puckered or, on average, planar, the simulations based on the teardrop structures are in better agreement with the observed spectrum than the boat structure. Recall that the anionic boat and teardrop structures have a fundamentally different orbital occupancy, with the boat structure having more negative charge carried by the $(B_6)^{4-}$ unit compared to the $(B_6)^{3-}$ planar unit of the teardrop. Figure 6.10 shows the NIOs associated with the lowest energy one-electron transitions from the ground states of the boat and teardrop structures. The NIO analysis clearly shows that detachment from the doublet anion state of the boat structure involves an orbital that is highly delocalized through the B_6 boat; detachment from the quartet anion involves a diffuse Ce 6s-like orbital that also includes very modest bonding character with the adjacent B atoms. In all cases, the photoelectron in the teardrop structures involves the Ce 6s-like orbital. The fact that the boat and teardrop structures are predicted to be isoenergetic

suggests competition between Coulombic stabilization and the particular stability of planar boron cluster structures. [408] In the boat structure, the negative charge spread over the $(B_6)^{4-}$ unit is more wrapped around the Ce^{3+} center, maximizing the Coulombic stabilization of this ionic compound. The HOMO of the teardrop structure of the anion is a diffuse Ce 6s-like orbital, which allows for a more stable planar structure of the B_6 unit. [400]

Finally, we note that band **A**, which lies under 1 eV above bands **X** and **x**, exhibits an isotropic photoelectron angular distribution (PAD) and is less intense than band **X**, suggesting that this detachment transition is likely associated with the hexaboride unit, resulting in a Ce^{2+} (4f 6s) $(B_6)^{2-}$ neutral. In addition, this band is embedded in a rising continuum, suggesting strong vibronic coupling between the ground state and the low-lying Ce^{2+} (4f 6s) $(B_6)^{2-}$ states. TDDFT calculations were carried out to explore this possibility. As shown in figure 6.12, excited electronic states were characterized using the NTO model. A neutral excited state corresponding to a transition from a Ce 6s-like orbital to a hexaboride-based orbital was located roughly 1.4 eV above the neutral ground state. Detachment from the anion to this neutral excited state would correspond to detachment of a photoelectron from the singly occupied B_6 localized p orbital.

Figure 6.11 shows a schematic of the orbital energies and occupancies of CeB_6^-, with green boxes indicating Ce 6s-like MOs, the orange lines indicating B 2p-based MOs, the blue indicating O 2p-based orbitals, and red lines indicating Ce 4f orbitals. To indicate single occupation of orbitals in the schematic, the widths of lines representing singly occupied orbitals are half that of doubly occupied orbitals. Unlike cerium oxide molecules in which there is a pronounced energy interval between the 4f and 6s orbitals similar to that in the bulk cerium oxide band structure, there are four B 2p orbitals crowded between the 4f orbital and the 6s orbital in CeB_6^-. To further underscore the relative high energy of the B 2p orbitals, schematics of the orbital energies and occupancies of $CeB_3O_2^-$, $Ce(BO)_2^-$, and CeO^- are included for comparison. The low-lying excitations in neutral CeB_6 are expected to involve promotion from the pool of electrons in close-lying B 2p orbitals into the Ce 6s orbital. As will be discussed below, this is evocative of the thermal conductivity of the bulk material.

6.4   Discussion

6.4.1   Structure and Bonding of $CeO_2B_2^-$ vs. $CeO_2B_3^-$

The anion PE spectra along with DFT calculations unveil unique bonding between Ce and both boronyl and oxoboryl ligands. $Ce(BO)_2^-$, in particular, dominated the mass spectrum, regardless of source conditions, suggesting that it is a particularly stable anion; therefore, Ce^+ readily stabilizes two BO^- ligands. This result was surprising, not only as Ce is electron-poor compared to the transition metals in previously realized metal-boronyl complexes like Pt and Ru but also because it is a novel example of a metal-diboronyl. Bonding in both $Ce(BO)_2^-$ and $Ce(BO)_2$ can be characterized as largely ionic, which is further stabilized by polarization of the Ce-local HOMO away from the negatively charged boronyl units which occurs via mixing of the 6s and 5d orbitals, allowing electron density to be moved off the B$-$Ce$-$B axis. The neutral has a very large calculated dipole moment, 7.7 D. In the anion, the distance between the Ce center and the boronyl groups is considerable, and calculations on structures confined to linear Ce$-$B$-$O bond angles converged with nearly the same energy (0.1 kcal/mol difference) as those found in unconstrained geometry
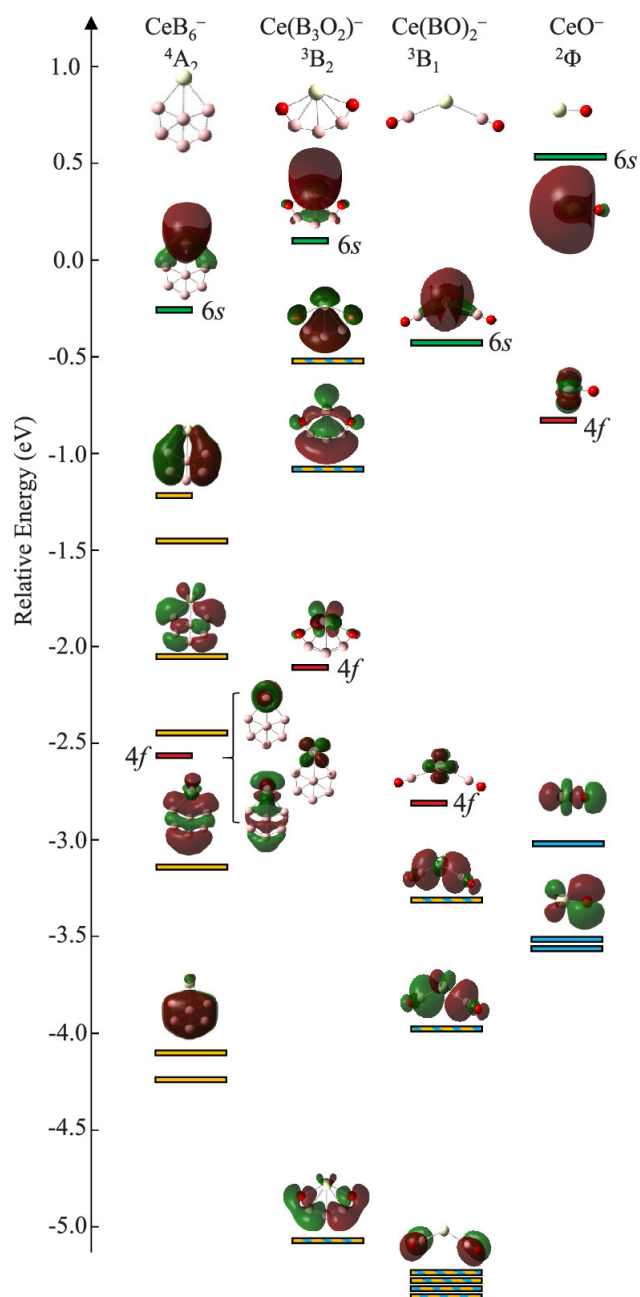
Figure 6.11: Schematic showing the relative orbital energies of CeB_6^-, $Ce(B_3O_2)^-$ [ref [127]], $Ce(BO)_2^-$ [127]], and CeO^- [ref [297]]. Orange lines indicate B 2p-based MOs, the blue lines indicate O 2p-based orbitals, and red lines indicate Ce 4f orbitals. Orbitals that are singly occupied are indicated with lines that are half the width of those representing doubly occupied orbitals.

Excitation Energy: 1.46 eV
Associated orbital eigenvalues = ± 0.99

Figure 6.12: Natural transition orbitals for the excited state calculated from $^1A''$. The hole is shown on the left and the particle is shown on the right.

optimizations that exhibit modestly bent Ce−B−O bond angles (175°).

An intriguing outcome of this study is the profoundly different structure assumed by the $CeO_2B_3^-$ anion, with the trianionic oxoboryl ligand bound to the Ce(II) center in a side-on fanlike structure, confirmed by the excellent agreement between the calculations-based spectral simulation and the ground-state electronic band (**X**) in the experimental spectrum. The electronic structure of this molecule is interesting in the context of lanthanide hexaborides, which are used as emitters in commercial electron guns. This structure features two nearly degenerate, delocalized MOs that lie energetically just below the singly occupied HOMO of the anion, and they are energetically above the singly occupied Ce 4f orbital. Further computational studies on neutral ionization energies and vibronic excitation may lend insight into the role of surface oxidation of LnB_6 emitters. [409] As noted above, the appearance of regular, sharp peaks spanning the gap between bands **X** and **A** suggests vibronic coupling between states connected by promotion of an electron from the delocalized B 2p orbitals and the Ce 6s-like diffuse orbital.

The striking difference in bonding schemes for the two complexes in this study likely arises from boron's one-electron deficiency compared to that of its neighbor carbon. The electron-poor Ce center accepts electronically dense ligands, shown by its propensity to bind two boronyls. While the monoanionic boronyls are stable as closed-shell, strong σ donors, direct coordination of a bare B atom beyond the $(BO)_2$ stoichiometry is highly unfavorable. In this case, the electron-deficiency of B outcompetes Ce. Alternatively, the three B atoms form highly delocalized multicenter two-electron bonds to stabilize this deficiency, seen in the diffuse molecular orbitals about the -system of the $O_2B_3^{3-}$ unit, has previously been observed in other metal-boride clusters. [238, 382, 384]

Considering the implications of this gas-phase spectroscopic and computational study in organometallic chemistry, boronyls have been demonstrated to be very robust ligands and, as CO and CN$^-$ analogues, are useful and interesting synthetic targets. We have demonstrated that Ce can bind two boronyls, joining the short list of experimentally observed metal-$(BO)_x$ compounds; moreover, it is a unique example of a metal-polyboronyl complex. From an electronic structure and computational spectroscopy standpoint, these molecules represent an opportunity to evaluate the effectiveness of tractable single-reference DFT calculations in modeling the complex electronic

structures that arise in partially filled 4f subshells in lanthanide complexes. The fair agreement between the calculated triplet-singlet splitting for this open-shell system suggests current models may be successful in such studies. This work also underscores the critical importance of corroborating computational results with high-quality experimental data when investigating systems with complex electronic structure. Moreover, the current work clearly highlights the potential for experimental collaboration in efforts aimed at developing more effective and accessible methods for treating complex systems.

6.4.2 CeB_6^- Cluster vs. Bulk CeB_6

The goal of this study was to determine how the electronic and molecular structure of the ionic CeB_6 cluster differed from the bulk material, as a way of gaining insight into structural and electronic relaxation on edge and corner sites. Our results suggest that the general charge separation between the Ce centers and the hexaboride clusters are similar in molecular units and the bulk, though the structures of the hexaborides are profoundly impacted when removed from the lattice, and the diffuse Ce 6s-like orbital is stabilized in the cluster relative to the bulk. While the molecular structures determined in this study deviate significantly from bulk CeB_6, particularly in the structure of the hexaboride unit, there are several notable similarities. Bulk CeB_6, as with most other LnB_6 compounds, is a trivalent material with each Ce center having a singly occupied 4f subshell, [410] a feature that is shown prominently in its electronic and magnetic properties. With its highly ionic character, the overall electronic structure of the material has been described as $Ce^{3+}(B_6)^{3-}$, [?] as the neutral molecular units probed in this study. However, with increasing temperature, conductivity increases [411] as electrons are promoted from the B 2p orbitals to partially occupy the Ce 5d conduction band. In the case of small molecular units, the diffuse Ce 6s-based molecular orbital is stabilized relative to the Ce 5d orbitals, suggesting that the bulk lattice confines and therefore destabilizes the Ce 6s band. This study therefore suggests that on the surface, edges, and corners, the lower energy excitations associated with promoting an electron to the 6s state, which can readily couple to the detachment continuum because it is diffuse, play a role in the electronic emission properties of this material. The bulk lattice constant is 4.14 Å, placing the Ce$-$B$_6$ center separation at 3.58 Å. [412] In the neutral relaxed teardrop, along the C_s plane, the average Ce$-$B internuclear distance is 3.33 Å.

Finally, we compare these results to recently reported studies on similar species. The planar, or near-planar, structure giving rise to the experimental spectrum in this study is nearly identical to the structure tentatively assigned to the spectrum of SmB_6^- by Bowen and co-workers. [238] While the molecular structures of SmB_6^- and CeB_6^- in the present work are predicted to be similar, a few key differences emerge in the electronic structure. The B_6 unit carries a different charge between complexes, adopting a B_6^{2-} electron configuration in SmB_6^- and B_6^{3-} in CeB_6^-. Following this, the lanthanoid centers, too, must adopt different oxidation states of Sm^{1+} and Ce^{2+}. One of the most striking differences between the PE spectra is the origins of the photoelectrons. In SmB_6^-, all of the photoelectrons originate from 2p-based molecular orbitals, leaving Sm in an oxidation state of +1 in both the anion and neutral. For CeB_6^-, the transition to the ground state neutral very clearly results from detachment of an electron in a Ce-based 6s-like molecular orbital, confirmed by the polarization dependence of bands **X** and **x**. Thus, in the neutral monomer, CeB_6 takes on the same ionic character of the bulk material. The Sm center distinctly lacks occupation of its

6s-like molecular orbital; though surprising, it has been shown previously that Sm can assume a superconfiguration that favors 4f occupancy over 6s. [126] The polarization dependence of band **A** in the 3.49 eV PE spectrum of CeB_6^- does, however, suggest detachment from B-based 2p-like orbitals as is seen with SmB_6^-.

As a point of comparison, the PE spectrum of the incrementally more boron rich PrB_7^- molecule is consistent with a $4f^2 6s$ electron configuration for the Pr center, which is analogous to the Ce center configuration in CeB_6^-. [382] And, as with CeB_6^-, the first transition observed corresponds to detachment from the 6s-like orbital. In the ground state neutral, both Ce and Pr assume oxidation states of +3, while the B_n unit maintains its trianionic charge. Subsequent excited neutral states in PrB_7 also correspond to detachment of orbitals with mostly B 2p character. The B-based orbitals, however, are significantly more stabilized compared to CeB_6^-. Two of the 2p orbitals in CeB_6^- are only about 1 eV lower in energy than the Ce 6s, with two additional orbitals lying just above the occupied 4f orbital (fig. 6.11). In PrB_7^-, the first occupied 2p orbitals are energetically below the singly occupied 4f orbitals, about 2 eV lower in energy than the 6s. These energetic differences may simply be the result of the different structure favored by PrB_7^-, in which the B_7^{3-} ligand adopts a highly symmetric six-membered ring with a central boron atom buckled out-of-plane.

The distorted geometry is reminiscent of the puckered teardrop of CeB_6^-, but in the case of PrB_7^-, Pr is located over the center of the ring and directly coordinates every B atom, which may result in better charge stabilization on the B_7^{3-} ligand. The puckering of the teardrop structure is also interesting when compared with the B-poorer clusters, PrB_3^- and PrB_4^-, which are planar. [386] This structural change demonstrates how the stabilization provided by the planarity of anionic boride clusters only begins to be outcompeted by Coulombic stabilization when the clusters approach the stoichiometry of the bulk hexaborides.

6.5   Conclusion

Two small Ce-based oxoboryl complexes generated from laser ablation of a pressed Ce and B mixed powder target were identified and characterized with anion PE spectroscopy and DFT calculations. While the two complexes, $CeO_2B_x^-$ (x = 2, 3), differ only by one B atom, they possess fundamentally different bonding motifs. For x = 2, the anion can be described as $Ce(BO)_2^-$, with a Ce(I) center in the anion and Ce(II) in the neutral. In contrast to other previously studied Pt and Ru boronyl complexes, the Ce center is comparatively electron-poor. Furthermore, it is a novel example of a metal-diboronyl complex. On the other hand, the stabilization of boron's one-electron deficiency by diffuse multicenter two-electron bonds outcompetes the stability of close-shelled anionic BO^- groups for $CeO_2B_3^-$. This fan-shaped molecule features a Ce(II) center in the anion and a Ce(III) center in the neutral. This change in ligation was clearly reflected in the considerable differences between PE spectra and is supported by computational results.

In addition, the electronic and molecular structure of CeB_6 has been probed by anion PE spectroscopy and DFT calculations to gain insight into structural and electronic relaxation on edge and corner sites of ionic material. Two competitive molecular structures were identified: an asymmetric boat-like structure and a planar or near-planar teardrop structure. Ce adopted different superconfigurations between isomers; the boat-like structure had a 4f superconfiguration while the teardrop favored a 4f 6s occupancy. The B_6 ligand in these structures carries a charge of -4 and -3, respectively. The teardrop structure, which was calculated to be 0.01 eV higher in energy than the boat

structure, was most consistent with the experimental spectrum. The conclusion is that the unique stability of planar B_6 structure [400, 408] compensates for the reduced Coulombic stabilization between the Ce cation and B_6 anion in the teardrop structure relative to the boat structure.

From an electronic structure standpoint, B_6-local orbitals crowd the energy window between the Ce 4f and 6s orbitals. A low-lying transition from the B-based orbitals is observed slightly less than 1 eV above the ground state. The transition is embedded in a continuum of detachment signal, which is evocative of the thermal conductivity that is characteristic of the bulk material. However, unlike the bulk, our results suggest that edge and corner conductivity involves stabilized, highly diffuse 6s orbitals or bands rather than the bulk-favored 5d band. Finally, high-spin and open-shell low-spin states were calculated to be very close in energy for both the anion and neutral, a characteristic that reflects how decoupled the 4f electron is from the B_6 2p- and Ce 6s-based molecular orbitals.

Chapter 7

Resolving the EuO⁻ Photoelectron Spectrum

"Science is more than a body of knowledge. It is a way of thinking; a way of skeptically interrogating the universe with a fine understanding of human fallibility.
If we are not able to ask skeptical questions, to interrogate those who tell us that something is true, to be skeptical of those in authority, then, we are up for grabs for the next charlatan (political or religious) who comes rambling along."

— *Carl Sagan.*
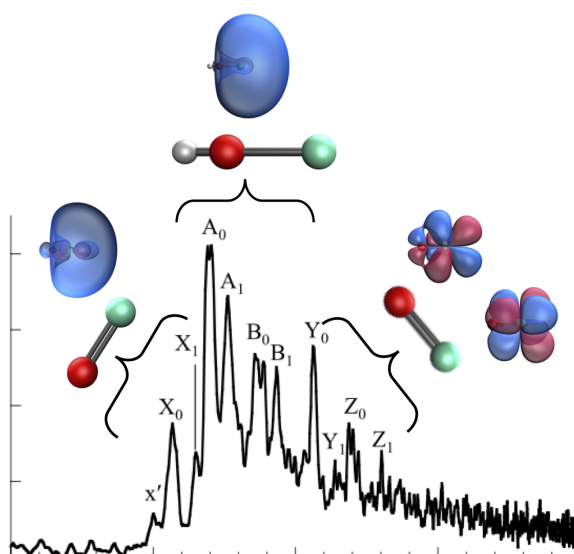
Abstract

Modeling the photodetachment of small lanthanide molecules has given rise to questions regarding the validity of DFT calculations in addition to the proper treatment of scalar-relativistic effects. Likewise, the inability to experimentally mass-select EuO and EuOH gives rise to a complicated and mixed photoelectron spectrum. In this chapter, we address both of these interconnected questions. The results of this work show that performing DFT calculations using an all-electron basis set and treating the relativistic effects using second-order Douglass-Kroll-Hess relativistic integrals yields simulated photoelectron spectra that show excellent agreement with experimental results. Notably, this agreement includes Franck-Condon progressions for the mixed EuO/EuOH photoelectron spectrum.

7.1 Introduction

Lanthanides exhibit unique electronic properties due to the partial occupation of the 4f orbitals resulting in high degrees of freedom in their electronic states. Such electronic flexibility enables their use in diverse applications. [79–83] The sequence ranging from La to Lu is usually accompanied with an increase in 4f occupancy. [126] Unlike trends observed in the transition metalseries, in which the increase in the nd occupation alters the chemistry of the corresponding metal, the increase in 4f occupancy has little effect on the structure and bonding of lanthanides. This result is attributed to the low orbital overlap associated with 4f orbitals which makes them more core-like than chemically active. [126, 399]

Europium has seven half-filled 4f orbitals in its typical oxidation states. The hydrides, oxides, and hydroxides of europium have been reported to efficiently catalyze various organic synthesis reactions, including oxidative dehydrogenation of alkenes and exchange of deuterium and oxygen [114, 241–251]. Such catalytic activity of the lanthanide hydrides, oxides and hydroxides is localized along extended defects and surface point defects. [87]

In order to develop new materials and improve catalysts, it is necessary to determine how specific types of surface defects affect catalytic activity. [84, 85] Direct experimental interrogation of surfaces is complicated by low defect concentration and the dynamic nature of the surfaces (e.g. defect formation, surface restructuring, subsurface oxygen diffusion, adsorption and desorption of reagents). [84–86] An alternative strategy is to study small gas-phase clusters that model the electronic structure of surface defects. Such a strategy allows for detailed exploration of the different electronic properties of these small molecules, and in turn site defects, with reasonable computational cost. [413–415]

Simulations of such clusters are complicated by the presence of several close-lying electronic states, in addition to a manifold of partially filled core-like 4f electrons, both of which give rise to highly-correlated systems. Another complication that arises in computational studies of lanthanide compounds is the treatment of relativistic effects, which directly affect energies and other properties. [416–418] For these two reasons, it is crucial to determine an appropriate model chemistry that can provide accurate results and scales in a way that permits thorough computational investigations. Following our previous work, [42, 112, 117, 125, 127, 128, 240] it is necessary to determine an appropriate method that (1) gives a adequate physical representation of the system's electron correlation and relativistic effects, and (2) efficiently allows us to perform the calculations required to simulate photodetachment spectra. [115, 126, 329, 340, 399]

Recently, Kafader and co workers reported the experimental photoelectron spectra of EuO, EuH, and EuOH anions. In order to further inspect the different species and their detachments, the authors supported their experimental results with DFT calculations on various anions and neutrals. Their results identify high-spin, ionically-bound species. In addition, the study reports the complications arising from the presence of multiple competing species and the inability to mass-select EuO and EuOH. Starting from the results of that study, we aim to assess the performance of various theoretical models in simulating the photodetachment spectra of EuH^-, EuO^- and $EuOH^-$. A particular interest is to compare the behavior and validity of density-functional theory calculations using both all-electron basis sets and ECP approaches in comparison with different correlated methods in reproducing experimental results. We then use DFT to resolve the peaks arising from EuO^- in the previously reported mixed EuO/EuOH photoelectron spectrum.

7.2 Methods

In order to examine the effect of model chemistry on the electronic structure and molecular properties of lanthanides, the optimized geometries of EuH, EuO, and EuOH were obtained using Hartree-Fock (HF), Density Functional Theory (DFT), second-order Moller-Plesset Perturbation Theory (MP2), Coupled-Cluster singles and doubles (CCSD), and CCSD with the inclusion of perturbative triplets method (CCSD(T)). For DFT calculations, the B3PW91 functional was employed. [24, 26, 27, 230, 231, 281] The unrestricted spin formalism was used in all cases. The stabilities of HF and Kohn-Sham determinants have been verified. [177, 178] Stable HF determinants were then used as reference wavefunctions for all post-SCF calculations. The Dunning-style correlation consistent basis set, aug-cc-pVTZ, was used for both hydrogen and oxygen centers. [285, 286] All calculations were carried out using a local development version of the GAUSSIAN suite of electronic structure programs. [176] Geometry optimization was carried out using standard methods and all nature of all potential energy surface stationary points was confirmed by second-derivative calculations. [179]

Accounting for relativistic effects in electronic structure theory calculations face several obstacles, including adding more complications and demanding more computational cost to the many body problem. [416] Among the most common approaches is the effective core potential (ECP) method, where the core electrons are implicitly accounted for by a specific adjustment to the Hamiltonian. [416, 419–421] By doing so, ECPs implicitly account for relativistic effects through parametrization to decrease the computational cost. However, the partial occupation of the 4f electrons and their core-like behavior make it harder to reliably separate the core and valence electrons, thus the choice of a proper set of ECPs can be challenging. [282] In addition, deficiencies in ECP calculations have been previously pointed out in various cases. [422–425] Swart and co-workers showed that, regardless of the extension of the core used in ECPs, the use of an effective core potential results in spin-state splitting that did not converge to the common limit attainable by all-electron basis sets. [426] Other pitfalls were also pointed out, including2 association of ECPs with artifacts in the topological analysis of electron density distributions, [427] and incorrect qualitative results in molecular magnetism calculations. [428] For this study, the Stuttgart RSC ANO/ECP basis set with 28 core electrons and contraction of 14s13p10d8f3g/[6s6p5d4f3g] type, as developed by Cao and Dolg, was employed. [341]

A different approach to account for relativistic effects is implementing the Douglass-Kroll

transformation of the Hamiltonian. For the geometry optimizations and frequency calculations included in this study, the second-order Douglass-Kroll-Hess (DKH) scalar relativistic correction was used. [287] DKH is a good approximation to the relativistic effects on heavy elements mainly because it is accurate enough to give results that are close to the one and many electron four-component approaches. [287] Segmented all-electron relativistically contracted basis set (SARC), developed by Pantazis and Neese, is used in our study. This basis set was optimized using the second-order Douglass-Kroll-Hess relativistic Hamiltonian. [282–284] Such basis sets, despite their compact size, provide a balanced treatment of different electronic configurations of lanthanides, thus they can be used with confidence.

To further study the electron detachment process and describe the nature of the detached electron, we used the natural ionization orbital (NIO) model. [117] The NIO model allows us to distinguish between one-electron transitions and transitions where ionization is accompanied electron rearrangement which is often associated with shake-up/shake-down states. [112, 125] The calculation of excited states was carried out using the linear response form of time-dependent density functional theory (TD-DFT). [236, 237] The calculations were performed starting from the optimized DFT ground-states. The nature of each excitation was characterized using the natural transition orbital model (NTO). [46]

7.3   Benchmarking Results

Experimental results obtained by Chick-Jarrold group reported the establishment of ionization potentials (IPs) of EuH⁻ and EuOH⁻ to be 0.771 eV and 0.700 eV, respectively. Backed by both photoelectron spectroscopy and quantum chemical calculations, they were able to determine the ground-state anion spin-states to be octets. In addition, they reported that the lowest-energy ionization occurs via a detachment of a 6s Eu-based β electron into the ground-state neutral. Starting from the provided experimental results, we first compare IP values obtained from various theoretical models. A summarized comparison of the deviations of calculated IPs from the experimental value is given in figure 7.1.
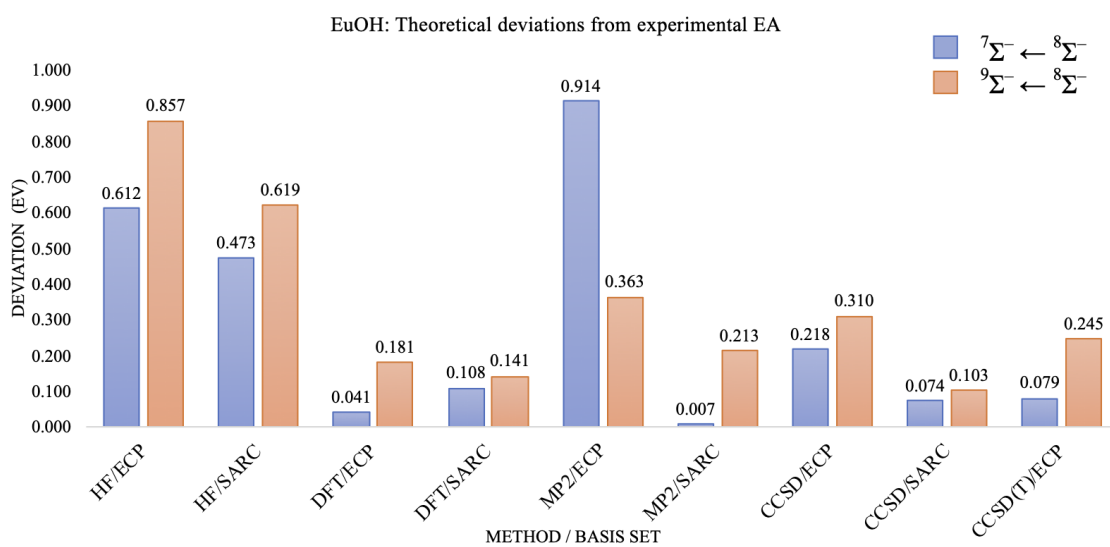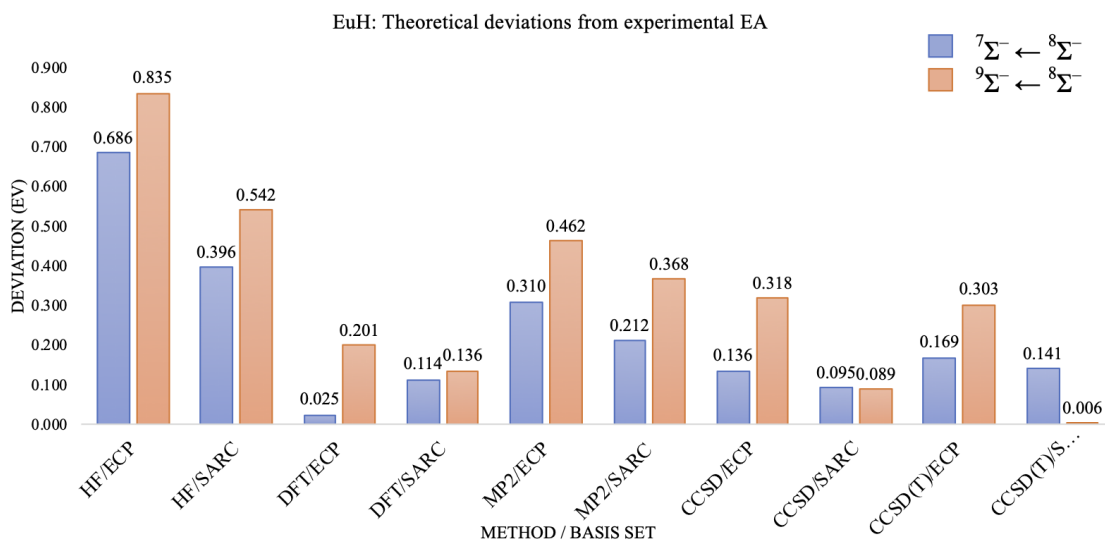
Figure 7.1: Bar graphs representing the deviation of the calculated electron affinities of EuH (Top) and EuOH (Bottom) anions from the experimental values (0.700 eV for EuOH and 0.771 eV for EuH). Values in blue represent detachment from the septet anion and values in orange represent detachments from the nonet anion. All calculations represent detachments into ground-state octet EuH and EuOH, respectively.

The lack of proper treatment of both static and dynamic correlation in Hartree-Fock model gives rise to unreasonable calculations of ionization potentials. Due to the presence of $4f^7$ manuifold and its near-degeneracy with the diffuse 6s orbital, effects of electron correlation on IP values is expected. For both α and β electron detachments from EuOH⁻ and EuH⁻, HF calculations predict energy gaps that are either too small (near-zero values) or too large. An example on the latter would be the $^7\Sigma^- \leftarrow {}^8\Sigma^-$ EuOH detachment calculated with HF using ECPs on Eu center (1.31 eV). Another inconsistency can be identified from fig. 7.1 with MP2 calculations. While MP2 calculations on open-shell species, including electron xdetachments, has been a matter of questioning, [429–435] we show here two extreme cases of inconsistency in MP2 results. Calculating the $^7\Sigma^- \leftarrow {}^8\Sigma^-$ EuOH⁻ detachment energy using ECPs on Eu gives an IP value of 1.61 eV, which is 0.91 eV higher than the experimental value. On the other hand, performing the same detachment calculations using MP2 but replacing the ECPs with the SARC all-electron basis set (in addition to incorporating the DKH integrals), we were able to calculate an accurate IP value of 0.69 eV, which is in perfect agreement with the experimental value (0.700 eV). However, different results were obtained when we calculated $^7\Sigma^- \leftarrow {}^8\Sigma^-$ EuH detachments. Both MP2/ECP and MP2/SARC/DKH calculations produce IP values that are lower than the experimental IP. This inaccuracy in IP calculation can be interpreted as the inability of MP2 to properly account for electron correlation in systems with a manifold of partially-occupied 4f subshells. CCSD and CCSD(T) calculations have shown good agreement with the experimental IPs of EuH⁻ and EuOH⁻. It is noteworthy to mention that in both CCSD and CCSD(T) calculations, starting from a Hartree-Fock reference calculated at the SARC/DKH method gives better agreement with the experimental values than starting with a HF reference obtained using ECPs on Eu. Fig. 7.1 shows that SARC/DKH calculations using CCSD and CCSD(T) produce IP values that are more accurate than their ECP analogue by 0.2-0.3 eV. All detailed calculations are given in the supporting information appendix.

Hybrid DFT functionals serve as a balanced treatmet between computationally expensive correlated models on one side and relatively-affordable mean-field approximations. Using the unrestricted formalism of B3PW91 functional, our calculations, using both SARC/DKH and ECPs give results that are in good agreement with experimental values (within accepted chemical accuracy). Errors in IP calculations using SARC/DKH on both EuOH⁻ and EuH⁻ were determined to be ˜0.1-0.14 eV while ECP calculations have a wider range of errors, ranging from 0.02 eV for the $^7\Sigma^- \leftarrow {}^8\Sigma^-$ EuH⁻ detachment to 0.2 eV for the $^9\Sigma^- \leftarrow {}^8\Sigma^-$ EuH⁻ detachment. The consistency and accuracy of our DFT results using SARC/DKH model, in addition to its mean-field cost, promotes this method's use for modeling photodetachments of small lanthanide-based clusters. Another advantage of using this model is its ability to calculate the septet-nonet energy gaps in both EuOH and EuH neutrals. In fact, most model chemistries used were able to accurately predict the septet-nonet gaps. More precisely, B3PW91/SARC/DKH predicts EuH $\Delta E_{septet-nonet}$ to be 0.27 eV, which is slightly higher than the experimental value (0.18 eV). A similar behavior was observed was observed with $\Delta E_{septet-nonet}$ for EuOH (DFT gets 0.25 eV vs. experimental 0.16 eV).

Further inspection of the results from B3PW91/SARC/DKH results allows us to determine a simplfied molecular orbital diagrams of the low-lying states of EuOH and EuH neutrals and anions. Starting with EuH, the ground-state anion was determined to have a $4f^7\sigma^2 6s^2$ electronic configuration, with the valence electrons occupying Eu-based orbitals. The doubly-occupied 6s orbital poses as the cite of electronic detachment. Detaching the α 6s orbital gives us the $4f^7\sigma^2 6s$ septet while detachment of the β 6s-based electron lands on the $4f^7\sigma^2 6s$ nonet neutral. A very similar behavior

was observed with the MO diagrams of EuOH anions and neutrals. The only point of difference between the MOs of EuOH and EuH is the presence of two doubly-occupied bonding π orbitals. This has been identified and quantified for the whole LnOH series in chapter 4. The electronic configuration arising from the MO diagram of EuOH⁻ is $4f^7\sigma^2\pi^4 6s^2$ and the corresponding septet and nonet neutrals exhibit an electron configuration of $4f^7\sigma^2\pi^4 6s$, where the two states differ in the spin of the electron residing in the 6s singly-occupied orbital.
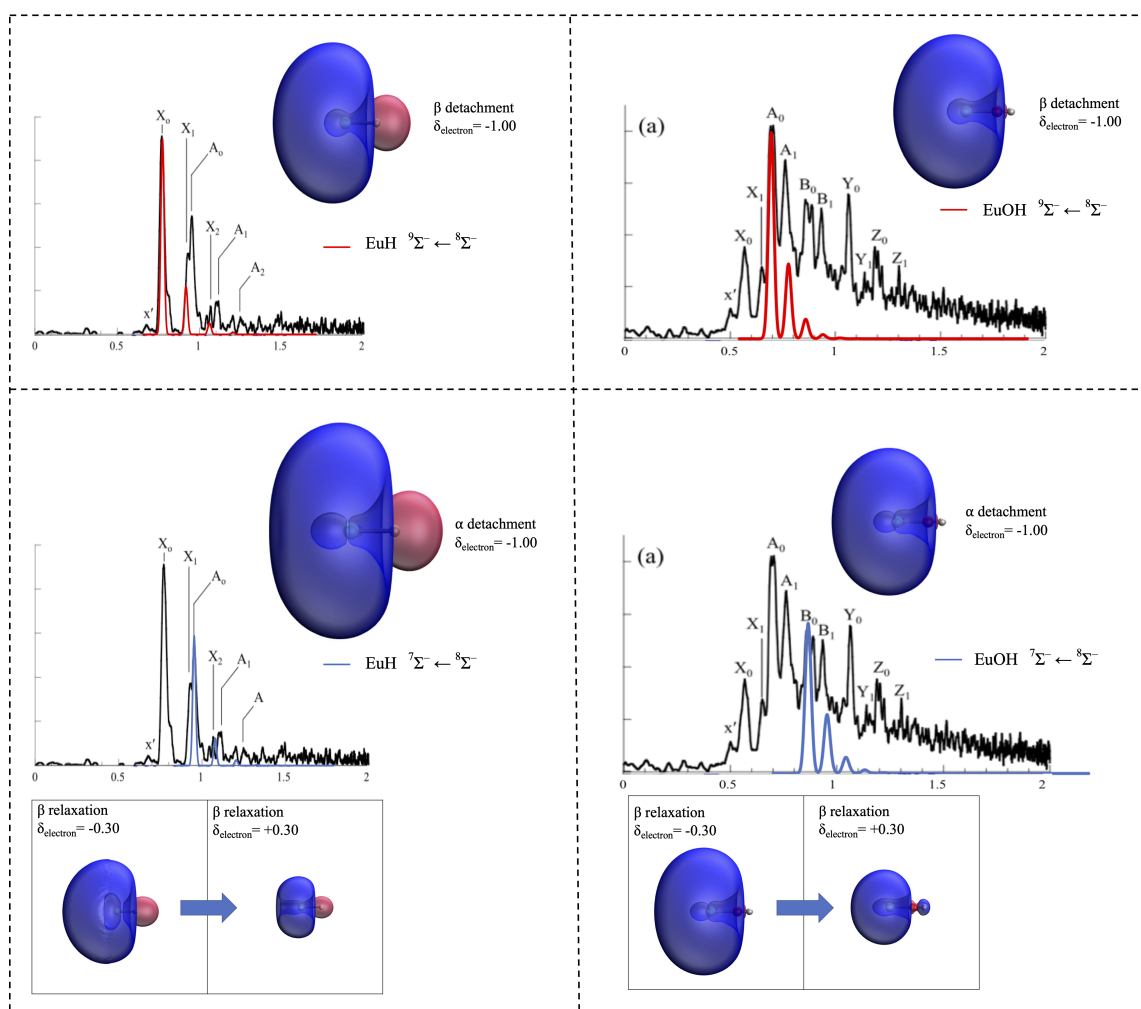
Figure 7.2: Franck-Condon simulations of EuH⁻ detachments (left) and EuOH⁻ detachments (right) alongside the NIOs that correspond to the detachments. $\delta_{electron}$ values represent occupation change numbers of the orbitals. The blue arrow indicates the orbitals involved in this electron relaxation.

To further confirm the validity of the model chemistry used (B3PW91/SARC/DKH), we perform Frank-Condon progressions and NIO analysis on the dfferent EuOH and EuH detachments. Figure 7.2 shows the franck-condon progressions for $^7\Sigma^- \leftarrow {}^8\Sigma^-$ and $^9\Sigma^- \leftarrow {}^8\Sigma^-$ detachments for EuH and EuOH anions. As shown , the simulated peaks are in good agreement with the experi-

mental photoelectron spectra as well as the simulations performed by the Chick-Jarrold Lab. NIO analysis provides the orbital picture of the detachments and indeed confirms that the reported detachments occur via removal of an electron from the 6s orbitals. NIO analysis also points out that in the cases of $^7\Sigma^- \leftarrow {}^8\Sigma^-$ detachments in both EuH$^-$ and EuOH$^-$, a partial electron relaxation is observed ($\delta_{electron} = \pm 0.3$). The orbital picture of this relaxation is best described as a contraction of the 6s α spin orbital upon detachment. Such a behavior arises from the loss of coulombic interaction between the α and β electrons that were initially present in the 6s orbital of the ground state anions of EuH$^-$ and EuOH$^-$. In addition, the NIOs provide a reasonable explanation on the relative intensities of the two detachments in each of the species. $^9\Sigma^- \leftarrow {}^8\Sigma^-$ is shown to be a strictly one-electron process, while $^7\Sigma^- \leftarrow {}^8\Sigma^-$ shows reasonable electron relaxation upon ionization, a factor that would lower the intensity of the latter detachment relative to an analogous one-electron process. The use of B3PW91 functional with an all-electron basis set and second-order Douglass-kroll-Hess relativistic integrals has been shown to accurately model the photodetachment of EuH and EuOH anions and will be used to resolve the spectral peaks in the photoelectron spectrum of mixed EuO/EuOH species.

7.4 Resolving the EuO$^-$ Photoelectron Spectrum

Kafader and coworkers have analyzed the mixed EuO/EuOH anion photoeletron spectrum. [114] Supported by DFT calculations, the group reports a linear EuOH geometry to be the ground-state structure for both the anion and the neutral. As mentioned before and further discussed in chapter 4, this has been shown by our previous work to be a feature common across the lanthanide series. The reported EuOH anionic state has a $^8\Sigma^-$ electronic state with $4f^7 6s^2$ electronic configuration. The neutral EuOH ground-state has a $^9\Sigma^-$ state. Additionally, a $^7\Sigma^-$ state was identified that lies at 0.18 eV higher in energy than the ground-state. Both neutrals exhibit a $4f^7 6s$ configurations. Franck-Condon simulations on the $^9\Sigma^- \leftarrow {}^8\Sigma^-$ and $^7\Sigma^- \leftarrow {}^8\Sigma^-$ detachments were performed. Comparison of these simulated spectra with the experimental photoelectron spectrum allowed the assignment of peaks A_0 (0.70 eV) and A_1 (0.76 eV) to the $^9\Sigma^- \leftarrow {}^8\Sigma^-$ detachment and peaks B_0 (0.86 eV) and B_1 (0.93 eV) to the $^7\Sigma^- \leftarrow {}^8\Sigma^-$ detachment. Combined calculations of the adiabatic detachment energies and Franck-Condon progressions allowed the establishment of the electron affinity of EuOH to be 0.70 eV.

Two competing electronic states for the anion EuO were also previously calculated [114]: the septet and the nonet states. Previous calculations confirmed the likelihood of presence of two anionic species within around 0.15 eV difference. The septet state, being the lower in energy, was determined to have an electronic configuration of 4f^{6}6s^2 while the nonet's electronic configuration was determined to be 4f^{7}6s. Detachments from both states into two octet electronic states were identified. The octet electronic states found had configurations of 4f^7 and 4f^{6}6s states. The relative energies of these states was found to be 0.63 eV and 1.03 eV, respectively. These electronic configurations have been supported by the Chick-Jarrold group using both the ionic bonding framework as well as the ligand field theory approach.

Thus from the calculated electron affinities, alongside the experimental photoelectron spectrum of mixed EuO/EuOH, partial spectral assignments for both EuO and EuOH were performed [114]. While the authors clearly define the electron affinity of EuOH, the existence of two energetically competitive EuO$^-$ spin states added complexity to the mixed photoeletron spectrum. Ths com-
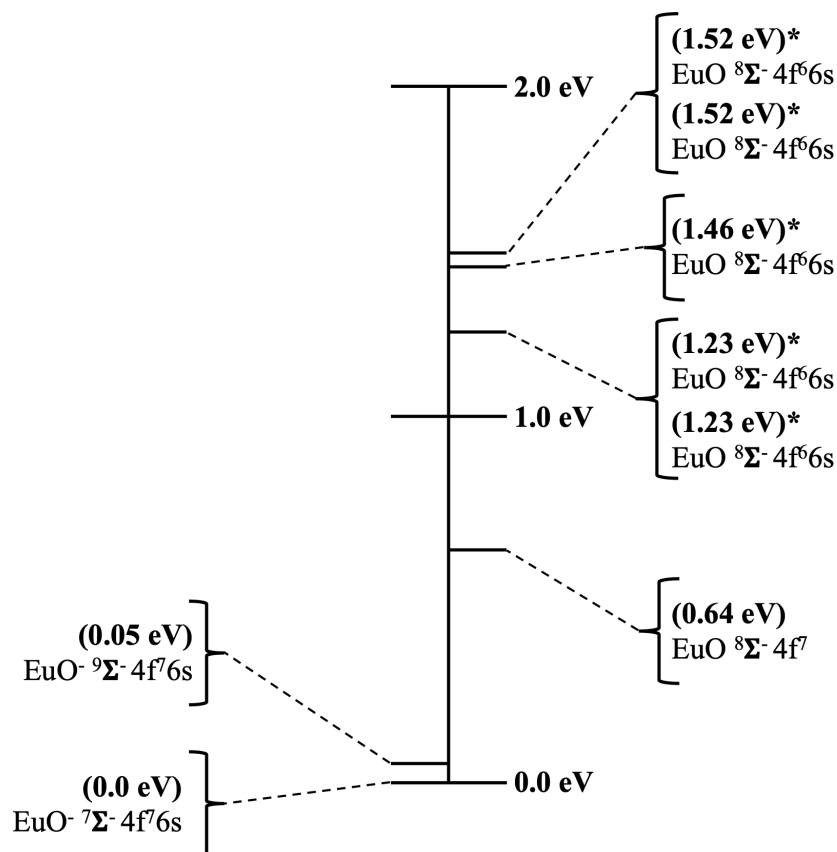
Figure 7.3: Relative energies (in eV) of the low-lying states of EuO anions and neutrals. Asterisks (*) indicate the presence of an excited state.

plexity prevented the definite assignment of spectral peaks corresponding to the photodetachments of EuO^-. The reported photoelectron spectrum can be split into three regions: region (a) includes the peaks located at ~0.5-0.7 eV, region (b) includes multiple peaks located at roughly around 0.7-1.0 eV, and region (c) includes several, lower-intensity peaks compared to those appearing at region (b). Peaks appearing in region (b) of the photoelectron spectrum were determined to be originating from detachments due to $EuOH^-$ ionization. The peaks in region (a) have been shown by DFT calculations to represent EuO^- nonet to octet detachments ($4f^7$ state). Such an ionization involves the detachment of a 6s orbital while preserving the set of half-filled 4f orbitals. On the other hand, two detachments from the septet state into both octet and sextet were tentatively assigned to region (c), both detachments require the ionization of 6s electron on the septet anion. Thus, the comparison of the experimental photoelectron spectroscopy and franck-condon progressions further support the presence of two energetically competitive ground-state anions of EuO and further complicates the resolution of the peaks corresponding to EuO^- photoelectron spectra.
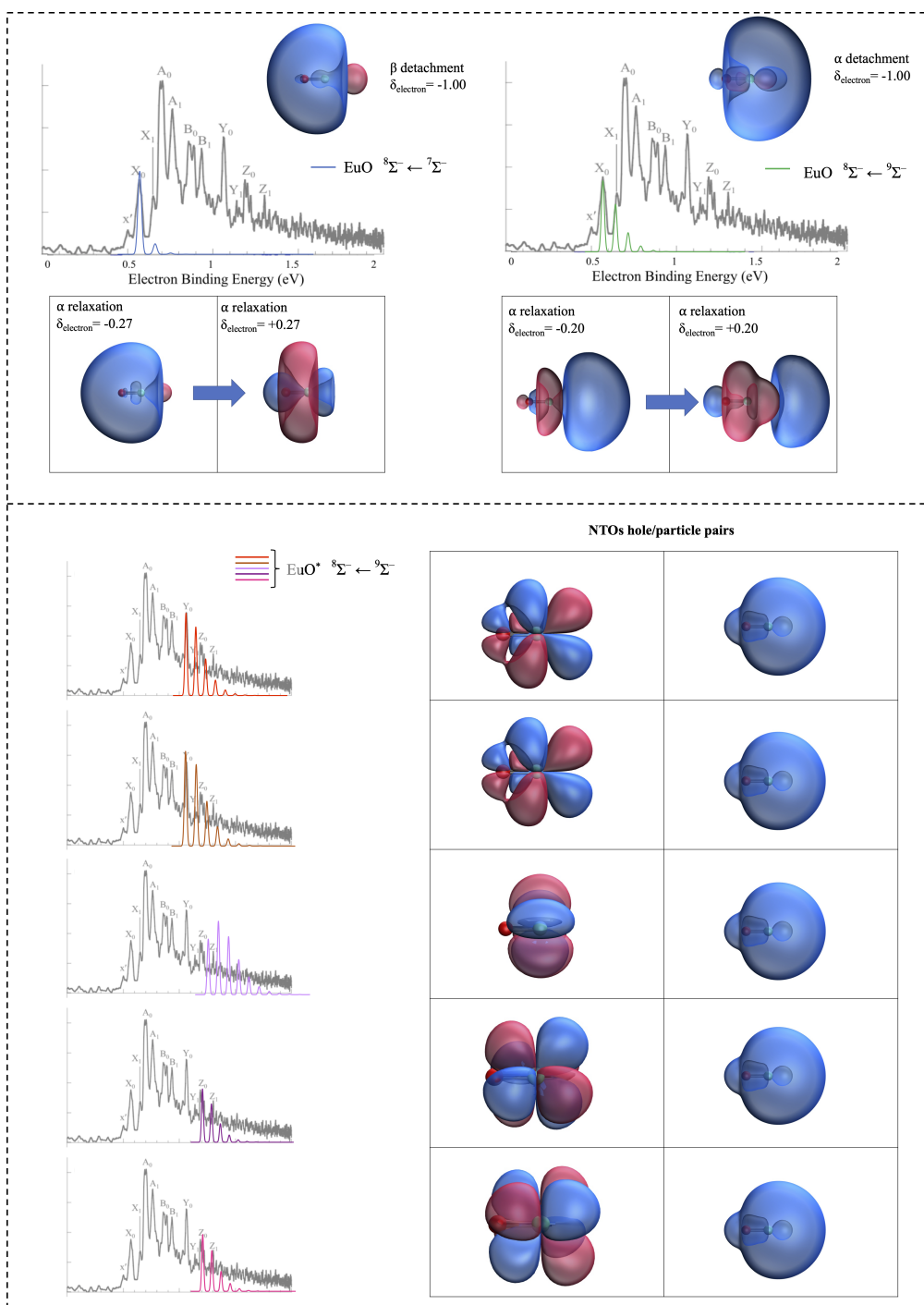
Figure 7.4: Franck-Condon simulations on septet and nonet detachments into the ground-state octet (top left), and detachments into the excited state neutrals (top right). Orbitals shown on the left side represent the NIOs for each of the detachments and values given in parenthesis represent occupation change numbers. Right-hand-side simulations include NTO hole/pair orbitals that represent a one-electron process which accesses the set of excited states.

While our calculations confirm the existence of several of the previously-reported states, we do note that treating relativistic effects in the system using both an all-electron basis set and second-order Douglass-Kroll-Hess Hamiltonian have aided us in finding new energetically-competitive electronic states. Of particular interest, our calculations have defined a competitive $4f^76s$ septet state, where the 6s electron is antiferromagnetically coupled with the $4f^7$ electron manifold. This new septet electronic state is close-lying in energy compared to the nonet anion, with an energy difference of only 0.05 eV. Such a small gap in energy paves the way for possible significant contributions to the experimental photoelectrom spectrum arising from electronic detachments from this particular electronic state. In addition, a manifold of five close-lying excited state EuO neutrals were identified. These states lie in the range of 1.23-1.52 eV above the ground state anion and 0.61-0.92 eV higher in energy than the ground state neutral octet. The calculated relative energies of the set of identified electronic configurations raise the possibility of their contribution to the previously described region (c) of the photoelectron spectrum. Moreover, these excited states share a common superconfiguration $4f^66s$, yet their difference is the location of the electron hole in the 4f manifold. While ideally, and due to the presence of seven half-filled 4f orbitals, we expect to locate all seven excited states within the 1.23-1.52 eV relative energy window.

However, our calculations show that only five of those states correspond to minima on the potential energy surface of EuO. The remaining two states do not correspond to minima on the potential energy surface of EuO and second-derivative calculations confirmed the nature of these two states as first-order saddle points and therefore will not be included as contributors for peaks in the experimental photoelectron spectrum.

Figure 7.3 shows the different low-lying anions and neutrals of EuO, with their relative energies and electronic configurations. Starting from the electronic configurations of anions and neutrals, we can clearly notice that the ground state EuO neutral is accessible via a one-electron process detachment from either one of the ground-state anions. This process is best described as a detachment from the singly-occuppied 6s orbital leading to a $4f^7$ ground-state neutral ($^8\Sigma^-$) which lies at 0.64 eV above the ground-state anion. Franck-Condon simulations on $^8\Sigma^- \leftarrow {}^9\Sigma^-$ and $^8\Sigma^- \leftarrow {}^7\Sigma^-$ are shown in figure 7.4 along with the NIOs corresponding to each detachment. Simulations have shown peaks appearing at ~0.6 eV in region (a) of the photoelectron spectrum. Previous work by the Chick-Jarrold group has identified the $^8\Sigma^- \leftarrow {}^9\Sigma^-$ detachment to be contributing to peaks X_0 (0.57 eV) and X_1 (0.65 eV), which is in agreement with our simulations. However, the $^8\Sigma^- \leftarrow {}^7\Sigma^-$ detachment also exhibits peaks at similar energies as the nonet detachment simulations. This suggests contributions from both anionic states to region (a) of the photoelectron spectrum. Furthermore, NIO analysis of both detachments show that the detached electron originates from Eu-based 6s orbital accompanied by a partial electron rearrangement ($\delta_{electron} = \pm 0.27$ for $^8\Sigma^- \leftarrow {}^9\Sigma^-$ and $\delta_{electron} = \pm 0.20$ for $^8\Sigma^- \leftarrow {}^7\Sigma^-$).

Figure 7.3 also shows the ground-state EuO neutral as well as the five neutral EuO excited states (indicated with an asterix). All of these identified states are less than 1 eV higher than the ground-state neutral. NTO analysis, combined with the NIOs of $^8\Sigma^- \leftarrow {}^9\Sigma^-$ detachment, show the one-electron nature of detachments from the nonet anion to one of the excited states. NTO analysis shows that accessing one of these excited states from the ground-state anion requires a detachment from a 4f orbital. These five detachment can be classified according to the symmetry of the orbital from which the electron ws detached from. Excited states appearing at 1.27 eV bear a $4f_\pi$ electron hole, while the next state has a $4f_\phi$ hole and the states at 1.52 eV bears the electron hole at $4f_\delta$.

Franck-Condon progressions on detachments from nonet anion into the manifold of excited states is shown in figure 7.4. Following up from these progressions we can notice the resemblance of the Franck-Condon profiles of all but the $4f_\phi$ detachment with the experimental photoelectron spectrum. Particularly, peaks Y_0 and Y_1 correspond to detachment of one of the two $4f_\pi$ electrons present in the ground-state nonet. Additionally, peaks Z_0 and Z_1 correspond to detachments from one of the occupied $4f_\delta$ orbitals. A simplified MO diagram of EuO anionic states is shown in fig. 7.5. The MO diagrams of both nonet and septet anions is quite similar, both exhibit a half-filled 4f manifold and a singly-occupied 6s orbital. Accessing the ground-state octet requires detachments from the 6s orbital (shown in red), while detaching into an excited state neutral requires detachment from one of the singly-occupied 4f orbitals (shown in green). The MO diagram of nonet EuO$^-$ shows a distinct feature: the near-degeneracy of 6s and 4f orbitals. This feature allows the feasibility of accessing the manifold of excited state EuO neutrals bearing a $4f^6 6s$ superconfiguration. All detachments that have been identified originate from Eu-based orbitals, while the σ and π bonding orbitals of both spin-states of EuO$^-$ remain intact.
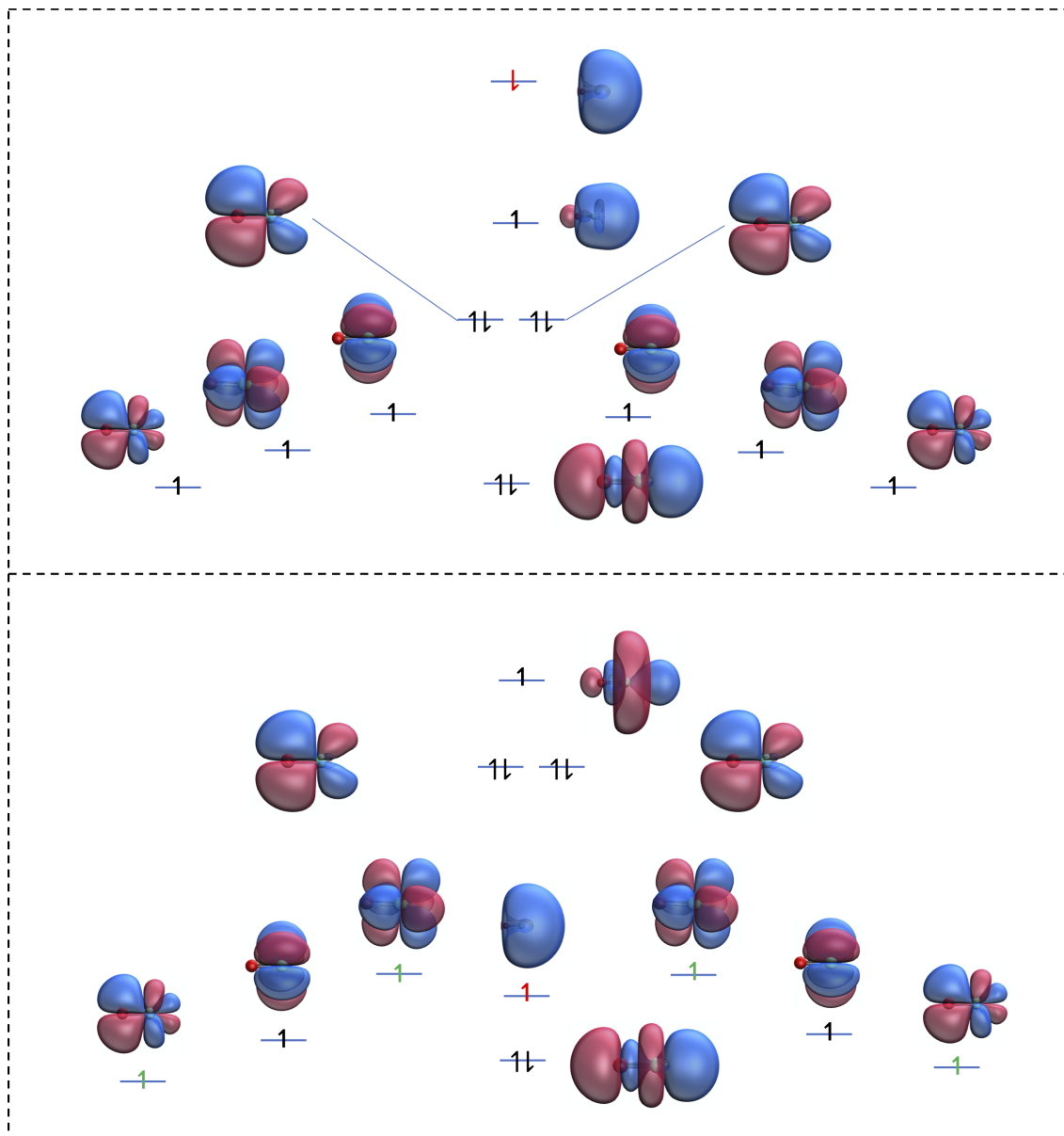
Figure 7.5: Simplified molecular orbital diagrams of septet (top) and nonet (bottom) EuO$^-$. Electrons shown in red correspond to detachments into the ground-state octet, while electrons shown in green represent detachments into excited states.

Previous studies on small lanthanide oxide clusters have been reported. [77, 114, 115, 126–128, 329, 331, 340, 399] These studies include various clusters of europium, samarium, cerium, and praseodymium oxides and all exhibit detachments from Ln 6s-like molecular orbitals. In all the studied detachments, results show that the partial $4f^n$ occupancy is highly preserved between the anion and its corresponding neutral. Yet, as the $4f^n$ occupancy increases on the lanthanide center(s), the photoelectron spectrum becomes more complicated. This effect reflects the increased coupling between core-like 4f orbitals and diffuse 6s orbitals. The special case of EuO presents itself as a central example to understand the nature and the effect of the 4f-6s mixing in lanthanides. This special case rises from the presence of a half-filled manifold of 4f orbitals in addition to a singly-occupied 6s orbital. While it is noteworthy to mention that accessing the ground-state octet EuO neutral requires detachment from a Eu-based 6s-like orbital, the half-filled manifold presents a small energy gap between the ground-state neutral EuO and its manifold of excited states bearing a $4f^6 6s$ superconfiguration. This was supported by out DFT calculations on excited states of EuO, in which the energy gap corresponding to the $4f^7 \rightarrow 4f^6 6s$ excitations was shown to be less than 1 eV.

7.5 Summary

Using the appropriate DFT-based model chemistry, the aim of this chapter is twofold: (1) highlight the adequacy of proper treatment of scalar-relativistic effects in modeling the photodetachment process of lanthanide-based clusters and (2) provide an enhanced rationalization of the mixed EuO/EuOH anion photoelectron spectrum.

Calculations on photodetachments of EuOH and EuH anions using explicit treatments of scalar-relativistic effects within the second-order Douglass-Kroll-Hess approach, coupled with an all-electron basis set optimized within the relativistic Hamiltonian have shown to accurately model the photodetachment within the chemical accuracy of DFT methods and give a clear description of the molecular and electronic structures of EuH and EuOH neutrals and anions. In addition, this method accurately performs Franck-Condon progressions that have been shown to be in good agreement with experimental results and thus provide a crucial metric in performing spectral assignments.

Based on this, we have performed DFT calculations to model the photodetachment of EuO⁻. Our calculations have shown two types of detachments: a 6s-detachment peak profile originating from detaching an electron from a nonet or a septet ($4f^7 6s$) into the $4f^7$ ground-state neutral octet. Peaks corresponding to this detachment appear at ˜0.6 eV. In addition, our calculations located five close-lying excited states of EuO neutral with a $4f^6 6s$ superconfiguration. These states are less than 1 eV higher in energy than the ground-state neutral. Franck-Condon progressions have shown that four of these states correspond to peaks on the photoelectron spectrum appearing at ˜1.5 eV. The ability of the used DFT model chemistry to simulate the peaks appearing at ˜1.5 eV reflects the accuracy of this model to describe the proper physical features resulting from the relativistic effects on the orbitals, as it is known [436] that s orbitals contract while 4f orbitals become more diffuse under proper treatment of relativistic effects. The increased diffuse in 4f orbitals, in addition to the increased coupling between 4f and 6s orbitals, allows the accessibility of detaching an electron from the 4f manifold.

The concept of 4f detachment in lanthanide-based clusters has been reported and described in this study, yet more insight into the nature of this type of detachment is required for the sake of providing an enhanced chemical and physical description of this detachment. Methods to im-

prove modeling of 4f detachments include implementation of more accurate treatments of relativistic effects in addition to enhancements of available spin projection tools that can properly handle a spectrum of close-lying spin states.

Chapter 8

Photoelectron Spectra of $Gd_2O_2^-$ and Non-Monotonic Photon-Energy Dependent Variations in Populations of Close-Lying Neutral States

"Dialectics is the logic of contradiction."

— *Reason in Revolt*, Alan Woods & Ted Grant.

This work is part of a collaboration between the Hratchian group at UC Merced and Chick-Jarrold group at Indiana University. All reported experimental procedures and results were performed by our collaborators. Further experimental details can be found in references [437].
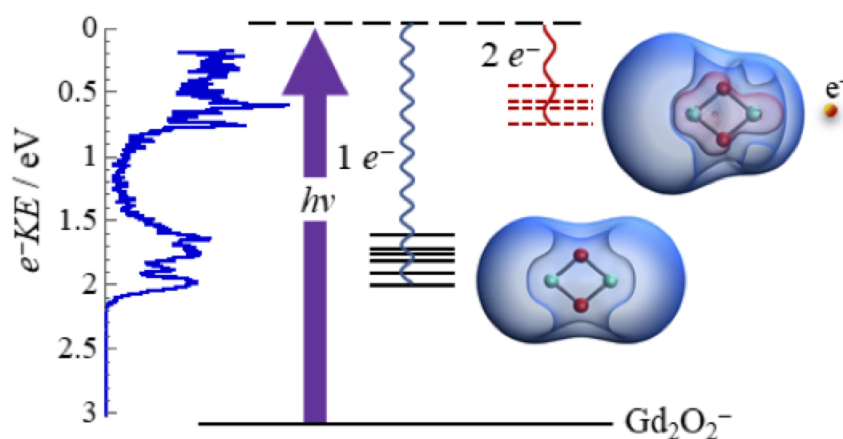
Abstract

Photoelectron spectra of $Gd_2O_2^-$ obtained with photon energies ranging from 2.033 eV to 3.495 eV exhibit numerous close-lying neutral states with photon-energy-dependent relative intensities. Transitions to these states, which fall within the electron binding energy window of 0.9 and 1.6 eV, are attributed to one- or two-electron transitions to the ground and low-lying excited neutral states. An additional, similar manifold of electronic states is observed in an electron binding energy window of 2.1 to 2.8 eV, which cannot be assigned to any simple one-electron transitions. This study expands on previous work on the Sm_2O^- triatomic, which has a more complex electronic structure because of the $4f^6$ subshell occupancy of each Sm center. Because of the simpler electronic structure from the half-filled $4f^7$ subshell occupancy in Gd_2O_2 and $Gd_2O_2^-$, the numerous close-lying transitions observed in the spectra are better resolved, allowing a more detailed view of the changes in relative intensities of individual transitions with photon energy. With supporting calculations on the numerous possible close-lying electronic states, we suggest a potential description of the strong photoelectron-valence electron interactions that may result in the photon-energy dependent changes in the observed spectra.

8.1 Introduction

Electron correlation is central to the electronic structures and properties of matter, and enhancing our understanding of strongly correlated electronic materials is a prominent theme of scientific grand challenges. The lanthanides (Ln) have proven to be fertile ground in this arena, [438] with Ln atomic ions, molecules, and materials finding applications in the areas of quantum simulators [439] and single molecule magnets, [440] the latter of which is associated with potential application in spintronics materials. [441] The Ln $4f^n$ series is characterized by elements having similar chemical properties, for as the atomic number increases, the occupancy of the contracted and nuclear-shielding $4f^n$ subshell increases.

Partially-filled $4f^n$ subshells and close-lying 5d and 6s orbitals give rise to a rich constellation of close-lying, nearly identical electronic states. If we consider LnO diatomic molecules, in which the valence orbital occupancy can be described in general terms as $[\sigma_{2p}^2 \pi_{2p}^4]\, 4f^n \sigma_{6s}$, numerous close-lying states associated with the coupling between the 4f and σ_{6s} electrons, and the manifold states associated with the projection of j_f and j_{6s} onto the internuclear axis (Ω). As an example, CeO ($4f^1\sigma_{6s}$) has 16 states within a 0.5 eV window of energy, [96–98] SmO ($4f^5\sigma_{6s}$) has 30 states in the same window, plus tens more slightly higher in energy. EuO ($4f^7$) and GdO ($4f^7\sigma_{6s}$), near the center of the row are much simpler, having one and two states arising from those occupancies, respectively, because of the zero-orbital angular momentum associated with the half-filled 4f (^8S) subshell. [442]

Electron correlation is also an important governing factor in photoionization and photodetachment processes. A recent study reported unusual phenomena observed in the anion photoelectron (PE) spectra of Sm_xO_y suboxide ($y \geq x$) cluster anions, along with mixed Ce-Sm suboxides. Specifically, a striking increase in the relative intensities of excited states with decreasing photon energy (decreasing electron kinetic energy, e^-KE), [77, 126, 399] was observed — opposite of the Wigner threshold law. [443] This effect was most pronounced in clusters with average oxidation states of the metal centers in the clusters being less than or equal to +2, and it was not at all ob-

served in pure cerium oxide clusters of any stoichiometry. This result suggested that the higher density of states associated with the Sm center contributed to the effect.

Resonance with excited anion states embedded in the detachment continuum can have pronounced effects on the intensities of detachment transitions, with a few examples included in the references. [405, 406, 444–447] However, the underlying source of the changes in excited state intensities in the case of these samarium-containing suboxide clusters appeared to be shake-up transitions or internal inelastic scattering from strong photoelectron-valence electron (PEVE) interactions. Previous work explored this effect in more detail, and an increase in the relative intensity of an unresolved manifold of excited state transitions in the Sm_2O^- PE spectrum was observed. This behavior was inversely proportional to the momentum of the photoelectrons by measuring the spectrum over a range of photon energies. [117] The trend of increasing excited state intensity with decreasing momentum additionally showed a broad oscillation that was likely due to a shape resonance. Overall, however, the effect was largely interpreted as PEVE interactions, which was attributed to the very high density of electronic states in a narrow window for Sm_2O, associated with the $4f^5$ or $4f^6$ subshell occupancy, the latter being predicted to be the lower lying configuration in DFT calculations.

In this report, we present a new and striking example of this intriguing inverse-threshold phenomenon by examining the $Gd_2O_2^-$ cluster. We hypothesized this system would provide a useful canvas for exploring the fundamental physics of this effect due to the much simpler electronic structure afforded by the $4f^7$ subshell occupancy. Based on DFT calculations, $Gd_2O_2^-$ is expected to have D_{2h} symmetry, with the two O-atoms bridging the Gd centers which are separated by ca. 3.1 Å. As depicted in Figure 8.1, the highest occupied orbitals are the in- and out-of-phase combination of the Gd 6s orbitals (a_g and b_{1u}, symmetries, respectively). According to the calculations (vide infra), the spin projection is entirely along the Gd–Gd axis. Therefore, for simplicity, we will forego the D_{2h} symmetry terms, and refer to the non-bonding Gd-local orbitals arising from 6s and 5d orbitals by their symmetry with respect to the Gd–Gd axis ($\sigma_{6s,g}, \sigma_{6s,u}, \delta_{5d,g}$ etc.).

As shown schematically in Figure 8.1, the $\sigma_{6s,g}$ and $\sigma_{6s,u}$ orbitals can be described as outer-valence. Covalent bonds are formed from the O 2p and Gd 5d orbitals, and are predicted to be more than 3 eV lower in energy, while the core-like non-bonding Gd 4f orbitals are an additional 2 eV lower in energy. Analogous to the GdO diatomic, the general electronic structure of the neutral can be described as two Gd^{2+} centers with $4f^76s^1$ electronic configurations. In an isolated Gd^{2+} atom, the half-filled 4f subshell would be a spherically symmetric, high spin core. Some polarization away from the O centers is expected in the Gd_2O_2 anion and neutral, but the overall contribution of the 4f orbitals to the electronic term would be a_g. The anion has an additional electron in the outer-valence 6s-based orbital, and a $^{16}B_{1u}$ electronic term would result from ferromagnetically (FM) coupled $4f^7$ centers; a $^2B_{1u}$ term would arise from antiferromagnetically (AFM) coupled centers and is calculated to be 0.07 eV higher in energy. The paramagnetism in di-Gd complexes has made them effective MRI contrast agents. [448]

$$\mathrm{Gd_2O_2^-}$$

$$[4f_{Gd}^{7,\alpha}4f_{Gd'}^{7,\alpha}]\,\sigma_{2p,g}^2\pi_{2p,u}^4\,\sigma_{6s}^2\sigma_{6s}^{1,\alpha}$$

Unoccupied Orbitals

Unoccupied close-lying Gd 5d-based orbitals

Outer Valence

Diffuse, singly occupied anti-bonding combination of Gd 6s orbitals

Diffuse, doubly occupied Gd 6s bonding orbital

Inner Valence

Six O 2p non-bonding and bonding orbitals

14 singly occupied nearly degenerate core-like Gd 4f orbitals
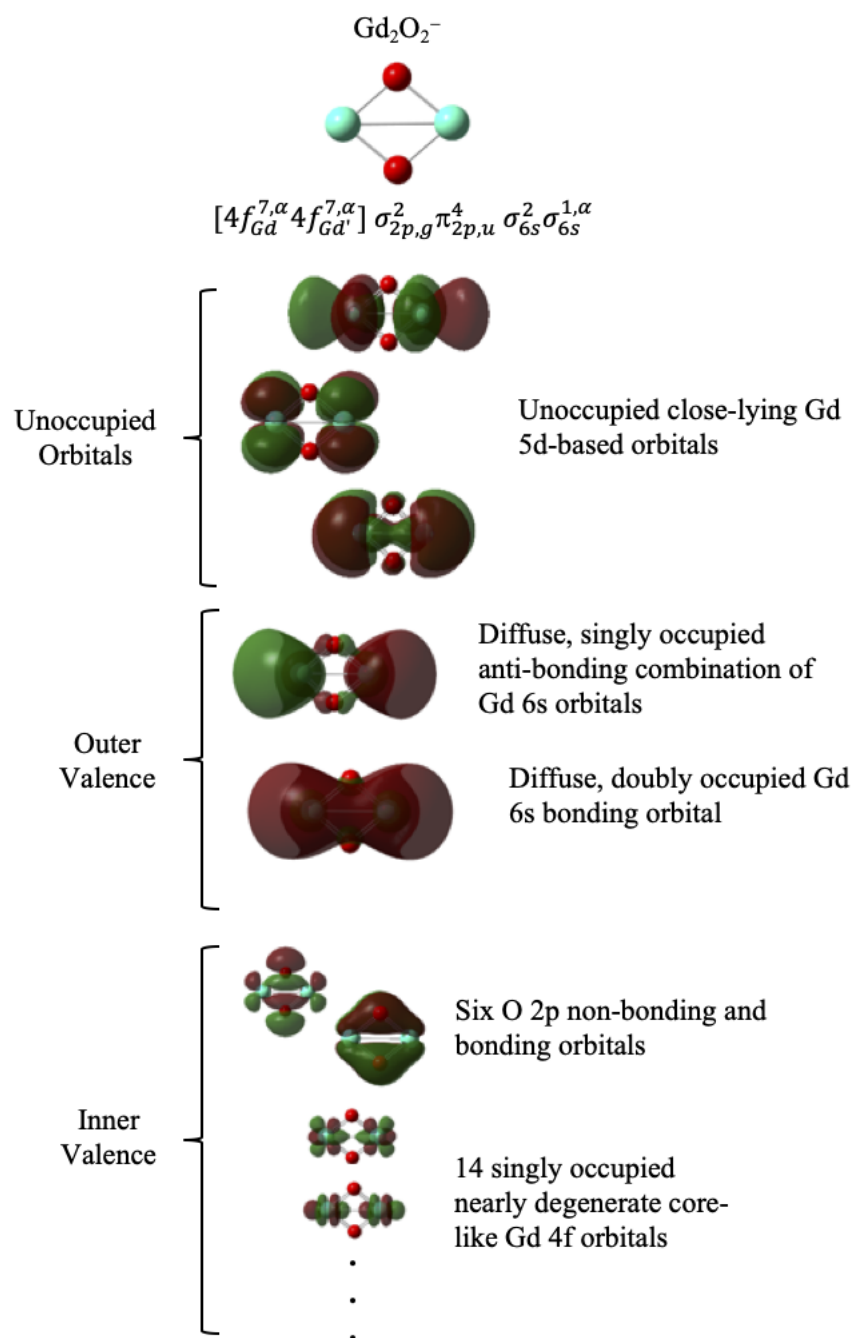
Figure 8.1: Molecular and electronic structure of the lowest energy state of $\mathrm{Gd_2O_2^-}$ computed using the B3LYPANO-ECPplusPVTZ method

Given this electronic structure, the detachment spectrum is expected to exhibit three close-lying one-electron transitions associated with detachment of any of the three outer valence electrons. Because the orbitals are diffuse and non-bonding, the anion and neutral should have nearly identical structures, yielding vertical detachment transitions. Additional nearly-vertical transitions would be observed if the ion beam were also populated with the AFM-coupled $^2B_{1u}$ state or the lower-spin $^{14}B_{1u}$ state arising from antiparallel alignment between the outer-valence electron and the (FM-coupled) $4f^7$ electrons.

In contrast, the PE spectra of $Gd_2O_2^-$ collected with photon energies ranging from 2.033 eV to 3.495 eV do not exhibit three simple, near-vertical transitions. Rather, they exhibit two distinct manifolds of close-lying electronic transitions, and the emergence of two-electron transitions with decreasing e^- KE. Unlike the results for Sm_2O^-, the relative excited state intensities do not change smoothly with photon energy. We consider the effect of the ejected electrons' electric field on the highly polarizable outer valence orbitals as well as the relative stability of the FM and AFM states, along with larger zero-field splitting parameter in particular spin states of neutral Gd_2O_2.

8.2 Computational Methods

Calculations were performed using local development and release versions of the Gaussian suite of electronic structure programs. [176, 394] All calculations were performed using the B3LYP functional and the unrestricted formalism for all open-shell species. [27] The Stuttgart relativistic small-core atomic natural orbital basis set and corresponding effective core potential with 28 core electrons and a contracted Gaussian basis for valence electrons was used for the gadolinium centers (ANO/ECP), [341] and a Dunning-style correlation consistent basis set for oxygens. [395] A thorough search of different geometries and spin-states was performed. Geometry optimizations were carried out using standard methods and the nature of all identified stationary points was confirmed by vibrational frequency analysis. [179] The stability of the Kohn-sham determinants was verified for all calculations and the electronic structures of all converged Kohn-Sham DFT determinants have been fully characterized. [177, 178] Spin contaminated determinants were spin purified using the Approximate Projection model of Yamaguchi and co-workers, as implemented and externed by Hratchian and co-workers. [403, 405–407, 449]

The natural ionization orbital model (NIO) has been used to provide an orbital representation of electron detachment processes. [117] This analysis utilizes the difference in calculated one-particle density matrices and allows the differentiation between one-electron transitions and shake-up/shake-off transitions.

To facilitate convergence to various neutral electronic states, we use the projected initial maximum overlap method (PIMOM), [450] which is a variant of the initial maximum overlap method (IMOM) recently reported Gill and coworkers. [451, 452, 452] This family of methods facilitate the calculation of electronic exited states using ground state self-consistent field (SCF) solutions. By using an initial guess generated from ground state Kohn-Sham molecular orbitals, and a projected overlap metric, the PIMOM method provides a means for smoothly driving SCF convergence toward challenging electronic structures.

We note that for molecules with exceptionally complex electronic structure, such as cases where gaps between electronic states are on the order of a few-tenths of an eV the true electronic structure may exhibit meaningful multi-determinantal character. Under such condition, Kohn-Sham

DFT results must be used with care. Evaluations of determinant stability and spin-squared expectation values for the most relevant low-energy states suggested that single-determinant treatment is sufficient. Indeed, anion-neutral energy gaps, Franck-Condon simulations, and NIO analyses using such DFT results yielded very good agreement with experimental results.

8.3   Results

The $Gd_2O_2^-$ photoelectron spectra obtained by Chick-Jarrold group is shown in figure 8.2. The spectra all show a group of transitions between 0.9 eV and 1.6 eV (manifold I), with fairly parallel photoelectron angular distributions (PADs). Additional transitions are observed above 2 eV (manifold II) in spectra obtained with higher photon energies. A general trend in the spectra measured with different photon energies is an increase in the relative intensities of higher e^-BE (excited state) transitions with decreasing photon energies, in apparent violation of the Wigner threshold law; we note that this behavior resembles previous results on Sm_2O^-. [453] However, in contrast to the Sm_2O^- spectra, many of the numerous electronic transitions are well-resolved, allowing the observation of non-monotonic change in relative intensity with photon energy.

8.3.1   Transitions in manifold I in the photoelectron spectrum

Based on previous work, [103, 114, 115, 115, 127, 128, 329, 331, 340] homo- and heteronuclear lanthanide oxide cluster anions with average metal oxidation state less than +3 exhibit photodetachment transitions around e^-BE ≈ 1 eV. The transitions can be described as creating a hole in a 6s-based molecular orbital. They are characterized by large photodetachment cross sections and parallel PADs. Manifold I in the $Gd_2O_2^-$ spectrum shares these characteristics.

The spectrum measured with the highest photon energy, 3.495 eV, is most appropriately interpreted in the "sudden" detachment framework. [453, 454] We therefore make an initial assignment of manifold I on the basis of the appearance of this spectrum [Figure 8.2]. Additional features in the $Gd_2O_2^-$ spectrum emerge in manifold I in the spectra measured with lower photon energies, as described below.

There are four distinct features in manifold I in Figure 8.2, labeled X, A, b, and c. X and b are broader than A and c, and the X-b and A-c energy splitting is very similar to the $X^9\Sigma^-$ – $a^7\Sigma^-$ splitting in the GdO diatomic (0.23 eV). [455, 456] The states of the diatomic both have $4f^7\sigma_{6s}$ electronic configurations and differ only in the spin of the electron in the σ_{6s} orbital. It is therefore tempting to assign these two sets of peaks to transitions associated with detaching either an α or β electron from one of the σ_{6s} MOs of Gd_2O_2. However, this splitting *also* coincides with the energy interval between two narrow and intense features observed in the much simpler PE spectrum of $Ce_2O_2^-$; in neutral Ce_2O_2, the coupling between the electrons occupying the 6s-based orbitals and the electrons singly occupying a 4f orbital on the two separate Ce centers is ca. 0.01 eV, and the 0.23 eV observed splitting was attributed to the difference in energy associated with detaching the electron from the $\sigma_{6s,g}$ and $\sigma_{6s,u}$ orbitals. The four features therefore suggests a combination of splitting between possible spin states and the splitting between different states accessed by detachment from the $\sigma_{6s,g}$ and $\sigma_{6s,u}$ outer valence orbitals.

As a starting point, we consider the computational results summarized in Figure 8.3 and Table 8.1. Table 8.1 also includes calculations on the GdO^- and GdO diatomics, along with previously
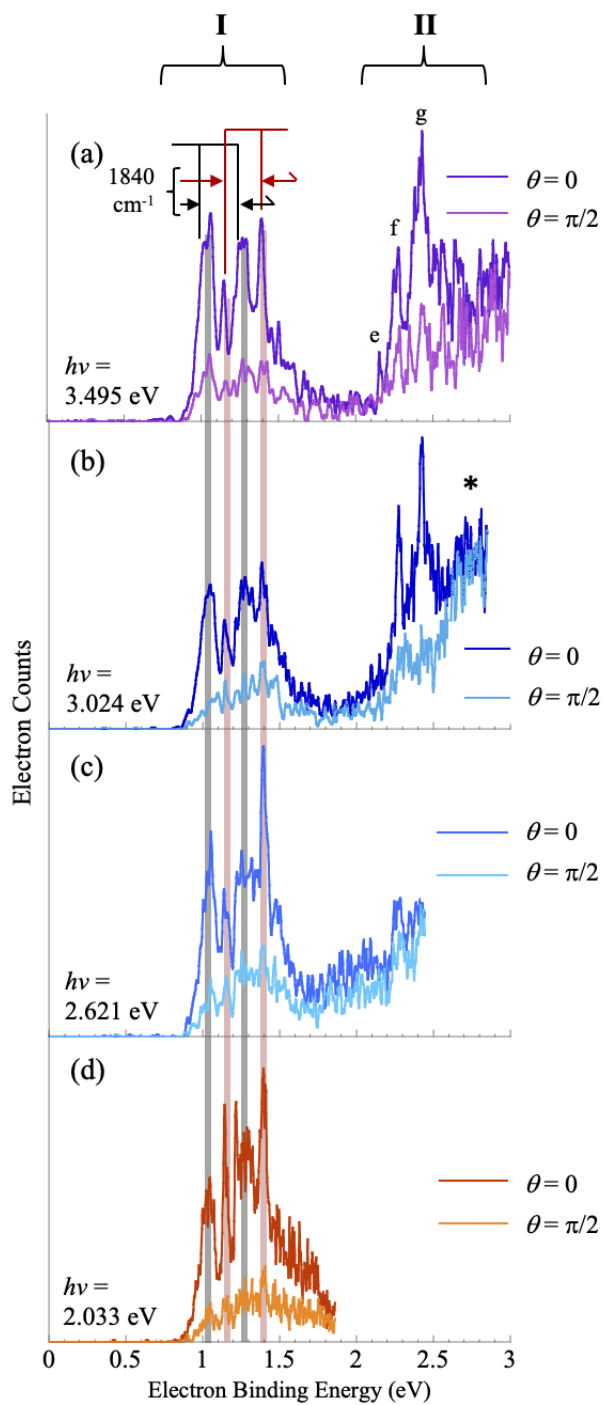
Figure 8.2: Anion PE spectra of $Gd_2O_2^-$ measured using (a) 3.495 eV, (b) 3.024 eV, (c) 2.621 eV, and (d) 2.033 eV photon energies. Darker colors are spectra measured with laser polarization parallel to the electron drift path, lighter colors with perpendicular polarization. Vertical rose and gray lines are included to guide the eye between transitions common to all four spectra.

reported experimental and ligand field theory results. [442] The reasonable agreement between DFT, LFT and experiment provides a measure of validation for the DFT calculations in predicting the energy ordering of the states. As shown in Figure 8.3, the highest spin anion $^{16}B_{1u}$ is predicted to be the lowest energy state, with the AFM-coupled analog, $^2B_{1u}$, state lying 0.07 eV higher. The small energy difference calls into question the identity of the true ground state. However, calculations including spin projection models predict the $^2B_{1u}$ state to be 0.09 eV higher than the $^{16}B_{1u}$ state, and calculations with varying degrees of exact exchange (B3LYP, BLYP, B3PW91, and M062x) all gave similar results, with AFM excitation energies ranging from 0.06 to 0.08 eV. The $^{14}B_{1u}$ state, in which the spin of the electron in the $\sigma_{6s,u}$ orbital is antiparallel to the 4f electrons, is predicted to be 0.18 eV higher in energy than the $^{16}B_{1u}$ ground state, which is reasonable considering the 0.23 eV $^7\Sigma - {}^9\Sigma$ splitting in GdO.

Neutral states are situated above the anion states that connect to them by strictly one-electron detachment transitions in Figure 8.3. A noteworthy result is that the lowest energy electronic state of the neutral is the ^1A_g (AFM-coupled) state, which is predicted to be 0.78 eV above the $^{16}B_{1u}$ state; the one-electron $^1A_g \leftarrow {}^2B_{1u}$ transition would be observed at e^-BE ≈ 0.7 eV. This result, however, calls into question how accurately DFT calculations quantitatively predict the difference in energy for the ^1A_g and $^{15}A_g$ states (0.78 eV versus 1.08 eV). Coupling between the $4f^7$ cores in dincuclear Gd(III) complexes is small, with energy differences between the FM- and AFM-coupled states on the order of 1 cm^{-1}, [457] though additional electrons in the outervalence orbitals may increase the coupling. [458,459] In the case of the ^1A_g and $^{15}A_g$ states, the outervalence electrons are paired. In contrast, the $^{17}B_{1u}$ state is predicted to be lower in energy than its AFM $^3B_{1u}$ analog, and similarly, the FM-coupled 16B1u state is predicted to be lower in energy than its AFM $^2B_{1u}$ analog, which suggests that unpaired outer-valence electrons stabilize FM coupling between the $4f^7$ cores.

Both the $^{16}B_{1u}$ ground state and $^{14}B_{1u}$ excited state have three one-electron accessible neutral states predicted in a ~ 0.9 to 1.7 eV window of energy above the $^{16}B_{1u}$ state, the $^{15}A_g$ state being a common final state, for a total of five neutral FM-coupled states. The open-shell 15-tets are predicted to be nearly isoenergetic at 1.70 eV. We note that the AFM-coupled analog to the open shell 15-tet states, the $^1B_{1u}$ state, is also calculated to be very close in energy to these three $^{15}B_{1u}$ states.

A simulation invoking a rigid one-electron detachment assumption and identical detachment cross sections for every transition is shown in Figure 8.4. The intensities of transitions from the $^{14}B_{1u}$ state are Boltzmann weighted assuming an excitation energy of 0.18 eV and a liberal temperature of 1000K. We also assume the AFM-coupled $^2B_{1u}$ state is not present in the ion beam. The spectrum is dominated by three transitions from the $^{16}B_{1u}$ state. Three predominant transitions do not qualitatively agree with the spectrum. The cryo-SEVI spectrum of SmO$^-$ reported by Weichman et al. [460] exhibited a number of transitions that fall outside of the rigid one-electron picture. If we include transitions to all five FM-coupled states, which implies that the four $^{2S+1}B_{1u}$ states are mixed and that spin is not a good quantum number, the simulation [Figure 8.4] does have four pronounced transitions, one of which involves overlapping transitions to the two nearly isoenergetic open-shell $^{15}B_{1u}$ states. Electronic hot bands shown also assume the $^{14}B_{1u}$ state can access all five neutral F-coupled states.

Agreement between the simulations and the transitions in manifold I is not perfect. The energy range in which the simulated transitions are predicted to lie is ca. 0.3 eV broader than the
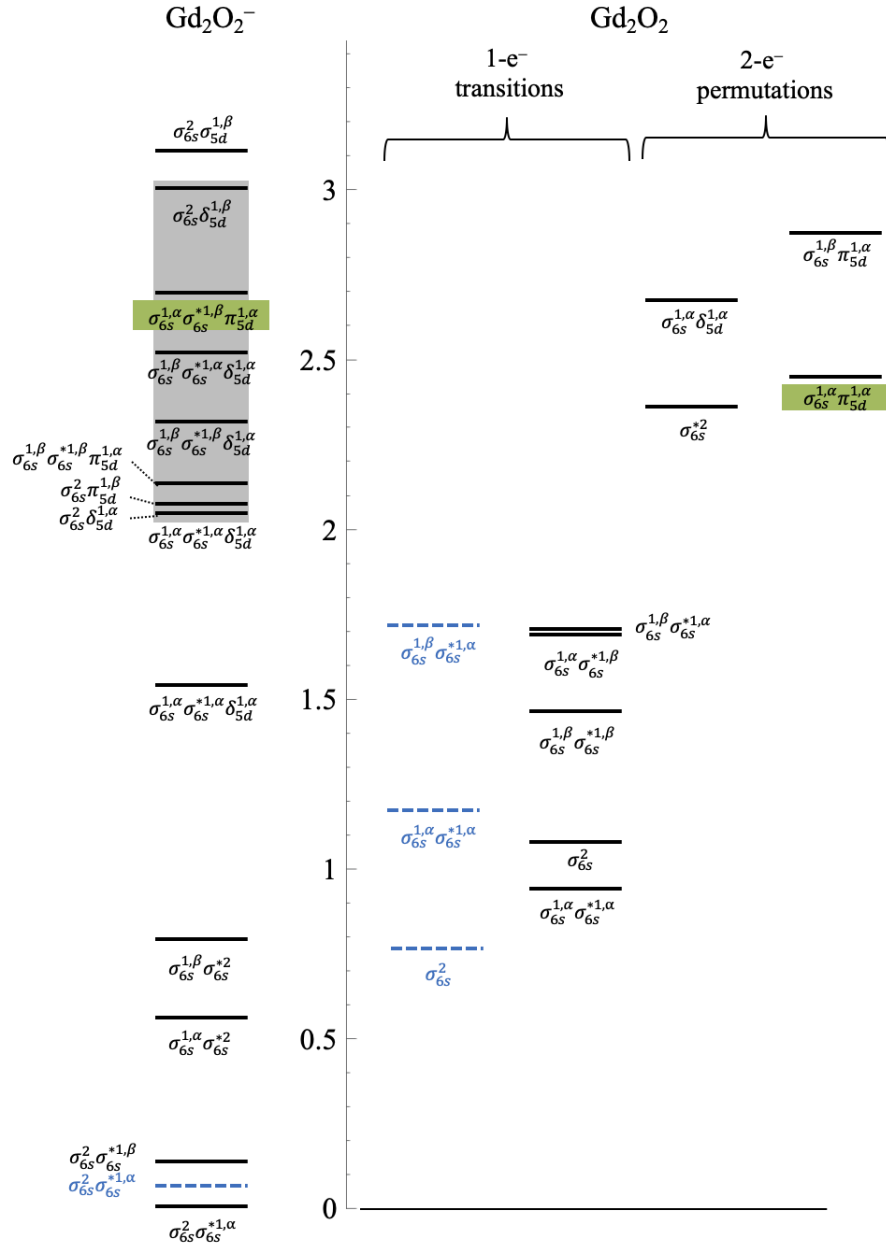
Figure 8.3: Schematic of the relative energies of the low-lying AFM- (blue dashed lines) and FM-coupled (black solid lines) anion and neutral states of Gd_2O_2, along with several higher-energy excited states of $Gd_2O_2^-$, including several lying within the experimental photon energy range (gray box). The states indicated by green boxes are connected by one-electron loss of the anion

	Electronic Structure	DFT Relative Energy (eV)	Exp. Relative Energy	LFT
GdO	$^9\Sigma(4f^7\sigma_{6p}^\alpha)$	2.54	2.62	2.61
	$^9\Pi(4f^7\pi_{6p}^\alpha)$	1.90	2.34	2.18
	$^9\Delta(4f^7\delta_{5d}^\alpha)$	1.39	—	1.44
	a$^9\Sigma(4f^7\sigma_{6s}^\beta)$	0.27	0.23	0.25
	X$^9\Sigma(4f^7\sigma_{6s}^\alpha)$	0	0	0
GdO$^-$	$^8\Sigma(4f^7\sigma_{6s}^2)$	$e^-BE = 1.05$	1.19	

		DFT Optimized Energy (eV)	Gd$-$Gd Internuclear Distance (Å)	Optimized Gd$-$O$-$Gd Angle (^{o})
Gd$_2$O$_2$	$^{17}B_{2g}(4f_a^{7,\alpha}4f_b^{7,\alpha}\sigma_{6s,g}^\alpha\pi_{5d}^\alpha)$	2.42	3.13	100
	$^1A'(4f_a^{7,\alpha}4f_b^{7,\beta}\sigma_{6s,g}^\beta\sigma_{6s,u}^\alpha)$	1.72	3.12	100
	$^{15}B_{1u}(4f_a^{7,\alpha}4f_b^{7,\alpha}\sigma_{6s,g}^\beta\sigma_{6s,u}^\alpha)$	1.71	3.12	100
	$^{15}B_{1u}(4f_a^{7,\alpha}4f_b^{7,\alpha}\sigma_{6s,g}^\beta\sigma_{6s,u}^\beta)$	1.45	3.13	100
	$^3A'(4f_a^{7,\alpha}4f_b^{7,\beta}\sigma_{6s,g}^\alpha\sigma_{6s,u}^\alpha)$	1.18	3.13	99
	$^{15}A_g(4f_a^{7,\alpha}4f_b^{7,\alpha}\sigma_{6s,g}^2)$	1.08	3.08	99
	$^{17}B_{1u}(4f_a^{7,\alpha}4f_b^{7,\alpha}\sigma_{6s,g}^\alpha\sigma_{6s,u}^\alpha)$	0.93	3.14	99
	$^1A'(4f_a^{7,\alpha}4f_b^{7,\beta}\sigma_{6s,g}^2)$	0.78	3.13	99
Gd$_2$O$_2^-$	$^{14}B_{1u}(4f_a^{7,\alpha}4f_b^{7,\alpha}\sigma_{6s,g}^2\sigma_{6s,u}^\beta)$	0.18	3.12	99
	$^2A'(4f_a^{7,\alpha}4f_b^{7,\beta}\sigma_{6s,g}^2\sigma_{6s,u}^\alpha)$	0.07	3.13	99
	$^{14}B_{1u}(4f_a^{7,\alpha}4f_b^{7,\alpha}\sigma_{6s,g}^\alpha\sigma_{6s,u}^\alpha$	0.00	3.12	99

Table 8.1: Summary of zero-point corrected relative energies of GdO/GdO$^-$ and Gd$_2$O$_2$/Gd$_2$O$_2^-$ electronic states calculated at the B3LYP level of theory. The experimental energies and ligand field theory (LFT) calculations are provided for comparison
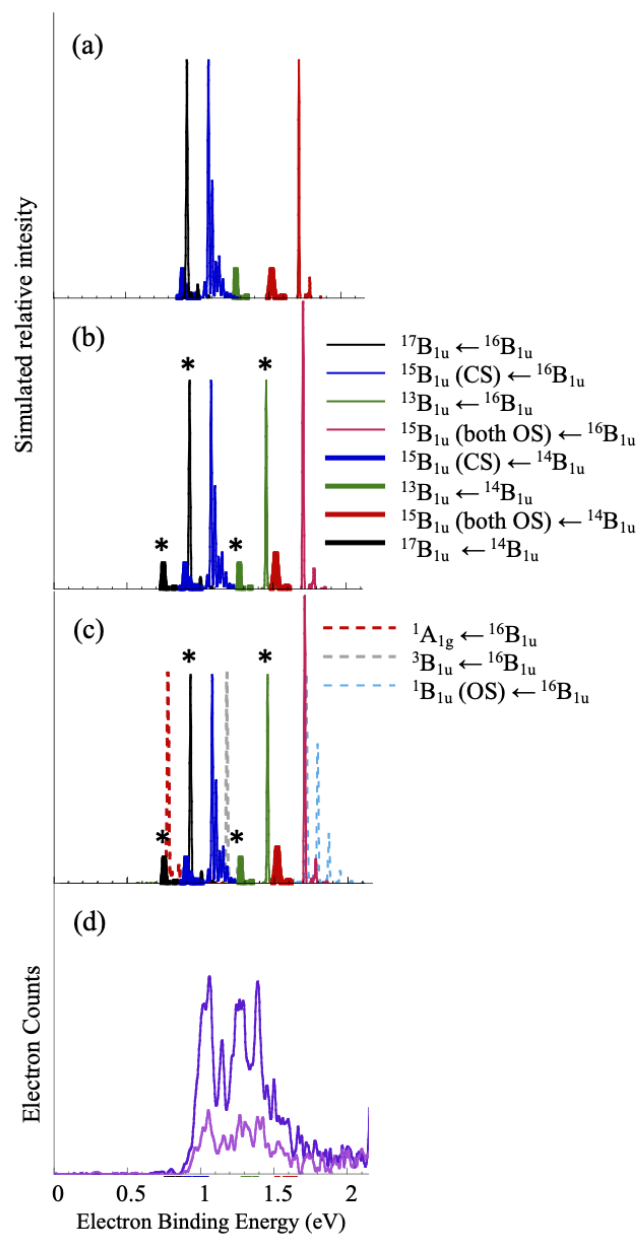
Figure 8.4: (a) Spectral simulations of the three strictly one-electron transitions accessible from the $^{16}B_{1u}$ state of $Gd_2O_2^-$ along with temperature-weighted one-electron transitions accessible from the $^{14}B_{1u}$ state. (b) Transitions to all low-lying neutral states originating from the $^{16}B_{1u}$ and (temperature weighted) $^{14}B_{1u}$ states assuming relaxation of $\Delta s = \pm\frac{1}{2}$ spin selection rule (c) Added to the simulations in (b), transitions to the AFM-coupled spin states. (d) PE spectrum obtained using 3.495 eV included for comparison.

111

observed transitions, though this magnitude of error is typical for detachment transition energies. [32] In addition, the individual detachment transitions are predicted to be nearly vertical, as expected from the diffuse, non-bonding character of the $\sigma_{6s,g}$ and $\sigma_{6s,u}$ orbitals, whereas bands X and b are broadened. Interestingly, based on the calculated relative energies of the neutral states, bands X and b would be assigned to the $^{17}B_{1u}$ and $^{13}B_{1u}$ states, both of which have parallel alignment of the electron spins in the outer-valence $\sigma_{6s,g}$ and $\sigma_{6s,u}$ orbitals (all other states predicted in this energy range have antiparallel spins). Zero-field splitting in the $^9\Sigma^+$ state of the GdO ($4f^7\sigma_{6s}$) state is $sub-cm^{-1}$, [461] and tri-nuclear Gd complexes have coupling between the $4f^7$ centers on the order of 0.2 cm^{-1}, [462] which is comparable to a simple classical calculation of the energy difference between M_s = 15 and M_s = 0 FM coupled Gd $4f^7$ subshells in the calculated Gd_2O_2 structure presented here ($\sim 1cm^{-1}$). However, additional coupling from the unpaired electrons in the outer-valence orbitals may come into play. Indeed, magnetic exchange coupling constants determined for digadolinium complex anions have been reported to be as large as -27 cm^{-1}. [458, 459] If we assume that a range of M_s values are accessed in the photodetachment transition (*vide infra*), a value of D = -15 cm^{-1} would account for the breadth of bands X and b. The simulated transitions to these states that may be broadened by large zero-field splitting are indicated with asterisks (*). Note, however, that band X could also be fit with a harmonic frequency of 217 cm^{-1} and an anharmonicity of 3 cm^{-1}, though again, the predicted vertical appearance of the transitions is consistent with the chemical intuition on detachment from non-bonding orbitals.

8.3.2   Manifold II is not assignable to one-electron transitions

Manifold II is somewhat puzzling, since transitions involving detachment from the inner valence orbitals are expected to be several eV higher in energy, whereas manifold II is approximately 1.2 eV higher in energy. The relative intensities of the transitions in manifold II are different from manifold I, but the peak spacings within the two manifolds are similar. The intensities of transitions in manifold II increase relative to manifold I with decreasing photon energy from 3.495 eV to 2.924 eV. This is shown in the contour plot in Figure 8.5 (obtained by the Chick-Jarrold group), which shows the relative intensities of all the spectra (collected with $\Theta = 0^o$ laser polarization) after normalizing all the spectra over manifold I. Such anti-threshold law behavior was a hallmark of strong electron-neutral interactions observed in previous studies. [77, 126, 453]

The position of manifold II relative to manifold I is nearly identical to a group of excited state transitions observed in the PE spectrum of GdO$^-$, which had been assigned to final neutral states with $4f^76p$ occupancies. [456] Our own calculations on GdO excited states (Table 8.1) suggest that the final state has $4f^75d_\delta$ occupancy, but either way, the transitions are better described as shake-up transitions, where electron promotion accompanies electron detachment. We note here that lower-intensity signal at similar e^-BE values in numerous $Ln_xO_y^-$ (Ln = Ce, Pr, Sm, Eu) suboxide clusters has been observed, and attributed to shake-up transitions. [77, 126, 399]

Included in Figure 8.3 are the relative energies of excited states that differ by more than one electron from the $^{16}B_{1u}$ anion (beyond spin of the electrons in the outer valence orbitals). For example, considering the $\sigma^2_{6s,g}\sigma^\alpha_{6s,u}$ occupancy of the $^{16}B_{1u}$ anion ground state, the $\sigma^2_{6s,u}$ $^{15}A_g$ neutral state would be accessed by detaching an electron from the $\sigma_{6s,g}$ orbital while promoting the remaining $\sigma_{6s,g}$ electron to the $\sigma_{6s,u}$ orbital. The calculations predict this transition to be at 2.35 eV, which falls within the energy range of manifold II. Similarly, detachment accompanied by promotion of an electron into the non-bonding combinations of the Gd 5d orbitals would fall in a
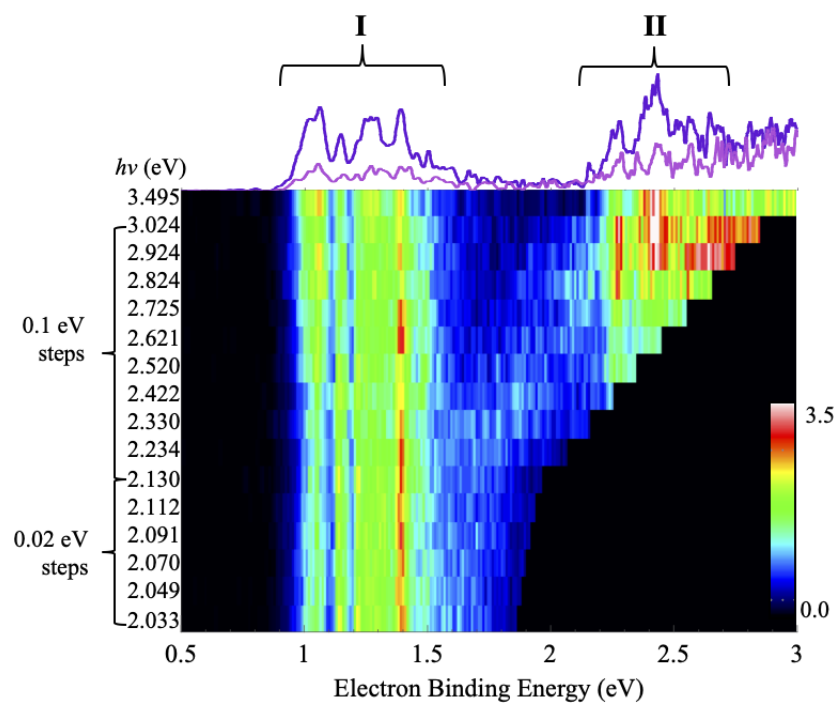
Figure 8.5: Contour plot showing the intensities of transitions in spectra measured with different photon energies. All spectra were normalized between the energies of 0.8 eV and 1.8 eV. The spectrum measured using 3.495 eV is shown across the top of the plot to guide the eye.

similar energy range.

Why are shake-up transitions prevalent and commonly observed in the spectra of lanthanide oxides with multiply occupied 6s-based orbitals? [114, 126, 297, 329, 331, 399] We consider the possibility of strong PEVE interactions. The diffuse 6s-based outer-valence orbitals are highly polarizable. Drawing from previous work, [77, 126, 453] we hypothesize that the electric field from the ejected electron transiently polarizes these orbitals, which would then be described as a time-dependent superposition of outer-valence orbitals. Using the example of the $\sigma_{6s,u}^2$ $^{15}A_g$ final neutral state above, detachment of a $\sigma_{6s,g}$ electron from the $\sigma_{6s,g}^2\sigma_{6s,u}^\alpha$ $^{16}B_{1u}$ would nominally yield the $^{17}B_{1u}$ in the sudden approximation, but while the electron is proximal to the neutral, the perturbed $\sigma_{6s,g}^{'}$ orbital could be described as:

$$\sigma_{6s,g}^{'}(t) = c_1(t)\sigma_{6s,g} + c_2(t)\sigma_{6s,u} + ... + c_i(t)\phi_i \qquad (8.1)$$

If, for example, the electron is ejected along the Gd-Gd axis, $c_2(t)$ would be transiently large, and the probability of populating the final state in which an electron populates the $\sigma_{6s,u}$ would follow. A similar rationale was posited by Wang and coworkers in their elegant description of polarization of valence orbitals by a dipole-bound electron. [463] A distinction between a dipole bound electron and an ejected electron is the time-dependent nature of the latter; decreasing the photon energy and, hence, the photoelectron momentum, increases the time over which the orbital mixing occurs.

While we calculated four neutral states in the energy range of manifold II, the close-lying 6p and 5d orbitals on the two Gd centers will give rise to many additional states. Therefore, we will not attempt to make specific assignments, and will instead generally point to two-electron transitions. We note that there are also numerous excited anion states in the range of photon energies spanned in this study, shown schematically by red lines in Figure 8.3, raising the possibility of resonance enhancements. For example, the state described by the $\sigma_{6s,g}^\alpha\sigma_{6s,u}^\beta\pi_{5d}^\alpha$ occupancy (shaded green) could be accessed by a dipole-allowed transition from the $^{16}B_{1u}$ state (assuming spin is not a good quantum number) followed by loss of the $\sigma_{6s,u}^\beta$ electron, which would be more akin to a conjugate shake-up transition (dipole-driven electron excitation, monopole detachment), which becomes more prevalent near threshold. [464, 465]

8.3.3 Emergence of additional photon-energy dependent transitions in manifold I

The vertical axis on the contour plot in Figure 8.5 is not evenly incremented, as labeled. However, it is evident that features within manifold I are also changing significantly both over 0.1 eV steps (2.130 eV $\leq h\nu \leq$ 3.024 eV) and 0.02 eV steps (2.033 eV $\leq h\nu \leq$ 2.130 eV). An expanded view of manifold I is shown in Figure 8.6, along with several spectra obtained using different photon energies and parallel polarization. Several distinct features are labeled, and the positions of the transitions are summarized in Table 8.2.

As noted previously, the lowest binding energy feature, X, is relatively broad, and at lower photon energies exhibits partially resolved, $\sim 220\,cm^{-1}$ spacings on the low e^-BE rising edge that converge with increasing e^-BE, suggesting significant anharmonicity or splitting between M_s levels of the $^{17}B_{1u}$ neutral state. The profile of this band is affected by X', a narrow feature at 1.05 eV that is pronounced in several, but not all, spectra collected using photon energies between 2.422 through

2.924 eV. Bands X and b in the 3.495 eV spectrum in Figure 8.5 [indicated by the gray vertical lines, Figure 8.2] are separated by 1840 cm^{-1} and have similar profiles, as noted above. However, with lower photon energies, band b is engulfed in a broader collection of close-lying features, labeled B, which itself changes profile with photon energy. Bands A and c [indicated by the rose vertical lines, Figure 8.2] are narrower and both increase in intensity relative to band X with decreasing photon energy, apparently uncorrelated. Transition a, appearing as a lower intensity shoulder in the 3.495 eV spectrum, grows in intensity with decreasing photon energy and appears to be correlated with variations in the intensity of band A.

The intensity changes with photon energy are not monotonic, and are in some cases anti-correlated, which suggests that either excited state resonances or interference between different shake-up channels are occurring. Again, as seen in Figure 8.3, there are a number of excited anion states that fall within the photon energy range used in this study, and many of these states (all FM-coupled) could undergo resonant electronic excitation followed by autodetachment of the excited electron, enhancing the final neutral state intensity formed from autodetachment. However, the total number of transitions that appear to be varying in intensity with photon energy exceeds the five FM-states calculated to lie in this energy range.

Given the sharp features in manifold I grow in intensity (though not monotonically) with decreasing photon energy, we consider the possibility that slower photoelectrons interact with the remnant neutral Gd_2O_2 in a way that switches FM-states to AFM-states. The relative stability of FM and AFM states can switch in the presence of an external electric field, [466–471] raising the possibility that the electric field from the photoelectron temporarily affects the neutral state energies. Treating the detachment process as sudden implies that the electron is instantaneously at much greater distances, leaving the magnetic moment unaffected. However, at the lowest photon energies, the electron would require several fs to escape the range of the outer-valence orbitals, generating an electric field radially pointing toward an electron of 3.6 $V\text{Å}^{-1}$ at a 2 Å distance, which is considerable. The electric field could temporarily stabilize the AFM spin state, driving a switch from the FM state, but as the electron–neutral distance increases, the external electric field felt by the Gd_2O_2 neutral goes to zero, and the AFM and FM states return to their unperturbed energies order, which in turn, slows the departing electron so that it reflects the unperturbed energy of the final state which would not have been observed without the switch.

Table 8.2 includes assignments based on the following: The narrowest features that increase in intensity with decreasing photon energy (decreasing electron momentum) are assigned to the AFM states that are not expected to be observed in a "sudden" detachment formulation. The intense narrow features observed with highest photon energy are assigned to the neutral states in which the total spin of electrons occupying outer valence orbitals is zero, which may result in a very small axial zero-field splitting parameter, and the broader transitions are assigned to neutral FM-coupled states with parallel spins between the outer-valence electrons.

8.4 Summary

There are two principle findings that arise from the results of this study. The first involves the strong electron-neutral interactions that change the relative energy ordering of FM and AFM states of Gd_2O_2, and the second involves the prevalence of PEVE interaction-driven transitions that fall outside of a one-electron description.
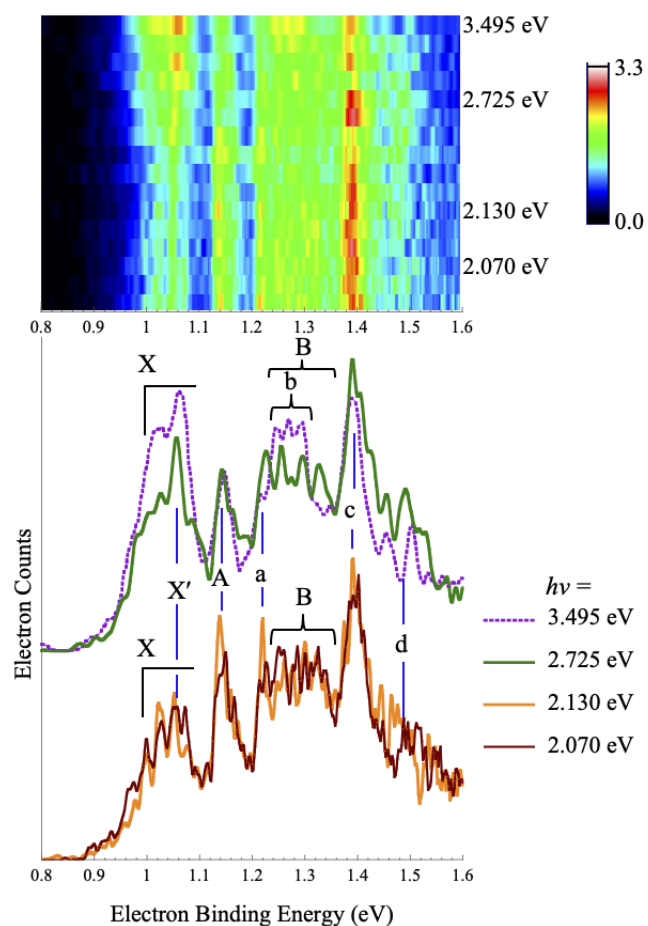
Figure 8.6: Contour plot of PE spectra measured with different photon energies plotted on an expanded scale to highlight manifold I, along with representative spectra measured at four different energies to illustrate changes in relative intensities over wider energy steps (purple and green) and a smaller, 0.06 eV step (orange and maroon). Positions of features labeled on the spectra are summarized in Table 8.2.

116

Peak	Position	Final Neutral State	
	$(e^-\mathrm{BE/eV})$	e^- configuration	Electronic Term
Manifold I			
X	ADE = 0.97 ± 0.03	$4f_a^{7\alpha}4f_b^{7\alpha}\sigma_{6s,g}^{\alpha}\sigma_{6s,u}^{\alpha}$	$^{17}B_{1u}$
	VDE = 1.052 ± 0.003		
X'	1.060 ± 0.005	$4f_a^{7\alpha}4f_b^{7\beta}\sigma_{6s,g}^{2}$	$^{1}A_{g}$
A	1.142 ± 0.005	$4f_a^{7\alpha}4f_b^{7\alpha}\sigma_{6s,g}^{2}$	$^{15}A_{g}$
a	1.219 ± 0.005	$4f_a^{7\alpha}4f_b^{7\beta}\sigma_{6s,g}^{\alpha}\sigma_{6s,u}^{\alpha}$	$^{3}B_{1u}$
b	1.24 - 1.30	$4f_a^{7\alpha}4f_b^{7\alpha}\sigma_{6s,g}^{\beta}\sigma_{6s,u}^{\beta}$	$^{13}B_{1u}$
B	1.25 - 1.36	?	?
		$4f_a^{7\alpha}4f_b^{7\alpha}\sigma_{6s,g}^{\alpha}\sigma_{6s,u}^{\beta}$	$^{15}B_{1u}$
c	1.390 ± 0.010	$4f_a^{7\alpha}4f_b^{7\alpha}\sigma_{6s,g}^{\beta}\sigma_{6s,u}^{\alpha}$	$^{15}B_{1u}$
		$4f_a^{7\alpha}4f_b^{7\beta}\sigma_{6s,g}^{\alpha}\sigma_{6s,u}^{\beta}$	$^{1}B_{1u}$
d	1.49 ± 0.03	?	?
Manifold II			
e	2.15 ± 0.05	Shake-up transitions	
f	2.27 ± 0.05	involving outer-valence	
g	2.42 ± 0.05	detachment and excitation	

Table 8.2: Summary of peak positions and tentative assignments.

At first glance, assignment of the group of transitions to the low-lying neutral states accessed via direct detachment of electrons from the close-lying, non-bonding $\sigma_{6s,g}$ and $\sigma_{6s,u}$ (manifold I) is straightforward, given the relatively simple appearance of the spectrum obtained with 3.495 eV photon energy and the agreement between the observed and predicted detachment energies. However, the emergence of and intensity changes exhibited by narrow features (X', A, a), the broader grouping of close-lying transitions (B) with decreasing photon energy is compelling evidence that the detachment process is more complex. Broad vibrational progressions are inapposite with the diffuse and non-bonding nature of the $\sigma_{6s,g}$ and $\sigma_{6s,u}$ orbitals, and extended vibrational transitions are not predicted by the calculations. The more likely explanation is that certain electronic transitions are exhibiting a splay of M_s states, giving an axial zero-field coupling constant on the order of -15 cm^{-1} for certain, but not all, states. Our results suggest that neutral states in which the spins of the two outer-valence electrons are parallel have this larger coupling constant, while states with zero spin in the outer-valence orbitals have a smaller coupling constant.

The external electric field introduced by the photoelectron approaches zero as the electron-neutral distance increases with time, but on the fs timescale, it remains over 0.4 $V\text{Å}^{-1}$, which is on the order of fields that can switch the relative energies of FM and AFM coupled states studied using scanning-tunneling electron microscopy tips. [471] As the photon energy is decreased, the time the ejected electron lies in a range that can induce the change in relative FM and AFM state energies increases, potentially switching an FM neutral remnant to an AFM neutral remnant, but if the state cannot switch back to FM as the field decays with electron-neutral distance, the final less stable neutral state's unperturbed energy will be encoded in the electron kinetic energy, and reflected as increased intensity of narrow transitions embedded among the transitions that can be characterized as direct detachment transitions.

The prevalence of transitions that cannot be characterized as strictly one-electron has been noted in previous studies on samarium suboxide clusters, with Sm_2O^- studied in the greatest detail. [453] In the "sudden" framework, manifold I in the $Gd_2O_2^-$ PE spectrum consists largely of transitions from the FM-coupled $^{16}B_{1u}$ anion to the five one-electron allowed (assuming spin is not a good quantum number) FM-coupled neutral states. Manifold II goes beyond simple spin change violations, in that no neutral states in this energy range are accessible via changing the orbital occupancy by one electron. Instead, all states would be accessible by shakeup transitions due to PEVE interactions, which become more pronounced with decreasing photon energy and photoelectron momentum.

While not explicitly described as such, an intense group of excited state transitions in the PE spectrum of GdO^- was assigned to a shake-up transition as well. [456] These ca. 1 eV excitations appear to be general for systems with doubly occupied 6s-based MOs, underscoring the role of the polarizability of the remnant neutral by the photoelectron being conducive to two-electron excitation.

Because the electronic structure of $Gd_2O_2^-$ is fundamentally simpler than that of Sm_2O^-, the non-monotonic changes in the relative intensities of individual transitions with decreasing photon energy (i.e., e^-KE) was more readily observed. While analyzing correlations and anti-correlations between the intensities of the crush of transitions in manifold is beyond the scope of this paper, the oscillations in the peak intensities with photon energy that are clearly evident in the contour plot (Figures 8.5 and 8.6) suggest a need to expand our theoretical platform to account for interference between different one- and two-electron detachment pathways. Clearly, these small molecules chal-

lenge our current understanding of electron detachment and electron-neutral interactions (or PEVE interactions) and correlation of electrons in diffuse orbitals with close-lying core-like orbitals with high spin.

Chapter 9

Summary & Outlooks

"The philosophers have only interpreted the world, in various ways. The point, however, is to change it"

— Eleven Theses on Feuerbach, Karl Marx (1845).

With the discovery of the laws of quantum mechanics on one hand and the rapid emergence of powerful computing powers on the other hand, the fields of computational and theoretical chemistry posed themselves as novel fields in studying a spectrum of chemical processes. Our inability to analytically solve the Schrodinger Equation beyond one-electron systems was the stepping stone in the development of families of models that are widely used to approximate the solution of the Schrodinger Equation, and in turn, provide accurate descriptions of energies, properties, and chemical processes.

Of particular interest is the study of electron detachment processes which provide a rich space for examining the structures and properties of atoms and molecules, specifically those that pose challenging electronic states, namely lanthanide-containing small gas-phase clusters. Anion photoelectron spectroscopy provides a powerful experimental tool for studying these systems, mapping the energies of the ground-state and low-lying excited states of the neutral relative to the initial anion state, providing spectroscopic patterns that reflect the lanthanides' frontier orbitals occupancy. The natural ionization model, developed by our group, provides a compact orbital representation of the ionization process and allows the differentiation between pure one-electron detachments and detachments that involve shake-up/shake-off transitions. From that, we also established a direct relationship between ΔSCF Dyson orbitals and natural ionization orbitals. Namely, we formulated polestrength calculations from the natural ionization orbital model. These pole strengths are directly related to experimental cross-sections observed in photoelectron spectroscopy.

Modeling the photoelectron spectra of lanthanide-based clusters provides unprecedent insight on the complex electronic structures of these clusters. Studying the photoelectron spectra of small lanthanide-based clusters, followed by DFT calculations, sets the stage for interpreting the spectra of polyatomic molecular and cluster species, especially those that exhibit multiple and mixed lanthanide centers. Several Ln-based clusters were studied in this dissertation. The photoelectron spectra of $CeO_2B_2^-$ and $CeO_2B_3^-$ show that one additional boron highly influences the structure of the clusters. The photoelectron spectrum of Ceb_6^- shows that the cluster exhibits a structure that

is formed of a Ce center with a B_6 ligand. T he latter was shown to either exhibit a teardrop or a boat-like structures, where the energy gap between the two is very small. Additionally, the photoelectron spectrum of $Gd_2O_2^-$ shows the existence of numerous low-lying and accessible neutral states that appear in the spectrum. This suggests a potential description of the strong photoelectron–valence electron interactions that may result in the photon-energy-dependent changes in the observed spectra.

Results from photoelectron spectroscopy allows us to further investigate the sturcture, bonding, and reactivity of these clusters. The previously-published photoelectron spectrum of EuOH shows that the cluster exhibits a linear conformation. Our work explored the nature of the bond between Eu and $-$OH and generalized the study over the series of lanthanide hydroxides. We show that in all cases, the bond is best described as a triple covalent bond that exhibits a small ionic character. Previous studies on reactivity of cerium oxide cluster with water shows different modes of reactivity that is governed by the ratio of cerium to oxygen. For this, we studied the reaction pathway of Ce_2O^- with water and provide an electronic structure standpoint on the reaction. Namely, we point out that the reaction, which leads to evolution of molecular hydrogen, is driven by the 5d-based Ce orbitals.

9.1 Natural Ionization Orbital Model

In this dissertation, we provided a compact orbital model to represent ionization process that utilizes the difference density matrix. This model, which we refer to as the natural ionization orbital model (NIO), simplifies electron detachment processes and allows the differentiation between one-electron transitions and shake-up/shake-off transitions. Building up from this, we have established a formal relationship between pole strengths, which are proportional to photoionization cross sections, and terms related to the NIO model for ΔSCF calculations. Pole strengths calculated using two approaches developed by ΔSCF calculations provide excellent agreement with pole strengths calculated with an EPT method.

Future work on the NIO model includes calculating photoelectron angular distributions (PAD). The calculation of PADs require calculating the anisotropy parameter, β, which in turn depends on the angular momentum l of the detached electron, the kinetic energy of the detached electron, and the $l \pm 1$ radial partial dipole matrix elements. In addition., future work will also focus on utilizing the NIOs, particularly the relaxation NIO pairs, to provide an enhanced description of the ΔSCF attachment and detachment processes. Interestingly, the use of ΔSCF NIO relaxation terms to calculate pole strengths provided good agreements with EPT pole strengths. This further suggests that the NIO relaxation orbitals can provide insigtful description of relaxation and correlation terms to the ionization potentials and electron affinities calculated at the ΔSCF level. Indeed, relaxation NIO pairs correspond to occupied-virtual rotations in a framework where the final SCF determinant is written in terms of the initial SCF determinant molecular orbitals.

9.2 Photoelectron Specta of Lanthanide molecules

The photoelectron (PE) spectra of various lanthanide-based small gas phase clusters were studied in this dissertation. Modeling the PE spectra escorted us into providing a deep insight on the electronic and molecular properties of small gas phase lanthanide molecules. Our studies on the

structure and bonding of lanthanide hydroxides, the change in bonding motifs of cerium boronyls upoin the addition of one boron atom, the photoelectron-valence electron interaction in $Gd_2O_2^-$, and the mechanistic study of reactivity of Ce_2O^- with water all have provided us with unprecedent chemical insight on the unique properties of lanthanide-based materials.

That being said, a number of unanswered questions remain. In various PE spectra of lanthanide-containing clusters, a strong photoelectron valence electron interaction was observed. The nature of this interaction is still unknown and is the subject of ongoing and future studies. An additional factor that plays a role here is the nature of the lanthanide center. In other words, would we be able to tune this electron-neutral interaction by changing the lanthanide center, or by using a combination of two different lanthanides in order to produce a more dramatic effect?

Appendix A

Summary of the steps followed to model the experimental photoelectron spectra of molecules
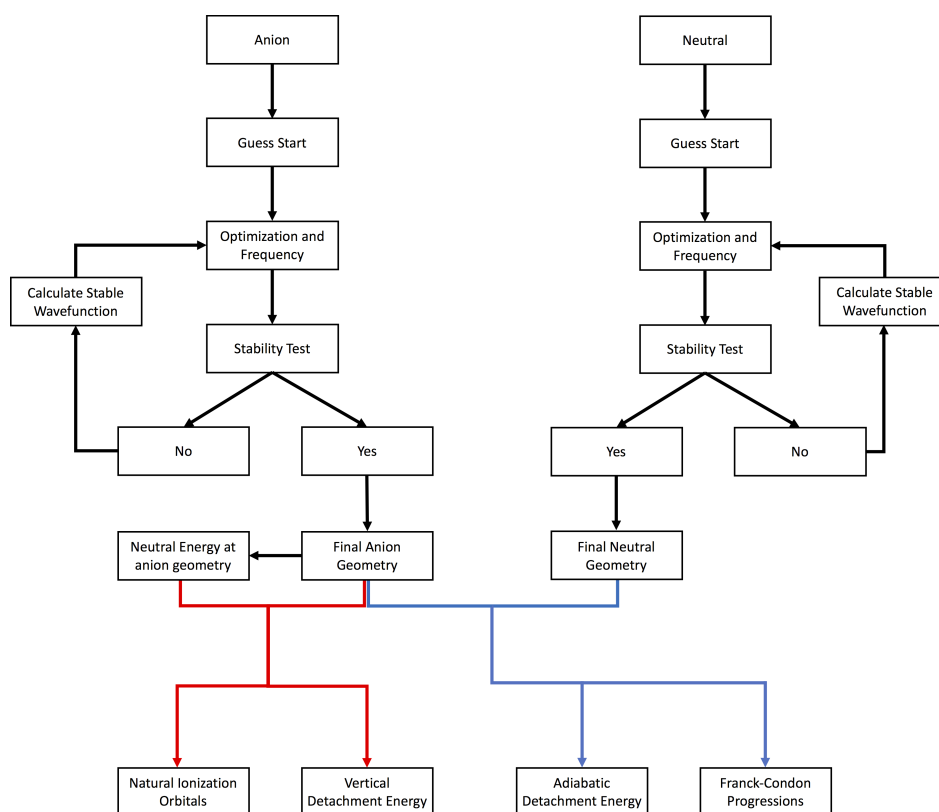
Figure A.1: Workflow diagram showing the computational steps required to model the photoelectron spectra of molecules.

Figure A.1 shows the calculations required to model the anion photoelectron spectrum of a particular species. The process shown in fig. A.1 summarizes the approach used this dissertation. As one can see from fig. A.1, two different energies are computed: Vertical and adiabatic detachment energies. Adiabatic detachment energy (ADE) is the energy difference between the zero-point corrected energies of the anion and one-electron accessible neutral. Vertical Detachment energy (VDE) is the difference between the ground-state energy of the anion and the single-point energy of the neutral confined at anion geometry. For detailed description of the natural ionization orbital model, please refer to chapter 2.

Appendix B

Deriving the ΔSCF Energy in terms of the NIOs

B.1 Δ SCF in the UHF Formalism

Starting from the unrestricted Hartree-Fock energy:

$$E_{UHF}^{N} = \frac{1}{2} \sum_{\mu\nu}^{k} [P_{\mu\nu}^{T} H_{\mu\nu}^{core} + P_{\mu\nu}^{\alpha} F_{\mu\nu}^{\alpha} + P_{\mu\nu}^{\beta} F_{\mu\nu}^{\beta}] \tag{B.1}$$

The energy for (N-1) system will then be:

$$E_{UHF}^{N-1} = \frac{1}{2} \sum_{\mu\nu}^{k} [P_{\mu\nu}^{T'} H_{\mu\nu}^{core} + P_{\mu\nu}^{\alpha'} F_{\mu\nu}^{\alpha'} + P_{\mu\nu}^{\beta'} F_{\mu\nu}^{\beta'}] \tag{B.2}$$

Using the Pople-Nesbet equations, we can derive the expression for ΔE:

$$\Delta E_{SCF} = \sum_{\mu\nu} H_{\mu\nu}^{core} \Delta P_{\mu\nu}^{T} + \frac{1}{2} \sum_{\mu\nu\lambda\sigma} [\Delta\Gamma_{\mu\nu\lambda\sigma}^{T}(\mu\nu|\lambda\sigma) - (\Delta\Gamma_{\mu\nu\lambda\sigma}^{\alpha} + \Delta\Gamma_{\mu\nu\lambda\sigma}^{\beta})(\mu\lambda|\sigma\nu)] \tag{B.3}$$

The terms in the previous equation are defined below:

$$\Delta P_{\mu\nu}^{T} = P_{\mu\mu}^{T'} - P_{\mu\nu}^{T} = \Delta P_{\mu\nu}^{\alpha} + \Delta P_{\mu\nu}^{\beta} \tag{B.4}$$

$$\Gamma_{\mu\nu\lambda\sigma} = P_{\mu\nu} P_{\lambda\sigma} \tag{B.5}$$

$$\Delta\Gamma_{\mu\nu\lambda\sigma}^{T} = \Gamma_{\mu\nu\lambda\sigma}^{T'} - \Gamma_{\mu\nu\lambda\sigma}^{T} \tag{B.6}$$

$$\Delta\Gamma_{\mu\nu\lambda\sigma}^{T} = P_{\mu\nu}^{T} \Delta P_{\lambda\sigma}^{T} + \Delta P_{\mu\nu}^{T} P_{\lambda\sigma}^{T} + \Delta P_{\mu\nu}^{T} \Delta P_{\lambda\sigma}^{T} \tag{B.7}$$

B.2 Defining terms in Δ SCF in terms of NIOs eigenvalues and eigenvectors

In the previous section, we defined Δ SCF in terms of $\Delta P_{\mu\nu}^T$ and $\Delta\Gamma_{\mu\nu\lambda\sigma}^T$, here we insert the relevant equations from section 1.1 to describe the ionization process within the NIO framework. (Note: in the following equations, α and β subscripts are used to refer to the set of NIOs while α and β superscripts are used to indicate spin.)

ΔE_{SCF} can be partitioned into contributions from changes one-electron and two-electron parts, Z_1 and Z_2. The two-electron part can be further decomposed into changes in coulomb and exchange parts, Z_2^C and Z_2^X We can now write the expression for ΔE_{SCF}:

$$\Delta E_{SCF} = Z_1 + Z_2 = Z_1 + Z_2^C - Z_2^X \tag{B.8}$$

B.2.1 One-electron part

The one-electron part of Δ SCF is:

$$Z_1 = \sum_{\mu\nu} H_{\mu\nu}^{core} \Delta P_{\mu\nu}^T \tag{B.9}$$

Which becomes:

$$Z_1 = \sum_{\alpha} \delta_{\alpha\alpha} \sum_{\mu\nu} H_{\mu\nu}^{core} V_{\alpha\mu} V_{\alpha\nu} \tag{B.10}$$

B.2.2 Two-electron term

The two electron term is:

$$Z_2 = \frac{1}{2} \sum_{\mu\nu\lambda\sigma} [\Delta\Gamma_{\mu\nu\lambda\sigma}^T (\mu\nu|\lambda\sigma) - (\Delta\Gamma_{\mu\nu\lambda\sigma}^\alpha + \Delta\Gamma_{\mu\nu\lambda\sigma}^\beta)(\mu\lambda|\sigma\nu)] \tag{B.11}$$

$$Z_2^C = \frac{1}{2} \sum_{\mu\nu\lambda\sigma} \Delta\Gamma_{\mu\nu\lambda\sigma}^T (\mu\nu|\lambda\sigma) \tag{B.12}$$

$$Z_2^X = \frac{1}{2} \sum_{\mu\nu\lambda\sigma} (\Delta\Gamma_{\mu\nu\lambda\sigma}^\alpha + \Delta\Gamma_{\mu\nu\lambda\sigma}^\beta)(\mu\lambda|\sigma\nu)] \tag{B.13}$$

The terms that we need to calculate are $\Delta\Gamma_{\mu\nu\lambda\sigma}^T$, $\Delta\Gamma_{\mu\nu\lambda\sigma}^\alpha$, and $\Delta\Gamma_{\mu\nu\lambda\sigma}^\beta$. These terms become:

$$\Delta\Gamma_{\mu\nu\lambda\sigma}^T = P_{\mu\nu}^T \sum_{\beta} V_{\beta\lambda}\delta_{\beta\beta} V_{\beta\sigma} + \sum_{\alpha} V_{\alpha\mu}\delta_{\alpha\alpha} V_{\alpha\nu} P_{\lambda\sigma}^T + \sum_{\alpha\beta} V_{\alpha\mu} V_{\alpha\nu}\delta_{\alpha\alpha} V_{\beta\lambda} V_{\beta\sigma}\delta_{\beta\beta} \tag{B.14}$$

$$\Delta\Gamma_{\mu\nu\lambda\sigma}^\alpha = P_{\mu\nu}^\alpha \sum_{\beta} V_{\beta\lambda}^\alpha\delta_{\beta\beta}^\alpha V_{\beta\sigma}^\alpha + \sum_{\alpha} V_{\alpha\mu}^\alpha\delta_{\alpha\alpha}^\alpha V_{\alpha\nu}^\alpha P_{\lambda\sigma}^\alpha + \sum_{\alpha\beta} V_{\alpha\mu}^\alpha V_{\alpha\nu}^\alpha\delta_{\alpha\alpha}^\alpha V_{\beta\lambda}^\alpha V_{\beta\sigma}^\alpha\delta_{\beta\beta}^\alpha \tag{B.15}$$

$$\Delta\Gamma^\beta_{\mu\nu\lambda\sigma} = P^\beta_{\mu\nu} \sum_\beta V^\beta_{\beta\lambda} \delta^\beta_{\beta\beta} V^\beta_{\beta\sigma} + \sum_\alpha V^\beta_{\alpha\mu} \delta^\beta_{\alpha\alpha} V^\beta_{\alpha\nu} P^\beta_{\lambda\sigma} + \sum_{\alpha\beta} V^\beta_{\alpha\mu} V^\beta_{\alpha\nu} \delta^\beta_{\alpha\alpha} V^\beta_{\beta\lambda} V^\beta_{\beta\sigma} \delta^\beta_{\beta\beta} \quad \text{(B.16)}$$

Since we are working with unrestricted wavefunctions, $\Delta\Gamma^T_{\mu\nu\lambda\sigma}$ needs to be expressed in terms of $\Delta\Gamma^\alpha_{\mu\nu\lambda\sigma}$ and $\Delta\Gamma^\beta_{\mu\nu\lambda\sigma}$:

$$\Delta\Gamma^T_{\mu\nu\lambda\sigma} = \Delta\Gamma^\alpha_{\mu\nu\lambda\sigma} + \Delta\Gamma^\beta_{\mu\nu\lambda\sigma} + \Delta\Gamma^{\alpha/\beta}_{\mu\nu\lambda\sigma} + \Delta\Gamma^{\beta/\alpha}_{\mu\nu\lambda\sigma} \quad \text{(B.17)}$$

The terms $\Delta\Gamma^{\alpha/\beta}_{\mu\nu\lambda\sigma}$ and $\Delta\Gamma^{\beta/\alpha}_{\mu\nu\lambda\sigma}$ are given as follows:

$$\Delta\Gamma^{\alpha/\beta}_{\mu\nu\lambda\sigma} = P^\alpha_{\mu\nu} \sum_\beta V^\beta_{\beta\lambda} \delta^\beta_{\beta\beta} V^\beta_{\beta\sigma} + \sum_\alpha V^\alpha_{\alpha\mu} \delta^\alpha_{\alpha\alpha} V^\alpha_{\alpha\nu} P^\beta_{\lambda\sigma} + \sum_{\alpha\beta} V^\alpha_{\alpha\mu} V^\alpha_{\alpha\nu} \delta^\alpha_{\alpha\alpha} V^\beta_{\beta\lambda} V^\beta_{\beta\sigma} \delta^\beta_{\beta\beta} \quad \text{(B.18)}$$

$$\Delta\Gamma^{\beta/\alpha}_{\mu\nu\lambda\sigma} = P^\beta_{\mu\nu} \sum_\beta V^\alpha_{\beta\lambda} \delta^\alpha_{\beta\beta} V^\alpha_{\beta\sigma} + \sum_\alpha V^\beta_{\alpha\mu} \delta^\beta_{\alpha\alpha} V^\beta_{\alpha\nu} P^\alpha_{\lambda\sigma} + \sum_{\alpha\beta} V^\beta_{\alpha\mu} V^\beta_{\alpha\nu} \delta^\beta_{\alpha\alpha} V^\alpha_{\beta\lambda} V^\alpha_{\beta\sigma} \delta^\alpha_{\beta\beta} \quad \text{(B.19)}$$

Appendix C

Supporting Information

C.1   SCF Pole Strenghts

Table C.1: Ground state and detached state SCF energies (E_h) for the test set employed in this study. See the paper for model chemistries.

Molecule	SCF Energy (GS)	SCF + ZPE (GS)	SCF Energy (Detached)
Formaldehyde	-113.8424577	-113.814807	-113.4931471
Nitromethyl radical	-243.0652646	-243.028013	-242.726416
Water	-76.04701192	-76.023936	-75.64597251
Chlorobenzene	-689.6793988	-689.584587	-689.3787373
CCl_4	-1875.852271	-1875.841561	-1875.43432
NH_3	-56.21039686	-56.173814	-55.87055921
Ethanol	-154.1257439	-154.040509	-153.7769086

Table C.2: Computed $\left\langle S^2 \right\rangle$ values for ground state and detached states for the test set employed in this study. See the paper for model chemistries.

Molecule	$\left\langle S^2 \right\rangle$ (GS)	$\left\langle S^2 \right\rangle$ (Detached)
Formaldehyde	0.06	0.81
Nitromethyl radical	1.17	0.92
Water	0.00	0.76
Chlorobenzene	0.48	0.92
CCl_4	0.00	0.76
NH_3	0.00	0.76
Ethanol	0.00	0.76

Table C.3: Vertical detachment energies using EPT and ΔSCF for the test set employed in this study. See the paper for model chemistries.

Molecule	EPT Pole (eV)	ΔSCF (eV)
Formaldehyde	10.90	9.50
Nitromethyl radical	11.43	9.22
Water	12.30	10.91
Chlorobenzene	8.70	8.18
CCl_4	11.44	11.37
NH_3	10.44	9.25
Ethanol	10.73	9.49

Optimized Geometries

Formaldehyde
0 1
C -0.00000472 0.53643804 0.00000000
H 0.92259690 1.10000124 0.00000000
H -0.92253080 1.10015705 0.00000000
O -0.00000472 -0.67734831 -0.00000000
Nitromethyl radical
0 2
C 0.31323339 -1.26866831 -0.00000000
H -0.50878427 -1.94949848 -0.00000000
H 1.35072584 -1.52320059 -0.00000000
O -1.20441932 0.36013710 0.00000000
O 0.86425159 0.94333535 0.00000000
N 0.00000000 0.09384703 0.00000000
Water
0 1
H -0.00000000 0.74915616 -0.45552444
O -0.00000000 0.00000000 0.11388111
H -0.00000000 -0.74915616 -0.45552444
Chlorobenzene
0 1
C -0.00000000 -0.00000000 0.50601828
C 0.00000000 0.00000000 -2.26697994
C 0.00000000 1.21310300 -0.17458846
C 0.00000000 1.20619616 -1.56834346
C -0.00000000 -1.21310300 -0.17458846
C -0.00000000 -1.20619616 -1.56834346
Cl -0.00000000 -0.00000000 2.25175171
H 0.00000000 0.00000000 -3.34177074
H 0.00000000 2.13633756 0.37271148
H 0.00000000 2.13973078 -2.10123919
H -0.00000000 -2.13633756 0.37271148
H -0.00000000 -2.13973078 -2.10123919
CCl$_4$
0 1
C 0.00000000 0.00000000 0.00000000
Cl -1.02038054 -1.02038054 1.02038054
Cl 1.02038054 1.02038054 1.02038054
Cl 1.02038054 -1.02038054 -1.02038054
Cl -1.02038054 1.02038054 -1.02038054
NH$_3$
0 1

N -0.00000000 0.00000000 0.10980580
H 0.00000000 0.93152839 -0.25621354
H -0.80672725 -0.46576419 -0.25621354
H 0.80672725 -0.46576419 -0.25621354
Ethanol
0 1
C 1.21792380 -0.21755956 0.00000405
H 2.05907958 0.47004511 -0.00020988
H 1.28714943 -0.84975253 -0.87907156
H 1.28731328 -0.84940205 0.87931470
C -0.09193998 0.54176307 -0.00000283
H -0.15078354 1.18214578 0.87938775
H -0.15075779 1.18209052 -0.87943338
O -1.14038118 -0.39236401 -0.00000460
H -1.96485439 0.05856418 0.00004184

C.2 On the Linear Geometry of Lanthanide Hydroxides

Species	SCF Energy (Hartree)	$\langle S^2 \rangle$
LaOH	-8563.003	0
CeOH	-8929.6236	3.75
PrOH	-9305.882	6
NdOH	-9691.9541	8.75
PmOH	-10087.856	12
SmOH	-10493.683	15.75
EuOH	-10909.557	20.01
GdOH	-11335.369	15.78
TbOH	-11771.272	12.01
DyOH	-12217.411	8.75
HoOH	-12673.825	6
ErOH	-13140.551	3.75
TmOH	-13617.667	2
YbOH	-14105.238	0.75
LuOH	-14603.002	0

Table C.4: SCF Energies (in Hartrees) and $\langle S^2 \rangle$ for the calculated lanthanide hydroxides.

As mentioned in chapter 4, SCF solutions with energies near the reported ground states were located for CeOH, NdOH, and PmOH. Tables C.6, C.7, and C.8 give energies and geometric parameters for the ground state solutions (those reported in the chapter) and the nearest energy low-lying state determined during our investigation.

Species	Orbital occupation
LaOH	$4f^0 6s^2$
CeOH	$4f^1 6s^1 5d^1$
PrOH	$4f^2 6s^1 5d^1$
NdOH	$4f^3 6s^1 5d^1$
PmOH	$4f^4 6s^1 5d^1$
SmOH	$4f^6 6s^1$
EuOH	$4f^7 6s^1$
GdOH	$4f^7 6s^2$
TbOH	$4f^9 6s^1$
DyOH	$4f^{10} 6s^1$
HoOH	$4f^{11} 6s^1$
ErOH	$4f^{12} 6s^1$
TmOH	$4f^{13} 6s^1$
YbOH	$4f^{14} 6s^1$
LuOH	$4f^{14} 6s^2$

Table C.5: Occupations of 4f, 5d, and 6s based non-bonding molecular orbitals of lanthanide hydroxides

Electronic Configuration	Energy (eV)	Ce–OH (Å)	CeO–H (Å)	Ce–O–H (°)
$4f^1 6s^1 5d^1$	0.00	2.05	0.96	180
$4f^1 6s^2$	0.18	2.06	0.95	180

Table C.6: Electronic configuration, energy, and geometric parameters for low-lying SCF solutions for CeOH.

Electronic Configuration	Energy (eV)	Nd–OH (Å)	NdO–H (Å)	Nd–O–H (°)
$4f^3 6s^1 5d^1$	0.00	2.01	0.95	180
$4f^3 6s^2$	0.03	2.07	0.95	180

Table C.7: Electronic configuration, energy, and geometric parameters for low-lying SCF solutions for NdOH.

Electronic Configuration	Energy (eV)	Pm–OH (Å)	PmO–H (Å)	Pm–O–H (°)
$4f^4 6s^1 5d^1$	0.00	2.03	0.95	180
$4f^4 6s^2$	0.04	2.03	0.95	180

Table C.8: Electronic configuration, energy, and geometric parameters for low-lying SCF solutions for PmOH.

Species	Calculated Bond Length	Calculated Dipole Moment (DFT)	Idealized Dipole Moment (Placed at O)	Percent Ionic Character	Idealized Dipole Moment (Placed at H)	Percent Ionic Character	Idealized Dipole moment (Placed halfway b/w O and H)	Percent Ionic Character
LaOH	2.04	0.04	9.76	0.4	14.36	0.29	12.06	0.35
CeOH	2.05	0.74	9.81	7.5	14.41	5.12	12.11	6.09
PrOH	2.05	0.87	9.77	8.9	14.41	6.02	12.11	7.17
NdOH	2.01	1.05	9.62	10.9	14.22	7.41	11.92	8.84
PmOH	2.03	1.15	9.68	11.9	14.31	8.07	12.01	9.61
SmOH	2.09	1.24	9.97	12.4	14.6	8.49	12.3	10.07
EuOH	2.08	1.42	9.95	14.3	14.55	9.76	12.25	11.6
GdOH	1.96	0.51	9.39	5.4	13.98	3.66	11.68	4.38
TbOH	2.01	0.6	9.61	6.2	14.22	4.2	11.92	5.01
DyOH	2.06	1.39	9.82	14.1	14.46	9.61	12.16	11.42
HoOH	2.05	1.52	9.79	15.5	14.41	10.52	12.11	12.52
ErOH	2.04	1.51	9.73	15.5	14.36	10.48	12.06	12.48
TmOH	2.03	1.6	9.69	16.5	14.31	11.2	12.01	13.34
YbOH	2.02	1.66	9.64	17.2	14.26	11.62	11.97	13.85
LuOH	1.9	0.47	9.05	5.2	13.69	3.46	11.39	4.15

Table C.9: Comparison of idealized dipole moments of purely ionic LnOH calculated with varied positions of anion charge along the O—H bond.

Mulliken population analyses for both α and β molecular orbitals are summarized in Tables C.10 and C.11 below. It is noteworthy that in several cases the Mulliken analyses exhibit non-zero contributions from lanthanide 4f functions. It is not clear if the participating f-orbitals are simply enhancing variational relaxation and polarization or if they are engaged in bonding in the conventional sense. Determination of the specifics of this matter is beyond the scope of the current paper and we defer such an analysis to the NBO based study described in the paper. Nevertheless, 4f/5d hybridization has been invoked in previous studies of lanthanide compounds, including a recent report by Zhang and co-workers studying PrO_2 [472].

The specific interpretation of these Mulliken population analysis results is beyond the scope of the present work. Instead, we rely on the NBO model for the bonding analysis described in the paper. This choice is partially based on the known behavior of Mulliken partitioning. As is well known, Mulliken partitioning can lead to unphysical results particularly when employing basis sets with diffuse functions. In particular, Mulliken analysis can fail to suggest expected electron donation behaviors of ligands. In work on actinide complexes, Clark and co-workers [473] showed that the Mulliken model incorrectly predicts that OH^- is a weaker electron donor than CN^-. An additional concern raised in Mulliken population analysis, also discussed by Clark and co-workers, is that the definition of bond order does not distinguish between bonding and antibonding interactions which can yield an inaccurate chemical description of the molecules.

Molecule	σ Bond	π Bond	π Bond
LaOH	55.3% O 2p 22.0% H 1s 8.6% La 6p 7.5% La 5d 6.3% O 2s	92.6% O 2p 5.4% La 5d	91.3% O 2p 6.2% La 5d
CeOH	57.0% O 2p 22.4% H 1s 7.1% Ce 5d 6.7% O 1s 6.5% Ce 6p 1.6% Ce 4f	91.1% O 2p 6.2% Ce 5d 1.3% H 2p 1.1% Ce 4f	91.0% O 2p 6.2% Ce 5d 1.3% H 2p 1.2% Ce 4f
PrOH	57.6% O 2p 22.7% H 1s 6.9% Pr 5d 6.7% O 2s 5.5% Pr 6p 2.1% Pr 4f	90.1% O 2p 6.0% Pr 5d 2.5% Pr 4f 1.2% H 2p	90.7% O 2p 6.4% Pr 5d 1.4% H 2p 1.2% Pr4f
NdOH	58.4% O 2p 23.0% H 1s 7.0% O 2s 6.1% Nd 5d 4.6% Nd 6p	89.5% O 2p 5.9% Nd 5d 2.3% Nd 4f	90.6% O 2p 6.1% Nd 5d

	2.3% Nd 4f		
PmOH	59.7% O 2p 23.4% H 1s 7.6% O 2s 5.3% Pm 6p 3.5% Pm 5d	90.2% O 2p 5.4% Pm 5d	91.0% O 2p 5.8% Pm 5d
SmOH	60.0% O 2p 23.7% H 1s 8.0% O 2s 5.1% Sm 5d 3.2% Sm 6p	91.0% O 2p 5.2% Sm 5d	91.2% O 2p 5.3% Sm 5d
EuOH	60.2% O 2p 24.0% H 1s 8.1% O 2s 4.9% Eu 5d 2.6% Eu 6p	89.4% O 2p 4.9% Eu 5d 3.4% Eu 4f	89.4% O 2p 4.9% Eu 5d 3.4% Eu 4f
GdOH	44.0% O 2p 32.5% Gd 4f 17.8% H 1s	89.6% O 2p 7.1% Gd 5d	89.6% O 2p 7.1% Gd 5d
TbOH	60.3% O 2p 24.0% H 1s 7.4% O 2s 4.7% Tb 4f 4.5% Tb 5d	84.1% O 2p 8.3% Tb 4f 5.8% Tb 5d	84.1% O 2p 8.3% Tb 4f 5.8% Tb 5d
DyOH	61.6% O 2p 24.5% H 1s 8.4% O 2s 4.0% Dy 5d 2.1% Dy 4f	58.3% O 2p 3.7% Dy 4f 2.5% Dy 5d	58.3% O 2p 3.7% Dy 4f 2.5% Dy 5d
HoOH	62.2% O 2p 24.6% H 1s 8.6% O 2s 3.6% Ho 5d 2.2% Ho 4f	47.8% O 2p 48.5% Ho 4f 2.63% Ho 5d	47.8% O 2p 48.5% Ho 4f 2.63% Ho 5d
ErOH	62.9% O 2p 24.8% H 1s 8.9% O 2s 3.2% Er 5d 2.4% Er 4f	51.7% O 2p 44.5% Er 4f 2.3% Er 5d	66.7% O 2p 28.3% Er 4f 3.3% Er 5d

TmOH	63.0% O 2p 24.9% H 1s 9.0% O 2s 3.5% Tm 4f 2.7% Tm 5d	60.0% O 2p 36.6% Tm 4f 2.3% Tm 5d	80.1% O 2p 14.0% Tm 4f 4.0% Tm 5d
YbOH	63.7% O 2p 25.2% H 1s 9.2% O 2s 4.0% Yb 4f 2.3% Yb 5d	87.5% O 2p 6.5% Yb 4f 4.0% Yb 5d	87.5% O 2p 6.5% Yb 4f 4.0% Yb 5d
LuOH	60.0% O 2p 23.3% H 1s 6.3% O 2s 6.0 % Lu 5d	90.4% O 2p 6.4% Lu 5d	91.4% O 2p 6.3% Lu 5d

Table C.10: Alpha Mulliken populations of the three bonding molecular orbitals of LnOH.

Molecule	σ Bond	π Bond	π Bond
LaOH	55.3% O 2p 22.0% H 1s 8.6% La 6p 7.5% La 5d 6.3% O 2s	92.6% O 2p 5.4% La 5d	91.3% O 2p 6.2% La 5d
CeOH	56.8% O 2p 22.6% H 1s 7.7% Ce 6p 6.9% O 2s 6.0% Ce 5d	93.6% O 2p 4.4% Ce 5d	93.5% O 2p 4.5% Ce 5d
PrOH	57.8% O 2p 22.8% H 1s 7.1% O 2s 6.7% Pr 6p 5.8% Pr 5d	93.6% O 2p 4.5% Pr 5d	93.9% O 2p 4.2% $Pr_5 d$
NdOH	58.9% O 2p 23.4% H 1s 7.5% O 2s 6.2% Nd 6p 5.3% Nd 5d	93.8% O 2p 4.1% Nd 5d	93.7% O 2p 4.1% Nd 5d
PmOH	59.7% O 2p 23.4% H 1s	93.8% O 2p 3.8% Pm 5d	94.0% O 2p 3.7% Pm 5d

	8.0% O 2s 5.3% Pm 6p 4.6% Pm 5d		
SmOH	59.2% O 2p 23.7% H 1s 8.3% O 2s 5.4% Sm 6p 4.3% Sm 5d	94.0% O 2p 3.7% Sm 5d	94.1% O 2p 3.5% Sm 5d
EuOH	59.7% O 2p 24.0% H 1s 8.5% O 2s 4.7% Eu 6p 4.1% Eu 5d	94.1% O 2p 3.6% Eu 5d	94.1% O 2p 3.6% Eu 5d
GdOH	59.9% O 2p 23.9% H 1s 6.9% O 2s 5.9% Gd 5d	92.0% O 2p 5.3% Gd 5d	92.0% O 2p 5.3% Gd 5d
TbOH	61.3% O 2p 24.1% H 1s 8.0% O 2s 4.6% Tb 5d 3.1% Tb 6p	92.9% O 2p 4.5% Tb 5d	92.9% O 2p 4.5% Tb 5d
DyOH	61.9% O 2p 24.3% H 1s 8.7% O 2s 3.7% Dy 5d 2.4% Dy 6p	93.4% O 2p 3.9% Dy 5d	93.4% O 2p 3.9% Dy 5d
HoOH	62.4% O 2p 24.5% H 1s 8.8% O 2s 3.5% Ho 5d	92.5% O 2p 3.6% Ho 5d	92.5% O 2p 3.6% Ho 5d
ErOH	63.1% O 2p 24.8% H 1s 9.0% O 2s 3.1% Er 5d 2.0% Er 4f	90.1% O 2p 3.5% Er 5d 3.4% Er 4f	92.4% O 2p 3.6% Er 5d
TmOH	63.4% O 2p 24.9% H 1s 9.2% O 2s 3.1% Tm 4f	73.2% O 2p 21.8% Tm 4f 2.7% Tm 5d	71.6% O 2p 23.9% Tm 4f 2.6% Tm 5d

	2.7% Tm 5d		
YbOH	64.1% O 2p 25.1% H 1s 9.4% O 2s 4.1% Yb 4f 2.3% Yb 5d	87.9% O 2p 7.0% Yb 4f 3.5% Yb 5d	87.9% O 2p 7.0% Yb 4f 3.5% Yb 5d
LuOH	60.1% O 2p 23.2% H 1s 6.6% O 2s 5.6 % Lu 5d	92.1% O 2p 5.2% Lu 5d	93.3% O 2p 4.7% Lu 5d

Table C.11: Beta Mulliken populations of the three bonding molecular orbitals of LnOH.

Determination of the effective ionic radii

Shannon [295] reports the variations in ionic radii in accordance to change in the coordination numbers of ions. While the paper does not provide the ionic radii for singly-coordinated Ln+ and OH-, one can estimate it using the available values and their respective trends. In order to provide a proper estimation of the effective ionic radii of Ln+, we consider a possible trend in the ionic radii of 2-coordinated M^+ versus 6-coordinated M^{3+}. For copper and silver, both of those values are reported and, in both cases, the 2-coordinated M^+ radii are around 85% of the 6-coordinated M^{3+}. Starting from this estimation, we scale the reported 6-coordinated Ln^{3+} by a factor of 0.85 and the resulting estimated effective ionic radii were used for further bonding analysis.

In a similar approach, and in order to determine an estimate to the effective ionic radius of OH^-, we explored the relationship between the coordination number and the effective ionic radius of OH^-. Shannon's reported ionic radii shows a linear relationship between the coordination number and the effective ionic radii. ($y = 0.012\ x + 1.3$, $R^2 = 0.969$). Using the above equation, we can estimate the effective ionic radius of 1-coordinated OH^- to be 1.31 Angstroms.

Species	R 6-coordinated Ln^{3+}	Estimated 2-coordinate Ln^+
LaOH	1.03	0.88
CeOH	1.01	0.86
PrOH	0.99	0.84
NdOH	0.98	0.84
PmOH	0.97	0.82
SmOH	0.96	0.81
EuOH	0.95	0.8
GdOH	0.93	0.79
TbOH	0.92	0.78
DyOH	0.91	0.78
HoOH	0.9	0.77
ErOH	0.89	0.76
TmOH	0.88	0.75
YbOH	0.87	0.74
LuOH	0.86	0.73

Table C.12: Reported effective ionic radii of 6-coordinated Ln^{3+} and the estimated Ln^+ effective ionic radii.

OH^- Coordination Number	Effective Ionic Radius
2	1.32
3	1.34
4	1.35
6	1.37

Table C.13: Effective ionic radius of OH^- as function of coordination number

C.3 Resolving the EuO⁻ Photoelectron Spectrum

Method	Basis Set	Charge	Electronic State	Relative Energy
HF/DKH	SARC	-1	$^8\Sigma^-$	0.0
		0	$^7\Sigma^-$	0.37
		0	$^9\Sigma^-$	0.23
HF	ECP	-1	$^8\Sigma^-$	0.0
		0	$^7\Sigma^-$	0.08
		0	$^9\Sigma^-$	-0.06
B3PW91/DKH	SARC	-1	$^8\Sigma^-$	0.0
		0	$^7\Sigma^-$	0.88
		0	$^9\Sigma^-$	0.63
B3PW91	ECP	-1	$^8\Sigma^-$	0.0
		0	$^7\Sigma^-$	0.80
		0	$^9\Sigma^-$	0.57
MP2/DKH	SARC	-1	$^8\Sigma^-$	0.0
		0	$^7\Sigma^-$	0.56
		0	$^9\Sigma^-$	0.40
MP2	ECP	-1	$^8\Sigma^-$	0.0
		0	$^7\Sigma^-$	0.46
		0	$^9\Sigma^-$	0.31
CCSD/DKH	SARC	-1	$^8\Sigma^-$	0.0
		0	$^7\Sigma^-$	0.87
		0	$^9\Sigma^-$	0.68
CCSD	ECP	-1	$^8\Sigma^-$	0.0
		0	$^7\Sigma^-$	0.63
		0	$^9\Sigma^-$	0.45
CCSD(T)/DKH	SARC	-1	$^8\Sigma^-$	0.0
		0	$^7\Sigma^-$	0.91
		0	$^9\Sigma^-$	0.78
CCSD(T)	ECP	-1	$^8\Sigma^-$	0.0
		0	$^7\Sigma^-$	0.60
		0	$^9\Sigma^-$	0.47

Table C.14: Relative energies of the low-lying states of EuH anions and neutrals calculated using different model chemistries

Method	Basis Set	Charge	Electronic State	Eu−H Bond length	Vibrational Frequency
HF/DKH	SARC	-1	$^8\Sigma^-$	2.29	1021.96
		0	$^7\Sigma^-$	2.20	1191.19
		0	$^9\Sigma^-$	2.20	1197.50
HF	ECP	-1	$^8\Sigma^-$	2.28	1050.81
		0	$^7\Sigma^-$	2.19	1207.90
		0	$^9\Sigma^-$	2.18	1216.39
B3PW91/DKH	SARC	-1	$^8\Sigma^-$	2.21	1042.02
		0	$^7\Sigma^-$	2.10	1205.17
		0	$^9\Sigma^-$	2.10	1223.92
B3PW91	ECP	-1	$^8\Sigma^-$	2.20	1091.05
		0	$^7\Sigma^-$	2.11	1209.37
		0	$^9\Sigma^-$	2.10	1226.82
MP2/DKH	SARC	-1	$^8\Sigma^-$	2.27	1016.80
		0	$^7\Sigma^-$	2.17	1209.72
		0	$^9\Sigma^-$	2.16	1213.89
MP2	ECP	-1	$^8\Sigma^-$	2.24	1044.32
		0	$^7\Sigma^-$	2.14	1241.14
		0	$^9\Sigma^-$	2.13	1246.56
CCSD/DKH	SARC	-1	$^8\Sigma^-$	2.22	1020.82
		0	$^7\Sigma^-$	2.12	1233.06
		0	$^9\Sigma^-$	2.11	1241.17
CCSD	ECP	-1	$^8\Sigma^-$	2.23	1047.28
		0	$^7\Sigma^-$	2.12	1259.34
		0	$^9\Sigma^-$	2.11	1259.34
CCSD(T)/DKH	SARC	-1	$^8\Sigma^-$	2.28	993.11
		0	$^7\Sigma^-$	2.17	1190.02
		0	$^9\Sigma^-$	2.17	1138.60
CCSD(T)	ECP	-1	$^8\Sigma^-$	2.26	1011.98
		0	$^7\Sigma^-$	2.15	1213.19
		0	$^9\Sigma^-$	2.15	1219.91

Table C.15: Calculated bond lengths and vibrational frequencies of the low-lying states of EuH anions and neutrals

Method	Basis Set	Charge	Electronic State	Relative Energy
HF/DKH	SARC	0	$^8\Sigma^-$	0.37
		-1	$^7\Sigma^-$	0.0
		-1	$^9\Sigma^-$	-.0.8
HF	ECP	0	$^8\Sigma^-$	0.17
		-1	$^7\Sigma^-$	0.0
		-1	$^9\Sigma^-$	0.82
B3PW91/DKH	SARC	0	$^8\Sigma^-$	0.62
		-1	$^7\Sigma^-$	0.0
		-1	$^9\Sigma^-$	0.05
B3PW91	ECP	0	$^8\Sigma^-$	0.45
		-1	$^7\Sigma^-$	0.0
		-1	$^9\Sigma^-$	0.05
MP2/DKH	SARC	0	$^8\Sigma^-$	0.36
		-1	$^7\Sigma^-$	0.0
		-1	$^9\Sigma^-$	-0.12
MP2	ECP	0	$^8\Sigma^-$	0.78
		-1	$^7\Sigma^-$	0.0
		-1	$^9\Sigma^-$	-0.68
CCSD/DKH	SARC	0	$^8\Sigma^-$	1.18
		-1	$^7\Sigma^-$	0.0
		-1	$^9\Sigma^-$	0.84
CCSD	ECP	0	$^8\Sigma^-$	0.66
		-1	$^7\Sigma^-$	0.0
		-1	$^9\Sigma^-$	0.24
CCSD(T)/DKH	SARC	0	$^8\Sigma^-$	1.13
		-1	$^7\Sigma^-$	0.0
		-1	$^9\Sigma^-$	-0.11
CCSD(T)	ECP	0	$^8\Sigma^-$	0.63
		-1	$^7\Sigma^-$	0.0
		-1	$^9\Sigma^-$	0.23

Table C.16: Relative energies of the low-lying states of EuO anions and neutrals calculated using different model chemistries

Method	Basis Set	Charge	Electronic State	Eu−O Bond length	Vibrational Frequency
HF/DKH	SARC	0	$^8\Sigma^-$	1.90	715.92
		-1	$^7\Sigma^-$	1.97	638.08
		-1	$^9\Sigma^-$	1.97	633.51
HF	ECP	0	$^8\Sigma^-$	1.79	867.77
		-1	$^7\Sigma^-$	1.83	807.47
		-1	$^9\Sigma^-$	1.97	630.92
B3PW91/DKH	SARC	0	$^8\Sigma^-$	1.86	711.64
		-1	$^7\Sigma^-$	1.89	651.29
		-1	$^9\Sigma^-$	1.93	631.48
B3PW91	ECP	0	$^8\Sigma^-$	1.87	697.72
		-1	$^7\Sigma^-$	1.90	632.99
		-1	$^9\Sigma^-$	1.94	637.06
MP2/DKH	SARC	0	$^8\Sigma^-$	1.88	725.07
		-1	$^7\Sigma^-$	1.94	650.75
		-1	$^9\Sigma^-$	1.94	656.21
MP2	ECP	0	$^8\Sigma^-$	1.79	862.48
		-1	$^7\Sigma^-$	1.83	794.82
		-1	$^9\Sigma^-$	1.94	663.34
CCSD/DKH	SARC	0	$^8\Sigma^-$	1.81	843.69
		-1	$^7\Sigma^-$	1.84	786.06
		-1	$^9\Sigma^-$	1.94	636.04
CCSD	ECP	0	$^8\Sigma^-$	1.85	615.01
		-1	$^7\Sigma^-$	1.83	786.29
		-1	$^9\Sigma^-$	1.95	635.02
CCSD(T)/DKH	SARC	0	$^8\Sigma^-$	2.11	1485.04
		-1	$^7\Sigma^-$	1.95	637.84
		-1	$^9\Sigma^-$	1.95	613.45
CCSD(T)	ECP	0	$^8\Sigma^-$	1.91	797.21
		-1	$^7\Sigma^-$	1.83	789.62
		-1	$^9\Sigma^-$	1.96	633.47

Table C.17: Calculated bond lengths and vibrational frequencies of the low-lying states of EuO anions and neutrals

Method	Basis Set	Charge	Electronic State	Relative Energy
HF/DKH	SARC	-1	$^8\Sigma^-$	0.0
		0	$^7\Sigma^-$	0.23
		0	$^9\Sigma^-$	0.08
HF	ECP	-1	$^8\Sigma^-$	0.0
		0	$^7\Sigma^-$	1.31
		0	$^9\Sigma^-$	-0.16
B3PW91/DKH	SARC	-1	$^8\Sigma^-$	0.0
		0	$^7\Sigma^-$	0.81
		0	$^9\Sigma^-$	0.56
B3PW91	ECP	-1	$^8\Sigma^-$	0.0
		0	$^7\Sigma^-$	0.74
		0	$^9\Sigma^-$	0.52
MP2/DKH	SARC	-1	$^8\Sigma^-$	0.0
		0	$^7\Sigma^-$	0.69
		0	$^9\Sigma^-$	0.49
MP2	ECP	-1	$^8\Sigma^-$	0.0
		0	$^7\Sigma^-$	1.61
		0	$^9\Sigma^-$	0.34
CCSD/DKH	SARC	-1	$^8\Sigma^-$	0.0
		0	$^7\Sigma^-$	0.77
		0	$^9\Sigma^-$	0.60
CCSD	ECP	-1	$^8\Sigma^-$	0.0
		0	$^7\Sigma^-$	0.48
		0	$^9\Sigma^-$	0.39
CCSD(T)/DKH	SARC	-1	$^8\Sigma^-$	0.0
		0	$^7\Sigma^-$	**n/a**
		0	$^9\Sigma^-$	**n/a**
CCSD(T)	ECP	-1	$^8\Sigma^-$	0.0
		0	$^7\Sigma^-$	0.62
		0	$^9\Sigma^-$	0.46

Table C.18: Relative energies of the low-lying states of EuOH anions and neutrals calculated using different model chemistries

Method	Basis Set	Charge	Electronic State	Eu−OH	EuO−H	Eu−O−H	Vibrational Frequencies Eu−O−H Bend	Eu−OH Stretch	EuO−H stretch
HF/DKH	SARC	-1	$^8\Sigma^-$	2.20	0.93	179.9	396	456	4251
		0	$^7\Sigma^-$	2.15	0.94	179.9	386	513	4247
		0	$^9\Sigma^-$	2.15	0.94	179.9	385	511	4248
HF	ECP	-1	$^8\Sigma^-$	2.20	0.93	180.0	246	449	4255
		0	$^7\Sigma^-$	2.10	0.94	179.4	288	619	4255
		0	$^9\Sigma^-$	2.15	0.94	180.0	381	511	4253
B3PW91/DKH	SARC	-1	$^8\Sigma^-$	2.14	0.96	179.9	214	466	3921
		0	$^7\Sigma^-$	2.08	0.95	179.9	322	536	3933
		0	$^9\Sigma^-$	2.09	0.95	179.9	323	536	3934
B3PW91	ECP	-1	$^8\Sigma^-$	2.15	0.95	180	194	463	3933
		0	$^7\Sigma^-$	2.09	0.95	180	334	532	3937
		0	$^9\Sigma^-$	2.09	0.95	180	334	531	3938
MP2/DKH	SARC	-1	$^8\Sigma^-$	2.14	0.96	180	298	476	3930
		0	$^7\Sigma^-$	2.09	0.96	179.5	397	540	3938
		0	$^9\Sigma^-$	2.09	0.96	178.7	393	541	3943
MP2	ECP	-1	$^8\Sigma^-$	2.15	0.96	180	255	463	3931
		0	$^7\Sigma^-$	1.94	0.96	180	403	732	3949
		0	$^9\Sigma^-$	2.09	0.96	180	381	541	3937
CCSD/DKH	SARC	-1	$^8\Sigma^-$	2.15	0.95	180	297	468	3994
		0	$^7\Sigma^-$	2.10	0.95	179.2	397	538	4005
		0	$^9\Sigma^-$	2.10	0.95	179.8	400	538	4006
CCSD	ECP	-1	$^8\Sigma^-$	2.17	0.95	180	257	458	3995
		0	$^7\Sigma^-$	2.12	0.95	180	400	522	4003
		0	$^9\Sigma^-$	2.10	0.95	180	383	535	4008
CCSD(T)/DKH	SARC	-1	$^8\Sigma^-$	**n/a**					
		0	$^7\Sigma^-$	**n/a**					
		0	$^9\Sigma^-$	**n/a**					
CCSD(T)	ECP	-1	$^8\Sigma^-$	2.16	0.95	180.0	252	458	3938
		0	$^7\Sigma^-$	2.10	0.95	180	376	538	3955
		0	$^9\Sigma^-$	2.10	0.95	180.0	377	538	3959

Table C.19: Calculated bond lengths and vibrational frequencies of the low-lying states of EuOH anions and neutrals

Species	EA (eV)	$T_o(eV)$	Vibrational Frequency (cm^{-1})	$r_{anion} - r_{neutral}(\mathring{A})$
EuH	0.771(9)	0.183(15)	1189.4	0.15(2)
EuO	$0.57 + \epsilon$	ϵ	667.8	–
EuOH	0.700(10)	0.160(13)	–	0.10(2)

Table C.20: Experimental Values, retrieved from J. Chem. Phys. 143, 034305 (2015)

C.4 A Density Functional Theory Investigation of the Mechanism of Water Reactivity with Ce_2O^-

Energy Profile calculated at zero Kelvin
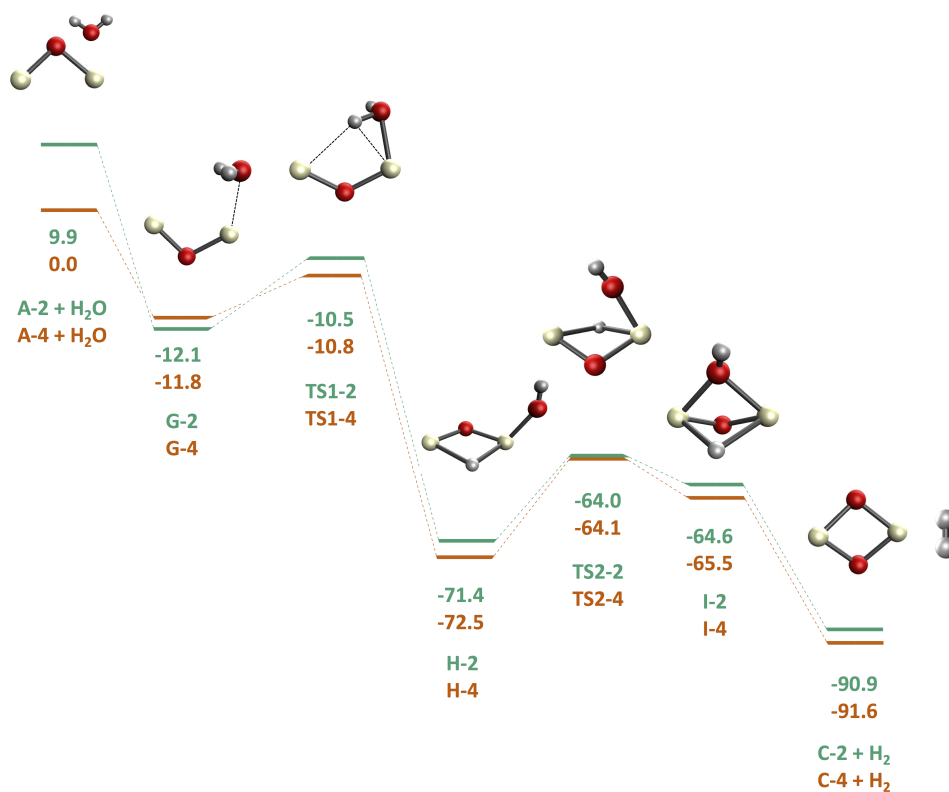
Figure C.1: Energy profile for the proposed $Ce_2O^- + H_2O \longrightarrow Ce_2O_2^- + H_2$ quartet (orange) and doublet (green) mechanisms calculated at 0K, energies given in units of kcal/mol

IRC plots corresponding to transition structures
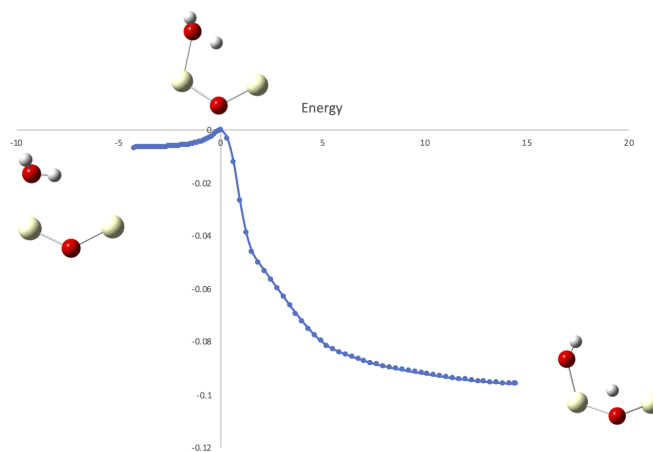
Figure C.2: TS1-2 IRC Plot
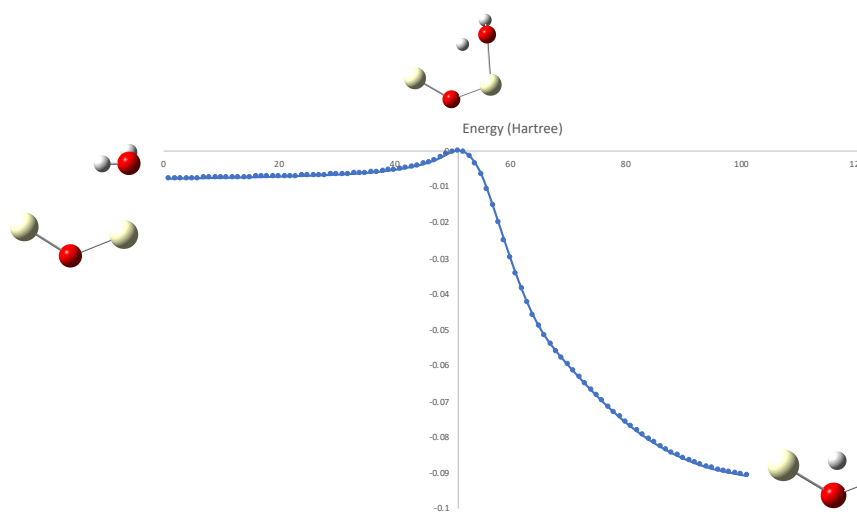
Figure C.3: TS1-4 IRC Plot
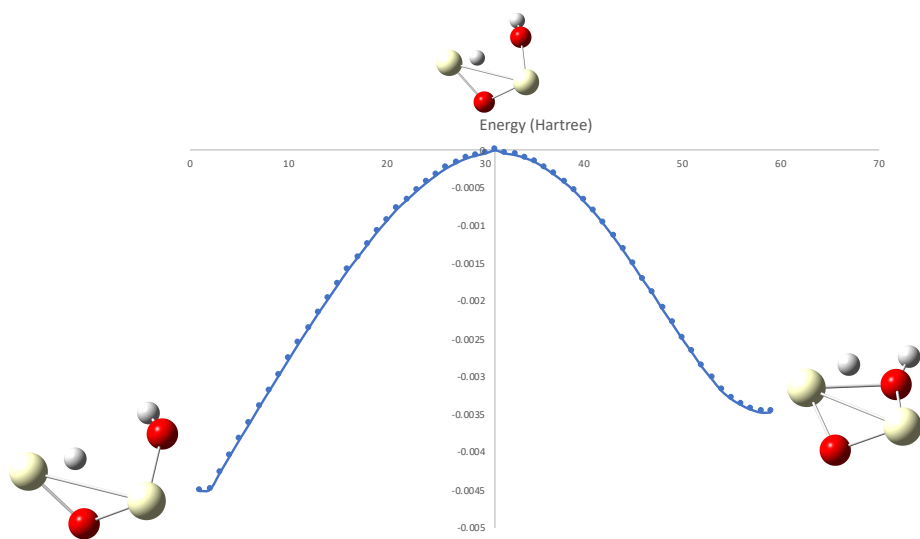
Figure C.4: TS2-2 IRC Plot
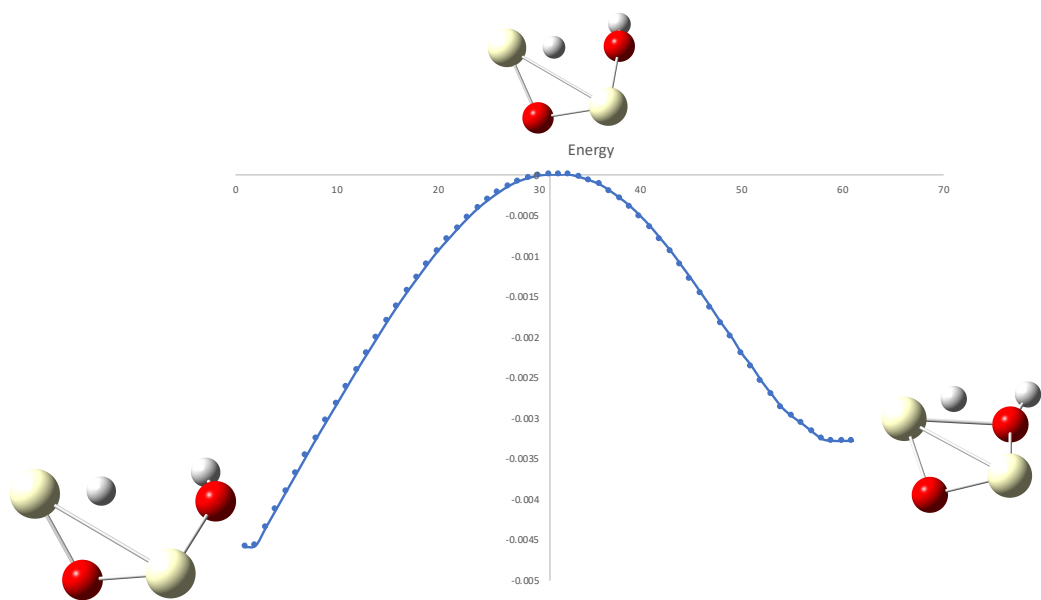
Figure C.5: TS2-4 IRC Plot

149

Bibliography

[1] R. P. Feynman, R. B. Leighton, M. Sands, The feynman lectures on physics; vol. i, American Journal of Physics 33 (9) (1965) 750–752.

[2] W. Heisenberg, Über den anschaulichen inhalt der quantentheoretischen kinematik und mechanik, in: Original Scientific Papers Wissenschaftliche Originalarbeiten, Springer, 1985, pp. 478–504.

[3] E. Schrödinger, An undulatory theory of the mechanics of atoms and molecules, Physical review 28 (6) (1926) 1049.

[4] E. Schrödinger, Quantisierung als eigenwertproblem, Annalen der physik 385 (13) (1926) 437–490.

[5] M. Born, R. Oppenheimer, Zur quantentheorie der molekeln, Annalen der physik 389 (20) (1927) 457–484.

[6] D. R. Hartree, The wave mechanics of an atom with a non-coulomb central field. part i. theory and methods, in: Mathematical Proceedings of the Cambridge Philosophical Society, Vol. 24, Cambridge University Press, 1928, pp. 89–110.

[7] D. R. Hartree, The wave mechanics of an atom with a non-coulomb central field. part ii. some results and discussion, in: Mathematical Proceedings of the Cambridge Philosophical Society, Vol. 24, Cambridge University Press, 1928, pp. 111–132.

[8] J. C. Slater, The self consistent field and the structure of atoms, Physical Review 32 (3) (1928) 339.

[9] J. C. Slater, Note on hartree's method, Physical Review 35 (2) (1930) 210.

[10] V. Fock, Näherungsmethode zur lösung des quantenmechanischen mehrkörperproblems, Zeitschrift für Physik 61 (1-2) (1930) 126–148.

[11] D. R. Hartree, W. Hartree, Self-consistent field, with exchange, for beryllium, Proceedings of the Royal Society of London. Series A-Mathematical and Physical Sciences 150 (869) (1935) 9–33.

[12] D. R. Hartree, W. Hartree, Self-consistent field, with exchange, for beryllium-ii—the (2 s)(2 p) 3p and 1p excited states, Proceedings of the Royal Society of London. Series A-Mathematical and Physical Sciences 154 (883) (1936) 588–607.

[13] J. Pople, R. Nesbet, Self-consistent orbitals for radicals, The Journal of Chemical Physics 22 (3) (1954) 571–572.

[14] P.-O. Löwdin, Quantum theory of many-particle systems. iii. extension of the hartree-fock scheme to include degenerate systems and correlation effects, Physical review 97 (6) (1955) 1509.

[15] W. Kohn, L. J. Sham, Self-consistent equations including exchange and correlation effects, Physical review 140 (4A) (1965) A1133.

[16] K. Burke, L. Wagner, Abc of ground-state dft, University Lecture (2014).

[17] K. Burke, et al., The abc of dft, Department of Chemistry, University of California (2007) 40.

[18] A. Pribram-Jones, D. A. Gross, K. Burke, Dft: A theory full of holes?, Annual review of physical chemistry 66 (2015) 283–304.

[19] J. A. Pople, Nobel lecture: Quantum chemical models, Reviews of Modern Physics 71 (5) (1999) 1267.

[20] Y. B. Band, Y. Avishai, Quantum mechanics with applications to nanotechnology and information science, Academic Press, 2013.

[21] W. Koch, M. C. Holthausen, A chemist's guide to density functional theory, John Wiley & Sons, 2015.

[22] J. P. Perdew, K. Schmidt, Jacob's ladder of density functional approximations for the exchange-correlation energy, in: AIP Conference Proceedings, Vol. 577, American Institute of Physics, 2001, pp. 1–20.

[23] W. Kohn, L. J. Sham, Self-consistent equations including exchange and correlation effects, Physical review 140 (4A) (1965) A1133.

[24] J. P. Perdew, J. A. Chevary, S. H. Vosko, K. A. Jackson, M. R. Pederson, D. J. Singh, C. Fiolhais, Atoms, molecules, solids, and surfaces: Applications of the generalized gradient approximation for exchange and correlation, Physical Review B 46 (11) (1992) 6671.

[25] D. C. Langreth, M. Mehl, Beyond the local-density approximation in calculations of ground-state electronic properties, Physical Review B 28 (4) (1983) 1809.

[26] A. D. Becke, Density-functional thermochemistry. iv. a new dynamical correlation functional and implications for exact-exchange mixing, The Journal of chemical physics 104 (3) (1996) 1040–1046.

[27] A. D. Becke, Density-functional thermochemistry. iii. the role of exact exchange, The Journal of chemical physics 98 (7) (1993) 5648–5652.

[28] F. Furche, Developing the random phase approximation into a practical post-kohn–sham correlation model, The Journal of Chemical Physics 129 (11) (2008) 114105.

[29] G. P. Chen, V. K. Voora, M. M. Agee, S. G. Balasubramani, F. Furche, Random-phase approximation methods, Annual Review of Physical Chemistry 68 (2017) 421–445.

[30] S. E. Waller, J. E. Mann, D. W. Rothgeb, C. C. Jarrold, Study of monbo y (y= 2–5) anion and neutral clusters using photoelectron spectroscopy and density functional theory calculations: Impact of spin contamination on single point calculations, The Journal of Physical Chemistry A 116 (39) (2012) 9639–9652.

[31] S. E. Waller, M. Ray, B. L. Yoder, C. C. Jarrold, Simple relationship between oxidation state and electron affinity in gas-phase metal–oxo complexes, The Journal of Physical Chemistry A 117 (50) (2013) 13919–13925.

[32] B. L. Yoder, J. T. Maze, K. Raghavachari, C. C. Jarrold, Structures of mo 2 o y- and mo 2 o y (y= 2, 3, and 4) studied by anion photoelectron spectroscopy and density functional theory calculations, The Journal of chemical physics 122 (9) (2005) 094313.

[33] J. E. Mann, D. W. Rothgeb, S. E. Waller, C. C. Jarrold, Study of movo y (y= 2- 5) anion and neutral clusters using anion photoelectron spectroscopy and density functional theory calculations, The Journal of Physical Chemistry A 114 (42) (2010) 11312–11321.

[34] N. J. Mayhall, D. W. Rothgeb, E. Hossain, K. Raghavachari, C. C. Jarrold, Electronic structures of mowo y- and mowo y determined by anion photoelectron spectroscopy and dft calculations, The Journal of chemical physics 130 (12) (2009) 124313.

[35] M. F. Hendrickx, V. T. Tran, On the electronic and geometric structures of feo2–/0 and the assignment of the anion photoelectron spectrum, Journal of chemical theory and computation 8 (9) (2012) 3089–3096.

[36] M. F. Hendrickx, K. R. Anam, A new proposal for the ground state of the feo- cluster in the gas phase and for the assignment of its photoelectron spectra, The Journal of Physical Chemistry A 113 (30) (2009) 8746–8753.

[37] V. T. Tran, M. F. Hendrickx, Description of the geometric and electronic structures responsible for the photoelectron spectrum of feo4-, The Journal of chemical physics 135 (9) (2011) 094505.

[38] G. Meloni, M. J. Ferguson, D. M. Neumark, Negative ion photodetachment spectroscopy of the al 3 o 2, al 3 o 3, al 4 o x, al 5 o x (x= 3–5), al 6 o 5, and al 7 o 5 clusters, Physical Chemistry Chemical Physics 5 (19) (2003) 4073–4079.

[39] J. B. Kim, M. L. Weichman, D. M. Neumark, Structural isomers of ti2o4 and zr2o4 anions identified by slow photoelectron velocity-map imaging spectroscopy, Journal of the American Chemical Society 136 (19) (2014) 7159–7168.

[40] J. B. Kim, M. L. Weichman, D. M. Neumark, High-resolution anion photoelectron spectra of tio 2-, zro 2-, and hfo 2- obtained by slow electron velocity-map imaging, Physical Chemistry Chemical Physics 15 (48) (2013) 20973–20981.

[41] G. Meloni, S. M. Sheehan, D. M. Neumark, Gallium oxide and dioxide: Investigation of the ground and low-lying electronic states via anion photoelectron spectroscopy, The Journal of chemical physics 122 (7) (2005) 074317.

[42] L. M. Thompson, H. P. Hratchian, Modeling the photoelectron spectra of monbo2– accounting for spin contamination in density functional theory, The Journal of Physical Chemistry A 119 (32) (2015) 8744–8751.

[43] T. Koopmans, Über die zuordnung von wellenfunktionen und eigenwerten zu den einzelnen elektronen eines atoms, Physica 1 (1-6) (1934) 104–113.

[44] J. P. Perdew, M. Levy, Comment on "significance of the highest occupied kohn-sham eigenvalue", Physical Review B 56 (24) (1997) 16021.

[45] U. Salzner, R. Baer, Koopmans' springs to life (2009).

[46] R. L. Martin, Natural transition orbitals, The Journal of chemical physics 118 (11) (2003) 4775–4777.

[47] M. Head-Gordon, A. M. Grana, D. Maurice, C. A. White, Analysis of electronic transitions as the difference of electron attachment and detachment densities, The Journal of Physical Chemistry 99 (39) (1995) 14261–14270.

[48] A. Michalak, M. Mitoraj, T. Ziegler, Bond orbitals from chemical valence theory, The Journal of Physical Chemistry A 112 (9) (2008) 1933–1939.

[49] R. L. Martin, E. R. Davidson, Halogen atomic and diatomic 1 s hole states, Physical Review A 16 (4) (1977) 1341.

[50] A. Amos, G. Hall, Single determinant wave functions, Proceedings of the Royal Society of London. Series A. Mathematical and Physical Sciences 263 (1315) (1961) 483–493.

[51] J. Ortiz, Brueckner orbitals, dyson orbitals, and correlation potentials, International journal of quantum chemistry 100 (6) (2004) 1131–1135.

[52] M. Dauth, M. Wiessner, V. Feyer, A. Schöll, P. Puschnig, F. Reinert, S. Kümmel, Angle resolved photoemission from organic semiconductors: orbital imaging beyond the molecular orbital interpretation, New journal of physics 16 (10) (2014) 103005.

[53] A. Perveaux, D. Lauvergnat, B. Lasorne, F. Gatti, M. A. Robb, G. Halász, A. Vibók, Attosecond electronic and nuclear quantum photodynamics of ozone: time-dependent dyson orbitals and dipole, Journal of Physics B: Atomic, Molecular and Optical Physics 47 (12) (2014) 124010.

153

[54] L. Grill, C. Joachim, Imaging and manipulating molecular orbitals, in: Workshop, Berlin, Vol. 24, Springer, 2012.

[55] C. Melania Oana, A. I. Krylov, Dyson orbitals for ionization from the ground and electronically excited states within equation-of-motion coupled-cluster formalism: Theory, implementation, and examples, The Journal of chemical physics 127 (23) (2007) 234106.

[56] P. A. Pieniazek, E. J. Sundstrom, S. E. Bradforth, A. I. Krylov, Degree of initial hole localization/delocalization in ionized water clusters, The Journal of Physical Chemistry A 113 (16) (2009) 4423–4429.

[57] C. M. Oana, A. I. Krylov, Cross sections and photoelectron angular distributions in photodetachment from negative ions using equation-of-motion coupled-cluster dyson orbitals, The Journal of chemical physics 131 (12) (2009) 124114.

[58] S. Gozem, A. O. Gunina, T. Ichino, D. L. Osborn, J. F. Stanton, A. I. Krylov, Photoelectron wave function in photoionization: Plane wave or coulomb wave?, The journal of physical chemistry letters 6 (22) (2015) 4532–4540.

[59] T.-C. Jagau, A. I. Krylov, Characterizing metastable states beyond energies and lifetimes: Dyson orbitals and transition dipole moments, The Journal of chemical physics 144 (5) (2016) 054113.

[60] K. B. Bravaya, O. Kostko, S. Dolgikh, A. Landau, M. Ahmed, A. I. Krylov, Electronic structure and spectroscopy of nucleic acid bases: ionization energies, ionization-induced structural changes, and photoelectron spectra, The Journal of Physical Chemistry A 114 (46) (2010) 12305–12317.

[61] S. Kambalapalli, J. Ortiz, Solvated succinate dianion: Structures, electron binding energies, and dyson orbitals, The Journal of Physical Chemistry A 107 (48) (2003) 10360–10369.

[62] A. Guevara-García, A. Martínez, J. Ortiz, Electron binding energies and dyson orbitals of al 5 o m-(m= 3, 4, 5) and al 5 o 5 h 2-, The Journal of chemical physics 127 (23) (2007) 234302.

[63] V. V. Zakjevskii, S. J. King, O. Dolgounitcheva, V. G. Zakrzewski, J. V. Ortiz, Base and phosphate electron detachment energies of deoxyribonucleotide anions, Journal of the American Chemical Society 128 (41) (2006) 13350–13351.

[64] O. Dolgounitcheva, V. Zakrzewski, J. Ortiz, Electron propagator calculations show that alkyl substituents alter porphyrin ionization energies, Journal of the American Chemical Society 127 (23) (2005) 8240–8241.

[65] O. Dolgounitcheva, V. Zakrzewski, J. Ortiz, Ab initio electron propagator calculations on the ionization energies of free base porphine, magnesium porphyrin, and zinc porphyrin, The Journal of Physical Chemistry A 109 (50) (2005) 11596–11601.

[66] S. Canuto, K. Coutinho, B. J. Cabral, V. Zakrzewski, J. Ortiz, Delocalized water and fluoride contributions to dyson orbitals for electron detachment from the hydrated fluoride anion, The Journal of chemical physics 132 (21) (2010) 214507.

[67] O. Dolgounitcheva, V. Zakrzewski, J. Ortiz, Ionization energies and dyson orbitals of thymine and other methylated uracils, The Journal of Physical Chemistry A 106 (36) (2002) 8411–8416.

[68] J. J. Neville, Y. Zheng, C. Brion, Glycine valence orbital electron densities: Comparison of electron momentum spectroscopy experiments with hartree- fock and density functional theories, Journal of the American Chemical Society 118 (43) (1996) 10533–10544.

[69] O. Alwan, O. Chuluunbaatar, X. Assfeld, A. Naja, B. Joulakian, (e, 2e) simple ionization of co2 by fast electron impact: use of three-center parameterized continuum wave function and dyson orbitals, Journal of Physics B: Atomic, Molecular and Optical Physics 47 (22) (2014) 225201.

[70] C. Brion, Looking at orbitals in the laboratory: the experimental investigation of molecular wavefunctions and binding energies by electron momentum spectroscopy, International journal of quantum chemistry 29 (5) (1986) 1397–1428.

[71] Y. Miao, J. Li, J. Deng, C. Ning, High resolution (e, 2e) spectroscopy of dimethyl ether, Journal of Electron Spectroscopy and Related Phenomena 193 (2014) 1–5.

[72] Y. Miao, C. Ning, J. Deng, Calculation of dyson orbitals using a symmetry-adapted-cluster configuration-interaction method for electron momentum spectroscopy: N 2 and h 2 o, Physical Review A 83 (6) (2011) 062706.

[73] F. Morini, B. Hajgató, M. S. Deleuze, Electron momentum spectroscopy of norbornadiene at the benchmark adc (3) level, The Journal of Physical Chemistry A 114 (34) (2010) 9374–9387.

[74] F. Morini, S. Knippenberg, M. Deleuze, B. Hajgató, Quantum chemical study of conformational fingerprints in the photoelectron spectra and (e, 2e) electron momentum distributions of n-hexane, The Journal of Physical Chemistry A 114 (12) (2010) 4400–4417.

[75] B. Hajgató, M. S. Deleuze, F. Morini, Probing nuclear dynamics in momentum space: A new interpretation of (e, 2e) electron impact ionization experiments on ethanol, The Journal of Physical Chemistry A 113 (25) (2009) 7138–7154.

[76] F. Morini, B. Hajgató, M. S. Deleuze, C. G. Ning, J. K. Deng, Benchmark dyson orbital study of the ionization spectrum and electron momentum distributions of ethanol in conformational equilibrium, The Journal of Physical Chemistry A 112 (38) (2008) 9083–9096.

[77] J. L. Mason, H. Harb, J. E. Topolski, H. P. Hratchian, C. C. Jarrold, Exceptionally complex electronic structures of lanthanide oxides and small molecules, Accounts of chemical research 52 (11) (2019) 3265–3273.

[78] E. van der Kolk, P. Dorenbos, Systematic and material independent variation of electrical, optical, and chemical properties of ln materials over the ln series (ln = la, ce, pr, ..., lu), Chemistry of Materials 18 (15) (2006) 3458–3462. arXiv:https://doi.org/10.1021/cm060775s, doi:10.1021/cm060775s.
URL https://doi.org/10.1021/cm060775s

[79] C. T. Campbell, C. H. Peden, Oxygen vacancies and catalysis on ceria surfaces, Science 309 (5735) (2005) 713–714.

[80] R. J. Gorte, Ceria in catalysis: From automotive applications to the water–gas shift reaction, AIChE journal 56 (5) (2010) 1126–1135.

[81] L. Saraf, C. M. Wang, V. Shutthanandan, Y. Zhang, O. Marina, D. R. Baer, S. Thevuthasan, P. Nachimuthu, D. W. Lindle, Oxygen transport studies in nanocrystalline ceria films, Journal of materials research 20 (5) (2005) 1295–1299.

[82] T. Montini, M. Melchionna, M. Monai, P. Fornasiero, Fundamentals and catalytic applications of ceo2-based materials, Chemical reviews 116 (10) (2016) 5987–6041.

[83] H. Yao, Y. Y. Yao, Ceria in automotive exhaust catalysts: I. oxygen storage, Journal of catalysis 86 (2) (1984) 254–265.

[84] A. Anshits, E. Voskresenskaya, L. Kurteeva, Role of defect structure of active oxides in oxidative coupling of methane, Catalysis Letters 6 (1) (1990) 67–75.

[85] M. Neurock, Molecular heterogeneous catalysis: a conceptual and computational approach, John Wiley & Sons, 2009.

[86] U. S. Ozkan, R. B. Watson, The structure–function relationships in selective oxidation reactions over metal oxides, Catalysis today 100 (1) (2005) 101–114.

[87] S. Biswas, J. Husek, S. Londo, L. R. Baker, Highly localized charge transfer excitons in metal oxide semiconductors, Nano letters 18 (2) (2018) 1228–1233.

[88] S. M. Lang, T. M. Bernhardt, Gas phase metal cluster model systems for heterogeneous catalysis, Physical Chemistry Chemical Physics 14 (26) (2012) 9255–9269.

[89] J. E. Mann, N. J. Mayhall, C. C. Jarrold, Properties of metal oxide clusters in non-traditional oxidation states, Chemical Physics Letters 525 (2012) 1–12.

[90] Y. Suchorski, R. Wrobel, S. Becker, H. Weiss, Co oxidation on a ceo x/pt (111) inverse model catalyst surface: catalytic promotion and tuning of kinetic phase diagrams, The Journal of Physical Chemistry C 112 (50) (2008) 20012–20017.

[91] F. Yang, J. Graciani, J. Evans, P. Liu, J. Hrbek, J. F. Sanz, J. A. Rodriguez, Co oxidation on inverse ceo x/cu (111) catalysts: High catalytic activity and ceria-promoted dissociation of o2, Journal of the American Chemical Society 133 (10) (2011) 3444–3451.

[92] S. D. Senanayake, P. J. Ramírez, I. Waluyo, S. Kundu, K. Mudiyanselage, Z. Liu, Z. Liu, S. Axnanda, D. J. Stacchiola, J. Evans, et al., Hydrogenation of co2 to methanol on ceo x/cu (111) and zno/cu (111) catalysts: Role of the metal–oxide interface and importance of ce3+ sites, The Journal of Physical Chemistry C 120 (3) (2016) 1778–1784.

[93] Z. Liu, D. C. Grinter, P. G. Lustemberg, T.-D. Nguyen-Phan, Y. Zhou, S. Luo, I. Waluyo, E. J. Crumlin, D. J. Stacchiola, J. Zhou, et al., Dry reforming of methane on a highly-active ni-ceo2 catalyst: Effects of metal-support interactions on c- h bond breaking, Angewandte Chemie International Edition 55 (26) (2016) 7455–7459.

[94] P. G. Lustemberg, P. J. Ramírez, Z. Liu, R. A. Gutierrez, D. G. Grinter, J. Carrasco, S. D. Senanayake, J. A. Rodriguez, M. V. Ganduglia-Pirovano, Room-temperature activation of methane and dry re-forming with co2 on ni-ceo2 (111) surfaces: effect of ce3+ sites and metal–support interactions on c–h bond cleavage, ACS Catalysis 6 (12) (2016) 8184–8191.

[95] J. A. Rodriguez, D. C. Grinter, Z. Liu, R. M. Palomino, S. D. Senanayake, Ceria-based model catalysts: fundamental studies on the importance of the metal–ceria interface in co oxidation, the water–gas shift, co 2 hydrogenation, and methane and alcohol reforming, Chemical Society Reviews 46 (7) (2017) 1824–1841.

[96] R. W. Field, Diatomic molecule electronic structure beyond simple molecular constants, Berichte der Bunsengesellschaft für physikalische Chemie 86 (9) (1982) 771–779. arXiv:https://onlinelibrary.wiley.com/doi/pdf/10.1002/bbpc.19820860903, doi:10.1002/bbpc.19820860903.
URL https://onlinelibrary.wiley.com/doi/abs/10.1002/bbpc.19820860903

[97] L. A. Kaledin, J. McCord, M. C. Heaven, Laser spectroscopy of ceo: Characterization and assignment of states in the 0-3 ev range, Journal of Molecular Spectroscopy 158 (1) (1993) 40–61.

[98] L. A. Kaledin, J. E. McCord, M. C. Heaven, Rotation-electronic deperturbation analysis of the 4f 6s configurational states of ceo, Journal of Molecular Spectroscopy 170 (1) (1995) 166–171.

[99] C. Linton, J. Chen, T. C. Steimle, Permanent electric dipole moment of cerium monoxide, The Journal of Physical Chemistry A 113 (47) (2009) 13379–13382.

[100] C. Linton, M. Dulick, R. Field, P. Carette, P. Leyland, R. Barrow, Electronic states of the ceo molecule: Absorption, emission, and laser spectroscopy, Journal of Molecular Spectroscopy 102 (2) (1983) 441–497.

[101] M. Dolg, H. Stole, H. Preuss, The low-lying electronic states of cerium monoxide ceo: ab initio calculations using energy-adjusted pseudopotentials and spin-orbit operators, Journal of Molecular Structure: THEOCHEM 231 (1991) 243–255.

[102] T. K. Todorova, I. Infante, L. Gagliardi, J. M. Dyke, The chemiionization reactions ce+ o and ce+ o2: Assignment of the observed chemielectron bands, International Journal of Quantum Chemistry 109 (10) (2009) 2068–2079.

[103] J. E. Topolski, J. O. Kafader, C. C. Jarrold, Ce in the +4 oxidation state: Anion photoelectron spectroscopy and photodissociation of small ce x o y h z- molecules, The Journal of chemical physics 147 (10) (2017) 104303.

[104] Q. Zhang, S.-X. Hu, H. Qu, J. Su, G. Wang, J.-B. Lu, M. Chen, M. Zhou, J. Li, Pentavalent lanthanide compounds: formation and characterization of praseodymium (v) oxides, Angewandte Chemie International Edition 55 (24) (2016) 6896–6900.

[105] S.-X. Hu, J. Jian, J. Su, X. Wu, J. Li, M. Zhou, Pentavalent lanthanide nitride-oxides: Npro and npro- complexes with n [triple bond, length as m-dash] pr triple bonds, Chemical science 8 (5) (2017) 4035–4043.

[106] J. Felton, M. Ray, C. C. Jarrold, Measurement of the electron affinity of atomic ce, Physical Review A 89 (3) (2014) 033407.

[107] S. M. O'Malley, D. R. Beck, Calculation of ce- binding energies by analysis of photodetachment partial cross sections, Physical Review A 74 (4) (2006) 042509.

[108] S. M. O'Malley, D. R. Beck, Calculations of nd- binding energies and photodetachment partial cross sections, Physical Review A 77 (1) (2008) 012505.

[109] J. Franck, E. Dymond, Elementary processes of photochemical reactions, Transactions of the Faraday Society 21 (February) (1926) 536–542.

[110] E. Condon, A theory of intensity distribution in band systems, Physical Review 28 (6) (1926) 1182.

[111] E. U. Condon, Nuclear motions associated with electron transitions in diatomic molecules, Physical Review 32 (6) (1928) 858.

[112] L. M. Thompson, C. C. Jarrold, H. P. Hratchian, Explaining the movo 4- photoelectron spectrum: Rationalization of geometric and electronic structure, The Journal of chemical physics 146 (10) (2017) 104301.

[113] A. N. Alexandrova, A. I. Boldyrev, H.-J. Zhai, L.-S. Wang, Photoelectron spectroscopy and ab initio study of the doubly antiaromatic b 6 2- dianion in the lib 6- cluster, The Journal of chemical physics 122 (5) (2005) 054313.

[114] J. O. Kafader, M. Ray, C. C. Jarrold, Low-lying electronic structure of euh, euoh, and euo neutrals and anions determined by anion photoelectron spectroscopy and dft calculations, The Journal of chemical physics 143 (3) (2015) 034305.

[115] J. Topolski, J. Kafader, M. Ray, C. Jarrold, Elucidating cerium+ h 2 o reactivity through electronic structure: A combined pes and dft study, Journal of Molecular Spectroscopy 336 (2017) 1–11.

[116] J. A. Felton, M. Ray, S. E. Waller, J. O. Kafader, C. C. Jarrold, Cexoy-(x= 2-3)+ d2o reactions: Stoichiometric cluster formation from deuteroxide decomposition and anti-arrhenius behavior, Journal of Physical Chemistry A 118 (43) (2014) 9960–9969.

[117] L. M. Thompson, H. Harb, H. P. Hratchian, Natural ionization orbitals for interpreting electron detachment processes, The Journal of chemical physics 144 (20) (2016) 204117.

158

[118] H. Harb, H. P. Hratchian, δscf dyson orbitals and pole strengths from natural ionization orbitals, The Journal of Chemical Physics 154 (8) (2021) 084104.

[119] H. Timmers, X. Zhu, Z. Li, Y. Kobayashi, M. Sabbar, M. Hollstein, M. Reduzzi, T. J. Martínez, D. M. Neumark, S. R. Leone, Disentangling conical intersection and coherent molecular dynamics in methyl bromide with attosecond transient absorption spectroscopy 10 (1) (2019) 1–8.

[120] M. L. Weichman, D. M. Neumark, Slow photoelectron velocity-map imaging of cryogenically cooled anions 69 (2018) 101–124.

[121] M. C. Heaven, K. A. Peterson, Probing actinide bonds in the gas phase: Theory and spectroscopy (2018) 1.

[122] M. C. Heaven, Spectroscopy and dynamics of open-shell van der waals molecules 43 (1) (1992) 283–310.

[123] W. H. Robertson, M. A. Johnson, Molecular aspects of halide ion hydration: The cluster approach 54 (1) (2003) 173–213.

[124] B. C. Garrett, D. A. Dixon, D. M. Camaioni, D. M. Chipman, M. A. Johnson, C. D. Jonah, G. A. Kimmel, J. H. Miller, T. N. Rescigno, P. J. Rossky, et al., Role of water in electron-initiated processes and radical chemistry: Issues and scientific advances 105 (1) (2005) 355–390.

[125] J. A. DeVine, A. Abou Taka, M. C. Babin, M. L. Weichman, H. P. Hratchian, D. M. Neumark, High-resolution photoelectron spectroscopy of tio3h2-: Probing the tio2-+ h2o dissociative adduct, The Journal of chemical physics 148 (22) (2018) 222810.

[126] J. E. Topolski, J. O. Kafader, V. Marrero-Colon, S. S. Iyengar, H. P. Hratchian, C. C. Jarrold, Exotic electronic structures of smxce3- xoy (x= 0-3; y= 2-4) clusters and the effect of high neutral density of low-lying states on photodetachment transition intensities, The Journal of chemical physics 149 (5) (2018) 054305.

[127] J. L. Mason, H. Harb, J. E. Topolski, H. P. Hratchian, C. C. Jarrold, A tale of two stabilities: How one boron atom affects a switch in bonding motifs in ceo2b x–(x= 2, 3) complexes, The Journal of Physical Chemistry A 122 (51) (2018) 9879–9885.

[128] J. L. Mason, H. Harb, C. D. Huizenga, J. C. Ewigleben, J. E. Topolski, H. P. Hratchian, C. C. Jarrold, Electronic and molecular structures of the ceb6 monomer, The Journal of Physical Chemistry A 123 (10) (2019) 2040–2048.

[129] J. Simons, W. D. Smith, Theory of electron affinities of small molecules 58 (11) (1973) 4899–4907.

[130] J. Simons, Theoretical studies of negative molecular ions 28 (1) (1977) 15–45.

[131] J. E. Mayer, Electron correlation 100 (6) (1955) 1579.

[132] J. Simons, P. Jorgensen, Perturbative solution of equations of motion for excitation and ionization processes 64 (4) (1976) 1413–1418.

[133] J. Simons, A note on differences between operator-level and function-level equations ol motion 12 (1977) 227–229.

[134] E. Dalgaard, J. Simons, Equations-of-motion formulation of many-body perturbation theory 10 (14) (1977) 2767.

[135] J. Simons, Equations of motion (eom) methods for computing electron affinities, Encyclopedia of Computational Chemistry (2002).

[136] J. Simons, Equations of motion methods for computing electron affinities and ionization potentials, in: Theory and Applications of Computational Chemistry, Elsevier, 2005, pp. 443–464.

[137] J. Simons, Equations of motion theory for electron affinities 70 (5) (2005) 579–604.

[138] W. von Niessen, J. Schirmer, L. S. Cederbaum, Computational methods for the one-particle green's function 1 (2) (1984) 57–125.

[139] J. Schirmer, L. Cederbaum, O. Walter, New approach to the one-particle green's function for finite fermi systems 28 (3) (1983) 1237.

[140] L. Cederbaum, One-body green's function for atoms and molecules: theory and application 8 (2) (1975) 290.

[141] L. S. Cederbaum, J. Zobeley, Ultrafast charge migration by electron correlation 307 (3-4) (1999) 205–210.

[142] A. I. Krylov, The quantum chemistry of open-shell species 30 (2017) 151–224.

[143] A. I. Krylov, Equation-of-motion coupled-cluster methods for open-shell and electronically excited species: The hitchhiker's guide to fock space 59 (2008).

[144] K. Kowalski, P. Piecuch, The active-space equation-of-motion coupled-cluster methods for excited electronic states: The eomccsdt approach 113 (19) (2000) 8490–8502.

[145] K. Kowalski, P. Piecuch, The active-space equation-of-motion coupled-cluster methods for excited electronic states: Full eomccsdt 115 (2) (2001) 643–651.

[146] J. R. Gour, P. Piecuch, M. Włoch, Active-space equation-of-motion coupled-cluster methods for excited states of radicals and other open-shell systems: Ea-eomccsdt and ip-eomccsdt 123 (13) (2005) 134113.

[147] J. R. Gour, P. Piecuch, M. Włoch, Extension of the active-space equation-of-motion coupled-cluster methods to radical systems: The ea-eomccsdt and ip-eomccsdt approaches 106 (14) (2006) 2854–2874.

[148] J. R. Gour, P. Piecuch, Efficient formulation and computer implementation of the active-space electron-attached and ionized equation-of-motion coupled-cluster methods 125 (23) (2006) 234107.

[149] K. Kowalski, P. Piecuch, New type of noniterative energy corrections for excited electronic states: Extension of the method of moments of coupled-cluster equations to the equation-of-motion coupled-cluster formalism 115 (7) (2001) 2966–2978.

[150] P. Piecuch, K. Kowalski, I. S. Pimienta, M. J. Mcguire, Recent advances in electronic structure theory: Method of moments of coupled-cluster equations and renormalized coupled-cluster approaches 21 (4) (2002) 527–655.

[151] P. Piecuch, R. J. Bartlett, Eomxcc: A new coupled-cluster method for electronic excited states, in: Advances in Quantum Chemistry, Vol. 34, Elsevier, 1999, pp. 295–380.

[152] J. F. Stanton, R. J. Bartlett, The equation of motion coupled-cluster method. a systematic biorthogonal approach to molecular excitation energies, transition probabilities, and excited state properties 98 (9) (1993) 7029–7039.

[153] D. C. Comeau, R. J. Bartlett, The equation-of-motion coupled-cluster method. applications to open-and closed-shell reference states 207 (4-6) (1993) 414–423.

[154] J. V. Ortiz, Dyson-orbital concepts for description of electrons in molecules 153 (7) (2020) 070902. arXiv:https://doi.org/10.1063/5.0016472, doi:10.1063/5.0016472.
URL https://doi.org/10.1063/5.0016472

[155] M. Díaz-Tinoco, H. H. Corzo, F. Pawłowski, J. Ortiz, Do dyson orbitals resemble canonical hartree–fock orbitals? 117 (17) (2019) 2275–2283.

[156] M. Díaz-Tinoco, H. Corzo, J. Ortiz, Electron propagator methods for vertical electron detachment energies of anions: Benchmarks and case studies 14 (11) (2018) 5881–5895.

[157] H. H. Corzo, J. V. Ortiz, Electron propagator theory: Foundations and predictions, in: Advances in Quantum Chemistry, Vol. 74, Elsevier, 2017, pp. 267–298.

[158] H. H. Corzo, J. Ortiz, Electron propagators based on generalised density operators 115 (5) (2017) 545–551.

[159] O. Goscinski, P. Lindner, Natural spin-orbitals and generalized overlap amplitudes 11 (4) (1970) 1313–1317.

[160] J. Linderberg, Y. Öhrn, Propagators in quantum chemistry, John Wiley & Sons, 2004.

[161] R. L. Martin, E. R. Davidson, Halogen atomic and diatomic 1s hole states 16 (4) (1977) 1341–1346.

[162] L. Cederbaum, W. Domcke, Theoretical aspects of ionization potentials and photoelectron spectroscopy: A green's function approach 36 (1977) 205–344.

[163] J. Ortiz, Toward an exact one-electron picture of chemical bonding 35 (1999) 33–52.

[164] A. I. Krylov, From orbitals to observables and back 153 (8) (2020) 080901.

[165] J. V. Ortiz, Electron propagator theory: an approach to prediction and interpretation in quantum chemistry 3 (2) (2012) 123–142.

[166] H. F. King, R. E. Stanton, H. Kim, R. E. Wyatt, R. G. Parr, Corresponding orbitals and the nonorthogonality problem in molecular quantum mechanics 47 (6) (1967) 1936–1941.

[167] A. Szabo, N. S. Ostlund, Modern quantum chemistry: introduction to advanced electronic structure theory, Courier Corporation, 2012.

[168] P. Politzer, F. Abu-Awwad, A comparative analysis of hartree-fock and kohn-sham orbital energies 99 (2) (1998) 83–87.

[169] S. Hamel, P. Duffy, M. E. Casida, D. R. Salahub, Kohn–sham orbitals and orbital energies: fictitious constructs but good approximations all the same 123 (2-3) (2002) 345–363.

[170] J. L. Mason, H. Harb, A. Abou Taka, A. J. McMahon, C. D. Huizenga, H. H. Corzo, H. P. Hratchian, C. C. Jarrold, Photoelectron spectra of $Gd_2O_2^-$ and non-monotonic photon-energy dependent variations in populations of close-lying neutral states, ChemRxiv (2020).

[171] A. Abou Taka, M. C. Babin, X. Sheng, J. A. DeVine, D. M. Neumark, H. P. Hratchian, Unveiling the coexistence of structural isomers in the hydrolysis of ZrO_2: A combined computational and photoelectron spectroscopy study, ChemRxiv (2020).

[172] Sylvester's determinant theorem shows that $\det(\mathbf{I}_m + \mathbf{AB}) = \det(\mathbf{I}_n + \mathbf{BA})$ where $\mathbf{A}$ is dimensioned $(m \times n)$ and $\mathbf{B}$ is dimensioned $(n \times m)$.

[173] J. J. Sylvester, Xxxvii. on the relation between the minor determinants of linearly equivalent quadratic functions, The London, Edinburgh, and Dublin Philosophical Magazine and Journal of Science 1 (4) (1851) 295–305.

[174] T. Muir, W. H. Metzler, A Treatise on the Theory of Determinants, Courier Corporation, 2003.

[175] A. G. Akritas, E. K. Akritas, G. I. Malaschonok, Various proofs of sylvester's (determinant) identity, Mathematics and Computers in Simulation 42 (4-6) (1996) 585–593.

[176] M. J. Frisch, G. W. Trucks, H. B. Schlegel, G. E. Scuseria, M. A. Robb, J. R. Cheeseman, G. Scalmani, V. Barone, B. Mennucci, G. A. Petersson, H. Nakatsuji, M. Caricato, X. Li, H. P. Hratchian, A. F. Izmaylov, J. Bloino, B. Janesko, F. Lipparini, G. Zheng, J. L. Sonnenberg, W. Liang, M. Hada, M. Ehara, K. Toyota, R. Fukuda, J. Hasegawa, M. Ishida, T. Nakajima, Y. Honda, O. Kitao, H. Nakai, T. Vreven, J. A. Montgomery, Jr., J. E. Peralta, F. Ogliaro, M. Bearpark, J. J. Heyd, E. Brothers, K. N. Kudin, V. N. Staroverov, T. Keith, R. Kobayashi, J. Normand, K. Raghavachari, A. Rendell, J. C. Burant, S. S. Iyengar, J. Tomasi, M. Cossi, N. Rega, J. M. Millam, M. Klene, J. E. Knox, J. B. Cross, V. Bakken, C. Adamo, J. Jaramillo,

R. Gomperts, R. E. Stratmann, O. Yazyev, A. J. Austin, R. Cammi, C. Pomelli, J. W. Ochterski, R. L. Martin, K. Morokuma, V. G. Zakrzewski, G. A. Voth, P. Salvador, J. J. Dannenberg, S. Dapprich, P. V. Parandekar, N. J. Mayhall, A. D. Daniels, O. Farkas, J. B. Foresman, J. V. Ortiz, J. Cioslowski, D. J. Fox, gaussian Development Version, Revision I.03+, Gaussian, Inc., Wallingford CT, 2014.

[177] R. Bauernschmitt, R. Ahlrichs, Stability analysis for solutions of the closed shell kohn–sham equation, The Journal of chemical physics 104 (22) (1996) 9047–9052.

[178] R. Seeger, J. A. Pople, Self-consistent molecular orbital methods. xviii. constraints and stability in hartree–fock theory, The Journal of Chemical Physics 66 (7) (1977) 3045–3050.

[179] H. P. Hratchian, H. B. Schlegel, Finding minima, transition states, and following reaction pathways on ab initio potential energy surfaces, in: Theory and applications of computational chemistry, Elsevier, 2005, pp. 195–249.

[180] H. Harb, H. P. Hratchian, Natural ionization orbitals v1.0, Code available at: https://github.com/HratchianGroup/niorep. doi:10.5281/zenodo.4282787.

[181] J. M. Herbert, M. Head-Gordon, Calculation of electron detachment energies for water cluster anions: an appraisal of electronic structure methods, with application to $(H_2O)_{20}{}^-$ AND $(H_2O)_{24}{}^-$. 109 (23) (2005) 5217 − 5229. doi:10.1021/jp051096s.

[182] S. Li, D. A. Dixon, Benchmark Calculations on the Electron Detachment Energies of $MO_3{}^-$ and $M_2O_6{}^-$ (M = Cr, Mo, W) 111 (46) (2007) 11908–11921. doi:10.1021/jp074768i.

[183] J. Simons, One-electron electron- molecule potentials consistent with ab initio møller- plesset theory 114 (33) (2010) 8631–8643.

[184] J. Simons, Theoretical study of negative molecular ions 62 (2011) 107–128.

[185] T.-T. Chen, W.-L. Li, W.-J. Chen, J. Li, L.-S. Wang, La 3 b 14-: an inverse triple-decker lanthanide boron cluster, Chemical Communications 55 (54) (2019) 7864–7867.

[186] T.-T. Chen, W.-L. Li, H. Bai, W.-J. Chen, X.-R. Dong, J. Li, L.-S. Wang, Re© b8–and re© b9–: New members of the transition-metal-centered borometallic molecular wheel family, The Journal of Physical Chemistry A 123 (25) (2019) 5317–5324.

[187] T. Jian, X. Chen, S.-D. Li, A. I. Boldyrev, J. Li, L.-S. Wang, Probing the structures and bonding of size-selected boron and doped-boron clusters, Chemical Society Reviews 48 (13) (2019) 3550–3591.

[188] J. Czekner, L. F. Cheung, G. S. Kocheril, M. Kulichenko, A. I. Boldyrev, L.-S. Wang, High-resolution photoelectron imaging of irb3-: Observation of a π-aromatic b3+ ring coordinated to a transition metal, Angewandte Chemie International Edition 58 (26) (2019) 8877–8881.

[189] Q. Chen, T.-T. Chen, H.-R. Li, X.-Y. Zhao, W.-J. Chen, H.-J. Zhai, S.-D. Li, L.-S. Wang, B 31- and b 32-: chiral quasi-planar boron clusters, Nanoscale 11 (19) (2019) 9698–9704.

[190] W.-L. Li, T.-T. Chen, Z.-Y. Jiang, W.-J. Chen, H.-S. Hu, L.-S. Wang, J. Li, Probing the electronic structure of the cob16- drum complex: Unusual oxidation state of co- 1, Chinese Journal of Chemical Physics 32 (2) (2019) 241–247.

[191] L. F. Cheung, J. Czekner, G. S. Kocheril, L.-S. Wang, High resolution photoelectron imaging of boron-bismuth binary clusters: Bi2b n-(n= 2–4), The Journal of chemical physics 150 (6) (2019) 064304.

[192] X. Chen, T.-T. Chen, W.-L. Li, J.-B. Lu, L.-J. Zhao, T. Jian, H.-S. Hu, L.-S. Wang, J. Li, Lanthanides with unusually low oxidation states in the prb3–and prb4–boride clusters, Inorganic chemistry 58 (1) (2018) 411–418.

[193] Q. Chen, W.-L. Li, X.-Y. Zhao, H.-R. Li, L.-Y. Feng, H.-J. Zhai, S.-D. Li, L.-S. Wang, B33–and b34–: Aromatic planar boron clusters with a hexagonal vacancy, European Journal of Inorganic Chemistry 2017 (38-39) (2017) 4546–4551.

[194] W.-L. Li, X. Chen, T. Jian, T.-T. Chen, J. Li, L.-S. Wang, From planar boron clusters to borophenes and metalloborophenes, Nature Reviews Chemistry 1 (10) (2017) 0071.

[195] E. Oger, N. R. Crawford, R. Kelting, P. Weis, M. M. Kappes, R. Ahlrichs, Boron cluster cations: transition from planar to cylindrical structures, Angewandte Chemie International Edition 46 (44) (2007) 8503–8506.

[196] A. N. Alexandrova, A. I. Boldyrev, H.-J. Zhai, L.-S. Wang, All-boron aromatic clusters as potential new inorganic ligands and building blocks in chemistry, Coordination Chemistry Reviews 250 (21-22) (2006) 2811–2866.

[197] A. P. Sergeeva, I. A. Popov, Z. A. Piazza, W.-L. Li, C. Romanescu, L.-S. Wang, A. I. Boldyrev, Understanding boron through size-selected clusters: structure, chemical bonding, and fluxionality, Accounts of chemical research 47 (4) (2014) 1349–1358.

[198] L.-S. Wang, Photoelectron spectroscopy of size-selected boron clusters: from planar structures to borophenes and borospherenes, International Reviews in Physical Chemistry 35 (1) (2016) 69–142.

[199] H.-J. Zhai, L.-S. Wang, A. N. Alexandrova, A. I. Boldyrev, V. G. Zakrzewski, Photoelectron spectroscopy and ab initio study of b3-and b4-anions and their neutrals, The Journal of Physical Chemistry A 107 (44) (2003) 9319–9328.

[200] H.-J. Zhai, L.-S. Wang, A. N. Alexandrova, A. I. Boldyrev, Electronic structure and chemical bonding of b 5- and b 5 by photoelectron spectroscopy and ab initio calculations, The Journal of Chemical Physics 117 (17) (2002) 7917–7924.

[201] A. N. Alexandrova, A. I. Boldyrev, H.-J. Zhai, L.-S. Wang, E. Steiner, P. W. Fowler, Structure and bonding in b6-and b6: Planarity and antiaromaticity, The Journal of Physical Chemistry A 107 (9) (2003) 1359–1369.

[202] A. N. Alexandrova, A. I. Boldyrev, H.-J. Zhai, L.-S. Wang, Electronic structure, isomerism, and chemical bonding in b7-and b7, The Journal of Physical Chemistry A 108 (16) (2004) 3509–3517.

[203] H.-J. Zhai, A. N. Alexandrova, K. A. Birch, A. I. Boldyrev, L.-S. Wang, Hepta-and octaco-ordinate boron in molecular wheels of eight-and nine-atom boron clusters: observation and confirmation, Angewandte Chemie International Edition 42 (48) (2003) 6004–6008.

[204] A. N. Alexandrova, H.-J. Zhai, L.-S. Wang, A. I. Boldyrev, Molecular wheel b82-as a new inorganic ligand. photoelectron spectroscopy and ab initio characterization of lib8, Inorganic chemistry 43 (12) (2004) 3552–3554.

[205] L.-L. Pan, J. Li, L.-S. Wang, Low-lying isomers of the b 9- boron cluster: The planar molecular wheel versus three-dimensional structures, The Journal of chemical physics 129 (2) (2008) 024302.

[206] H.-J. Zhai, B. Kiran, J. Li, L.-S. Wang, Hydrocarbon analogues of boron clusters—planarity, aromaticity and antiaromaticity, Nature materials 2 (12) (2003) 827–833.

[207] A. P. Sergeeva, D. Y. Zubarev, H.-J. Zhai, A. I. Boldyrev, L.-S. Wang, A photoelectron spectroscopic and theoretical study of b16- and b162-: an all-boron naphthalene, Journal of the American Chemical Society 130 (23) (2008) 7244–7246.

[208] A. P. Sergeeva, B. B. Averkiev, H.-J. Zhai, A. I. Boldyrev, L.-S. Wang, All-boron analogues of aromatic hydrocarbons: B17- and b18-, The Journal of chemical physics 134 (22) (2011) 224304.

[209] W. Huang, A. P. Sergeeva, H.-J. Zhai, B. B. Averkiev, L.-S. Wang, A. I. Boldyrev, A concentric planar doubly π-aromatic b 19- cluster, Nature chemistry 2 (3) (2010) 202–206.

[210] B. Kiran, S. Bulusu, H.-J. Zhai, S. Yoo, X. C. Zeng, L.-S. Wang, Planar-to-tubular structural transition in boron clusters: B20 as the embryo of single-walled boron nanotubes, Proceedings of the National Academy of Sciences 102 (4) (2005) 961–964.

[211] X.-M. Luo, T. Jian, L.-J. Cheng, W.-L. Li, Q. Chen, R. Li, H.-J. Zhai, S.-D. Li, A. I. Boldyrev, J. Li, et al., B26-: The smallest planar boron cluster with a hexagonal vacancy and a complicated potential landscape, Chemical Physics Letters 683 (2017) 336–341.

[212] Z. A. Piazza, W.-L. Li, C. Romanescu, A. P. Sergeeva, L.-S. Wang, A. I. Boldyrev, A photoelectron spectroscopy and ab initio study of b21-: Negatively charged boron clusters continue to be planar at 21, The Journal of chemical physics 136 (10) (2012) 104310.

[213] A. P. Sergeeva, Z. A. Piazza, C. Romanescu, W.-L. Li, A. I. Boldyrev, L.-S. Wang, B22– and b23–: all-boron analogues of anthracene and phenanthrene, Journal of the American Chemical Society 134 (43) (2012) 18065–18073.

[214] I. A. Popov, Z. A. Piazza, W.-L. Li, L.-S. Wang, A. I. Boldyrev, A combined photoelectron spectroscopy and ab initio study of the quasi-planar b24- cluster, The Journal of chemical physics 139 (14) (2013) 144307.

165

[215] Z. A. Piazza, I. A. Popov, W.-L. Li, R. Pal, X. Cheng Zeng, A. I. Boldyrev, L.-S. Wang, A photoelectron spectroscopy and ab initio study of the structures and chemical bonding of the b25- cluster, The Journal of chemical physics 141 (3) (2014) 034303.

[216] W.-L. Li, R. Pal, Z. A. Piazza, X. C. Zeng, L.-S. Wang, B27-: Appearance of the smallest planar boron cluster containing a hexagonal vacancy, The Journal of chemical physics 142 (20) (2015) 204305.

[217] Y.-J. Wang, Y.-F. Zhao, W.-L. Li, T. Jian, Q. Chen, X.-R. You, T. Ou, X.-Y. Zhao, H.-J. Zhai, S.-D. Li, et al., Observation and characterization of the smallest borospherene, b28- and b28, The Journal of chemical physics 144 (6) (2016) 064307.

[218] H.-R. Li, T. Jian, W.-L. Li, C.-Q. Miao, Y.-J. Wang, Q. Chen, X.-M. Luo, K. Wang, H.-J. Zhai, S.-D. Li, et al., Competition between quasi-planar and cage-like structures in the b 29-cluster: photoelectron spectroscopy and ab initio calculations, Physical Chemistry Chemical Physics 18 (42) (2016) 29147–29155.

[219] W.-L. Li, Y.-F. Zhao, H.-S. Hu, J. Li, L.-S. Wang, [b30]-: a quasiplanar chiral boron cluster, Angewandte Chemie International Edition 53 (22) (2014) 5540–5545.

[220] W.-L. Li, Q. Chen, W.-J. Tian, H. Bai, Y.-F. Zhao, H.-S. Hu, J. Li, H.-J. Zhai, S.-D. Li, L.-S. Wang, The b35 cluster with a double-hexagonal vacancy: a new and more flexible structural motif for borophene, Journal of the American Chemical Society 136 (35) (2014) 12257–12260.

[221] Z. A. Piazza, H.-S. Hu, W.-L. Li, Y.-F. Zhao, J. Li, L.-S. Wang, Planar hexagonal b 36 as a potential basis for extended single-atom layer boron sheets, Nature communications 5 (1) (2014) 1–6.

[222] Q. Chen, W.-J. Tian, L.-Y. Feng, H.-G. Lu, Y.-W. Mu, H.-J. Zhai, S.-D. Li, L.-S. Wang, Planar b 38- and b 37- clusters with a double-hexagonal vacancy: molecular motifs for borophenes, Nanoscale 9 (13) (2017) 4550–4557.

[223] K. B. Bravaya, A. I. Krylov, On the photodetachment from the green fluorescent protein chromophore, The Journal of Physical Chemistry A 117 (46) (2013) 11815–11822.

[224] F. Santoro, R. Improta, A. Lami, J. Bloino, V. Barone, Effective method to compute franck-condon integrals for optical spectra of large molecules in solution, The Journal of chemical physics 126 (8) (2007) 084509.

[225] F. Santoro, A. Lami, R. Improta, J. Bloino, V. Barone, Effective method for the computation of optical spectra of large molecules at finite temperature including the duschinsky and herzberg–teller effect: The qx band of porphyrin as a case study, The Journal of Chemical Physics 128 (22) (2008) 224311. arXiv:https://doi.org/10.1063/1.2929846, doi:10.1063/1.2929846.
URL https://doi.org/10.1063/1.2929846

[226] F. Santoro, A. Lami, R. Improta, V. Barone, Effective method to compute vibrationally resolved optical spectra of large molecules at finite temperature in the gas phase and in solution, The Journal of Chemical Physics 126 (18) (2007) 184102. arXiv:https://doi.org/10.1063/1.2721539, doi:10.1063/1.2721539. URL https://doi.org/10.1063/1.2721539

[227] J. L. Sonnenberg, H. B. Schlegel, H. P. Hratchian, Spin contamination in inorganic chemistry calculations, Encyclopedia of Inorganic and Bioinorganic Chemistry (2011).

[228] J. M. Wittbrodt, H. B. Schlegel, Some reasons not to use spin projected density functional theory, The Journal of Chemical Physics 105 (15) (1996) 6574–6577. arXiv:https://doi.org/10.1063/1.472497, doi:10.1063/1.472497. URL https://doi.org/10.1063/1.472497

[229] H. B. Schlegel, J. McDouall, Do you have scf stability and convergence problems?, in: Computational advances in organic chemistry: Molecular structure and reactivity, Springer, 1991, pp. 167–185.

[230] A. D. Becke, Density-functional thermochemistry. ii. the effect of the perdew–wang generalized-gradient correlation correction, The Journal of chemical physics 97 (12) (1992) 9173–9177.

[231] A. D. Becke, Density-functional thermochemistry. i. the effect of the exchange-only gradient correction, The Journal of chemical physics 96 (3) (1992) 2155–2160.

[232] R. Krishnan, J. S. Binkley, R. Seeger, J. A. Pople, Self-consistent molecular orbital methods. xx. a basis set for correlated wave functions, The Journal of Chemical Physics 72 (1) (1980) 650–654. arXiv:https://doi.org/10.1063/1.438955, doi:10.1063/1.438955. URL https://doi.org/10.1063/1.438955

[233] H. P. Hratchian, H. B. Schlegel, Accurate reaction paths using a hessian based predictor–corrector integrator, J. Chem. Phys. 120 (21) (2004) 9918–9924.

[234] H. Hratchian, H. Schlegel, Using hessian updating to increase the efficiency of a hessian based predictor-corrector reaction path following method, J. Chem. Theory Comput. 1 (1) (2005) 61–69.

[235] F. Santoro, R. Improta, A. Lami, J. Bloino, V. Barone, Effective method to compute franck-condon integrals for optical spectra of large molecules in solution, The Journal of Chemical Physics 126 (8) (2007) 084509.

[236] F. Furche, R. Ahlrichs, Adiabatic time-dependent density functional methods for excited state properties, The Journal of chemical physics 117 (16) (2002) 7433–7447.

[237] R. Bauernschmitt, R. Ahlrichs, Treatment of electronic excitations within the adiabatic approximation of time dependent density functional theory, Chemical Physics Letters 256 (4-5) (1996) 454–464.

[238] P. J. Robinson, X. Zhang, T. McQueen, K. H. Bowen, A. N. Alexandrova, Smb6–cluster anion: Covalency involving f orbitals, The Journal of Physical Chemistry A 121 (8) (2017) 1849–1854.

[239] H. Trommsdorff, A. Corval, L. Von Laue, Spectral hole burning: Spontaneous and photoinduced tunneling reactions in low temperature solids, Pure and applied chemistry 67 (1) (1995) 191–198.

[240] H. Harb, L. M. Thompson, H. P. Hratchian, On the linear geometry of lanthanide hydroxide (ln-oh, ln= la–lu), Physical Chemistry Chemical Physics 21 (39) (2019) 21890–21897.

[241] A. Mustachi, Mössbauer studies of europium and ytterbium hydrides, Journal of Physics and Chemistry of Solids 35 (10) (1974) 1447–1450.

[242] H. Ott, S. Heise, R. Sutarto, Z. Hu, C. Chang, H. Hsieh, H.-J. Lin, C. Chen, L. Tjeng, Soft x-ray magnetic circular dichroism study on gd-doped euo thin films, Physical Review B 73 (9) (2006) 094407.

[243] A. Schmehl, V. Vaithyanathan, A. Herrnberger, S. Thiel, C. Richter, M. Liberati, T. Heeg, M. Röckerath, L. F. Kourkoutis, S. Mühlbauer, et al., Epitaxial integration of the highly spin-polarized ferromagnetic semiconductor euo with silicon and gan, Nature materials 6 (11) (2007) 882.

[244] A. Swartz, J. Ciraldo, J. Wong, Y. Li, W. Han, T. Lin, S. Mack, J. Shi, D. Awschalom, R. Kawakami, Epitaxial euo thin films on gaas, Applied Physics Letters 97 (11) (2010) 112509.

[245] I. Infante, L. Gagliardi, X. Wang, L. Andrews, Binding motifs for lanthanide hydrides: A combined experimental and theoretical study of the mh x (h2) y species (m= la- gd; x= 1- 4; y= 0- 6), The Journal of Physical Chemistry A 113 (11) (2009) 2446–2455.

[246] D. DiMarzio, M. Croft, N. Sakai, M. Shafer, Effect of pressure on the electrical resistance of euo, Physical Review B 35 (16) (1987) 8891.

[247] Y. Shapira, S. Foner, T. Reed, Euo. i. resistivity and hall effect in fields up to 150 koe, Physical Review B 8 (5) (1973) 2299.

[248] R. Zanowick, W. Wallace, Ferromagnetism in eu h 2, Physical Review 126 (2) (1962) 537.

[249] H. Saitoh, A. Machida, T. Matsuoka, K. Aoki, Phase diagram of the eu–h system at high temperatures and high hydrogen pressures, Solid State Communications 205 (2015) 24–27.

[250] N. M. Souza-Neto, D. Haskel, Y.-C. Tseng, G. Lapertot, Pressure-induced electronic mixing and enhancement of ferromagnetic ordering in eu x (x= te, se, s, o) magnetic semiconductors, Physical review letters 102 (5) (2009) 057206.

[251] T. J. Konno, N. Ogawa, K. Wakoh, K. Sumiyama, K. Suzuki, Synthesis and magnetic properties of non-equilibrium eu-rich euo thin films, Japanese journal of applied physics 35 (12R) (1996) 6052.

[252] J.-D. Axe, G. Burns, Influence of covalency upon rare-earth ligand field splittings, Physical Review 152 (1) (1966) 331.

[253] B. Bursten, E. Palmer, J. Sonnenberg, On the role of f-obitals in the bonding in f-element complexes: the, Special Publication-Royal Society of Chemistry 305 (1) (2006) 157–162.

[254] S. G. Minasian, E. R. Batista, C. H. Booth, D. L. Clark, J. M. Keith, S. A. Kozimor, W. W. Lukens, R. L. Martin, D. K. Shuh, S. C. E. Stieber, et al., Quantitative evidence for lanthanide-oxygen orbital mixing in ceo2, pro2, and tbo2, Journal of the American Chemical Society 139 (49) (2017) 18052–18064.

[255] L. Maron, O. Eisenstein, Do f electrons play a role in the lanthanide- ligand bonds? a dft study of ln (nr2) 3; r= h, sih3, The Journal of Physical Chemistry A 104 (30) (2000) 7140–7143.

[256] N. Barros, D. Maynau, L. Maron, O. Eisenstein, G. Zi, R. A. Andersen, Single but stronger uo, double but weaker unme bonds: the tale told by cp2uo and cp2unr, Organometallics 26 (20) (2007) 5059–5065.

[257] N. Kaltsoyannis, Does covalency increase or decrease across the actinide series? implications for minor actinide partitioning, Inorganic chemistry 52 (7) (2013) 3407–3413.

[258] M. P. Kelley, J. Su, M. Urban, M. Luckey, E. R. Batista, P. Yang, J. C. Shafer, On the origin of covalent bonding in heavy actinides, Journal of the American Chemical Society 139 (29) (2017) 9901–9908.

[259] W. W. Lukens, N. M. Edelstein, N. Magnani, T. W. Hayton, S. Fortier, L. A. Seaman, Quantifying the σ and π interactions between u (v) f orbitals and halide, alkyl, alkoxide, amide and ketimide ligands, Journal of the American Chemical Society 135 (29) (2013) 10742–10754.

[260] M. L. Neidig, D. L. Clark, R. L. Martin, Covalency in f-element complexes, Coordination Chemistry Reviews 257 (2) (2013) 394–406.

[261] J.-P. Dognon, P. Pyykkö, Chemistry of the 5g elements: relativistic calculations on hexafluorides, Angewandte Chemie 129 (34) (2017) 10266–10268.

[262] B. O. Roos, P. Pyykkö, Bonding trends in molecular compounds of lanthanides: The double-bonded carbene cations lnch2+ (ln= sc, y, la–lu), Chemistry–A European Journal 16 (1) (2010) 270–275.

[263] A. Kovács, Relativistic multireference quantum chemical study of the electronic structure of actinide trioxide molecules, The Journal of Physical Chemistry A 121 (12) (2017) 2523–2530.

[264] P. Pyykkö, Additive covalent radii for single-, double-, and triple-bonded molecules and tetrahedrally bonded crystals: a summary, The Journal of Physical Chemistry A 119 (11) (2015) 2326–2337.

[265] A. Kovács, R. J. Konings, Computed vibrational frequencies of actinide oxides ano0/+/2+ and ano20/+/2+(an= th, pa, u, np, pu, am, cm), The Journal of Physical Chemistry A 115 (24) (2011) 6646–6656.

[266] A. Kovács, R. J. Konings, Z. Varga, D. Szieberth, Structure and other molecular properties of actinide trichlorides ancl3 (an= th–cm), The Journal of Physical Chemistry A 117 (44) (2013) 11357–11363.

[267] H. P. Hratchian, J. L. Sonnenberg, P. J. Hay, R. L. Martin, B. E. Bursten, H. B. Schlegel, Theoretical investigation of uranyl dihydroxide: oxo ligand exchange, water catalysis, and vibrational spectra, The Journal of Physical Chemistry A 109 (38) (2005) 8579–8586.

[268] J. L. Sonnenberg, P. J. Hay, R. L. Martin, B. E. Bursten, Theoretical investigations of uranyl-ligand bonding: Four-and five-coordinate uranyl cyanide, isocyanide, carbonyl, and hydroxide complexes, Inorganic chemistry 44 (7) (2005) 2255–2262.

[269] P. Pogány, A. Kovács, Z. Varga, F. M. Bickelhaupt, R. J. Konings, Theoretical study of the structure and bonding in thc2 and uc2, The Journal of Physical Chemistry A 116 (1) (2012) 747–755.

[270] X. Zhang, H. Schwarz, Bonding in cationic moh n+(m= k- la, hf- rn; n= 0–2): Dft performances and periodic trends, Theoretical Chemistry Accounts 129 (3-5) (2011) 389–399.

[271] J. E. Mann, N. J. Mayhall, C. C. Jarrold, Properties of metal oxide clusters in non-traditional oxidation states, Chemical Physics Letters 525 (2012) 1–12.

[272] E. Miliordos, K. L. Hunt, First-principles calculations of the electronic and geometrical structures of neutral [sc, o, h] molecules and the monocations, scoh0,+ and hsco0,+, The Journal of Physical Chemistry A 115 (17) (2011) 4436–4447.

[273] E. Miliordos, J. F. Harrison, K. L. Hunt, Ab initio investigation of titanium hydroxide isomers and their cations, tioh0,+ and htio0,+, The Journal of chemical physics 135 (14) (2011) 144111.

[274] E. Miliordos, J. F. Harrison, K. L. Hunt, Ground and excited states of vanadium hydroxide isomers and their cations, voh0,+ and hvo0,+, The Journal of chemical physics 138 (11) (2013) 114305.

[275] E. Rezabal, F. Ruipérez, J. Ugalde, Quantum chemical study of the catalytic activation of methane by copper oxide and copper hydroxide cations, Physical Chemistry Chemical Physics 15 (4) (2013) 1148–1153.

[276] I. L. Soroka, A. Shchukarev, M. Jonsson, N. V. Tarakina, P. A. Korzhavyi, Cuprous hydroxide in a solid form: does it exist?, Dalton Transactions 42 (26) (2013) 9585–9594.

[277] Y. Li, C. M. Lousada, I. L. Soroka, P. A. Korzhavyi, Bond network topology and antiferro-electric order in cuprice cuoh, Inorganic chemistry 54 (18) (2015) 8969–8977.

[278] P. A. Korzhavyi, I. L. Soroka, E. I. Isaev, C. Lilja, B. Johansson, Exploring monovalent copper compounds with oxygen and hydrogen, Proceedings of the National Academy of Sciences 109 (3) (2012) 686–689.

[279] W. Stählin, H. R. Oswald, The crystal structure of zinc hydroxide nitrate, zn5 (oh) 8 (no3) 2.2 h2o, Acta Crystallographica Section B: Structural Crystallography and Crystal Chemistry 26 (6) (1970) 860–863.

[280] G. G. C. Arizaga, K. G. Satyanarayana, F. Wypych, Layered hydroxide salts: synthesis, properties and potential applications, Solid State Ionics 178 (15-18) (2007) 1143–1162.

[281] J. P. Perdew, Y. Wang, Accurate and simple analytic representation of the electron-gas correlation energy, Physical Review B 45 (23) (1992) 13244.

[282] D. A. Pantazis, F. Neese, All-electron scalar relativistic basis sets for the lanthanides, Journal of chemical theory and computation 5 (9) (2009) 2229–2238.

[283] D. A. Pantazis, F. Neese, All-electron scalar relativistic basis sets for the 6p elements, Theoretical Chemistry Accounts 131 (11) (2012) 1292.

[284] M. Dolg, Segmented contracted douglas–kroll–hess adapted basis sets for lanthanides, Journal of chemical theory and computation 7 (10) (2011) 3131–3142.

[285] R. A. Kendall, T. H. Dunning Jr, R. J. Harrison, Electron affinities of the first-row atoms revisited. systematic basis sets and wave functions, The Journal of chemical physics 96 (9) (1992) 6796–6806.

[286] E. Papajak, J. Zheng, X. Xu, H. R. Leverentz, D. G. Truhlar, Perspectives on basis sets beautiful: Seasonal plantings of diffuse basis functions, Journal of chemical theory and computation 7 (10) (2011) 3027–3034.

[287] T. Nakajima, K. Hirao, The douglas–kroll–hess approach, Chemical reviews 112 (1) (2012) 385–402.

[288] E. D. Glendening, C. R. Landis, F. Weinhold, Nbo 6.0: Natural bond orbital analysis program, Journal of computational chemistry 34 (16) (2013) 1429–1437.

[289] a. J. Foster, F. Weinhold, Natural hybrid orbitals, Journal of the American Chemical Society 102 (24) (1980) 7211–7218.

[290] A. E. Reed, F. Weinhold, Natural bond orbital analysis of near-hartree–fock water dimer, The Journal of chemical physics 78 (6) (1983) 4066–4073.

[291] P. Pyykkö, M. Atsumi, Molecular double-bond covalent radii for elements li–e112, Chemistry–A European Journal 15 (46) (2009) 12770–12779.

[292] P. Pyykkö, M. Atsumi, Molecular single-bond covalent radii for elements 1–118, Chemistry–A European Journal 15 (1) (2009) 186–197.

171

[293] P. Pyykkö, S. Riedel, M. Patzschke, Triple-bond covalent radii, Chemistry–A European Journal 11 (12) (2005) 3511–3520.

[294] L. Pauling, General chemistry, Courier Corporation, 1988.

[295] R. D. Shannon, Revised effective ionic radii and systematic studies of interatomic distances in halides and chalcogenides, Acta crystallographica section A: crystal physics, diffraction, theoretical and general crystallography 32 (5) (1976) 751–767.

[296] F. Weinhold, Natural bond orbital analysis: a critical overview of relationships to alternative bonding perspectives, Journal of computational chemistry 33 (30) (2012) 2363–2379.

[297] M. Ray, J. A. Felton, J. O. Kafader, J. E. Topolski, C. C. Jarrold, Photoelectron spectra of ceo- and ce (oh) 2-, The Journal of chemical physics 142 (6) (2015) 064305.

[298] L. G. M. Pettersson, R. H. Henchman, A. Nilsson, Water – the most anomalous liquid (2016).

[299] R. J. Speedy, Stability-limit conjecture. an interpretation of the properties of water, J. Phys. Chem. 86 (6) (1982) 982–991.

[300] P. H. Poole, F. Sciortino, U. Essmann, H. E. Stanley, Phase behaviour of metastable water, Nature 360 (6402) (1992) 324.

[301] H. Tanaka, Simple physical model of liquid water, J. Chem. Phys. 112 (2) (2000) 799–809.

[302] V. Holten, M. Anisimov, Entropy-driven liquid–liquid separation in supercooled water, Sci. Rep. 2 (2012) 713.

[303] J. D. Smith, C. D. Cappa, K. R. Wilson, R. C. Cohen, P. L. Geissler, R. J. Saykally, Unified description of temperature-dependent hydrogen-bond rearrangements in liquid water, Proc. Natl. Acad. Sci. 102 (40) (2005) 14171–14174.

[304] J. Liu, R. S. Andino, C. M. Miller, X. Chen, D. M. Wilkins, M. Ceriotti, D. E. Manolopoulos, A surface-specific isotope effect in mixtures of light and heavy water, J. Phys. Chem. C 117 (6) (2013) 2944–2951.

[305] G. R. Medders, V. Babin, F. Paesani, Development of a "first-principles" water potential with flexible monomers. iii. liquid phase properties, J. Chem. Theory Comput. 10 (8) (2014) 2906–2910.

[306] A. P. Bartók, M. C. Payne, R. Kondor, G. Csányi, Gaussian approximation potentials: The accuracy of quantum mechanics, without the electrons, Phys. Rev. Lett. 104 (13) (2010) 136403.

[307] M. J. Gillan, D. Alfè, A. Michaelides, Perspective: How good is dft for water?, J. Chem. Phys. 144 (13) (2016) 130901.

172

[308] P. Gallo, K. Amann-Winkel, C. A. Angell, M. A. Anisimov, F. Caupin, C. Chakravarty, E. Lascaris, T. Loerting, A. Z. Panagiotopoulos, J. Russo, et al., Water: A tale of two liquids, Chem. Rev. 116 (13) (2016) 7463–7500.

[309] B. M. Hunter, H. B. Gray, A. M. Muller, Earth-abundant heterogeneous water oxidation catalysts, Chem. Rev. 116 (22) (2016) 14120–14136.

[310] J. P. McEvoy, G. W. Brudvig, Water-splitting chemistry of photosystem ii, Chem. Rev. 106 (11) (2006) 4455–4483.

[311] M. G. Walter, E. L. Warren, J. R. McKone, S. W. Boettcher, Q. Mi, E. A. Santori, N. S. Lewis, Solar water splitting cells, Chem. Rev. 110 (11) (2010) 6446–6473.

[312] Y. Tachibana, L. Vayssieres, J. R. Durrant, Artificial photosynthesis for solar water-splitting, Nat. Photonics 6 (8) (2012) 511.

[313] D. Kang, T. W. Kim, S. R. Kubota, A. C. Cardiel, H. G. Cha, K.-S. Choi, Electrochemical synthesis of photoelectrodes and catalysts for use in solar water splitting, Chem. Rev. 115 (23) (2015) 12839–12887.

[314] J. Graciani, A. M. Márquez, J. J. Plata, Y. Ortega, N. C. Hernández, A. Meyer, C. M. Zicovich-Wilson, J. F. Sanz, Comparative study on the performance of hybrid dft functionals in highly correlated oxides: The case of CeO_2 and Ce_2O_3, J. Chem. Theory Comput. 7 (1) (2010) 56–65.

[315] X.-N. Wu, X.-L. Ding, S.-M. Bai, B. Xu, S.-G. He, Q. Shi, Experimental and theoretical study of the reactions between cerium oxide cluster anions and carbon monoxide: Size-dependent reactivity of $Ce_nO_{2n+1}^-$ (n= 1–21), J. Phys. Chem. C 115 (27) (2011) 13329–13337.

[316] T. Nagata, K. Miyajima, F. Mafuné, Gold atoms supported on gas-phase cerium oxide cluster ions: Stable stoichiometry and reactivity with co, J. Phys. Chem. A 120 (39) (2016) 7624–7633.

[317] T. Nagata, K. Miyajima, F. Mafuné, Oxidation of nitric oxide on gas-phase cerium oxide clusters via reactant adsorption and product desorption processes, J. Phys. Chem. A 119 (41) (2015) 10255–10263.

[318] Y.-X. Zhao, Q.-Y. Liu, M.-Q. Zhang, S.-G. He, Reactions of metal cluster anions with inorganic and organic molecules in the gas phase, Dalton Trans. 45 (28) (2016) 11471–11495.

[319] V. Idakiev, T. Tabakova, K. Tenchev, Z.-Y. Yuan, T.-Z. Ren, B.-L. Su, Gold nanoparticles supported on ceria-modified mesoporous titania as highly active catalysts for low-temperature water-gas shift reaction, Catal. Today 128 (3-4) (2007) 223–229.

[320] Q. Fu, H. Saltsburg, M. Flytzani-Stephanopoulos, Active nonmetallic au and pt species on ceria-based water-gas shift catalysts, Science 301 (5635) (2003) 935–938.

[321] A. Martınez-Arias, M. Fernández-Garcıa, J. Soria, J. Conesa, Spectroscopic study of a cu/CeO$_2$ catalyst subjected to redox treatments in carbon monoxide and oxygen, J. Catal. 182 (2) (1999) 367–377.

[322] H. Takamura, T. Kobayashi, T. Kasahara, A. Kamegawa, M. Okada, Oxygen permeation and methane reforming properties of ceria-based composite membranes, Journal of alloys and compounds 408 (2006) 1084–1089.

[323] M. Fernández-Garcıa, A. Martınez-Arias, L. Salamanca, J. Coronado, J. Anderson, J. Conesa, J. Soria, Influence of ceria on pd activity for the co +O$_2$ reaction, J. Catal. 187 (2) (1999) 474–485.

[324] V. Esposito, E. Traversa, Design of electroceramics for solid oxides fuel cell applications: playing with ceria, J. Am. Ceram. Soc. 91 (4) (2008) 1037–1051.

[325] E. Aneggi, M. Boaro, C. de Leitenburg, G. Dolcetti, A. Trovarelli, Insights into the redox properties of ceria-based oxides and their implications in catalysis, J. Alloys Compd. 408 (2006) 1096–1102.

[326] Y. Li, Q. Fu, M. Flytzani-Stephanopoulos, Low-temperature water-gas shift reaction over cu-and ni-loaded cerium oxide catalysts, Appl. Catal., B 27 (3) (2000) 179–191.

[327] T. Bunluesin, R. Gorte, G. Graham, Studies of the water-gas-shift reaction on ceria-supported pt, pd, and rh: implications for oxygen-storage properties, Appl. Catal., B 15 (1-2) (1998) 107–114.

[328] A. Luengnaruemitchai, S. Osuwan, E. Gulari, Comparative studies of low-temperature water–gas shift reaction over pt/CeO$_2$, au/CeO$_2$, and au/Fe$_2$O$_3$ catalysts, Catal. Commun. 4 (5) (2003) 215–221.

[329] J. O. Kafader, J. E. Topolski, C. C. Jarrold, Molecular and electronic structures of cerium and cerium suboxide clusters, The Journal of chemical physics 145 (15) (2016) 154306.

[330] O. Eisenstein, L. Maron, Dft studies of some structures and reactions of lanthanides complexes, J. Organomet. Chem. 647 (1-2) (2002) 190–197.

[331] J. O. Kafader, M. Ray, C. C. Jarrold, Photoelectron spectrum of pro-, The Journal of chemical physics 143 (6) (2015) 064305.

[332] R. Zhou, Y. Yang, S. Pande, B. Qu, D. Li, X. C. Zeng, Reaction mechanism between small-sized ce clusters and water molecules: an ab initio investigation on Ce$_n$ + H$_2$O, Phys. Chem. Chem. Phys. 21 (7) (2019) 4006–4014.

[333] R. Zhou, S. Ma, Y. Yang, D. Li, B. Qu, X. C. Zeng, Reaction mechanism between small-sized ce clusters and water molecules ii: an ab initio investigation on Ce$_n$ (n= 1–3)+ m H$_2$O (m= 2–6), Phys. Chem. Chem. Phys. 21 (17) (2019) 8945–8955.

[334] Y. Li, Y. Gong, X. Zhou, J. Su, J. Li, M. Zhou, Infrared spectroscopic and theoretical study of the reactions of cerium atoms with methanol in solid argon, J. Mol. Spectrosc. 310 (2015) 50–56.

[335] B. Xu, P. Shi, T. Huang, X. Wang, Hydrogen-bridge Si(μ–H)$_3$CeH and inserted H$_3$SiCeH molecules: Matrix infrared spectra and dft calculations for reaction products of silane with ce atoms, J. Mol. Struct. 1146 (2017) 692–702.

[336] X. Wang, L. Andrews, Z. Fang, K. S. Thanthiriwatte, M. Chen, D. A. Dixon, Properties of lanthanide hydroxide molecules produced in reactions of lanthanide atoms with H$_2$O$_2$ and H$_2$+ O$_2$ mixtures: Roles of the +i, +ii, +iii, and +iv oxidation states, J. Phys. Chem. A 121 (8) (2017) 1779–1796.

[337] Z. Fang, K. S. Thanthiriwatte, D. A. Dixon, L. Andrews, X. Wang, Properties of cerium hydroxides from matrix infrared spectra and electronic structure calculations, Inorg. Chem. 55 (4) (2016) 1702–1714.

[338] Z. Pu, W. Yu, S. K. Roy, C. Li, B. Ao, T. Liu, M. Shuai, X. Wang, Insights into the enhanced cen triple bond in the hcen molecule, Phys. Chem. Chem. Phys. 19 (12) (2017) 8216–8222.

[339] T. C. Mikulas, M. Chen, Z. Fang, K. A. Peterson, L. Andrews, D. A. Dixon, Structures and properties of the products of the reaction of lanthanide atoms with H$_2$O: Dominance of the +ii oxidation state, J. Phys. Chem. A 120 (5) (2016) 793–804.

[340] M. Ray, J. O. Kafader, J. E. Topolski, C. C. Jarrold, Mixed cerium-platinum oxides: Electronic structure of [ceo] pt n (n= 1, 2) and [ceo2] pt complex anions and neutrals, The Journal of chemical physics 145 (4) (2016) 044317.

[341] X. Cao, M. Dolg, Valence basis sets for relativistic energy-consistent small-core lanthanide pseudopotentials, The Journal of Chemical Physics 115 (16) (2001) 7348–7355.

[342] N. J. Mayhall, D. W. Rothgeb, E. Hossain, C. C. Jarrold, K. Raghavachari, Water reactivity with tungsten oxides: H$_2$ production and kinetic traps, J. Chem. Phys. 131 (14) (2009) 144302.

[343] N. J. Mayhall, K. Raghavachari, Two methanes are better than one: A density functional theory study of the reactions of Mo$_2$O$_y^-$ (y= 2- 5) with methane, J. Phys. Chem. A 111 (33) (2007) 8211–8217.

[344] J. L. Mason, A. K. Gupta, A. J. McMahon, C. N. Folluo, K. Raghavachari, C. C. Jarrold, The striking influence of oxophilicity differences in heterometallic mo–mn oxide cluster reactions with water, J. Chem. Phys. 152 (5) (2020) 054301.

[345] J. Etourneau, J. Mercurio, A. Berrada, P. Hagenmuller, R. Georges, R. Bourezg, J. Gianduzzo, The magnetic and electrical properties of some rare earth tetraborides, Journal of the Less Common Metals 67 (2) (1979) 531–539.

[346] G. Schell, H. Winter, H. Rietschel, F. Gompf, Electronic structure and superconductivity in metal hexaborides, Physical Review B 25 (3) (1982) 1589.

[347] D. Jie, Z. Tong, Z. Li, D. Ji-Guang, J. Gang, W. Hong-Bin, Elastic properties and electronic structures of lanthanide hexaborides, Chinese Physics B 24 (9) (2015) 096201.

[348] A. W. Ehlers, E. J. Baerends, F. M. Bickelhaupt, U. Radius, Alternatives to the co ligand: Coordination of the isolobal analogues bf, bnh2, bn (ch3) 2, and bo- in mono-and binuclear first-row transition metal complexes, Chemistry–A European Journal 4 (2) (1998) 210–221.

[349] H. Werner, Complexes of carbon monoxide and its relatives: An organometallic family celebrates its birthday, Angewandte Chemie International Edition in English 29 (10) (1990) 1077–1089.

[350] P. PyykkÖ, Ab initio study of bonding trends among the 14-electron diatomic systems: from b2 4-to f2 4+, Molecular physics 67 (4) (1989) 871–878.

[351] X. Gong, Q.-s. Li, Y. Xie, R. B. King, H. F. Schaefer III, Boronyl ligand as a member of the isoelectronic series bo-→ co→ no+: Viable cobalt carbonyl boronyl derivatives?, Inorganic chemistry 49 (23) (2010) 10820–10832.

[352] J. Brand, H. Braunschweig, S. S. Sen, B b and b e (e= n and o) multiple bonds in the coordination sphere of late transition metals, Accounts of chemical research 47 (1) (2014) 180–191.

[353] H.-J. Zhai, Q. Chen, H. Bai, S.-D. Li, L.-S. Wang, Boronyl chemistry: The bo group as a new ligand in gas-phase clusters and synthetic compounds, Accounts of chemical research 47 (8) (2014) 2435–2445.

[354] Z. Zhang, L. Pu, Q.-s. Li, R. B. King, Controlling the reactivity of the boronyl group in platinum complexes toward cyclodimerization: A theoretical survey, Inorganic chemistry 54 (21) (2015) 10281–10286.

[355] H. Braunschweig, K. Radacki, A. Schneider, Cyclodimerization of an oxoboryl complex induced by trans ligand abstraction, Angewandte Chemie International Edition 49 (34) (2010) 5993–5996.

[356] Y. Liu, C. Liu, L. Pu, Z. Zhang, R. King, Boron monoxide dimer as a building block for boroxine based buckyballs and related cages: a theoretical study, Chemical Communications 53 (22) (2017) 3239–3241.

[357] R. H. Crabtree, The organometallic chemistry of the transition metals, John Wiley & Sons, 2009.

[358] H. Braunschweig, K. Radacki, A. Schneider, Oxoboryl complexes: boron- oxygen triple bonds stabilized in the coordination sphere of platinum, Science 328 (5976) (2010) 345–347.

[359] G. Zeng, S. Sakaki, Theoretical study on the transition-metal oxoboryl complex: M–bo bonding nature, mechanism of the formation reaction, and prediction of a new oxoboryl complex, Inorganic chemistry 51 (8) (2012) 4597–4605.

[360] S. Bertsch, J. Brand, H. Braunschweig, F. Hupp, K. Radacki, Platinum oxoboryl complexes as substrates for the formation of 1: 1, 1: 2, and 2: 1 lewis acid–base adducts and 1, 2-dipolar additions, Chemistry–A European Journal 21 (16) (2015) 6278–6285.

[361] H. Braunschweig, K. Radacki, A. Schneider, Reactivity of an oxoboryl complex toward fluorinated aryl boron reagents, Chemical Communications 46 (35) (2010) 6473–6475.

[362] Á. Vega-Vega, C. Barrientos, A. Largo, Metallic monoboronyl compounds: Prediction of their structure and comparison with the cyanide analogues, Journal of computational chemistry 38 (11) (2017) 807–815.

[363] J. Moon, J. Kim, Theoretical investigation of the molecular properties of ptbo and pdbo, Computational and Theoretical Chemistry 1108 (2017) 23–28.

[364] Y. Chang, Q.-S. Li, Y. Xie, R. B. King, Preference of three-electron donor boronyl groups over metal-metal multiple bonding in unsaturated binuclear manganese carbonyl boronyls: Comparison with isoelectronic binuclear chromium carbonyls, Inorganica Chimica Acta 471 (2018) 211–218.

[365] T. Jian, G. V. Lopez, L.-S. Wang, Photoelectron spectroscopy of biau–and bibo–: further evidence of the analogy between au and boronyl, The Journal of Physical Chemistry B 120 (8) (2016) 1635–1640.

[366] Y. Chang, Q.-S. Li, Y. Xie, R. B. King, Prospects for three-electron donor boronyl (bo) ligands and dioxodiborene (b2o2) ligands as bridging groups in binuclear iron carbonyl derivatives, Inorganic chemistry 51 (16) (2012) 8904–8915.

[367] L. Duan, B. Peng, Q. Luo, Q.-s. Li, Y. Xie, R. B. King, Diverse bonding modes and coupling reactions of the boronyl ligand in binuclear cyclopentadienyl cobalt derivatives: Analogies with isoelectronic binuclear cyclopentadienyliron carbonyls, Journal of Organometallic Chemistry 751 (2014) 662–669.

[368] Y. Chang, Q.-S. Li, Y. Xie, R. B. King, H. F. Schaefer III, Binuclear iron boronyl carbonyls isoelectronic with the well-known decacarbonyldimanganese, New Journal of Chemistry 36 (4) (2012) 1022–1030.

[369] T. Kaneko, T. Takao, H. Suzuki, A triruthenium complex capped by a triply bridging oxoboryl ligand, Angewandte Chemie International Edition 52 (45) (2013) 11884–11887.

[370] H.-J. Zhai, S.-D. Li, L.-S. Wang, Boronyls as key structural units in boron oxide clusters: B (bo) 2-and b (bo) 3, Journal of the American Chemical Society 129 (30) (2007) 9254–9255.

[371] R. Barrow, R. Clements, S. Harris, P. Jenson, The electronic spectrum of gaseous ceo, The Astrophysical Journal 229 (1979) 439–447.

[372] M. Dulick, R. Field, Electronic structure of pro: An analysis summary, Journal of Molecular Spectroscopy 113 (1) (1985) 105–141.

[373] S. A. McDonald, S. F. Rice, R. W. Field, C. Linton, Laser spectroscopy of low-lying excited states in ybo: Linkage of the yb2+ f 13 s and f 14 configurations, The Journal of chemical physics 93 (11) (1990) 7676–7686.

[374] P. Carette, The ultraviolet emission spectrum of lao, Journal of Molecular Spectroscopy 140 (2) (1990) 269–279.

[375] C. Linton, M. Dulick, R. W. Field, P. Carette, R. Barrow, Low lying electronic states of ceo, The Journal of Chemical Physics 74 (1) (1981) 189–191.

[376] R. Klingeler, N. Pontius, G. Lüttgens, P. Bechthold, M. Neeb, W. Eberhardt, Photoelectron spectroscopy of gdo-, Physical Review A 65 (3) (2002) 032502.

[377] M. C. Heaven, Probing actinide electronic structure using fluorescence and multi-photon ionization spectroscopy, Physical Chemistry Chemical Physics 8 (39) (2006) 4497–4509.

[378] G. Bujin, C. Linton, High resolution analysis of transitions to the five lowest electronic states of samarium monoxide, Journal of Molecular Spectroscopy 137 (1) (1989) 114–126.

[379] N. Kulikov, L. Kaledin, A. Kobyliansky, L. Gurvich, Dye laser and thermal emission spectroscopy of the tbo molecule, Canadian journal of physics 62 (12) (1984) 1855–1870.

[380] L. Kaledin, C. Linton, T. Clarke, R. Field, Laser spectroscopy of the lanthanide monofluorides: the ground state configuration of holmium fluoride, Journal of Molecular Spectroscopy 154 (2) (1992) 417–426.

[381] R. Klingeler, G. Lüttgens, N. Pontius, R. Rochow, P. Bechthold, M. Neeb, W. Eberhardt, Photoelectron spectra of small lao n- clusters: decreasing electron affinity upon increasing the number of oxygen atoms, in: The European Physical Journal D, Springer, 1999, pp. 263–267.

[382] T.-T. Chen, W.-L. Li, T. Jian, X. Chen, J. Li, L.-S. Wang, Prb7-: A praseodymium-doped boron cluster with a prii center coordinated by a doubly aromatic planar η7-b73- ligand, Angewandte Chemie 129 (24) (2017) 7020–7024.

[383] W.-L. Li, T.-T. Chen, D.-H. Xing, X. Chen, J. Li, L.-S. Wang, Observation of highly stable and symmetric lanthanide octa-boron inverse sandwich complexes, Proceedings of the National Academy of Sciences 115 (30) (2018) E6972–E6977.

[384] S.-B. Cheng, C. Berkdemir, A. Castleman, Observation of d–p hybridized aromaticity in lanthanum-doped boron clusters, Physical Chemistry Chemical Physics 16 (2) (2014) 533–539.

[385] T.-T. Chen, W.-L. Li, J. Li, L.-S. Wang, [la (η x-b x) la]-(x= 7–9): a new class of inverse sandwich complexes, Chemical Science 10 (8) (2019) 2534–2542.

[386] X. Chen, T.-T. Chen, W.-L. Li, J.-B. Lu, L.-J. Zhao, T. Jian, H.-S. Hu, L.-S. Wang, J. Li, Lanthanides with unusually low oxidation states in the prb3–and prb4–boride clusters, Inorganic chemistry 58 (1) (2018) 411–418.

[387] T. Kitsopoulos, C. Chick, Y. Zhao, D. Neumark, Threshold photodetachment spectroscopy of c- 5, The Journal of chemical physics 95 (7) (1991) 5479–5481.

[388] M. A. Duncan, Advances in Metal and Semiconductor Clusters: Metal Ion Solvation and Metal-Ligand Interactions, Elsevier, 2001.

[389] K. Raghavachari, C. McMichael Rohlfing, Electronic structures of the negative ions si- 2–si- 10: Electron affinities of small silicon clusters, The Journal of chemical physics 94 (5) (1991) 3670–3678.

[390] T. Kitsopoulos, C. Chick, A. Weaver, D. Neumark, Vibrationally resolved photoelectron spectra of si- 3 and si- 4, The Journal of chemical physics 93 (8) (1990) 6108–6110.

[391] D. W. Rothgeb, J. E. Mann, S. E. Waller, C. C. Jarrold, Structures of trimetallic molybdenum and tungsten suboxide cluster anions, The Journal of chemical physics 135 (10) (2011) 104312.

[392] A. Saha, K. Raghavachari, Hydrogen evolution from water through metal sulfide reactions, The Journal of chemical physics 139 (20) (2013) 204301.

[393] H.-J. Zhai, L.-M. Wang, S.-D. Li, L.-S. Wang, Vibrationally resolved photoelectron spectroscopy of bo-and bo2-: A joint experimental and theoretical study, The Journal of Physical Chemistry A 111 (6) (2007) 1030–1035.

[394] M. Frisch, G. Trucks, H. Schlegel, G. Scuseria, M. Robb, J. Cheeseman, G. Scalmani, V. Barone, G. Petersson, H. Nakatsuji, et al., Gaussian 16 (2016).

[395] T. H. Dunning Jr, Gaussian basis sets for use in correlated molecular calculations. i. the atoms boron through neon and hydrogen, The Journal of chemical physics 90 (2) (1989) 1007–1023.

[396] F. Santoro, A. Lami, R. Improta, V. Barone, Effective method to compute vibrationally resolved optical spectra of large molecules at finite temperature in the gas phase and in solution, The Journal of Chemical Physics 126 (18) (2007) 184102.

[397] F. Santoro, A. Lami, R. Improta, J. Bloino, V. Barone, Effective method for the computation of optical spectra of large molecules at finite temperature including the duschinsky and herzberg–teller effect: The qx band of porphyrin as a case study, The Journal of Chemical Physics 128 (22) (2008) 224311.

[398] V. Barone, J. Bloino, M. Biczysko, F. Santoro, Fully integrated approach to compute vibrationally resolved optical spectra: From small molecules to macrosystems, Journal of Chemical Theory and Computation 5 (3) (2009) 540–554.

[399] J. O. Kafader, J. E. Topolski, V. Marrero-Colon, S. S. Iyengar, C. C. Jarrold, The electron shuffle: Cerium influences samarium 4 f orbital occupancy in heteronuclear ce–sm oxide clusters, The Journal of chemical physics 146 (19) (2017) 194310.

[400] A. N. Alexandrova, A. I. Boldyrev, H.-J. Zhai, L.-S. Wang, E. Steiner, P. W. Fowler, Structure and bonding in b6-and b6: Planarity and antiaromaticity, The Journal of Physical Chemistry A 107 (9) (2003) 1359–1369.

[401] C. Romanescu, A. P. Sergeeva, W.-L. Li, A. I. Boldyrev, L.-S. Wang, Planarization of b7- and b12- clusters by isoelectronic substitution: Alb6- and alb11-, Journal of the American Chemical Society 133 (22) (2011) 8646–8653.

[402] E. I. Solomon, R. A. Scott, R. B. King, Computational inorganic and bioinorganic chemistry, John Wiley & Sons, 2013.

[403] K. Yamaguchi, F. Jensen, A. Dorigo, K. Houk, A spin correction procedure for unrestricted hartree-fock and møller-plesset wavefunctions for singlet diradicals and polyradicals, Chemical physics letters 149 (5-6) (1988) 537–542.

[404] Y. Kitagawa, T. Saito, M. Ito, M. Shoji, K. Koizumi, S. Yamanaka, T. Kawakami, M. Okumura, K. Yamaguchi, Approximately spin-projected geometry optimization method and its application to di-chromium systems, Chemical physics letters 442 (4-6) (2007) 445–450.

[405] H. P. Hratchian, Communication: An efficient analytic gradient theory for approximate spin projection methods, The Journal of Chemical Physics 138 (10) (2013) 101101. arXiv:https://doi.org/10.1063/1.4795429, doi:10.1063/1.4795429.
URL https://doi.org/10.1063/1.4795429

[406] L. M. Thompson, H. P. Hratchian, Second derivatives for approximate spin projection methods, The Journal of chemical physics 142 (5) (2015) 054106.

[407] L. M. Thompson, H. P. Hratchian, On approximate projection models, Molecular Physics 117 (9-12) (2019) 1421–1429.

[408] W.-L. Li, X. Chen, T. Jian, T.-T. Chen, J. Li, L.-S. Wang, From planar boron clusters to borophenes and metalloborophenes, Nature Reviews Chemistry 1 (10) (2017) 0071.

[409] J. Lafferty, Boride cathodes, Journal of Applied Physics 22 (3) (1951) 299–309.

[410] L. Liu, Y.-M. Yiu, T.-K. Sham, Electronic structures of lab6 and ceb6 single crystals: X-ray absorption near-edge structure studies at the b k-edge and the la and ce giant resonance, Journal of Electron Spectroscopy and Related Phenomena 184 (3-6) (2011) 188–191.

[411] Y. Peysson, C. Ayache, B. Salce, S. Kunii, T. Kasuya, Thermal conductivity of ceb6 and lab6, Journal of magnetism and magnetic materials 59 (1-2) (1986) 33–40.

[412] B. Lüthi, S. Blumenröder, B. Hillebrands, E. Zirngiebl, G. Güntherodt, K. Winzer, Elastic and magnetoelastic effects in ceb 6, Zeitschrift für Physik B Condensed Matter 58 (1) (1984) 31–38.

[413] A. L. Kaledin, M. C. Heaven, R. W. Field, L. A. Kaledin, The electronic structure of the lanthanide monohalides: A ligand field approach, Journal of Molecular Spectroscopy 179 (2) (1996) 310–319.

[414] D. K. Böhme, H. Schwarz, Gas-phase catalysis by atomic and cluster metal ions: The ultimate single-site catalysts, Angewandte Chemie International Edition 44 (16) (2005) 2336–2354.

[415] W.-J. Chen, H.-J. Zhai, X. Huang, L.-S. Wang, On the electronic structure of mono-rhenium oxide clusters: and reon (n= 3, 4), Chemical Physics Letters 512 (1) (2011) 49–53.

[416] W. Kutzelnigg, The relativistic many body problem in molecular theory, Physica scripta 36 (3) (1987) 416.

[417] G. Hong, M. Dolg, L. Li, A comparison of scalar-relativistic zora and dkh density functional schemes: monohydrides, monooxides and monofluorides of la, lu, ac and lr, Chemical physics letters 334 (4-6) (2001) 396–402.

[418] P. Pyykko, Relativistic effects in structural chemistry, Chemical Reviews 88 (3) (1988) 563–594.

[419] M. C. Payne, M. P. Teter, D. C. Allan, T. A. Arias, J. D. Joannopoulos, Iterative minimization techniques for ab initio total-energy calculations: molecular dynamics and conjugate gradients, Rev. Mod. Phys. 64 (1992) 1045–1097. doi:10.1103/RevModPhys.64.1045.
URL https://link.aps.org/doi/10.1103/RevModPhys.64.1045

[420] T. R. Cundari, M. T. Benson, M. L. Lutz, S. O. Sommerer, Effective core potential approaches to the chemistry of the heavier elements, Reviews in computational chemistry (1996) 145–202.

[421] G. Frenking, I. Antes, M. Böhme, S. Dapprich, A. W. Ehlers, V. Jonas, A. Neuhaus, M. Otto, R. Stegmann, A. Veldkamp, et al., Pseudopotential calculations of transition metal compounds: scope and limitations, Reviews in computational chemistry (1996) 63–144.

[422] T. Leininger, A. Nicklass, W. Küchle, H. Stoll, M. Dolg, A. Bergner, The accuracy of the pseudopotential approximation: Non-frozen-core effects for spectroscopic constants of alkali fluorides xf (x= k, rb, cs), Chemical physics letters 255 (4-6) (1996) 274–280.

[423] P. Schwerdtfeger, T. Fischer, M. Dolg, G. Igel-Mann, A. Nicklass, H. Stoll, A. Haaland, The accuracy of the pseudopotential approximation. i. an analysis of the spectroscopic constants for the electronic ground states of incl and incl3 using various three valence electron pseudopotentials for indium, The Journal of chemical physics 102 (5) (1995) 2050–2062.

[424] T. Leininger, A. Nicklass, H. Stoll, M. Dolg, P. Schwerdtfeger, The accuracy of the pseudopotential approximation. ii. a comparison of various core sizes for indium pseudopotentials in calculations for spectroscopic constants of inh, inf, and incl, The Journal of chemical physics 105 (3) (1996) 1052–1059.

[425] P. Schwerdtfeger, J. R. Brown, J. K. Laerdahl, H. Stoll, The accuracy of the pseudopotential approximation. iii. a comparison between pseudopotential and all-electron methods for au and auh, The Journal of Chemical Physics 113 (17) (2000) 7110–7118.

[426] M. Guell, J. M. Luis, M. Sola, M. Swart, Importance of the basis set for the spin-state energetics of iron complexes, The Journal of Physical Chemistry A 112 (28) (2008) 6384–6391.

[427] S. F. Vyboishchikov, A. Sierraalta, G. Frenking, Topological analysis of electron density distribution taken from a pseudopotential calculation, Journal of computational chemistry 18 (3) (1997) 416–429.

[428] J. Cirera, E. Ruiz, Exchange coupling in cuiigdiii dinuclear complexes: A theoretical perspective, Comptes Rendus Chimie 11 (10) (2008) 1227–1234.

[429] K. Hirao, Multireference møller—plesset perturbation theory for high-spin open-shell systems, Chemical physics letters 196 (5) (1992) 397–403.

[430] T. Kar, S. Scheiner, A. Sannigrahi, Ab initio calculations of hardness and chemical potential of open shell systems using scf, mp2 and mp4 methods, Journal of Molecular Structure: THEOCHEM 427 (1-3) (1998) 79–85.

[431] K. Wolinski, H. L. Sellers, P. Pulay, Consistent generalization of the møller-plesset partitioning to open-shell and multiconfigurational scf reference states in many-body perturbation theory, Chemical physics letters 140 (3) (1987) 225–231.

[432] J. J. McDouall, K. Peasley, M. A. Robb, A simple mc scf perturbation theory: Orthogonal valence bond møller-plesset 2 (ovb mp2), Chemical physics letters 148 (2-3) (1988) 183–189.

[433] K. Andersson, P. A. Malmqvist, B. O. Roos, A. J. Sadlej, K. Wolinski, Second-order perturbation theory with a casscf reference function, Journal of Physical Chemistry 94 (14) (1990) 5483–5488.

[434] K. Hirao, Multireference møller—plesset method, Chemical physics letters 190 (3-4) (1992) 374–380.

[435] O. Sinanoğlu, Many-electron theory of atoms and molecules. i. shells, electron pairs vs many-electron correlations, The Journal of Chemical Physics 36 (3) (1962) 706–717.

[436] F. Jensen, Introduction to computational chemistry, John wiley & sons, 2017.

[437] J. L. Mason, H. Harb, A. A. Taka, A. J. McMahon, C. D. Huizenga, H. Corzo, H. P. Hratchian, C. C. Jarrold, Photoelectron spectra of gd2o2–and nonmonotonic photon-energy-dependent variations in populations of close-lying neutral states, The Journal of Physical Chemistry A 125 (3) (2021) 857–866.

[438] V. Antonov, L. Bekenov, A. Yaresko, Electronic structure of strongly correlated systems, Advances in Condensed Matter Physics 2011 (2011).

[439] C. Monroe, W. Campbell, L.-M. Duan, Z.-X. Gong, A. Gorshkov, P. Hess, R. Islam, K. Kim, G. Pagano, P. Richerme, et al., Programmable quantum simulations of spin systems with trapped ions, arXiv preprint arXiv:1912.07845 (2019).

[440] C. A. Gould, K. R. McClain, J. M. Yu, T. J. Groshens, F. Furche, B. G. Harvey, J. R. Long, Synthesis and magnetism of neutral, linear metallocene complexes of terbium (ii) and dysprosium (ii), Journal of the American Chemical Society 141 (33) (2019) 12967–12973.

[441] A. M. Tokmachev, D. V. Averyanov, A. N. Taldenkov, O. E. Parfenov, I. A. Karateev, I. S. Sokolov, V. G. Storchak, Lanthanide f 7 metalloxenes–a class of intrinsic 2d ferromagnets, Materials Horizons 6 (7) (2019) 1488–1496.

[442] P. Carette, A. Hocquet, Ligand field calculation of the lower electronic energy levels of the lanthanide monoxides, Journal of Molecular Spectroscopy 131 (2) (1988) 301–324.

[443] E. P. Wigner, On the behavior of cross sections near thresholds, Physical Review 73 (9) (1948) 1002.

[444] K. Amann-Winkel, D. T. Bowron, T. Loerting, Structural differences between unannealed and expanded high-density amorphous ice based on isotope substitution neutron diffraction, Molecular Physics 117 (22) (2019) 3207–3216.

[445] V. D. Moravec, C. C. Jarrold, Study of the low-lying states of nio- and nio using anion photoelectron spectroscopy, The Journal of chemical physics 108 (5) (1998) 1804–1810.

[446] S. E. Waller, J. E. Mann, C. C. Jarrold, Asymmetric partitioning of metals among cluster anions and cations generated via laser ablation of mixed aluminum/group 6 transition metal targets, The Journal of Physical Chemistry A 117 (8) (2013) 1765–1772.

[447] L. M. Thompson, H. P. Hratchian, On approximate projection models, Molecular Physics 117 (9-12) (2019) 1421–1429.

[448] F. La Cava, A. Fringuello Mingo, L. Miragoli, E. Terreno, E. Cappelletti, L. Lattuada, L. Poggi, S. Colombo Serra, Synthesis, characterization, and biodistribution of a dinuclear gadolinium complex with improved properties as a blood pool mri agent, ChemMedChem 13 (8) (2018) 824–834.

[449] M. Shoji, K. Koizumi, Y. Kitagawa, T. Kawakami, S. Yamanaka, M. Okumura, K. Yamaguchi, A general algorithm for calculation of heisenberg exchange integrals j in multispin systems, Chemical physics letters 432 (1-3) (2006) 343–347.

[450] H. Corzo, A. A. Taka, A. Pribram-Jones, H. P. Hratchian, Projection-based converging different SCF solutions. *manuscript in prepararion*.

[451] A. T. Gilbert, N. A. Besley, P. M. Gill, Self-consistent field calculations of excited states using the maximum overlap method (mom), The Journal of Physical Chemistry A 112 (50) (2008) 13164–13171.

[452] G. M. Barca, A. T. Gilbert, P. M. Gill, Communication: Hartree-fock description of excited states of h2 (2014).

[453] J. L. Mason, J. E. Topolski, J. Ewigleben, S. S. Iyengar, C. C. Jarrold, Photoelectrons are not always quite free, The journal of physical chemistry letters 10 (2) (2018) 144–149.

[454] A. Messiah, L. I. Schiff, Quantum mechanics, Vol. 643, McGraw-Hill College, 1968.

[455] L. A. Kaledin, M. G. ERICKsoN, M. C. HEAvEN, Laser spectroscopy of gdo: ligand field assignments of 4f7 (8s) 6p← 4f7 (8s) 6s transitions, Journal of Molecular Spectroscopy 165 (2) (1994) 323–333.

[456] R. Klingeler, N. Pontius, G. Lüttgens, P. Bechthold, M. Neeb, W. Eberhardt, Photoelectron spectroscopy of gdo-, Physical Review A 65 (3) (2002) 032502.

[457] L. E. Roy, T. Hughbanks, Magnetic coupling in dinuclear gd complexes, Journal of the American Chemical Society 128 (2) (2006) 568–575.

[458] K. R. Meihaus, J. F. Corbey, M. Fang, J. W. Ziller, J. R. Long, W. J. Evans, Influence of an inner-sphere k+ ion on the magnetic behavior of n23–radical-bridged dilanthanide complexes isolated using an external magnetic field, Inorganic chemistry 53 (6) (2014) 3099–3107.

[459] J. D. Rinehart, M. Fang, W. J. Evans, J. R. Long, Strong exchange and magnetic blocking in n 2 3–radical-bridged lanthanide complexes, Nature Chemistry 3 (7) (2011) 538–542.

[460] M. L. Weichman, B. Vlaisavljevich, J. A. DeVine, N. S. Shuman, S. G. Ard, T. Shiozaki, D. M. Neumark, A. A. Viggiano, Electronic structure of smo and smo- via slow photoelectron velocity-map imaging spectroscopy and spin-orbit caspt2 calculations, The Journal of Chemical Physics 147 (23) (2017) 234311.

[461] R. Van Zee, R. Ferrante, K. Zeringue, W. Weltner Jr, The ground state and zero-field splitting of the gdo molecule, The Journal of Chemical Physics 75 (11) (1981) 5297–5299.

[462] J.-P. Costes, F. Dahan, F. Nicodeme, A trinuclear gadolinium complex: structure and magnetic properties, Inorganic Chemistry 40 (20) (2001) 5285–5287.

[463] D.-F. Yuan, Y. Liu, C.-H. Qian, G. S. Kocheril, Y.-R. Zhang, B. M. Rubenstein, L.-S. Wang, Polarization of valence orbitals by the intramolecular electric field from a diffuse dipole-bound electron, The Journal of Physical Chemistry Letters 11 (18) (2020) 7914–7919.

[464] B. Langer, J. Viefhaus, O. Hemmers, A. Menzel, R. Wehlitz, U. Becker, High-resolution photoelectron spectrometry study of conjugate shakeup processes in the li 1s threshold region, Physical review A 43 (3) (1991) 1652.

[465] K. Randall, A. Kilcoyne, H. Köppe, J. Feldhaus, A. Bradshaw, J.-E. Rubensson, W. Eberhardt, Z. Xu, P. Johnson, Y. Ma, Photon energy dependence of the high resolution c 1s photoelectron spectrum of co in the threshold region, Physical review letters 71 (8) (1993) 1156.

[466] M. Fechner, P. Zahn, S. Ostanin, M. Bibes, I. Mertig, Switching magnetization by 180 with an electric field, Physical review letters 108 (19) (2012) 197206.

[467] K.-H. Yun, M. Lee, Y.-C. Chung, Electric field as a novel switch for magnetization of fe/graphene system, Journal of magnetism and magnetic materials 362 (2014) 93–96.

184

[468] S. E. Barnes, J. Ieda, S. Maekawa, Rashba spin-orbit anisotropy and the electric field control of magnetism, Scientific reports 4 (1) (2014) 1–5.

[469] Z. Zhou, M. Trassin, Y. Gao, Y. Gao, D. Qiu, K. Ashraf, T. Nan, X. Yang, S. R. Bowden, D. T. Pierce, et al., Probing electric field control of magnetism using ferromagnetic resonance, Nature communications 6 (1) (2015) 1–7.

[470] W.-G. Wang, M. Li, S. Hageman, C. Chien, Electric-field-assisted switching in magnetic tunnel junctions, Nature materials 11 (1) (2012) 64–68.

[471] N. Negulyaev, V. Stepanyuk, W. Hergert, J. Kirschner, Electric field as a switching tool for magnetic states in atomic-scale nanostructures, Physical review letters 106 (3) (2011) 037202.

[472] L. Zhang, J. Meng, F. Yao, X. Liu, J. Meng, H. Zhang, Strong-correlated behavior of 4 f electrons and 4 f 5 d hybridization in pro 2, Scientific reports 8 (1) (2018) 1–8.

[473] A. E. Clark, J. L. Sonnenberg, P. J. Hay, R. L. Martin, Density and wave function analysis of actinide complexes: What can fuzzy atom, atoms-in-molecules, mulliken, löwdin, and natural population analysis tell us?, The Journal of chemical physics 121 (6) (2004) 2563–2570.